Metal nanoparticles encapsulated in membrane-like zeolite single crystals : application to selective catalysis

Shiwen Li

N° d'ordre : 57 - 2015

Année 2015

THESE DE L'UNIVERSITE DE LYON

Présentée devant

L'UNIVERSITE CLAUDE BERNARD LYON 1

École doctorale de Chimie

Pour l'obtention du **DIPLOME DE DOCTORAT**

(arrêté du 7 août 2006)

soutenue publiquement le 05/05/2015

par

Shiwen LI

Metal Nanoparticles Encapsulated in Membrane-like Zeolite Single Crystals Application to Selective Catalysis

Directeur de thèse : David FARRUSSENG
Alain TUEL

Jury :

M. Stéphane DANIELE	Professeur, Université Claude Bernard Lyon 1
Mme Claudia WEIDENTHALER (Rapporteur)	DR-HABIL, Max-Planck-Institut, Germany
Mme Pascale MASSIANI (Rapporteur)	DR-CNRS, LRS, Paris
M. Nicolas BATS	Dr, IFP Energies Nouvelles, Solaize
M. David FARRUSSENG	DR-CNRS, IRCELYON, Villeurbanne
M. Alain TUEL	DR-CNRS, IRCELYON, Villeurbanne

UNIVERSITE CLAUDE BERNARD - LYON 1

Président de l'Université	**M. François-Noël GILLY**
Vice-président du Conseil d'Administration	M. le Professeur Hamda BEN HADID
Vice-président du Conseil des Etudes et de la Vie Universitaire	M. le Professeur Philippe LALLE
Vice-président du Conseil Scientifique	M. le Professeur Germain GILLET
Directeur Général des Services	M. Alain HELLEU

COMPOSANTES SANTE

Faculté de Médecine Lyon Est – Claude Bernard	Directeur : M. le Professeur J. ETIENNE
Faculté de Médecine et de Maïeutique Lyon Sud – Charles Mérieux	Directeur : Mme la Professeure C. BURILLON
Faculté d'Odontologie	Directeur : M. le Professeur D. BOURGEOIS
Institut des Sciences Pharmaceutiques et Biologiques	Directeur : Mme la Professeure C. VINCIGUERRA
Institut des Sciences et Techniques de la Réadaptation	Directeur : M. le Professeur Y. MATILLON
Département de formation et Centre de Recherche en Biologie Humaine	Directeur : Mme. la Professeure A-M. SCHOTT

COMPOSANTES ET DEPARTEMENTS DE SCIENCES ET TECHNOLOGIE

Faculté des Sciences et Technologies	Directeur : M. F. DE MARCHI
Département Biologie	Directeur : M. le Professeur F. FLEURY
Département Chimie Biochimie	Directeur : Mme Caroline FELIX
Département GEP	Directeur : M. Hassan HAMMOURI
Département Informatique	Directeur : M. le Professeur S. AKKOUCHE
Département Mathématiques	Directeur : M. le Professeur Georges TOMANOV
Département Mécanique	Directeur : M. le Professeur H. BEN HADID
Département Physique	Directeur : M. Jean-Claude PLENET
UFR Sciences et Techniques des Activités Physiques et Sportives	Directeur : M. Y.VANPOULLE
Observatoire des Sciences de l'Univers de Lyon	Directeur : M. B. GUIDERDONI
Polytech Lyon	Directeur : M. P. FOURNIER
Ecole Supérieure de Chimie Physique Electronique	Directeur : M. G. PIGNAULT
Institut Universitaire de Technologie de Lyon 1	Directeur : M. le Professeur C. VITON
Ecole Supérieure du Professorat et de l'Education	Directeur : M. le Professeur A. MOUGNIOTTE
Institut de Science Financière et d'Assurances	Directeur : M. N. LEBOISNE

Acknowledgements:

I would like first to thank the European Community for providing me the scholarship for this PhD work within the CAREAN project.

I would like to give my deepest appreciations to my supervisors: David, my charming and wisest boss, who provides me this opportunity to pursue my study in France. I enjoy a lot of working in his team and with him during these three years. He guides me both in the field of science and humanities. Several times I got blocked in my work and losing the confidence for my PhD and my future, he can always give me the effective solutions and cheer me up!
Alain is like my family in France; we work and discuss a lot during these three years. His brilliant ideas and efficiencies in research inspire me a lot. He is the one who let me turn my work into my passion, who makes me never stop French learning. I appreciated a lot of all his help every time when I had problems or I got confused. Without his guidance this dissertation would not appear like the one in front of you.

I would like to deeply thank the committee for accepting this PhD work.

I would to thank the scientific services of IRCELYON, especially, the microscopy group, Laurence and Mimoun who teach me and let me use JEOL 2010 frequently, and the great contributions on ETEM measurements carried out by Thierry, Mimoun, Francisco and Lucian. I would like to thank Cindy who is doing CO oxidation with propylene reaction with me. Thank to Frederic for the help of hydrogenation reactions in his “smart” DRIFT cell. And thank Jean-Luc and Franck, who guide me a lot on the work of alloy particles and CO oxidation tests. I would like also to thank Laurent, Cecile, David, Edouard and Emmanuel for the experimental and technical help. Thank my colleagues in my office and all the group members in engineer and material team. Thanks to my Chinese friends in Lyon, Youmin, Xiaolong, Hongpeng, Jingxuan, Yuting, Shanshan ……

Finally, I would like to thank my family who supports me all the time no matter how far away I am and my husband Xuehao who is always on my side for years……

Table of Contents

Résumé:

De par leurs propriétés particulières, les nanoparticules métalliques trouvent aujourd'hui de nombreuses applications en optique, électronique et chimie, en particulier en catalyse hétérogène. L'emploi de nanoparticules de métaux nobles supportées (Pt, Pd…) comme catalyseurs d'hydrogénation est connue depuis longtemps. Plus récemment, de nombreux travaux ont montré que l'or peut également être très actif en catalyse d'oxydation s'il est suffisamment dispersé sur des supports tels que l'oxyde de titane.

L'activité catalytique dépend directement de la dispersion des nanoparticules, c'est-à-dire de leur taille sur le support. Différentes méthodes ont été développées pour déposer des nanoparticules de taille contrôlées sur différents supports, certaines chimiques (imprégnation, dépôt-précipitation), d'autres physiques (ablation Laser). Cependant, ces solides doivent résister à des conditions souvent extrêmes lors de réactions catalytiques, en particulier à de très fortes températures. Sous l'effet de la température, l'interaction entre le métal et le support n'est pas suffisamment forte pour empêcher le frittage, c'est-à-dire le regroupement des particules en agrégats qui conduit à une perte irréversible de l'activité catalytique. Afin de prolonger durablement l'activité des catalyseurs, il est donc impératif de ralentir, voire éliminer totalement le frittage. Différentes stratégies peuvent être utilisées comme la formation d'alliages ou l'encapsulation dans des systèmes poreux. Si la première méthode modifie les propriétés intrinsèques de la particule, la seconde pose des problèmes de limitations diffusionnelles, particulièrement lors de réactions en phase liquide.

Une alternative consiste à préparer des composés de type « core-shell » ou « yolk-shell », dans lesquels les particules sont isolées entre elles et protégées par une coquille suffisamment poreuse pour permettre l'accès aux petites molécules. Ces matériaux ont été particulièrement étudiés ces dernières années et ils ont montré une excellente stabilité lors de réactions catalytiques à haute température. Néanmoins, les particules sont souvent relativement grosses (> 10 nm), ce qui impacte fortement l'activité catalytique en particulier dans le cas de particules d'or. D'autre part, les coquilles étant mésoporeuses (taille de pores de quelques nm), elles ne jouent aucun rôle en tant que membranes pour influer sur l'activité et la sélectivité des réactions.

Le but de cette thèse était donc de préparer de nouveaux matériaux de type « yolk-shell » dans lesquels une nanoparticule (métallique ou oxyde) est protégée par une coquille microporeuse (pores entre 0,5 et 1 nm). Notre choix s'est alors tourné vers les zéolithes, qui sont des aluminosilicates microporeux cristallisés avec des tailles de pores parfaitement calibrées. Les zéolithes utilisées dans ce travail possèdent la structure MFI (pores d'environ 0.55 nm) et leur composition est variable, depuis les solides purement siliciques (silicalite-1) jusqu'aux aluminosilicates (ZSM-5).

I. Métaux nobles (Au, Pt, Pd, Au) dans la silicalite-1

Nous avions montré que les cristaux de silicalite-1 pouvaient être facilement transformés en nanoboites fermées sous l'effet d'une dissolution et d'une recristallisation à haute température.[1, 2] La formation de nanoparticules dans ces boites par imprégnation d'une solution métallique suivie d'une réduction s'étant avérée inefficace, nous avons alors développé une méthode directe, qui consiste à former la nanoparticule d'or, de platine ou de palladium conjointement à la création de la boite zéolithique.[3-5] La zéolithe est d'abord imprégnée par une solution d'un sel du métal puis ensuite traitée par une solution de TPAOH : sous l'effet de la basicité et de la température, le métal est réduit et forme une unique particule à l'intérieur de chaque cristal (Fig. 1).

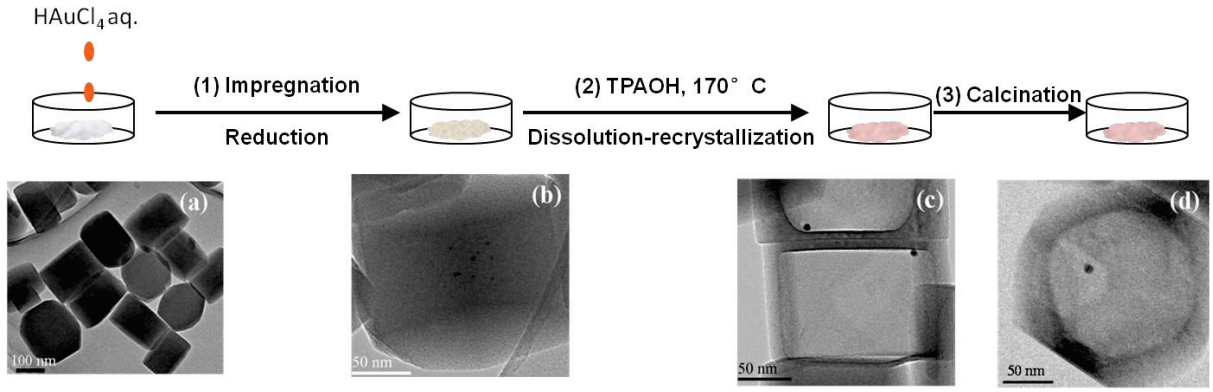

Figure 1 : schéma de formation des composés de type yolk-shell avec particules d'or.

Ces matériaux seront dénommés Au@Sil-1, Pt@Sil-1… par la suite. Dans le cas de l'or et du palladium, nous avons montré que la taille moyenne des particules pouvait être facilement contrôlée par la concentration de la solution métallique utilisée lors de l'imprégnation. Le cas de l'argent est un peu plus problématique : lors du traitement par TPAOH, il ne se forme pas une particule unique mais une dizaine de nanoparticules par boite. Lors de la calcination sous air, ces particules migrent hors des boites sous la forme d'oxydes d'argent. Cette migration hors des boites sous l'effet de la température a été suivie par microscopie électronique environnementale à transmission (ETEM, 1mbar O_2). L'étude a montré que les particules sortent vers 450°C, température à laquelle la porosité de la zéolithe est libérée par décomposition des molécules organiques.

Des tests de frittage sur des particules de platine ont montré que les métaux encapsulés dans la silicalite-1 sont nettement plus résistants que des nanoparticules déposées sur silice.

Certains de ces matériaux ont été comparés à des catalyseurs standards dans des réactions catalytiques impliquant les propriétés membranaires de la zéolithe. Ainsi, Pt@Sil-1 catalyse l'oxydation du monoxyde de carbone CO, même en présence d'un poison comme le propylène. En

revanche, les catalyseurs supportés voient leur activité considérablement diminuée par empoisonnement des sites catalytiques. La forte activité de Pt@Sil-1 a été attribuée à la présence de

La zéolithe qui joue le rôle d'une membrane et limite considérablement l'accès de l'oléfine aux particules de platine. Pt@Sil-1 a également été utilisé comme catalyseur d'hydrogénation des benzènes substitués et son activité comparée à celle d'un catalyseur supporté sur silice. Alors que ce dernier hydrogène indifféremment le toluène et le mésitylène, Pt@Sil-1 ne converti que le toluène. La différence a été attribuée au fait que le mésitylène est trop volumineux (diamètre cinétique 0.87 nm) pour pénétrer les pores de la zéolithe.

II. Extension aux métaux de transition (Co, Ni, Cu) dans la silicalite-1

Contrairement aux métaux nobles, l'utilisation de métaux de transition ne conduit pas à la formation de particules lors du traitement par TPAOH. Les nanoboites de silicalite-1 contiennent des phyllosilicates lamellaires qui recouvrent les parois internes de la zéolithe (Fig. 2).[6] Les particules ne sont obtenues qu'après réduction des phyllosilicates à haute température (T > 700°C) sous hydrogène. Il ne se forme pas une unique particule, comme dans le cas des métaux nobles, mais plusieurs petites, dont certaines sont localisées à l'intérieur des parois de la boite zéolithique.

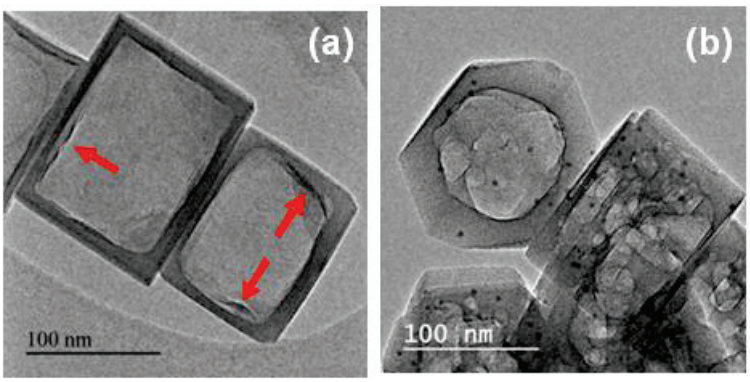

Figure 2 : phyllosilicates de cobalt et particules correspondantes dans la silicalite-1.

Pour la silicalite-1, les teneurs sont limitées à quelques pourcents avec une taille comprise entre 3 et 4 nm pour Co et Ni. Le cas du cuivre est légèrement différent puisqu'on observe deux populations distinctes dans un solide chargé à 2,8% en poids: l'une autour de 1,5 nm, l'autre d'environ10 nm.

III.Nanoparticules dans la ZSM-5

La synthèse a alors été étendue à la zéolithe ZSM-5, ouvrant la voie à de nouveaux catalyseurs bifonctionnels, conjuguant les fonctions hydrogénante ou oxydante de la particule à l'acidité de la zéolithe.

III.1. Synthèses par dissolution/recristallisation en présence de TPAOH

Nous avons tout d'abord optimisé le protocole d'obtention des nanoboites avec TPAOH en partant d'une ZSM-5 à fort gradient de composition, avec une surface enrichie en aluminium. Les nanoboites ainsi obtenues possèdent des caractéristiques identiques à celles préparées avec la silicalite-1, à savoir des parois régulières d'environ 15-20 nm d'épaisseur. L'addition de platine conduit également à la formation de nanoparticules, avec une taille tout à fait similaire à celle obtenue avec la silicalite-1. En revanche, il n'a pas été possible d'obtenir des particules d'or en traitant une ZSM-5 par TPAOH. Une seconde stratégie a alors été mise au point, qui consiste à imprégner une silicalite-1 avec le sel d'or et à introduire les ions Al^{3+} lors de la recristallisation. Comme pour la silicalite-1, l'addition de métaux de transition (Co, Ni, Cu) conduit à la formation de phyllosilicates qui tapissent les parois internes de la cavité et les nanoparticules ne sont obtenues qu'après réduction à haute température. Néanmoins, les solides obtenus diffèrent notablement de ceux obtenus avec la silicalite-1 : les nanoboites de ZSM-5 ne contiennent généralement que 2 à 3 particules, la teneur maximale en métal est plus élevée (jusqu'à 7-8% en poids) et la taille des particules est plus importante (15-20 nm pour des teneurs de 7,5 % en poids) (Fig. 3).

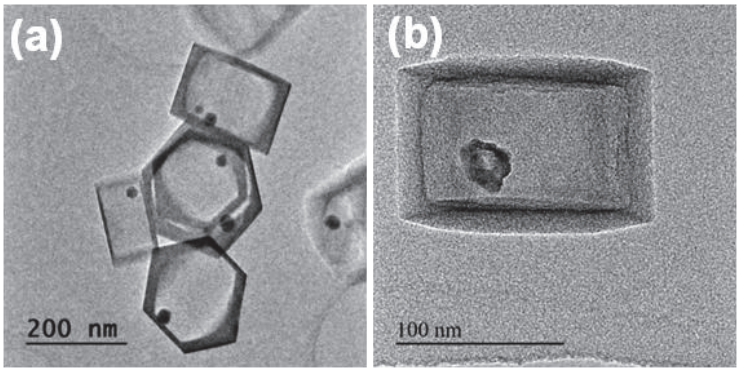

Figure 3 : particules de cobalt dans la ZSM-5 après réduction sous H_2 et réoxydation sous air.

Comme précédemment avec la silicalite-1, le cuivre se comporte différemment des deux autres métaux (Co et Ni) avec deux populations de particules qui peuvent coexister au sein même d'un cristal. Le comportement thermique des particules de cobalt dans Co@ZSM-5 a été étudié en effectuant des cycles d'oxydation/réduction à haute température. Lors de l'oxydation à 250°C, les

particules de Co s'évident et se transforment en coquilles creuses poly-cristallines (Fig. 3). Lors de la réduction sous hydrogène, ces structures s'effondrent avec formation de plusieurs petites particules dans la nanoboite. Le solide Ni@ZSM-5 a été utilisé comme catalyseur d'hydrogénation des benzènes substitués et comparé avec un catalyseur commercial déposé sur alumine. Comme pour le platine, Ni@ZSM-5 ne converti que le toluène alors que le catalyseur déposé est également actif pour hydrogéner le mésitylène.

III.2. Synthèses par désilication en présence de Na_2CO_3

La dissolution d'une zéolithe à fort gradient de composition par le carbonate de sodium conduit à la formation de nanoboites dont l'épaisseur des parois dépend directement de la concentration initiale en Na_2CO_3. A forte concentration (solution 1M) il est possible d'obtenir des solides dont les parois ne dépassent pas 10 nm et qui sont considérablement plus riches en aluminium que la zéolithe de départ. Contrairement au traitement par TPAOH, les parois des boites ne sont pas parfaitement rectilignes ; on observe plutôt des cristaux plus ou moins sphériques. Le traitement d'une zéolithe préalablement imprégnée avec une solution de platine conduit à une multitude de petites particules (diamètre environ 2,5 nm), même après réduction à 500°C (Fig. 4).

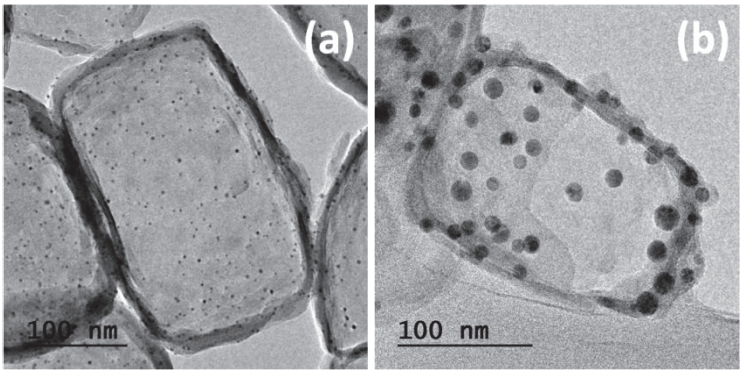

Figure 4 : particules de Pt et Co dans une ZSM-5 traitée par une solution de Na_2CO_3.

Ces particules sont particulièrement stables sous hydrogène avec une taille qui n'excède pas 2,8 nm à 750°C. Pt@ZSM-5 obtenue après désilication par Na_2CO_3 est un excellent catalyseur d'hydrogénation des benzènes substitués. Il est beaucoup plus actif que le solide préparé avec TPAOH mais il est moins sélectif : la fragilité des parois zéolithiques (épaisseur 10-15 nm) fait que de nombreuses boites sont cassées et que le platine est alors accessible aux grosses molécules comme le mésitylène.

La dissolution par Na_2CO_3 a également été effectuée sur des ZSM-5 imprégnées par des solutions de Co, Ni et Cu. Comme avec TPAOH, le traitement produit des phyllosilicates, qui doivent être alors réduits à haute température pour former les particules. Malgré des teneurs en métal

particulièrement élevées (environ 20 % de cobalt ou nickel en poids), la dispersion des particules reste bonne avec une taille en dessous de 10 nm. Contrairement au traitement avec TPAOH, la taille des particules varie peu avec la teneur en métal; par contre elle dépend fortement de la concentration de la solution de carbonate de sodium utilisée.

IV. Alliages métalliques

Comme pour les particules mono métalliques, différents matériaux ont été préparés en traitant les zéolithes soit par TPAOH, soit par Na_2CO_3.

IV.1. Traitement par TPAOH

Les métaux constitutifs de l'alliage peuvent être introduits soit simultanément (mélange des solutions lors de l'imprégnation), soit l'un après l'autre. L'introduction simultanée de Pt et Pd dans la silicalite-1 conduit à des particules régulières identiques à celles obtenues avec un métal pur. Une analyse EDX effectuée sur plusieurs particules montre qu'elles contiennent les deux métaux, avec un rapport Pt/Pd qui varie d'une particule à une autre, mais dont la valeur moyenne est très proche du rapport Pt/Pd introduit au départ. Une étude plus poussée en STEM-HAADF indique que chaque particule est homogène, et qu'il n'y a pas ségrégation d'un métal avec formation de type cœur-coquille ou Janus (Fig. 5).

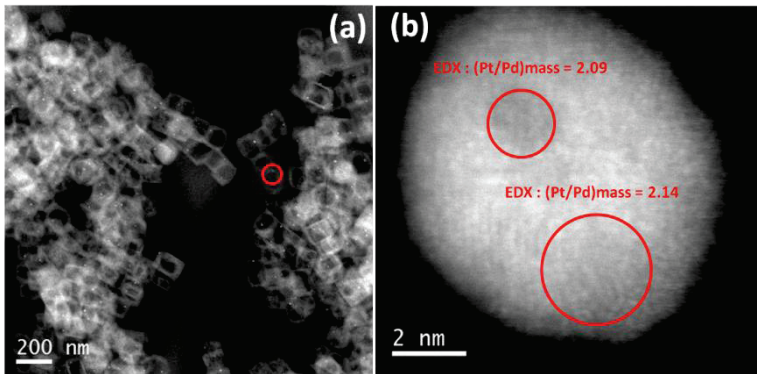

Figure 5 : Image HAADF d'une particule Pt/Pd dans la ZSM-5 et mesures EDX sur une particule.

Des résultats similaires ont été obtenues avec des mélanges Pt/Ag et Pd/Ag ainsi que sur des solides avec différents rapports Pt/Pd. Néanmoins, dans le cas d'alliages avec l'argent, une partie du métal sort des cavités lors de la calcination et la composition des particules encapsulées est toujours déficitaire en Ag.

La méthode a également permis d'encapsuler des nanoparticules d'alliages dans la ZSM-5 avec, dans le cas des alliages Pt/Pd, la possibilité de séparer les deux métaux en une grosse particule de Pd

dans la cavité et de nombreuses petites particules de Pt dans les parois de la zéolithe. La co-imprégnation ne fonctionne pas pour les alliages Au/Ag; il est en revanche possible de former des alliages par imprégnation d'argent sur des particules d'or déjà formées. La formation d'un alliage a été confirmée par les résultats d'oxydation du CO à faible température. Les particules Au/Ag sont stables et résistent à des températures de 500°C, même en présence de vapeur d'eau.

IV.2. Traitement par Na_2CO_3

Des nanoparticules Pt/Pd ont également été obtenues par co-imprégnation d'une ZSM-5 suivie d'un traitement par Na_2CO_3. Comme dans le cas de Pt seul, les nanoparticules d'environ 2 nm en taille sont réparties sur la surface interne des parois.

V. Conclusions et perspectives

Nous avons développé un protocole de synthèse original pour encapsuler des nanoparticules de taille ajustable dans des nanoboites zéolithiques de structure MFI. Excepté le cas des éléments de transition pour lesquels la synthèse passe par l'intermédiaire d'un silicate lamellaire, la synthèse se fait en une étape, la particule étant formée lors de la dissolution du centre du cristal en milieu basique. Deux méthodes de dissolution ont été utilisées :

- par TPAOH, qui permet une recristallisation de la zéolithe, avec formation de cavités régulières contenant en général une seule particule,
- par Na_2CO_3 dans le cas de la ZSM-5, qui donne des parois plus fines avec formation de nombreuses petites particules.

La paroi zéolithique protège les particules contre le frittage à haute température et joue un rôle de membrane lors de réactions catalytiques impliquant des molécules volumineuses.

Ce travail préliminaire ouvre de nombreuses perspectives :

- la protonation des zéolithes (H-ZSM-5) devrait permettre de développer de nouveaux catalyseurs bifonctionnels en synthèse Fischer-Tropsch, hydro-isomérisation …
- la méthode de synthèse pourra être appliquée sous certaines conditions à d'autres structures zéolithiques, permettant ainsi de modifier la porosité des parois,
- dans le cas de bimétalliques, le contrôle de la répartition de chaque métal au sein de la particule (alliage, structure cœur-coquille, particules Janus…) devrait permettre de moduler l'activité catalytique.

Bibliography

1. Wang, Y., Lin, M. & Tuel, A. Hollow TS-1 crystals formed via a dissolution-recrystallization process. *Microporous Mesoporous Mater.* **102**, 80-85 (2007).

2. Wang, Y. & Tuel, A. Nanoporous zeolite single crystals: ZSM-5 nanoboxes with uniform intracrystalline hollow structures. *Microporous Mesoporous Mater.* **113**, 286-295 (2008).

3. Li, S., Burel, L., Aquino, C., Tuel, A., Morfin, F., Rousset, J.-L. & Farrusseng, D. Ultimate size control of encapsulated gold nanoparticles. *Chem. Commun.* **49**, 8507-8509 (2013).

4. Li, S., Boucheron, T., Tuel, A., Farrusseng, D. & Meunier, F. Size-selective hydrogenation at the subnanometer scale over platinum nanoparticles encapsulated in silicalite-1 single crystal hollow shells. *Chem. Commun.* **50**, 1824-1826 (2014).

5. Li, S., Aquino, C., Gueudré, L., Tuel, A., Schuurman, Y. & Farrusseng, D. Diffusion-Driven Selectivity in Oxidation of CO in the Presence of Propylene Using Zeolite Nano Shell as Membrane. *ACS Catalysis*, 4299-4303 (2014).

6. Li, S., Tuel, A., Laprune, D., Meunier, F. & Farrusseng, D. Transition-Metal Nanoparticles in Hollow Zeolite Single Crystals as Bifunctional and Size-Selective Hydrogenation Catalysts. *Chem. Mater.* **27**, 276-282 (2015).

Introduction:

I. Context of this work

I.1. Brief introduction to CARENA project

This PhD work was supported by the European Union Seventh Framework Programme FP7-NMP-2010, under grant agreement No. 263007 (CAtalytic membrane REactors based on New mAterials, acronym CARENA, http://www.carenafp7.eu/).

In the past decade, the rapid increase of oil combustion has led to unprecedented increase of oil price. Investigations with respect to chemical processes to make use of alternative feedstocks are essential for the future of chemical industry. An important breakthrough would be to open new direct routes to convert rarely used, less reactive feedstocks such as short chain hydrocarbons and CO_2 for the production of chemicals. Light alkanes (C1-C4) and CO_2 are small molecules which are difficult to transform directly and selectively to the added value products. These challenges could be overcame by developing catalytic membrane reactors, which have been studied in the last decades.

The objectives of CARENA project are to develop catalytic membrane reactors for the efficient conversion of light alkanes and CO_2 to the higher value chemicals resulting in reduced number of process steps and an increase in feedstock flexible for the European chemical industry. Three primary feedstocks methane, propane and CO_2 are selected; the scheme of these processes is shown in Fig. 1. The main routes are:

1. Direct and indirect conversion of methane into methanol and olefins
2. (Oxidative) dehydrogenation of propane and subsequent selective oxidation of propylene in the mixture of propane and propylene to acrylic acid
3. Direct conversion of CO_2 into dimethyl carbonate (DMC), dimethylether (DME) and methanol (MeOH)

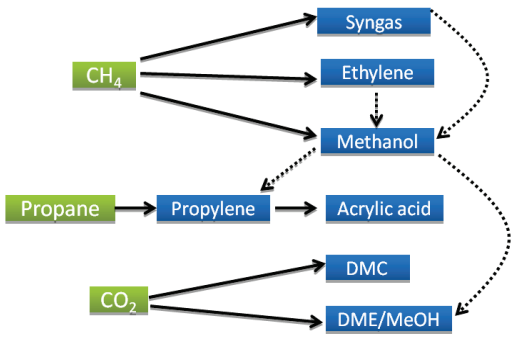

Figure 1: Feedstocks and valuable products targeted in CARENA project.

I.2. CARENA project Work Package 2 (WP2)

The overall objective of WP 2 in CARENA project is to develop a highly integrated and efficient process for the conversion of propane to acrylic acid. Three different processes are integrated in the propane to acrylic acid process, as shown in Fig.2. The vision of WP2 and the three main processes is:

1. A novel catalytic membrane reactor to achieve propane dehydrogenation and produce a propane/propylene mixture
2. A novel process that oxidizes propylene from a propane/propylene mixture to produce acrylic acid
3. A process that selectively oxidizes CO from a propane/propylene mixture to produce CO-free and recycled propane

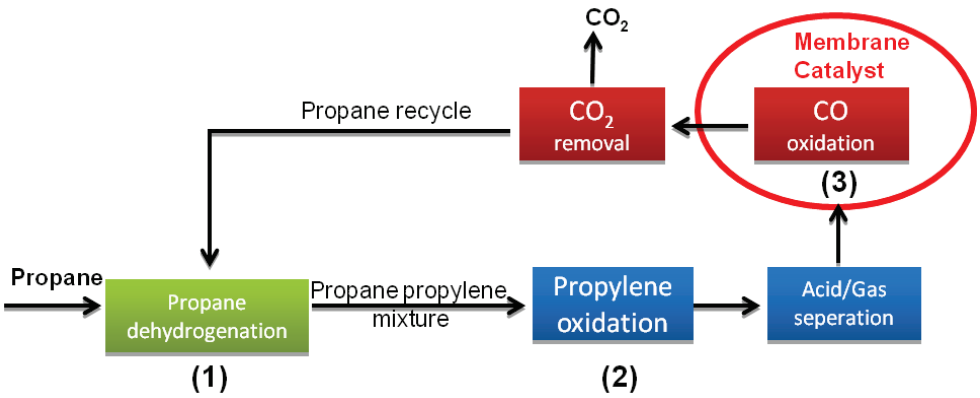

Figure 2: The vision and the three processes focused in CARENA project of work package 2.

One of the objectives of this PhD thesis is to achieve the third process of WP2 which concerns selective CO oxidation in the presence of propane and propylene. As CO produced by the oxidation reaction in the acrylic acid process is diluted in the hydrocarbon rich gas, this poisonous CO needs to be removed by selectively oxidizing CO without oxidizing hydrocarbons. For this special task, CARENA will develop a radically new concept of catalyst based on oxidation catalyst coated with a nano-scale membrane layer. This layer allows only CO to reach the oxidation active sites of the catalysts whereas the transport of hydrocarbons to the active sites is highly hindered. Thus CO removal from propane and propylene mixture gas is achieved leaving hydrocarbons unaffected and being recycled.

II. State-of-the-art

II.1. Metal nanoparticles and the synthesis methods

Metal nanoparticles were first used as pigments in glass enamel and chinaware because of their brilliant colors. They are generally defined as particles between 1 to 100 nm in size; particularly, particles between 1 to 20 nm in size are most concerned in catalysis. The number of their applications has been growing rapidly because of their unique electronic, optical, electrical, magnetic, chemical and mechanical properties which are significantly different from those of corresponding bulk metals. For example, the conduction band, which is present in bulk metal, is absent in metal nanoparticles and replaced by discrete bands at the band edge. Therefore, in very small metal nanoparticles, electrons may undergo quantum confinement showing the properties of quantum dots. [1] The characteristic Localized Surface Plasmon Resonances (LSPR) of noble metal nanoparticles found potential applications in biosensing, Raman scattering enhancement, photochemistry and many other fields.[2-5] A considerable number of scientific reports has been dedicated to these subjects in the last few decades.[6-9] Furthermore, in metal nanoparticles, a high proportion of the atoms is on the surface of the particles. The surface-to-bulk ratio which is represented by the particle dispersion increases significantly with the decrease of the particle diameters. For example, 10% of the atoms are on the surface in a particle 10 nm in size, compared to 100% when the particle diameter is 1 nm. Highly dispersed mono- and bi- metallic particles have been widely used as catalysts in quasi-homogeneous and heterogeneous reactions as well as in fuel cell fields.[10, 11]

II.1.1. "Bottom-up" methods to prepare metal nanoparticles

II.1.1.1. Wet chemical method to prepare metal nanoparticles

Since the first report of Faraday in 1857 on the preparation and mechanism of zero-valent metal colloid formation in the presence of stabilizing agents in aqueous or organic media, this approach became one of the most common and powerful methods to synthesize nanoparticles. [12] The chemical preparation relies on the chemical reduction of metal salts in appropriate solvents, generally including wet chemical preparation, electrochemical pathways and controlled decomposition of metastable organometallic compounds. To avoid metal particles aggregation in solution, a stabilizer such as polyvinylpyrrolidone (PVP), is often used to protect the particles.[13, 14]

1) Formation mechanism of metal nanoparticles

The first reproducible strategy to prepare metal particles by reducing $[AuCl_4]^-$ by sodium citrate was reported by the group of Turkevich.[6, 7, 15] A metal particle formation mechanism including nucleation, growth, and agglomeration was proposed. Lately, this mechanism was refined by modern analytical techniques with more recent thermodynamic and kinetic results as shown in Fig.3.[16-18]

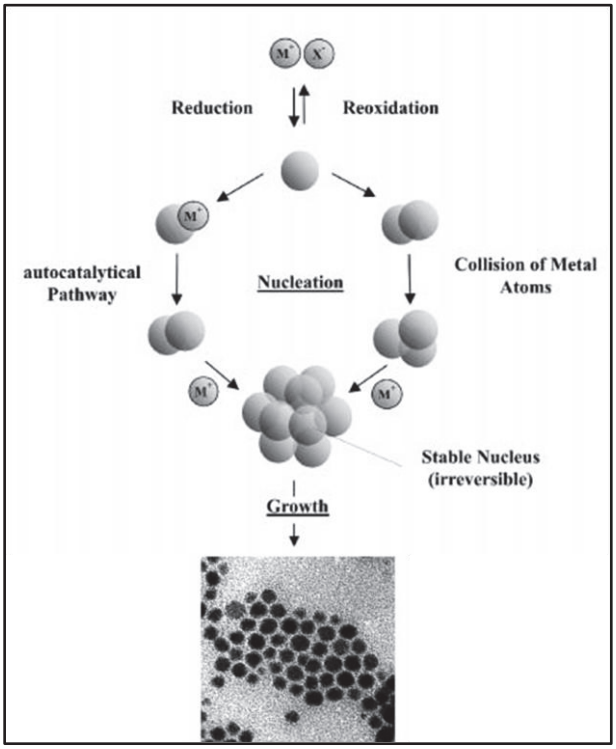

Figure 3: stepwise formation of metal particle colloids by metal salts reduction method, (from ref[19]).

In the early stage of the nucleation, metal salts are reduced to metal atoms. Then the nucleation continues in two processes simultaneously:

1) An autocatalytic pathway, in which metal ions are adsorbed on metal atoms and reduced successively by metal atoms. This mechanism was investigated by H.Bonnemann et al. using in-situ X-ray spectroscopy to study the formation of Cu colloid from Cu^{2+}, which showed the presence of Cu^{+} before the particle nucleation.[18] Reduction of the intermediate compound by zero-valent Cu atoms is involved in the nucleation.

2) The metal atoms collision, in which metal atoms collide with metal ions and atoms in solution to form stable nuclei.[20]

Finally, nuclei grow to form the final metal particles. Here, the size of the nuclei is depending on the metal-metal bonds and the difference in redox potentials between metal salts and the reducing agents. The particle size is determined by the rates of nucleation and particle growth.[21]

2) Stabilizers for the preparation of metal nanoparticles

To avoid metal particles aggregation and obtain isolated metal particles, it is necessary to use a stabilizer to protect the metal particles. There are generally two main ways to stabilize particles and protect them from aggregation: the electrostatic stabilization and the steric stabilization (see Fig. 4).

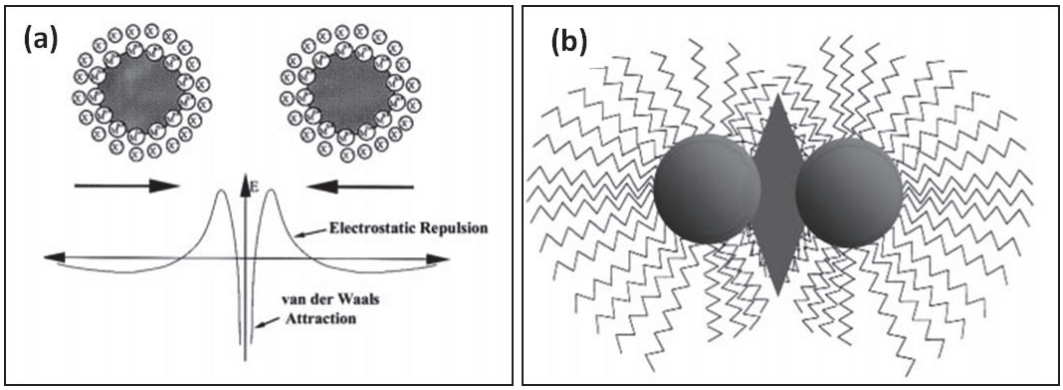

Figure 4: two main principles of stabilization of metal particle colloids: electrostatic stabilization (a) and steric stabilization (b) (from ref [22]).

As Fig.4-a shows the electrostatic stabilization is based on the Coulombic repulsion between the particles which possess the same charges on the surface. The steric stabilization shown in Fig.4-b arises from the steric repulsion between the organic molecules which are absorbed on the surface of the metal particles. The mostly used steric stabilizers in the literature are: polymers and block copolymers[23-25]; phosphanes, amines, thioethers[26-29]; long chain alcohols[30-33]; surfactants[34-36]; solvents such as THF[26] and organometallics[37, 38]. Most interestingly, the solubility of the metal particles can be easily modifiled by using different steric stabilizers. Generally, by using lipophilic stabilisers, the resulting metal particles are soluble in organic solvents while hydrophilic stabilisers produce water soluble metal particles.

3) Reducing agents for the preparation of metal nanoparticles

In the Faraday route, the use of sodium citrate as reducing agent leads to gold particles with a size around 20nm.[12] In the last few decades, many metal nanoparticles have been successfully produced by different stabilizers and reducing agents.

For example, Schmid et al. have reported the synthesis of $Au_{55}(PPh_3)_{12}Cl_6$(1.4nm) (PPh_3 represents triphenylphosphine) by using phosphane ligands as stabilizers and reduction to metallic Au_{55} by a B_2H_6 steam through the solution.[27, 28, 39-41] Other examples concern the general synthesis method of silica coated metal particles developed by the group of Mulvaney[42] and the polymer stabilized noble particles which are reduced by alcohols from Hirai and Toshima.[23-25, 43-46] Hydrogen is also an efficient and common reducing agent for the synthesis of electrostatic stabilized and polymer stabilized metal particles, such as Pt, Pd, Rh, and Ir.[47-50]

Advantages of wet chemical synthesis are that the method is highly reproducible and allows particles with relatively narrow particle size distribution.

II.1.1.2. Electrochemical synthesis method to prepare metal nanoparticles

In 1994 Reetz et al. have developed the electrochemical synthesis of metal particles[51]; the principle mechanism is depicted in Fig.5. First, an oxidative dissolution of sacrificial anode occurs, then the metal ions migrate to the cathode where they are reduced to zero-valent metal atoms. In the next step, the metal particles are formed by nucleation and growth. Finally, the particles are stabilized by the protecting agents $[(C_8H_{17})N^+Cl^-]$ and precipitated in the solution.

Reetz et al have reported that Pd particle size is turnable from 1.4 nm to 4.8 nm by adjusting the current density during the electrochemical synthesis using $(C_8H_{17})N^+Cl^-$ as stabilizer.[35] The higher current density produces smaller particles (1.4nm), wherears lower density lead to larger particles. Besides the current density, the particle size can be also varied by the distance between the electrodes, the reaction time, the temperature and the polarity of the solvent.

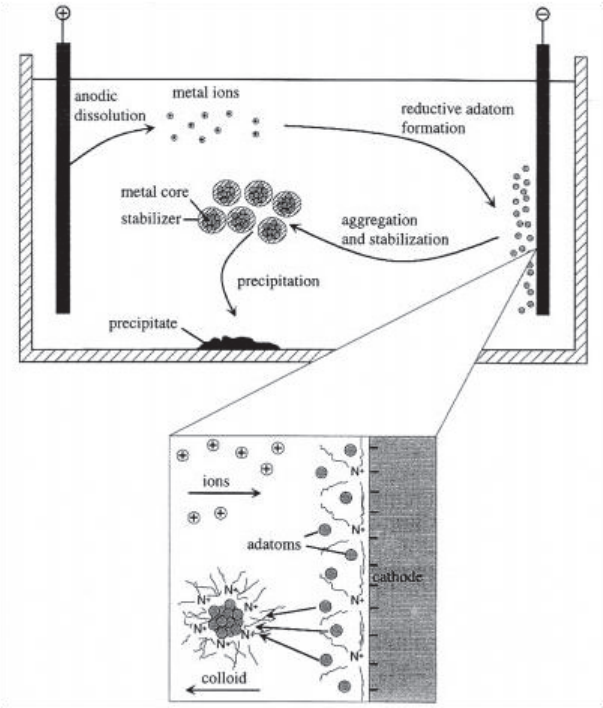

Figure 5: Electrochemical formation of metal particles stabilized by $N^+R_4Cl^-$ (from ref[51]).

The electrochemical method has been successfully used in the preparation of monometallic particles[34], such as Pd, Pt, Ni, Fe, Co[35, 36, 52] ect., as well as alloy particles like Pd/Ni, Fe/Co,Fe/Ni and Pt/Pd.[36, 53]

Advantages of the electrochemical synthesis method are that it can avoid the contamination from the by-products compared to chemical reduction methods and that particles can be easily seperated from the solution.

II.1.1.3. Decomposition of low valent transition metals to prepare metal nanoparticles

Metal particles can also be synthesized by decomposition of low valent organometallic complexes and organic derivatives of transition metals under heat, light and ultrasound in the presence of stabilizers. For example, thermolysis leads to the decomposition of cobalt carbonyl and the formation of cobalt nanoparticles in organic solutions.[54, 55] The presence of a stabilizer can greatly improve the synthesis to obtain particles with narrow size distributions.[56] The decomposition of organometallic complexes can also be performed by microwave radiation[57, 58] and sonochemistry.[59, 60] The group of Chaudret has demonstrated the synthesis of mono- and bimetallic nanoparticles from the decomposition of transition metal olefin complexes by the addition of CO or H_2 in the presence of appropriate stabilizers such as PVP.[50, 61-65]

Besides the above methods, metal nanoparticles can also be prepared in direct or inverse micelles [17]or by encapsulation.[66-68]

II.1.2. "Top-down" methods to prepare metal nanoparticles

Metal nanoparticles can also be prepared by the so called "top-down" methods, in which particles are obtained from bulk metals and further deposited on a substrate. [69-73] Nanoparticles can be obtained by physical methods such as heating, mechanical grinding or laser ablation. Another method which consists in evaporating micro-sized droplets of metal precursors in proximity of the substrate is called Chemical Vapor Deposition (CVD). The main challenge of this CVD method is that the particle form and size are difficult to control during the evaporation step. Efforts to control the evaporation rate, to modify the distance between the evaporator and the substrate and the use nucleating inert gas, have been developed to get relative narrow particle size distributions.

The particles deposition is also improved by using a soft-landing method in which the metal particles are first generated in argon and then landed on a cold substrate, as shown in Fig. 6.[73] The soft landing method produces more spherical and uniform particles. The advantage of these physical preparation methods is that particles are usually purer than those produced in solution. However, this "top-down" physical method is still limited due to very low production rates.

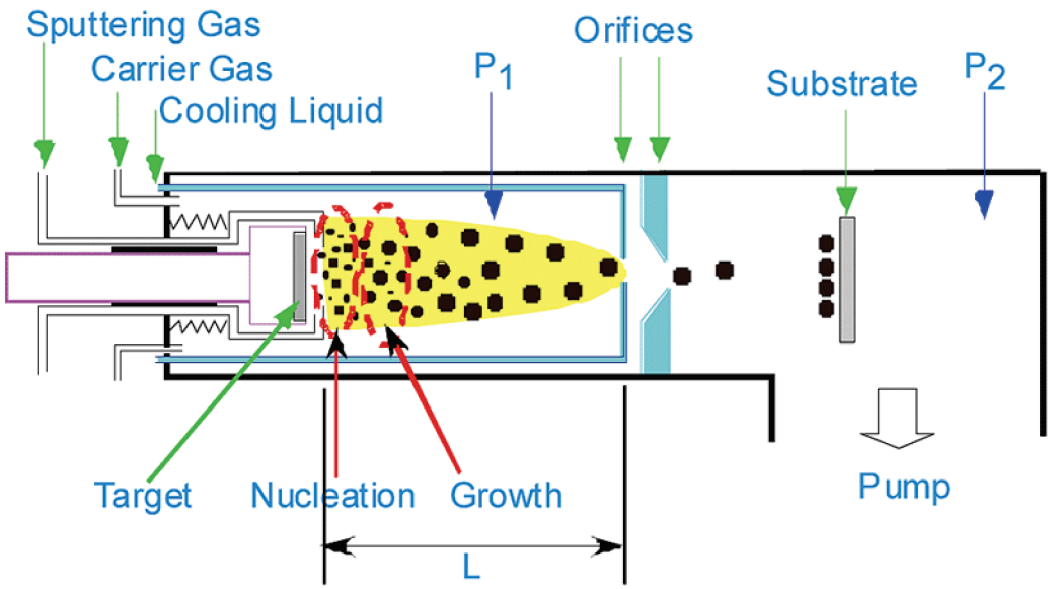

Figure 6: Schematic illustration of the nanoparticle soft landing method deposition system, P_1: 150~600 mtorr and P_2 is ‹ 3 mtorr, (from ref[73]).

II.2. The challenge of metal nanoparticle sintering in catalysis

For many applications, nanoparticles stabilized by polymers, surfactants or phosphines are dispersed on high-surface materials such as silica, alumina or TiO_2. For example, these supported metals have been used for several decades as industrial catalysts[7]. Their activity results from a synergy between mono-dispersed particles, with a high fraction of surface atoms, and high surface area supports. Organic molecules used to stabilize nanoparticles and prevent their aggregation are usually thermally unstable and they decompose at high temperature, typically 300°C. Above this temperature, bare particles tend to sinter to larger particles with a boarder size distribution and a significant loss of activity.[74] Many catalytic processes like reforming, DeNOx and combustion are carried out at a temperature above 500°C. The understanding of the sintering mechanism and the development of stable, sintering resistant catalyst is thus of prime important, both from the academic and industrial sides.

II.2.1. Mechanisms of particle sintering

II.2.1.1. Two mechanisms of particle sintering

Scientists have proposed two different mechanisms for sintering, namely the Ostwald ripening and the coalescence (Fig. 7).

The Ostwald ripening involves atoms or mobile molecular species migration from small particles to bigger ones, the driven force being the difference in free energy (bigger particles possess a lower free energy, which leads to particle aggregation) and the local atom concentrations on the support surface. In contrast, coalescence is driven by the Brownian motion of nanoparticles which diffuse and collide to form bigger particles.

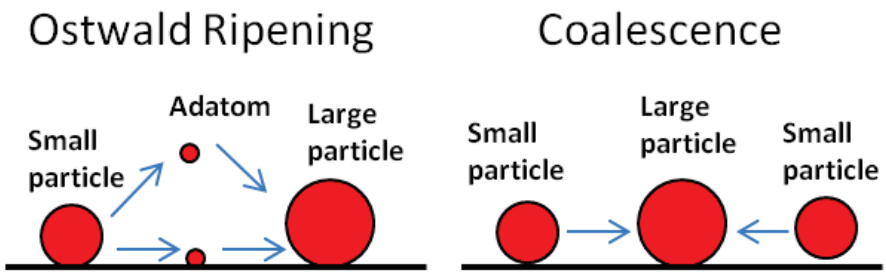

Figure 7: Schematic illustration of Ostwald ripening and Coalescence.

An ideal solid catalyst with low metal loading should usually contain highly dispersed particles. According the classical theory,[75, 76] when such a catalyst is used in a reaction environment, the Ostwald ripening tends to occur first, leading to the formation of bigger particles which are effectively mobile and will migrate and sinter together. This migration and sintering between particles is the coalescence process.

Baker[77] et al. suggested that surface atoms begin to be mobile at the Tammann temperature ($0.5T_{bulk\ melting}$ [K]) and that the mobility increases with temperature. Harris published a review on different models of particle migration on supported metal catalysts,[78] in which the mobility of particles with different sizes was predicted. For instance, in Pt/Al_2O_3 supported catalyst, small particles around 5 nm could migrate by about 540nm in 2 hours at 600°C; whereas larger particles above 20nm moved only by 20 nm.

II.2.1.2. Three phases of particle sintering

Recently, Datye et al. published a paper on the study of metal particle sintering process in $Ni/MgAl_2O_4$, Pt/Al_2O_3 and Pd/SiO_2 materials using in-situ TEM technique.[79] The sintering process has been divided into three phases as shown in Fig.8.

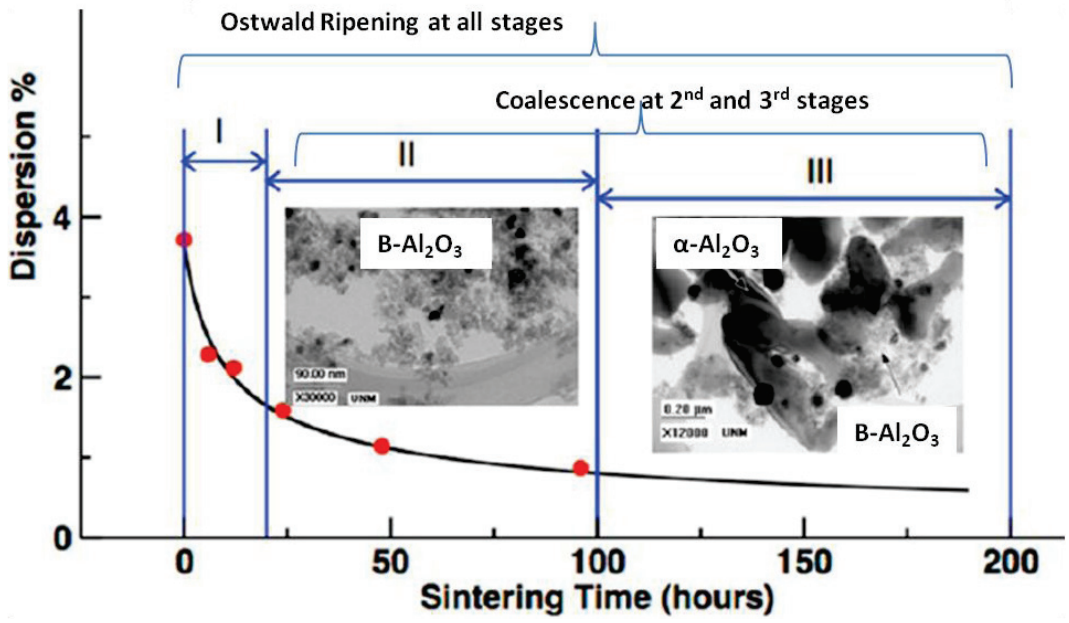

Figure 8: Schematic illustration of the three phases in the sintering of 7% Pd/Al_2O_3 heated at 900°C in 10% H_2O/N_2, Pd particles dispersion at three stages and TEM images of the Pd/Al_2O_3 at 2nd and 3rd stages, (from Ref [79]).

During the 1st phase which usually occurs within the first few hours,[80] the small particles decrease in size until they disappear, while other particles grow slowly and steady without jumping in size. This

stage is dominated by Ostwald ripening which was confirmed by in situ TEM[81] and Monte Carlo simulation.[82] The disappearance of small particles leads to significant loss of surface area and lower particle dispersion, which cause the catalyst deactivation.

All along the 2nd phase, the sintering rate slows down because of the disappearance of the small particles. Hansen et al.[83] have demonstrated the sintering stages of $Ni/MgAl_2O_4$ under H_2/H_2O at 650°C by using in situ microscopy technique. Coalescence was observed after 5 hour observation, while during these 5 hours particles grow from the starting 3.2 nm to 10 nm driven by Ostwald ripening. From the in-situ TEM observation, the coalescence occurred when particles were mobile and get close enough to each other.[83, 84]

Researchers have predicted that particle sintering at high temperature may never complete, Datye et al. have studied the sintering of a Pt/Al_2O_3 catalyst at 900°C under an atmosphere of H_2O vapor and O_2 (~1 atm for both) and they showed that particle sintering lasts approximately 4000 hours.[85] Furthermore, the thermal stability of the support is also important in the last phase. In the particular case of Pd/Al_2O_3 the high surface β-alumina was transformed into α-alumina (TEM images in Fig.8). The support chemistry also plays an important role in influencing the rate of catalyst sintering.[79]

II.2.2. Approaches to control particle sintering

II.2.2.1. Alloying and over-coating of the particles

One approach proposed in the literature to suppress particle sintering is particle alloying.[86] Verser et al.[86] demonstrated that the introduction of a second metal with higher melting point could reduce or completely suppress the particle sintering. Pt particles of 4nm in size are thermally stable at around 500°C, while similar particles synthesized by alloying with Rh (melting point about 200°C higher than Pt) are stable upon thermal treatment at 850°C. The thermal stability of the alloy particles could be adjusted by varying the Pt/Rh ratio, the higher the Rh loading, the higher stability of the alloy particles. However, alloying does not only result in the intended change in the physical properties of the nanoparticles (i.e. the thermal stability), but it may also modify the chemical properties and hence the catalytic activity and/or selectivity of the catalyst.

Stair et al.[87] developed a Pd catalyst coated by an atomic alumina layer which showed improved sintering resistance compared to uncoated Pd catalyst. The morphology of the alumina coated catalyst showed no changes after 28 hours of oxidative dehydrogenation reaction at 675°C. That was attributed to the blocking of edge and corner sites from where atoms would be mobile in the ripening process. Similar cases of particles over-coated by a layer of oxide were also reported for a

wide range of compositions, such as SiO_2 coated on Au[88] and TiO_2 coated Au.[89] In both cases, coatings have improved the stability of Au particles.

All these efforts are related to the changes in particle compositions, which would lower the atom movement and transport rates on the support.

II.2.2.2. Anchoring particles into porous supports

More and more attentions have been paid to solving the sintering problem of supported catalysts by anchoring the particles into a porous support, such as silica or carbon nanotubes, thus lowering the overall rate of sintering.

The functionalization of the silica surface (MCM-41, SBA-15) by amine groups enhances the sintering resistance and allows the synthesis of gold nanoparticles of 4-8 nm.[90] Dayte et al. have studied the thermal stability of Au encapsulated in mesoporous silicas.[91-95] Results show that sintering of Au particles is dependent on pore size, wall thickness, as well as pore connectivity. Small particles are obtained using silica with small pores, as shown in Fig.9. More recent studies show that very small particles which are thermally stable at 750°C can be obtained when silica surface is functionalized by a thiol group.[96]

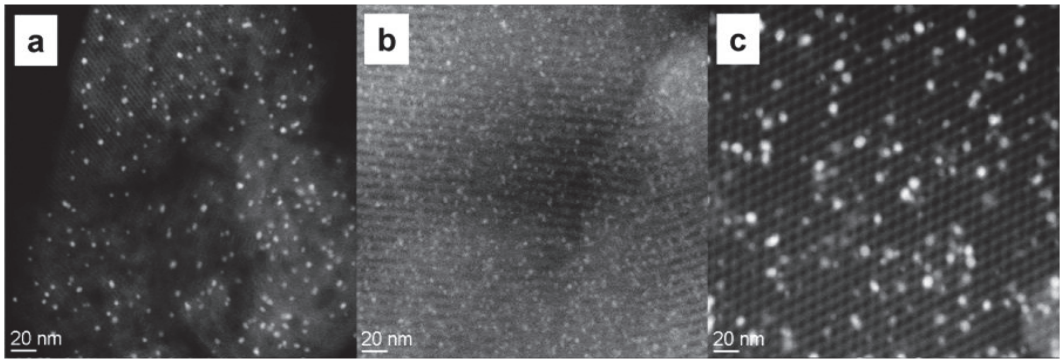

Figure 9: HAADF STEM images of samples after reduction at 200 °C for 2 h in hydrogen. (a) Au (mean size 3.5 nm) within MCM-41 (pore size 2.9 nm); (b) Au (mean size 4.1 nm) within SBA-15 (pore size 4.1 nm): (c) Au (mean size 6.9 nm) within SBA-15/2 (pore size 6.5 nm), (from ref [91]).

The pore size delimits the particles only in the case of a functionalization with amino or ammonium groups. A higher connectivity of the pores provides more channels for Au particles migration and accelerates the sintering process, Au particles in 3D-hexagonal pores sintering much faster than those in 2D structured silicas. Nevertheless, the dimension of gold particles cannot be tailored in a wide range by using this synthesis pathway and sintering can be controlled only if porous structure is stable enough to maintain the particles inside under harsh conditions. For example, MCM-41 with a wall thickness of 1 nm is unstable at 400°C.

II.3. Core/yolk-shell catalysts

Nanostructured core-shell and yolk-shell materials, which consist of metal nanoparticle cores encapsulated inside bulk or hollow shells, have attracted great attention during the last years, due to their particularly interesting catalytic performances in terms of activity, selectivity and stability.[97, 98] Usually, they do not only combine the properties of the core/yolk and shell, but also bring unique synergistic properties compared to supported catalysts.

The core/yolk part is generally a mono dispersed nanoparticle and the shell is a porous layer, mainly an inorganic oxide or carbon, which protects particles under catalytic reaction conditions.[99-104] Since particles are individually encapsulated in the shell, migration and sintering are significantly inhibited, which explains their great potential in practical applications.

II.3.1. Core shell

Since the pioneering work on Au@silica core-shell catalyst developed by Liz-Marzan[97], a lot of work has been performed to design and synthesize core-shell catalysts with different compositions.[102, 104] The synthetic strategy usually involves two steps: a particle colloid core is first prepared, followed by the formation of the shell.

Somorjai et al. have reported a thermally stable Pt@mesoporous SiO_2 (Pt@mSiO_2 for short) core shell catalyst, the synthesis pathway and the TEM image of which are represented in Fig.10.[102]

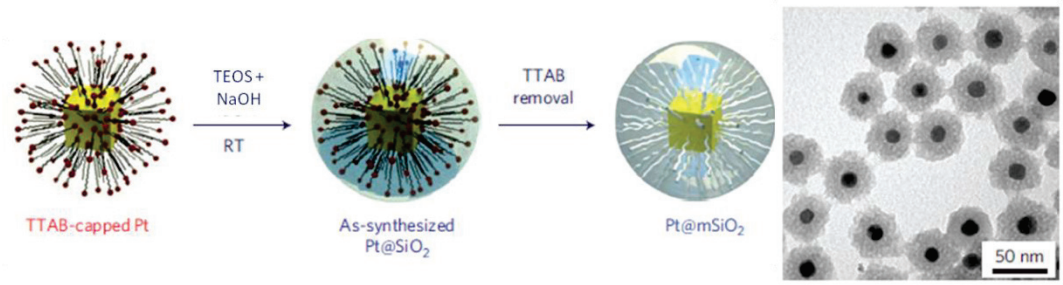

Figure 10: The synthesis pathway (left) and TEM images (right) of Pt@mSiO_2 material, (from ref [102]).

Pt particles are first synthesized in solution by chemical reduction method, then a layer of mesoporous SiO_2 is coated on Pt via a sol-gel chemistry using tetradecyltrimethylammonium bromide (TTAB) as a pore directing agent. After calcination, TTAB is removed and Pt particles are accessible to reactant molecules via the mesopores of silica. This core shell material is thermally stable at 750°C and exhibits high activity in ethylene hydrogenation and CO oxidation. Furthermore, as a

heterogeneous catalyst, this core shell structure can maximize the interfacial area between metal particles and the support, which may generate more active sites and further enhance the catalytic performance. Tang et al. developed $Au@ZrO_2$ core shell material which exhibited much higher activity and better stability in CO oxidation than Au/ZrO_2 supported catalysts.[105]

However, it should be noticed that core-shell catalysts also possess disadvantages, for instance low diffusion rates of both reactants and products to the active core due to the shell coating effects, particularly in liquid phase catalytic reactions.

II.3.2. Yolk shell

Yolk-shell catalysts consist of nanoparticles encapsulated into a thin hollow shell which is generally made of mesoporous oxides (ZrO_2,[99, 100, 106] SiO_2,[107, 108] TiO_2[101]) or amorphous carbon.[103, 109, 110] They are particularly attractive because they could show high catalytic activities per metal atom, due not only to the stabilization and protection of the isolated particles against sintering and aggregation, but also to low diffusion limitations through the thin shell.[100, 101, 103, 106-110]

Schüth et al. have reported the synthesis of a series of yolk-shell materials based on $Au@ZrO_2$.[98-100, 106] The synthesis process is shown in Fig. 11. A gold colloid with a diameter around 15nm synthesized via sodium citrate reduction is first coated by a layer of SiO_2 obtained by the Stöber process.[111] Then another layer of ZrO_2 is coated on SiO_2 and then $Au@ZrO_2$ yolk shell material is obtained by subsequent SiO_2 leaching in NaOH aqueous solution. Each ZrO_2 hollow shell contains a unique gold particle with a size around 15nm, as seen in TEM pictures in Fig. 11. Because of the protection of the shell, this catalyst shows structural stability and catalytic performances in CO oxidation even after calcination at 800°C (Fig.11 right).

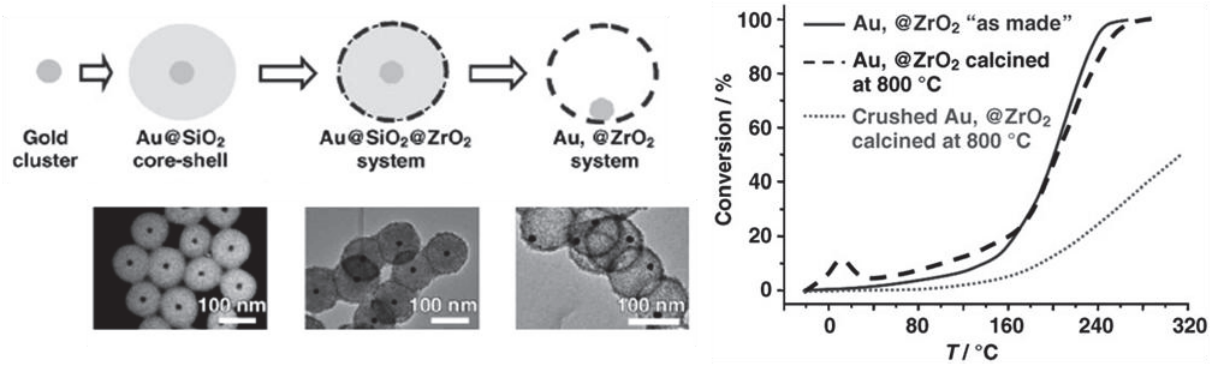

Figure 11: synthesis process of $Au@ZrO_2$ yolk-shell materials and TEM images of the samples at each step (left), the catalytic performance of $Au@ZrO_2$, calcined $Au@ZrO_2$ and crush calcined $Au@ZrO_2$ in CO oxidation reactions (right), (from ref [106]).

Later on, the authors reported a $Au/TiO_2@ZrO_2$ catalyst with an improved activity in CO oxidation reactions compared to $Au@ZrO_2$ catalyst, which is prepared from a TiO_2 layer doped Au particles and then followed the same protocol as Fig.11.[106] Au particle size could also be adjusted in the range of 7-15 nm by etching $Au@SiO_2$ materials with NaCN solutions, thus allowing the study of the particle size effect in CO oxidation.[98] Many other kinds of yolk shell materials have been developed with success, for example, $Au@TiO_2$,[101] $Au@Fe_2O_3$,[112] Pt@Carbon,[103] $Pt@TiO_2$,[113] $Pd@CeO_2$[114] and $Ag@Fe_2O_3$.[115]

However, despite advances made in the preparation of yolk shell catalysts, there are still many remaining challenges. Indeed, synthesis methods are long and complicated and they generally necessitate many condensation/calcination/dissolution steps. Moreover, shell compositions are limited to a few metal oxides or carbon and the shell generally possess a unique function, which is to prevent particle sintering during reactions at high temperatures. Very few examples concern multi-functional catalysts, providing clear evidence for synergistic effects between metal nanoparticle and shells.[116] Furthermore, the diffusion rates of both reactants and products are still not well understood.

Song et al. have reported the synthesis of Pd@mesoporous SiO_2 for Suzuki reaction and they have shown that the mesoporous SiO_2 shell exhibited size selectivity for phenylboronic acid derivatives (Fig. 12).[116] Phenylboronic acid can pass through the silica shell and react with iodobenzene on Pt particles but not the bulky o-carboxyphenylboronic acid which is too large to penetrate the mesopores.

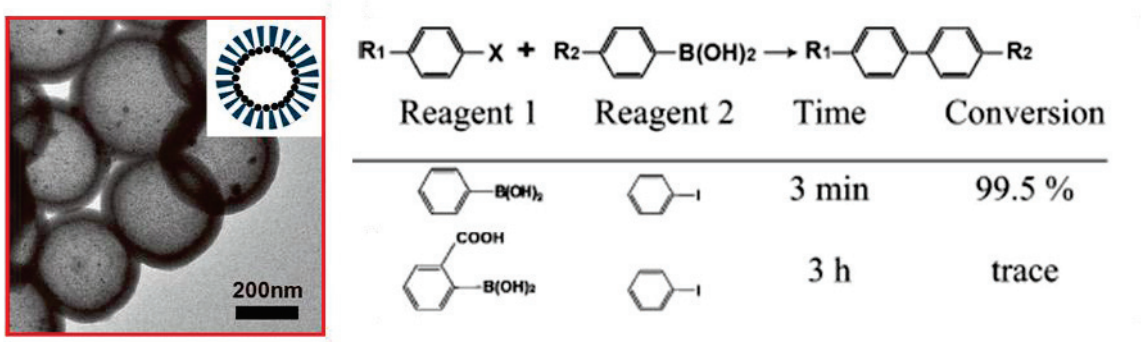

Figure 12: TEM image of Pd@mesoporous SiO_2 (left); Suzuki Reaction of phenylboronic Acid, o-carboxyphenylboronic acid and iodobenzene catalyzed by Pd@meso-SiO_2 (right). Reaction conditions: 80 °C, ethanol (10 mL), iodobenzene (0.5 mmol), phenylboronic acid (1 mmol), K_2CO_3 (1 mmol), and catalyst (10 mg), (from ref[116]).

However, mesoporous shells are not appropriate to separate gas molecules such as light hydrocarbons and gases (CO, CO_2...) because of the mismatch between the pore size of the shell (> 2 nm) and that of the substrates (kinetic diameter < 1 nm). This prevents a sieving separation mechanism and limits the application of this kind of yolk-shell catalyst in many gas phase catalytic

processes. A yolk-shell catalyst which combines metal particles with microporous zeolite shell should then be a very promising multifunctional catalyst.

II.4. Catalysts based on microporous zeolites

Zeolites exist in nature essentially as aluminosilicate minerals (rarely as beryllosilicates, zincosilicates or beryllophosphates) with approximately 50 different structures. Synthetic zeolites were first prepared in chemical lab in the 1950s, essentially by the group of Barrer.[117] Since 1962 the industrial application of faujasites in fluid catalytic cracking (FCC) of heavy petroleum distillates, zeolites have been one of the most wildly used catalysts in industry. They are crystalline microporous solids, which are widely used in ion-exchange, adsorption, separation and many catalytic processes.[118-120]

II.4.1. Zeolite structures and definitions

Zeolites are built from SiO_4 and AlO_4 tetrahedral units (generally denoted TO_4) linked by corners via a common oxygen atom, which results in a three-dimensional framework with a distinct topology. This framework contains channels, channel intersections and/or cages with dimensions between 0.3 to 1.5 nm, which are in the range of many molecules of interest. These voids usually contain water molecules and cations (generally Na, K, Ca or Mg) that balance the negative charge resulting from the presence of trivalent Al atoms at tetrahedral sites. Thus the chemical composition of a zeolite can be represented by the following formula:

$$A^{m+}_{y/m}[(SiO_2)_x \cdot (AlO_2^-)_y] \cdot zH_2O$$

Where A is the cation(s) with charge m and x and y are the numbers Si and Al atoms in the unit cell, respectively. The x/y ratio (generally denoted Si/Al ratio) is a very important characteristic of zeolite frameworks since it determines the exchange capacity of the zeolite and its acidic character. Following the Löwenstein's rule which prohibits direct bonding between two AlO_4 tetrahedra, the Si/Al molar ratio in zeolites cannot be smaller than 1.

Zeolite frameworks can be described as an assembly of small units which generally contain up to 16T atoms and are denoted SBU's (for Secondary Building Units). In the case of zeolite ZSM-5, SBU's are pentasil units formed by 5-ring units linked together to form pentasil chains (Fig.13). Chains are connected together via oxygen atoms, which delimit two types of 10-rings channels: a straight channel (0.56 x 0.53 nm) intersecting with a sinusoidal one (0.55x 0.51 nm). All different zeolite frameworks are designated by a three capital letters code generally derived from the name of the type materials. For example, the FAU code has been assigned to zeolite X and Y because they possess

the structure of the natural mineral faujasite. For ZSM-5, the code MFI (Mobil Five) refers to the company which first synthesized the zeolite. To date, approximately 225 different framework types have been approved by the International Zeolite Association (IZA).

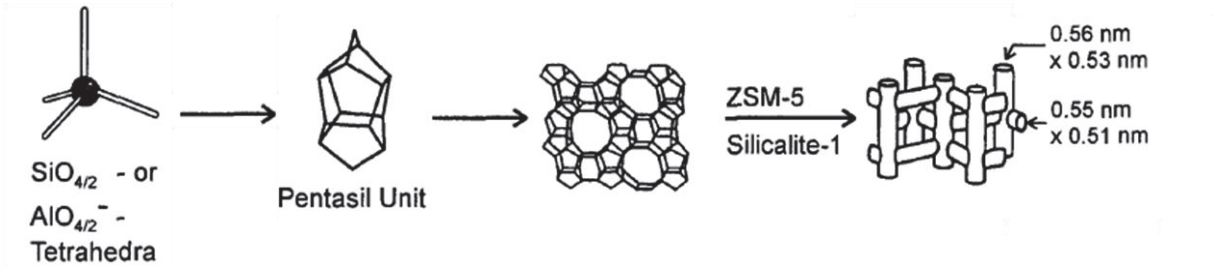

Figure 13: Structure of ZSM-5 or silicalite-1 zeolite, the micropore system and the channel dimensions (from ref [121]).

II.4.2. Zeolite properties and applications in catalysis

II.4.2.1. Shape-selective properties and their applications

Zeolites have been used as shape selective catalysts at industrial scale for major chemical and energy processes such as disproportionation of toluene, [122] alkylation,[123] methanol to olefin (MTO) [124] and fluid catalytic cracking (FCC).[125] The shape selectivity of zeolites results from the similarity that exists between the size of micropores and that of interacting molecules. Since most of the catalytic sites of zeolites are confined within micropores, their access is restricted to small molecules and reaction profiles (conversion, nature of products formed) are determined mostly by the molecular dimensions and the configurations of the channels. Generally, three types of shape selectivity can be distinguished: [126-128]

1) The reactant shape selectivity in which reactant molecules are too large to enter the pores of the zeolite and have no access to catalytic sites.

2) The product shape selectivity in which only product molecules that can rapidly diffuse out of the zeolite are detected.

3) The restricted transition state selectivity which prevents certain reactions because transition states would require more space as that available in channels and cavities. Thus, shape selectivity is highly depending on the pore size and the pore architecture of the zeolite.

In the two first cases, selectivity arises from the mass transfer effect which can be modified by changing the crystal size of the zeolite or by using zeolites with slightly different pore sizes. By contrast, the last case is an intrinsic chemical effect, which depends only on the structure and is independent of the crystal size.

II.4.2.2. Acidity of zeolites and their applications

Zeolites can generally be synthesized with different aluminum contents. In the case of ZSM-5 with a chemical formula: $[Na^{+}_{n}\ (H_2O)_{16}]$ $[Al_nSi_{96-n}\ O_{192}]$, for which the Si/Al ratio can be varied from ca. 10 to ∞ (in the case of the pure-silica framework, the zeolite is named silicalite-1). The aluminum content affects most of the zeolite properties, in particular the ion exchange capacity, the density of Brønsted acid sites, their thermal stability and the hydrophilic or hydrophobic surface properties.

As discussed before, aluminum tetrahedra generate negative charges in the framework that have to be compensated by cations. These cations, typically Na^{+}, Ca^{2+}, Mg^{2+} or K^{+}, can be exchanged by others under mild conditions. When the compensating cation in the zeolite structure is exchanged by ammonium cations and a subsequent heat treatment at high temperature generates protons by the removal of ammonia (Eq.1). This proton is actually part of a bridged hydroxyl group Si-O(H)-Al, which functions as a Brønsted acid site.

$$NH_4^+ + Na^+Z^- \xrightarrow[-Na^+]{} NH_4^+Z^- \xrightarrow[-NH_3]{300\text{-}400\ ^\circ C} H^+Z^- \qquad (1)$$

Lewis acid sites usually co-exist in zeolites with Brønsted acid sites. Kühl proposed that Lewis acid sites were formed after several heating treatments of zeolites; the removal of AlO_4 tetrahedra from the framework generates the so called Lewis acid sites.[121] Acidity is one of the most important properties of zeolites with respect to their use in catalytic processes such as industrial Fluid Catalytic Cracking (FCC) and isomerization.[129, 130]

Furthermore, acid zeolites are usually an important component of bifunctional heterogeneous catalysts which combine acid and hydrogenation/dehydrogenation functions. As the name "bifunctional" suggests, acid sites from the zeolite catalyze the cracking and isomerization reactions, while metal particles active hydrogen and carry out hydrogenation reactions. The general scheme of an alkane hydroisomerization over bifunctional catalysts is shown in Fig. 14.

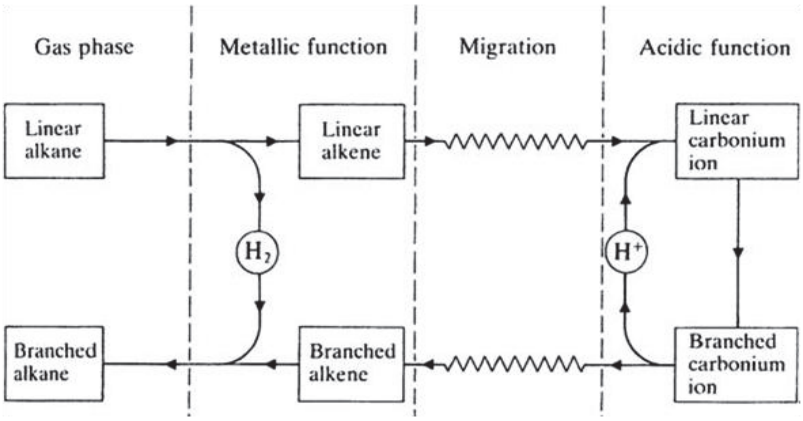

Fig.14: Schematic representation of the mechanism of skeletal isomerisation on a bifunctional catalyst.

II.4.3. Metal particles in zeolites hybrid catalysts

As mentioned before, sintering can be avoided by encapsulation of particles in core shell or yolk shell nanostructures. However, in most of these hybrid catalysts, shells are mesoporous, which are useless in terms of molecular sieving at the sub-nanometer scale. Selectivity of the shell at molecular level can be achieved using metallic particles embedded in[126, 131-133] or covered by zeolite.[133, 134] Particles are only accessible through the zeolite micropore system while zeolite themselves protect the nanoparticles against sintering. Such catalysts, which combine sinter-resistant nanoparticles with a shape selective zeolite, may find applications in selective catalysis and material science.

Several authors have reported the synthesis of particles encapsulated in the pore or the cage of zeolites by directly synthesis[131-133, 135-137] or post synthesis methods.[138-142] They have been applied in size/shape selective hydrogenation and oxidation reactions.

II.4.3.1. Metal nanoparticles encapsulated in zeolites prepared by directly synthesis

Metal particles such as Pt, Pd, Rh, Ir, Re, and Ag can be encapsulated in zeolites by direct addition of the corresponding metal precursor in the synthesis gel followed by reduction.[132, 136]

This method was used by Iglesia et al. to synthesize particles of different metals in small pore zeolites, such as SOD, GIS and ANA.[132] Particles were efficiently protected by the zeolite from bulk poisoning molecules such as thiophene in the hydrogenation of ethane over GIS and ANA-supported catalysts or H_2S in the H_2-D_2 exchange over SOD-based materials (Fig. 15).

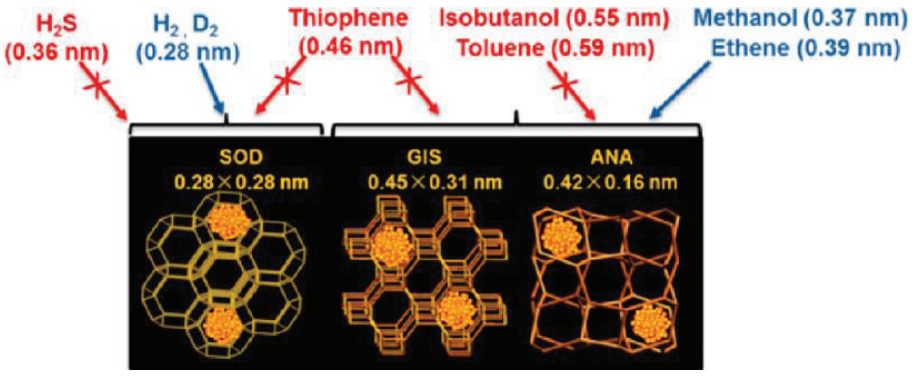

Figure 15: Pictorial representation of metal clusters encapsulated within different zeolite structures with zeolite apertures and size selectivity among different molecules. (from Ref [132]).

In a related process, gold nanoparticles encapsulated in silicalite-1 have been synthesized by crystallizing the zeolite in the presence of gold colloids[133, 137] (synthesis scheme in Fig. 16). Gold

particles with a diameter around 2 nm are thermally stable upon calcination at 550°C for 3 hours. Compared to a standard Au/TiO_2 supported catalyst, Au@slicalite-1 shows a high selectivity in the aerobic oxidation of benzaldehyde in a mixture of benzaldehyde and 3, 5-di-tert-butyl benzaldehyde in methanol. Silicalite-1 acts as a molecular sieve that stops the bulky di-substituted molecule while Au particles remain accessible to benzaldehyde which is converted to the corresponding methyl ester (Fig.17-left). The reactant size selectivity and the sinter resistant of nanoparticles are both well accomplished with this material.

However, a significant proportion of gold particles are located on the outer surface of the crystals and the particle size distribution is broad with a significant portion of particles larger than 10nm (Figure 17-right).[133]

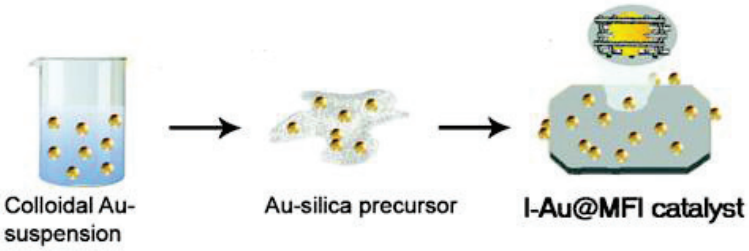

Figure 16: synthesis route of Au@silicalite-1 materials, (from ref[133]).

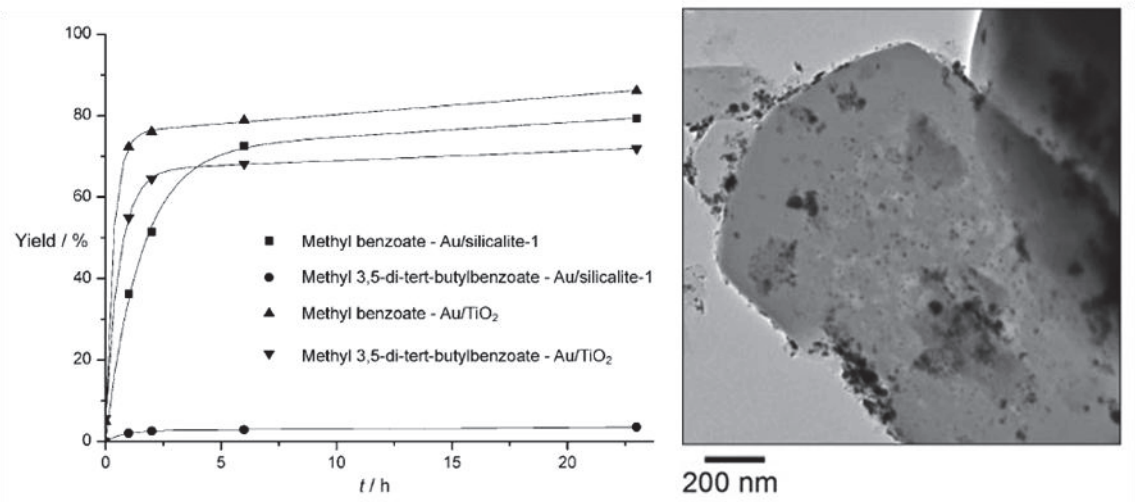

Figure 17: Oxidation of benzaldehyde and 3, 5-di-tert-butyl benzaldehyde in methanol over Au@silicalite-1 and $AuTiO_2$ catalysts (left); TEM image of Au@silicalite-1 materials (right), (from ref [133]).

II.4.3.2. Metal nanoparticles encapsulated in zeolites prepared by post synthesis

Post synthesis incorporation of metals and/or oxides in zeolites is usually achieved by wet impregnation or ion exchange methods, followed by drying and reduction steps.[143] Wet impregnation consists in filling the pores of the zeolites with a solution containing a metal precursor followed by drying and calcination/reduction steps. When the volume of solution is equal or less than the total pore volume of the support, the technique is referred to as incipient wetness impregnation (IWI). In the ion exchange process, cations of the zeolite are replaced by metallic ions (for example $Ag^{+}$and Pt^{2+}), however, this method cannot be performed on neutral zeolites such as silicalite-1. Au/Y zeolites prepared by wet impregnation followed by a reduction process show that Au particles are encapsulated in the cages of the zeolite with a diameter around 1 nm (Fig.18). This catalyst showed high stability and efficiency in the catalytic oxidation of 5-hydroxymethyl-2-furfural (HMF) into 2,5-furandicarboxylic acid (FDCA).[138]

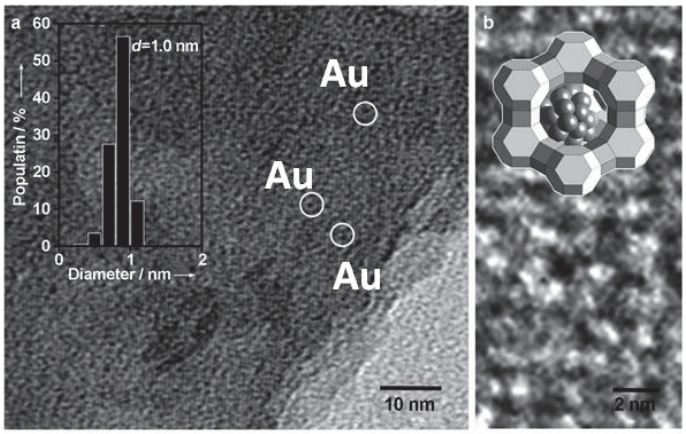

Figure 18: TEM image, particle size distributions (left) and high resolution TEM image (right) of Au/Y zeolite synthesized by impregnation method, (from ref[138]).

Another Pt/ZSM-5 prepared by ion exchange showed shape selectivity in the hydrogenation of triacylglycerol molecules, with preferred trans- over cis- in hydrogenation of the fatty acid chains.[141] However, in this type of hybrid materials, the particle diameter is restricted by the size of the pores or cavities of zeolite (dimensions between 0.3 to 1.5 nm).

II.4.3.3. Core-shell catalysts with zeolite shells

Another option to achieve the combination of zeolite properties and sinter-stable particles is to form core-shell nanostructures by zeolite coating on spherical supported catalysts typically active metal nanoparticles supported on SiO_2, Al_2O_3 or TiO_2.[122, 144] The selectivity of metal catalysts is controlled by the shell of zeolite that acts as a membrane; the basic principle is given in Fig. 19. In such a core-shell structure, reactants must first diffuse through the porous zeolite layer before reaching the metal center leading to high selectivity among the reactant molecules by molecular sieving mechanisms.[145] Collier et al. demonstrated the CO selective oxidation in the presence of butane achieved by a zeolite 4A coated Pt-Fe/SiO_2 catalyst.[134] Nishiyama et al. showed the transport driven selectivity in the hydrogenation of a mixture of linear and branched C_6 alkenes on Pt/TiO_2 beads coated with silicalite-1 polycrystalline layer with thickness around 40µm. Later on, ZSM-5 crystals have been coated with silicalite-1 layers of various thicknesses. Decreasing the coating thickness from 40µm to 200nm greatly improved toluene conversion and p-xylene selectivity in toluene alkylation due to the shorter diffusion length through the zeolite shell.[146, 147]

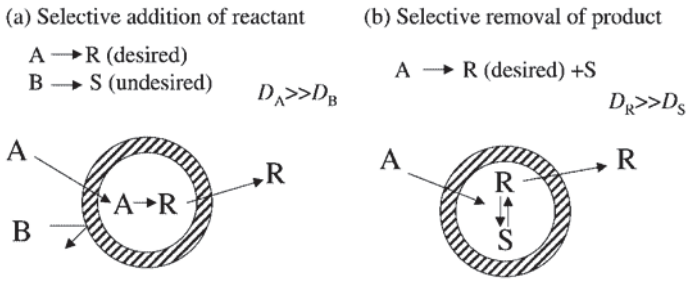

Figure 19: Principle of operation of a catalyst coated with a permselective membrane, (from ref [116]).

The zeolite shell can also determine the product selectivity by favoring the diffusion of less bulky molecules as shown in Fig.19 right. Van de Puil et al. showed that silicalite-1 coated Pt/TiO_2 core-shell catalyst showed much higher yield in linear alkenes than branched ones in the hydrogenation of linear and branched alkenes.[148-150] A similar behavior was also reported in the highly selective formation of para-xylene as compare to ortho- and meta- isomers in the disproportionation of toluene over silicalite-1 coated Pt/silica-alumina particles.[122]

II.4.3.4. Core-shell catalysts with acidic zeolite shells

Fischer-Tropsch synthesis (FTS) is one of the most investigated catalytic processes nowadays. It is first reported by Fischer and Tropsch in 1925. It produces sulfur and aromatic free liquid fuels from syngas (mixture of CO and H_2). The global reaction in FTS can be presented as CO + H_2 → hydrocarbons + H_2O. It is an alternative and sustainable solution compared to the conventional crude oil refinery due to the abundance of syngas resources. The products of FTS synthesis are normal hydrocarbons, while short-chain isoparaffins and alkylates with high octane numbers are preferential products for gasoline. An ideal catalyst for FTS would be a bifunctional catalyst, in which acid sites catalyze the (hydro) isomerization while chain growth occurs on metal sites, typically group-VIII metals, such as Fe or Co.

A simple mechanical mixture of components does not necessarily ensure appropriate proximity between the acid and hydrogenating sites. This can be achieved by using a core-shell catalyst, consisting of an acid zeolite layer coated on Co or Fe/SiO_2 grains (Fig. 20). In the reaction the syngas diffuses through zeolite and reacts on Co/SiO_2 to form hydrocarbons, and then hydrocarbons with diameter smaller than the zeolite pores diffuse through the zeolite and undergo cracking and isomerization reactions on the acid sites. Thus, improved selectivity in short chain hydrocarbons in FTS is achieved by this bifunctional catalyst.[151]

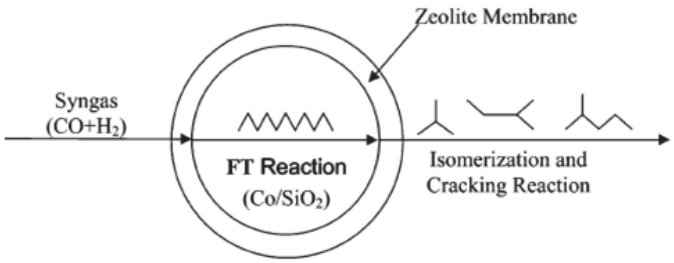

Figure 20: Catalytic process over bifunctional core-shell catalyst (H-ZSM-5 coated on Co/SiO_2 particles) in FTS, (from ref [151]).

Kapteijn et al. described H-ZSM-5 coated Co/SiO_2 catalyst were capable of producing a certain range of hydrocarbons in Fischer–Tropsch synthesis.[151-153] Good selectivities in short chain hydrocarbons and isoparaffins were reported for zeolite-coated Co and Fe based bifunctional catalysts.[153-155]

However, the thickness of the zeolite shell varies usually from 1µm up to several microns[146, 156]which eventually limits the overall reaction rates due to diffusion transport limitations.[146] Yet, an excessive thickness of the zeolite shell may lead to undesirable mass transport limitations, thus affecting the productivity of the desired reaction products.[146]

II.5. Molecule transport and diffusion limitation in zeolites

The presence of active sites confined in well-defined micropores makes zeolites one of the most used catalysts in petroleum industry. On the other side, micropores may constraint mass transfer diffusion, thus lowering the catalytic rates and even leading to coke formation when large molecules deposit in and block the pore system. Diffusion limitation, which is one of the main drawbacks in zeolite application, restricts the catalyst utilization to a certain depth under the crystal surface. Krishna proposed to represent the percentage of zeolite effectively used in a reaction by the effectiveness factor η, which increases when the Thiele modulus value (ø) decreases (Fig.21).[157] For example ø≈0, corresponding to η=1 indicates that the reaction rate is the same as the intrinsic reaction rate; zeolite is fully used without diffusion limitations. From the equation of the Thiele modulus in Fig. 21-c, $ø = \frac{\text{r intrinsic}}{\text{r diffusion}} = L\frac{\sqrt{Kv}}{\sqrt{Deff}}$, small values can be obtained by shortening the diffusion length (L) or/and by enhancing the effective diffusivity (D_{eff}) in the zeolite (K_v is an intrinsic rate coefficient fixed by the zeolite and reaction). Effective diffusivity D_{eff} can be increased by enlarging the pore size of the zeolite. However, the number of zeolites with large pores or even extra-large pores is quite limited, and most of them are expensive because their synthesis involves the use of germanium precursors and complex structure-directing molecules.[158]

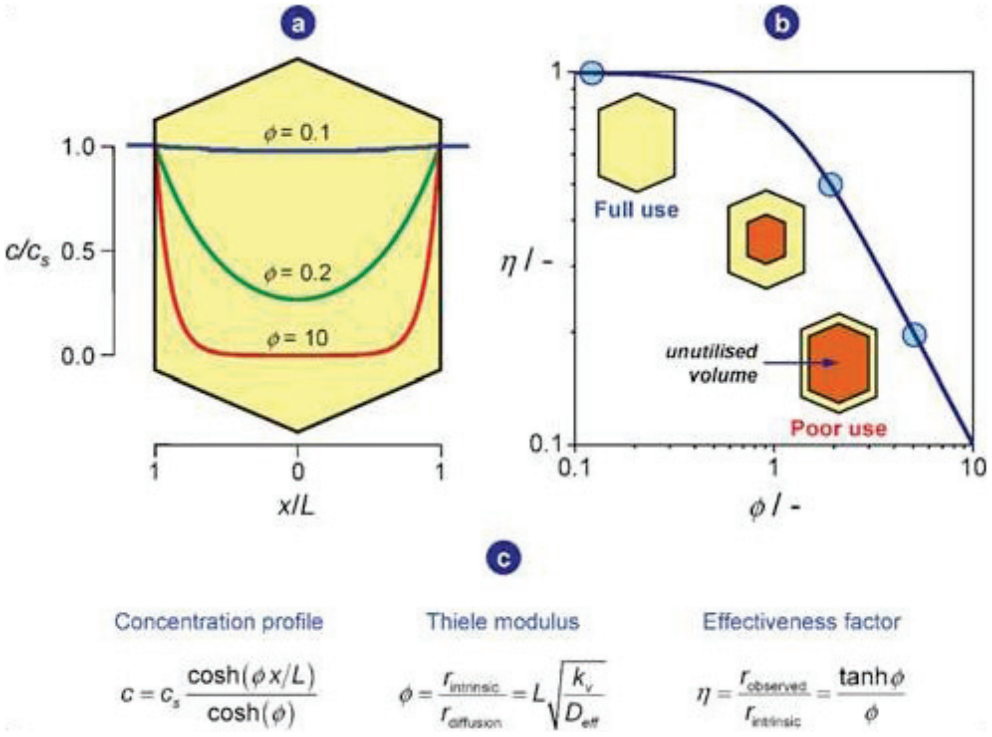

Figure 21: (a): The concentration profile across a zeolite crystal at different values of Thiele modulus (ø); (b): The dependence of the effectiveness factor on the Thiele modulus value; (c): relevant equations to construct the graphs (a) and (b), Baur and Krishna addressed the applicability of classical definitions of Thiele modulus and effectiveness factor for zeolites, (from ref [157, 159]).

Much more efforts have been devoted to the first strategy which can be generally achieved by synthesizing small crystals or by developing hierarchical systems which are zeolite crystals with multiple levels of porosity.[147,160]

Several synthesis strategies can be used to shorten diffusion length and obtain zeolites with improved mass-transfer properties such as decrease of the crystal size down to a few tens of nanometers (nanocrystals, nanosheets) or creation of hierarchical porosity in large crystals. Those zeolites can be obtained either by direct synthesis of zeolites or by post-synthesis treatments over zeolites such as dealumination or desilication.

II.5.1. Direct synthesis zeolites with improved mass-transfer properties

Fig.22 gives examples of different strategies used to decrease the size of zeolite crystals or shorten the diffusion length in zeolite through a bottom-up approach which generally includes non-templating and templating methods.[147] Nanosized zeolites can be obtained by controlling crystallization parameters, for example by modifying dilution, adding growth inhibitors, increasing the supersaturation or quenching crystallization.[161, 162] However, there is no generic approach to achieve different zeolite structures. Rather, it appears that special synthesis schemes have to be developed for each desired zeolite material.[163]

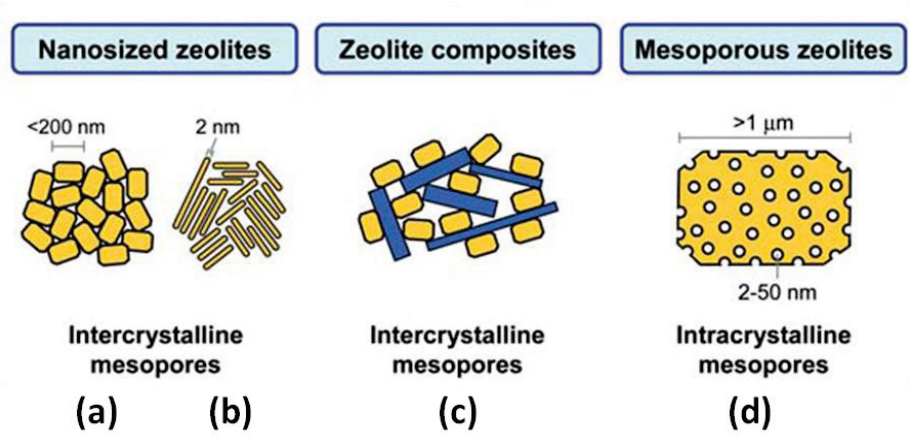

Figure 22: Categorisation of improved effective mass-transfer zeolites synthesized by template routes. (from ref [159])

In template synthesis, templates are usually carbons, supramolecules, polymers, organic aerogels, inorganic compounds or biological molecules. Their functions can be divided into two groups: 1) serving as hard templates and restricting the crystal growth; 2) forcing or affecting zeolite crystallization in a specific direction. For instance, MFI and BEA zeolites with a crystal size down to

approx. 10 nm have been synthesized by confining the zeolite crystallization in the pores of a carbon matrix as the template which was further removed by subsequently calcination (Fig.22-a).[164 165]

Ryoo et al. have reported the synthesis of zeolite nanosheets using $C_{22}H_{45}$-$N^+(CH_3)_2$-C_6H_{12}-$N^+(CH_3)_2$-C_6H_{13} organosilanes as structure directing agents (Fig.22-b). In this case, the di-ammonium head group acts as an effective structure directing agent for the zeolite crystallization whilst the hydrophobic long chain tails restrict zeolite growth and induce the formation of a lamellar structure between zeolite layers. The diffusion and mass transfer through micropores of these 2nm thick ZSM-5 nanosheets could be strongly improved with a decrease of coke formation and a significant longer lifetime in methanol to olefins reaction.[166] Pt and Fe encapsulated in ZSM-5 nanosheets have been prepared by post-synthesis (ion-exchange or impregnation) and they showed not only effective improved mass-transfer properties but also higher shape selectivity in hydroisomerization and oxidation reactions.[128, 167, 168] Fe/ZSM-5 nanosheets showed higher activity and longer lifetime compared to conventional Fe/ZSM-5 catalyst in benzene oxidation reaction. The authors showed that coke formed on the external surface of the nanosheets, which mainly deposited into the micropores of Pt/ZSM-5 and led to catalyst deactivation.[165]

Fig.22-c shows another material with improved mass-transfer properties which consists of zeolite crystals supported on a material which is typically mesoporous or macroporous. In this case, the supporting material provides the pores required for improving mass transport to and from the zeolite crystals. Generally, it can be achieved either by directly assembling of crystalline particles or by indirect templating.[169] Kloetstra et al. reported the preparation of MCM-41/USY layered composite by crystalline particle assembling, which exhibited higher catalytic activity in the cracking of vacuum gasoil compared to USY zeolites.[170] In the indirect synthesis, crystallization starts from an amorphous mesoporous material resulting in highly mesoporous and relatively stable zeolites, particularly when SBA-15 is used as starting support.[171]

Furthermore, mesoporous zeolite crystals can be obtained when carbon particles or carbon nanotubes are encapsulated in the zeolite in course of crystallization. Mesoporosity is then generated by calcination of the sacrificial templates, as shown in Fig22-d.[160, 172, 173] Those mesoporous ZSM-5 showed higher activity compared to conventional ZSM-5 catalysts in the alkylation of benzene due to the reduced diffusion limitations.[173]

II.5.2. Post-synthesis zeolites with improved mass-transfer properties

In addition to templating methods, mesoporous zeolites can also be generated by post-synthesis treatments which rely on extracting preferentially one of the constituents from zeolite framework. Dealumination and desilication are the most studied among this "top-down" approach.

II.5.2.1. Dealumination treatments of zeolites

Dealumination is performed either by acid treatment or high temperature steaming (above 500°C). Steam treatment is presently used in industry to introduce mesopores in zeolites.[174] During dealumination, part of aluminum species is removed from framework positions, with formation of silanol nests. When the zeolite is streamed at high temperature, those nests are generally refilled by Si species resulting from a partial dissolution of the framework by water vapor at high temperature. However, breaking Al-O-Si bonds also leads to changes in zeolite acidic properties, such as acid strength, acid site concentration and acid site distribution. Moreover, formation of acid sites (mainly Lewis acid sites) resulting from extra-framework aluminum also needs to be taken into account.
In contract to dealumination, desilication is another strategy to create mesopores as well as to preserve Brønsted acid sites.

II.5.2.2. Desilication treatments of zeolites

Desilication is usually achieved by selective silicon removal from the zeolite framework under alkaline pH conditions. The hydrolysis of Si-O-Si bonds results in a partial dissolution of the zeolite framework with formation of mesopores, while silicon atoms in Al-O-Si bonds are stabilized by framework aluminum species.[175] Thus framework aluminum plays an important role in desilication since it stabilizes the zeolite structure and prevents a complete dissolution. Moreover, the differences in solubility between silica-rich and aluminum-rich parts have been widely used to create materials with special architectures such as hollow crystals. Groen et al. have applied this method to large ZSM-5 crystals with an Al gradient, i.e. with Al-rich surface and Si-rich core. The preferential desilication of the Si-rich core produced intra-crystalline cavities without changing the original microporosity.[176, 177] The authors studied different factors that could affect the desilication process (crystal size, temperature, PH value) and they found that ZSM-5 with overall Si/Al ratios between 25-50 were optimized for generating hollow structures by desilication (Fig.23-a).[178] The porosity is confirmed by a hysteresis in the N_2 adsorption/desorption isotherm with a forced closure at $P/P_0 \approx 0.42$, characteristic of cavities connected to the outer surface by the zeolite micropores (Fig. 23-b).[179]

Fig.23-c shows that the same treatment performed on small ZSM-5 crystalls of ca. 400 nm in which Al is randomly distributed did not lead to large cavities but to the formation of mesopores throughout the crystals.

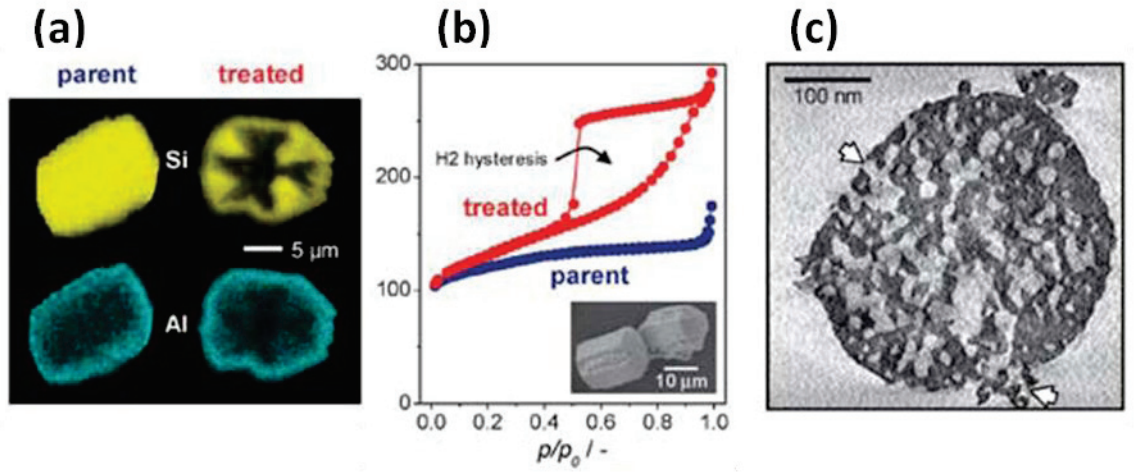

Figure 23: SEM-EDX images of parent and alkaline treated ZSM-5 crystals (a), N_2 adsorption desorption isotherms of parent and alkaline treated ZSM-5 crystals (b) and TEM images of alkaline treated small ZSM-5 (c), (from ref [179]).

Several reports have showed the impact of zeolites desilication on the catalytic performances, particularly on the activity and lifetime.[180] For example, higher activities and longer lifetimes were observed during methanol to gasoline and methanol to propylene processes over desilicated ZSM-5[181, 182] and benzene alkylation over mesoporous Beta zeolite.[183] In the reaction of benzene hydroxylation to phenol with N_2O, the desilicated ZSM-5 showed significantly higher stability and excellent phenol selectivity, see Fig. 24.[184]

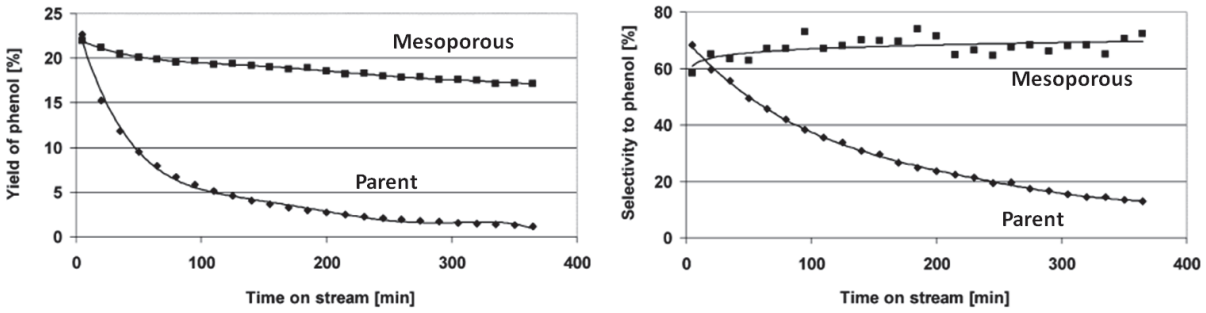

Figure 24: Phenol yeild and selectivity with time on stream over parent and desilicated ZSM-5, (from ref[180, 184]).

As an example of desilicated-zeolite encapsulated nanoparticles, the introduction of mesoporosity in Ru and Co/zeolite catalysts increases the activity and selectivity to the gasoline fraction (C_5-C_{11}) and leads to an enhanced octane number of the products in the isomerization reactions and Fischer-Tropsch synthesis.[185-188] Recently, Kapteijn et al. have reported the optimized desilication conditions of ZSM-5 using TPAOH and NaOH solutions, TPAOH leads to a higher degree of hierarchy of

mesopores with larger cavities connected by small mesopores. Furthermore ZSM-5 desilicated by TPAOH exhibited higher CO conversion in FTS (15% more) than those treated by NaOH.[186-189]

Desilication has also been performed on all-silica zeolites such as silicalite-1. Weidenthaler et al. have reported the synthesis of Au particles encapsulated in mesoporous silicalite-1 materials obtained by a desilication-reassembly process.[190] Encapsulated Au particles showed highly thermal stability, activity and selectivity in the gas-phase oxidation of ethanol to acetaldehyde.

As a short conclusion, the combination of hierarchical zeolites with sinter-stable nanoparticles at nanoscale level seems to be one of the most promising routes to design composite materials with reduced diffusion limitations and optimized operating catalytic performances.

II.5.2.3. Preparation of hollow zeolites

Several groups have reported the preparation of hollow zeolite spheres using different synthesis strategies. Tang et al. developed the synthesis of hollow silicalite-1 and Beta in the presence of hard templates such as mesoporous silica or polystyrene beads.[191-195] Small zeolite particles are gathered around the bead to form a compact zeolite shell, and then templates are removed either by dissolution or by calcination. Pt and Ag particles can also be encapsulated into these hollow zeolite shells by using template-supported nanoparticles and these solids showed much better selectivity and stability than supported catalysts in liquid oxidation reactions.[194] Hollow zeolite shells obtained by this method are polycrystalline with a thickness approximately 200 nm, which composed from aggregation of small zeolite particles. Shells are thick enough to still show diffusion limitations and they are probably less efficient as membrane as compared to single crystals.

We have previously mentioned the formation of hollow ZSM-5 zeolites by preferential desilication of crystals possessing a gradient of aluminum concentration (Fig.23-a). Under alkaline conditions, the Si-rich core is dissolved while Al-rich outer layer remains intact, which leads to large cavities and unique thin zeolite walls.[179] Those post-treatment can effectively shorten the diffusion length (L) and thus release diffusion limitations, as shown in many catalytic reactions. However, standard desilication usually result in non-uniform structures, thus, revealing the heterogeneity in Al distribution throughout the crystal. Besides, single crystal hollow zeolites can also be achieved by mild desilication conditions using NaOH or Na_2CO_3.[196, 197]

II.5.2.4. Hollow zeolites and pioneered achievements on hollow zeolites at IRCELYON

Tuel et al. have reported the preparation of hollow zeolites with wall thickness of approximately 20 to 30 nm by dissolution/recrystallization of bulk crystals in the presence of TPAOH (Fig. 25).[198, 199] By contrast to a standard dissolution using NaOH, dissolved species could recrystallize on the outer surface of the crystals, thus leading to uniform structures with well-defined edges. As a consequence, no zeolite is lost during the process (all dissolved species could recrystallize) and the overall composition is unchanged. It is interesting to note that the mechanism of dissolution/recrystallization is intrinsically different from a conventional desilication: the method does not necessitate the presence of Al in the crystals and dissolution preferentially occurs in defect-rich areas, typically the center of the crystals.[200, 201]

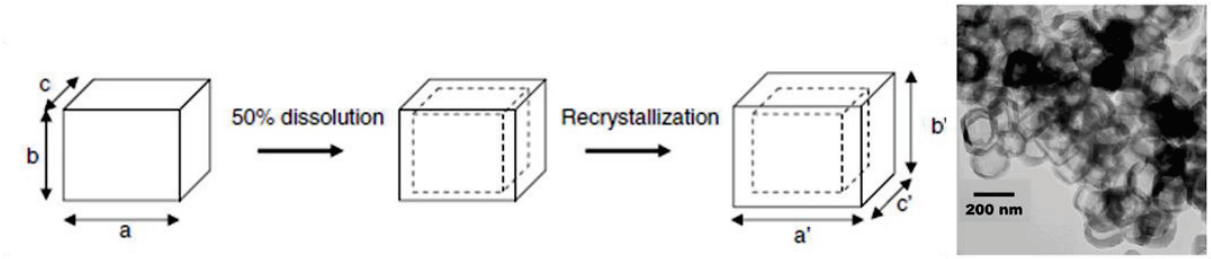

Figure 25: scheme of the dissolution/recrystallization process (left) and TEM image (right) of the hollow zeolite, (from ref [202]).

Beyond these preliminary reports, the systematic study of metal nanoparticles encapsulated in single crystal hollow zeolites has not yet been reported. These Yolk-shell catalysts could benefit of the synergistic effects of small particles in contact with thin zeolite shells and be of particular interest in material science and catalysis.

III.Concept of this PhD work

Based on the work previously reported by Tuel et al., this PhD work is dealing with the synthesis of yolk-shell catalysts in which metal nanoparticles are encapsulated in single crystal hollow zeolite shells. In such composite materials the thin zeolite shell will be used for:

1) protecting metal nanoparticles from sintering
2) changing reaction selectivity by molecular sieving
3) nansized alloy particles with controllable size and compositions

Au and Pt have been selected as yolk metals at the beginning of this PhD work. Synthesis parameters were systematically studied to improve metal location, dispersion and to control the average nanoparticles size. After optimization of synthesis conditions, the method has been extended to other noble metals (Ag and Pd), transition metals (Co, Ni and Cu) and alloys. Other synthesis methods have also been examined to improve the characteristics of the hollow zeolite and the encapsulation method.

This PhD thesis is consisted of 6 chapters; except the first chapter (state-of-the-art) and the second one (experimental part), each chapter introduces the synthesis, characterizations and catalytic applications of one type of metal nanoparticle encapsulated in hollow zeolite material;

- Chapter 1: state-of-the-art which is the literature study on each component and the delicate structure of our materials which are metal nanoparticles, zeolites and yolk-shell structure.

- Chapter 2: experimental part which includes the preparation methods of all the materials, characterization techniques and catalytic reactions.

- Chapter 3: noble metal nanoparticles (Au, Pt, Pd and Ag) in hollow silicalite-1 (nanocrystals and large crystals) prepared by dissolution recrystallization method. The catalytic selectivity has been achieved either by molecular sieving (study case: hydrogenation of light aromatics) or by molecular diffusion effects (study case: CO selective oxidation in the presence of propylene) over Pt nanoparticle in hollow silicalite-1 catalyst.

- Chapter 4: transition metal nanoparticles (Co, Ni and Cu) in hollow silicalite-1 and hollow ZSM-5 materials prepared by dissolution recrystallization method, which are completely different from the cases of noble metal nanoparticles in hollow silicalite-1. The molecular sieving effects have been demonstrated in the hydrogenation reactions of light aromatics.

- Chapter 5: metal nanoparticles (Au, Pt, Pd and Ni) in hollow ZSM-5 prepared by different synthesis methods. Pt nanoparticles in hollow ZSM-5 have been prepared by desilication method which showed high activities in the hydrogenation reactions compared to the materials prepared by dissolution recrystallization method.

- Chapter 6: alloy nanoparticles (PtPd, PtAg, PdAg and AuAg) in hollow silicalite-1 and hollow ZSM-5 prepared by different methods. The synergistic effects of alloy particles have been provided in the CO oxidation reactions over AuAg in hollow silicalite-1 catalyst, meanwhile the protected particles by the zeolite shells leads to long life-time catalyst.

Bibliography

1. Alivisatos, A.P. Semiconductor clusters, nanocrystals, and quantum dots. *Science* **271**, 933-937 (1996).

2. Daniel, M.C. & Astruc, D. Gold nanoparticles: Assembly, supramolecular chemistry, quantum-size-related properties, and applications toward biology, catalysis, and nanotechnology. *Chem. Rev.* **104**, 293-346 (2004).

3. Eustis, S. & El-Sayed, M.A. Why gold nanoparticles are more precious than pretty gold: Noble metal surface plasmon resonance and its enhancement of the radiative and nonradiative properties of nanocrystals of different shapes. *Chem. Soc. Rev.* **35**, 209-217 (2006).

4. Brus, L. Noble Metal Nanocrystals: Plasmon Electron Transfer Photochemistry and Single-Molecule Raman Spectroscopy. *Acc. Chem. Res.* **41**, 1742-1749 (2008).

5. Watanabe, K., Menzel, D., Nilius, N. & Freund, H.-J. Photochemistry on metal nanoparticles. *Chem. Rev.* **106**, 4301-4320 (2006).

6. Turkevich, J. Colloidal gold. Part II. *Gold Bull.* **18**, 125-131 (1985).

7. Turkevic.J & Kim, G. Palladium – Preparation and Catalytic Properties of Particles of Uniform Size. *Science* **169**, 873-879 (1970).

8. Murray, R.W. Nanoelectrochemistry: Metal nanoparticles, nanoelectrodes, and nanopores. *Chem. Rev.* **108**, 2688-2720 (2008).

9. Xia, Y., Xiong, Y., Lim, B. & Skrabalak, S.E. Shape-Controlled Synthesis of Metal Nanocrystals: Simple Chemistry Meets Complex Physics? *Angew. Chem. Int. Ed.* **48**, 60-103 (2009).

10. Schmidt, T.J., Noeske, M., Gasteiger, H.A., Behm, R.J., Britz, P. & Bonnemann, H. PtRu alloy colloids as precursors for fuel cell catalysts - A combined XPS, AFM, HRTEM, and RDE study. *J. Electrochem. Soc.* **145**, 925-931 (1998).

11. Gotz, M. & Wendt, H. Binary and ternary anode catalyst formulations including the elements W, Sn and Mo for PEMFCs operated on methanol or reformate gas. *Electrochim. Acta* **43**, 3637-3644 (1998).

12. Faraday, M. The Bakerian lecture: experimental relations of gold (and other metals) to light. *Philosophical Transactions of the Royal Society of London*, 145-181 (1857).

13. Liu, H.F., Mao, G.P. & Meng, S.J. Preparation and Characterization of the Polymer-Protected Palladium Gold colloidal Bimetallic Catalysts. *J. Mol. Catal.* **74**, 275-284 (1992).

14. Narayanan, R. & El-Sayed, M.A. Effect of catalysis on the stability of metallic nanoparticles: Suzuki reaction catalyzed by PVP-palladium nanoparticles. *J. Am. Chem. Soc.* **125**, 8340-8347 (2003).

15. Turkevich, J., Stevenson, P.C. & Hillier, J. A Study of the Nucleation and Growth Processes in the colloidal Gold. *Discussions of the Faraday Society*, 55-75 (1951).

16. Tauschtreml, R., Henglein, A. & Lilie, J. Reactivity of Silver Atoms in Aqueous-Solution.2. Pulse-Radiolysis Study. *Berichte Der Bunsen-Gesellschaft-Physical Chemistry Chemical Physics* **82**, 1335-1343 (1978).

17. Michaelis, M. & Henglein, A. Reduction of Pd(II) in Aqueous-Solution-Stabilization and Reactions od an Intermediate Cluster and Pd Colloid Formation. *J. Phys. Chem.* **96**, 4719-4724 (1992).

18. Rothe, J., Hormes, J., Bonnemann, H., Brijoux, W. & Siepen, K. In situ X-ray absorption spectroscopy investigation during the formation of colloidal copper. *J. Am. Chem. Soc.* **120**, 6019-6023 (1998).

19. Bradley, J.S., Tesche, B., Busser, W., Masse, M. & Reetz, R.T. Surface spectroscopic study of the stabilization mechanism for shape-selectively synthesized nanostructured transition metal colloids. *J. Am. Chem. Soc.* **122**, 4631-4636 (2000).

20. Leisner, T., Rosche, C., Wolf, S., Granzer, F. & Woste, L. The catalytic role of small coinage-metal clusters in photography. *Surface Review and Letters* **3**, 1105-1108 (1996).

21. Bönnemann, H. & Richards, R.M. Nanoscopic metal particles− synthetic methods and potential applications. *Eur. J. Inorg. Chem.* **2001**, 2455-2480 (2001).

22. Bradley, J.S. The chemistry of transition metal colloids. *Clusters and colloids: from theory to applications*, 459-544 (1994).

23. Hirai, H., Nakao, Y. & Toshima, N. Colloidal Rhodium in Polyvinyl-Alcohol as Hydrogenation Catalyst of Olefins. *Chem. Lett.*, 905-910 (1976).

24. Hirai, H., Nakao, Y. & Toshima, N. Colloidal Rhodium in Poly(vinylpyrrolidone) as Hydrogenation Catalyst for Internal Olefins. *Chem. Lett.*, 545-548 (1978).

25. Hirai, H., Nakao, Y. & Toshima, N. Preparation of colloidal Rhodium in Polyvinyl-alcohol by Reduction with Methanol. *Journal of Macromolecular Science-Chemistry* **A12**, 1117-1141 (1978).

26. Bonnemann, H., Brijoux, W., Brinkmann, R., Fretzen, R., Joussen, T., Koppler, R., Korall, B., Neiteler, P. & Richter, J. Preparation, Characterization, and Application of Fine Metal Particles and Metal Colloids Using Hydro-tri-organoborates. *J. Mol. Catal.* **86**, 129-177 (1994).

27. Schmid, G., Pfeil, R., Boese, R., Bandermann, F., Meyer, S., Calis, G.H.M. & Vandervelden, W.A. $Au_{55}[P(C_6H_5)_3]_{12}Cl_6$ - A Gold Cluster of an Exceptional Size. *Chemische Berichte-Recueil* **114**, 3634-3642 (1981).

28. Schmid, G., Morun, B. & Malm, J.O. Pt_{309} $Phen^*_{36}O_{30\pm10}$, A Four-Shell Platinum Cluster. *Angew. Chem. Int. Ed.* **28**, 778-780 (1989).

29. Amiens, C., Decaro, D., Chaudret, B., Bradley, J.S., Mazel, R. & Roucau, C. Selective Synthesis, Characterization, and Spectroscopic Studies on a Novel Class of Reduced Platinum and Palladium Particles Stabilized by Carbonyl and Phosphine-Ligands. *J. Am. Chem. Soc.* **115**, 11638-11639 (1993).

30. Antonietti, M. & Goltner, C. Superstructures of functional colloids: Chemistry on the nanometer scale. *Angew. Chem. Int. Ed.* **36**, 910-928 (1997).

31. Pileni, M.P. Colloidal self-assemblies used as templates to control size, shape and self-organization of nanoparticles. *Supramolecular Science* **5**, 321-329 (1998).

32. Forster, S. Amphiphilic block copolymers. *Berichte Der Bunsen-Gesellschaft-Physical Chemistry Chemical Physics* **101**, 1671-1678 (1997).

33. Miyao, T., Toyoizumi, N., Okuda, S., Imai, Y., Tajima, K. & Naito, S. Preparation of Pt/SiO2 ultra-fine particles in reversed micelles and their catalytic activity. *Chem. Lett.*, 1125-1126 (1999).

34. Reetz, M.T. & Lohmer, G. Propylene carbonate stabilized nanostructured palladium clusters as catalysts in Heck reactions. *Chem. Commun.*, 1921-1922 (1996).

35. Reetz, M.T. & Helbig, W. Size-Selective Synthesis of Nanostructured Transition-Metal Clusters. *J. Am. Chem. Soc.* **116**, 7401-7402 (1994).

36. Reetz, M.T. & Quaiser, S.A. A New Method for the Preparation of Nanostructured Metal-Clusters. *Angew. Chem. Int. Ed.* **34**, 2240-2241 (1995).

37. Bonnemann, H., Brijoux, W., Brinkmann, R., Endruschat, U., Hofstadt, W. & Angermund, K. The reductive stabilzation of nanometal colloids by organo-aluminum compounds. *Rev. Roum. Chim.* **44**, 1003-1010 (1999).

38. Bradley, J.S., Hill, E., Leonowicz, M.E. & Witzke, H. Clusters, Colloids and Catalysis. *J. Mol. Catal.* **41**, 59-74 (1987).

39. Schmid, G. & Lehnert, A. The Complexation of Gold Colloids. *Angew. Chem. Int. Ed.* **28**, 780-781 (1989).

40. Schmid, G. Large Clusters and Colloids – Metal in the Embryonic State. *Chem. Rev.* **92**, 1709-1727 (1992).

41. Simon, U., Flesch, R., Wiggers, H., Schon, G. & Schmid, G. Chemical tailoring of the charging energy in metal cluster arrangements by use of bifunctional spacer molecules. *J. Mater. Chem.* **8**, 517-518 (1998).

42. Giersig, M., Liz-Marzan, L.M., Ung, T., Su, D.S. & Mulvaney, P. Chemistry of nanosized silica-coated metal particles EM-study. *Berichte Der Bunsen-Gesellschaft-Physical Chemistry Chemical Physics* **101**, 1617-1620 (1997).

43. Toshima, N. & Yonezawa, T. Bimetallic nanoparticles - novel materials for chemical and physical applications. *New J. Chem.* **22**, 1179-1201 (1998).

44. Hirai, H., Nakao, Y. & Toshima, N. Preparation of Colloidal Transition-Metal in Polymers by Reduction with Alcohols or Ethers. *Journal of Macromolecular Science-Chemistry* **A13**, 727-750 (1979).

45. Lu, P., Teranishi, T., Asakura, K., Miyake, M. & Toshima, N. Polymer-protected Ni/Pd bimetallic nano-clusters: Preparation, characterization and catalysis for hydrogenation of nitrobenzene. *J. Phys. Chem. B* **103**, 9673-9682 (1999).

46. Toshima, N. & Hirakawa, K. Polymer-protected bimetallic nanocluster catalysts having core/shell structure for accelerated electron transfer in visible-light-induced hydrogen generation. *Polymer Journal* **31**, 1127-1132 (1999).

47. Vargaftik, M.N., Zagorodnikov, V.P., Stolyarov, I.P., Moiseev, II, Likholobov, V.A., Kochubey, D.I., Chuvilin, A.L., Zaikovsky, V.I., Zamaraev, K.I. & Timofeeva, G.I. A Novel Giant Palladium Cluster. *Journal of the Chemical Society-Chemical Communications*, 937-939 (1985).

48. Volkov, V.V., VanTendeloo, G., Tsirkov, G.A., Cherkashina, N.V., Vargaftik, M.N., Moiseev, II, Novotortsev, V.M., Kvit, A.V. & Chuvilin, A.L. Long- and short-distance ordering of the metal cores of giant Pd clusters. *J. Cryst. Growth* **163**, 377-387 (1996).

49. Moiseev, II, Vargaftik, M.N., Volkov, V.V., Tsirkov, G.A., Cherkashina, N.V., Novotortsev, V.M., Ellert, O.G., Petrunenko, I.A., Chuvilin, A.L. & Kvit, A.V. Palladium-561 Giant Clusters – Chemical Aspects of Self-Organization on a Nano Level. *Mendeleev Commun.*, 87-89 (1995).

50. Osuna, J., deCaro, D., Amiens, C., Chaudret, B., Snoeck, E., Respaud, M., Broto, J.M. & Fert, A. Synthesis, characterization, and magnetic properties of cobalt nanoparticles from an organometallic precursor. *J. Phys. Chem.* **100**, 14571-14574 (1996).

51. Reetz, M.T., Quaiser, S.A. & Merk, C. Electrochemical preparation of nanostructured titanium clusters: Characterization and use in McMurry-type coupling reactions. *Chem. Ber.* **129**, 741-743 (1996).

52. Becker, J.A., Schafer, R., Festag, R., Ruland, W., Wendorff, J.H., Pebler, J., Quaiser, S.A., Helbig, W. & Reetz, M.T. Electrochemical Growth of Superparamagnetic Cobalt Clusters. *J. Chem. Phys.* **103**, 2520-2527 (1995).

53. Reetz, M.T., Helbig, W. & Quaiser, S.A. Electrochemical preparation of nanostructured bimetallic clusters. *Chem. Mater.* **7**, 2227-2228 (1995).

54. Hess, P.H. & Parker, P.H. Polymers for Stabilization of Colloidal Cobalt Particles. *J. Appl. Polym. Sci.* **10**, 1915-1927 (1966).

55. Thomas, J.R. Preparation and Magnetic Properties of Colloidal Cobalt Particles. *J. Appl. Phys.* **37**, 2914-2915 (1966).

56. Bradley, J.S., Hill, E.W., Klein, C., Chaudret, B. & Duteil, A. Synthesis of Monodispersed Bimetallic Palladium Copper Nanoscale Colloids. *Chem. Mater.* **5**, 254-256 (1993).

57. Yu, W.Y., Tu, W.X. & Liu, H.F. Synthesis of nanoscale platinum colloids by microwave dielectric heating. *Langmuir* **15**, 6-9 (1999).

58. Wada, Y., Kuramoto, H., Sakata, T., Mori, H., Sumida, T., Kitamura, T. & Yanagida, S. Preparation of nano-sized nickel metal particles by microwave irradiation. *Chem. Lett.*, 607-608 (1999).

59. Dhas, N.A. & Gedanken, A. Sonochemical preparation and properties of nanostructured palladium metallic clusters. *J. Mater. Chem.* **8**, 445-450 (1998).

60. Koltypin, Y., Fernandez, A., Rojas, T.C., Campora, J., Palma, P., Prozorov, R. & Gedanken, A. Encapsulation of nickel nanoparticles in carbon obtained by the sonochemical decomposition of Ni(C8H12)(2). *Chem. Mater.* **11**, 1331-1335 (1999).

61. Duteil, A., Queau, R., Chaudret, B., Mazel, R., Roucau, C. & Bradley, J.S. Preparation of Organic Solutions or Solid Films of Small Particles of Ruthenium, Palladium, and Platinum from Organometallic precursors in the presence of Cellulose Derivatives. *Chem. Mater.* **5**, 341-347 (1993).

62. deCaro, D., Agelou, V., Duteil, A., Chaudret, B., Mazel, R., Roucau, C. & Bradley, J.S. Preparation from organometallic precursors, characterization and some reactivity of copper and gold colloids sterically protected by nitrocellulose, polyvinylpyrrolidone or polydimethyl phenylene oxide. *New J. Chem.* **19**, 1265-1274 (1995).

63. Bardaji, M., Vidoni, O., Rodriguez, A., Amiens, C., Chaudret, B., Casanove, M.J. & Lecante, P. Synthesis of platinum nanoparticles stabilized by CO and tetrahydrothiophene. Facile conversion to molecular species. *New J. Chem.* **21**, 1243-1249 (1997).

64. Ould-Ely, T., Pan, C., Amiens, C., Chaudret, B., Dassenoy, F., Lecante, P., Casanove, M.J., Mosset, A., Respaud, M. & Broto, J.M. Nanoscale bimetallic CoxPt1-x particles dispersed in poly(vinylpyrrolidone): Synthesis from organometallic precursors and characterization. *J. Phys. Chem. B* **104**, 695-702 (2000).

65. Soulantica, K., Maisonnat, A., Fromen, M.C., Casanove, M.J., Lecante, P. & Chaudret, B. Synthesis and self-assembly of monodisperse indium nanoparticles prepared from the organometallic precursor In(eta(5)-C5H5). *Angew. Chem. Int. Ed.* **40**, 448-451 (2001).

66. Reetz, M.T., Quaiser, S.A., Winter, M., Becker, J.A., Schafer, R., Stimming, U., Marmann, A., Vogel, R. & Konno, T. Nanostructured metal oxide clusters by oxidation of stabilized metal clusters with air. *Angew. Chem. Int. Ed.* **35**, 2092-2094 (1996).

67. Verelst, M., Ould-Ely, T., Amiens, C., Snoeck, E., Lecante, P., Mosset, A., Respaud, M., Broto, J.M. & Chaudret, B. Synthesis and characterization of CoO, Co3O4, and mixed Co/CoO nanoparticules. *Chem. Mater.* **11**, 2702-2708 (1999).

68. Wang, C.B. & Yeh, C.T. Effects of particle size on the progressive oxidation of nanometer platinum by dioxygen. *J. Catal.* **178**, 450-456 (1998).

69. Rao, C.N.R. Chemical approaches to the synthesis of inorganic materials. (Wiley New Delhi, 1994).

70. Haberland, H. Clusters of atoms and molecules, Vol. 52. (Springer Berlin, 1994).

71. Gaffet, E., Tachikart, M., ElKedim, O. & Rahouadj, R. Nanostructural materials formation by mechanical alloying: Morphologic analysis based on transmission and scanning electron microscopic observations. *Materials Characterization* **36**, 185-190 (1996).

72. Amulyavichus, A., Daugvila, A., Davidonis, R. & Sipavichus, C. Study of chemical composition of nanostructural materials prepared by laser cutting of metals. *Fiz. Met. Metalloved.* **85**, 111-117 (1998).

73. Wang, J.-P. FePt magnetic nanoparticles and their assembly for future magnetic media. *Proceedings of the IEEE* **96**, 1847-1863 (2008).

74. Michel Che & Bennett, C.O. The Influence of Particle-Size on the Catalytic Properties of Supported Metals, Vol. 36. (1989).

75. Beck, D.D. & Carr, C.J. A study of thermal aging of PtAl2O3 using temperature-programmed desorption spectroscopy. *J. Catal.* **110**, 285-297 (1988).

76. Wynblatt, P. & Gjostein, N. Supported metal crystallites. *Prog. Solid State Chem.* **9**, 21-58 (1975).

77. Baker, R.T.K. The relationship between particle motion on a graphite surface and Tammann temperature. *J. Catal.* **78**, 473-476 (1982).

78. Harris, P. Growth and structure of supported metal catalyst particles. *International materials reviews* **40**, 97-115 (1995).

79. Hansen, T.W., DeLaRiva, A.T., Challa, S.R. & Datye, A.K. Sintering of Catalytic Nanoparticles: Particle Migration or Ostwald Ripening? *Acc. Chem. Res.* **46**, 1720-1730 (2013).

80. Bartholomew, C.H. Sintering kinetics of supported metals: new perspectives from a unifying GPLE treatment. *Appl. Catal., A* **107**, 1-57 (1993).

81. Challa, S.R., Delariva, A.T., Hansen, T.W., Helveg, S., Sehested, J., Hansen, P.L., Garzon, F. & Datye, A.K. Relating Rates of Catalyst Sintering to the Disappearance of Individual Nanoparticles during Ostwald Ripening. *J. Am. Chem. Soc.* **133**, 20672-20675 (2011).

82. Challa, S.R., Song, Y., Shelnutt, J.A., Miller, J.E. & Swol, F.v. Evolution of dendritic nanosheets into durable holey sheets: a lattice gas simulation study. *Journal of Porphyrins and Phthalocyanines* **15**, 449-458 (2011).

83. Hansen, T.W., Wagner, J.B., Hansen, P.L., Dahl, S., Topsøe, H. & Jacobsen, C.J. Atomic-resolution in situ transmission electron microscopy of a promoter of a heterogeneous catalyst. *Science* **294**, 1508-1510 (2001).

84. Yang, W.-C., Zeman, M., Ade, H. & Nemanich, R. Attractive Migration and Coalescence: A Significant Process in the Coarsening of T i S i 2 Islands on the Si (111) Surface. *Phys. Rev. Lett.* **90**, 136102 (2003).

85. McCarty, J., Malukhin, G., Poojary, D., Datye, A. & Xu, Q. Thermal coarsening of supported palladium combustion catalysts. *The Journal of Physical Chemistry B* **109**, 2387-2391 (2005).

86. Cao, A. & Veser, G. Exceptional high-temperature stability through distillation-like self-stabilization in bimetallic nanoparticles. *Nat Mater* **9**, 75-81 (2010).

87. Lu, J., Fu, B., Kung, M.C., Xiao, G., Elam, J.W., Kung, H.H. & Stair, P.C. Coking- and Sintering-Resistant Palladium Catalysts Achieved Through Atomic Layer Deposition. *Science* **335**, 1205-1208 (2012).

88. Gabaldon, J.P., Bore, M. & Datye, A.K. Mesoporous silica supports for improved thermal stability in supported Au catalysts. *Top. Catal.* **44**, 253-262 (2007).

89. Rashkeev, S.N., Dai, S. & Overbury, S.H. Modification of Au/TiO2 nanosystems by SiO2 monolayers: Toward the control of the catalyst activity and stability. *The Journal of Physical Chemistry C* **114**, 2996-3002 (2010).

90. Chi, Y.S., Lin, H.P. & Mou, C.Y. CO oxidation over gold nanocatalyst confined in mesoporous silica. *Appl. Catal., A* **284**, 199-206 (2005).

91. Bore, M.T., Pham, H.N., Switzer, E.E., Ward, T.L., Fukuoka, A. & Datye, A.K. The role of pore size and structure on the thermal stability of gold nanoparticles within mesoporous silica. *The Journal of Physical Chemistry B* **109**, 2873-2880 (2005).

92. Gabaldon, J., Bore, M. & Datye, A. Mesoporous silica supports for improved thermal stability in supported Au catalysts. *Top. Catal.* **44**, 253-262 (2007).

93. Datye, A.K. Electron microscopy of catalysts: recent achievements and future prospects. *J. Catal.* **216**, 144-154 (2003).

94. Bore, M.T., Pham, H.N., Ward, T.L. & Datye, A.K. Role of pore curvature on the thermal stability of gold nanoparticles in mesoporous silica. *Chem. Commun.*, 2620-2621 (2004).

95. Kerdi, F., Caps, V. & Tuel, A. Mesostructured Au/C materials obtained by replication of functionalized SBA-15 silica containing highly dispersed gold nanoparticles. *Microporous Mesoporous Mater.* **140**, 89-96 (2011).

96. Lavenn, C., Demessence, A. & Tuel, A. Atomically well-defined Au25(SR)17/18 nanoclusters deposited on silica supports for the aerobic epoxidation of trans-stilbene. *Catal. Today* **235**, 72-78 (2014).

97. Liz-Marzan, L.M., Giersig, M. & Mulvaney, P. Synthesis of Nanosized Gold-Silica Core-Shell Particles. *Langmuir* **12**, 4329-4335 (1996).

98. Guettel, R., Paul, M. & Schüth, F. Ex-post size control of high-temperature-stable yolk-shell Au, @ ZrO2 catalysts. *Chem. Commun.* **46**, 895-897 (2010).

99. Galeano, C., Guettel, R., Paul, M., Arnal, P., Lu, A.-H. & Schueth, F. Yolk-Shell Gold Nanoparticles as Model Materials for Support-Effect Studies in Heterogeneous Catalysis: Au, @C and Au, @ZrO2 for CO Oxidation as an Example. *Chem. Eur. J.* **17**, 8434-8439 (2011).

100. Arnal, P.M., Comotti, M. & Schüth, F. High-temperature-stable catalysts by hollow sphere encapsulation. *Angew. Chem. Int. Ed.* **45**, 8224-8227 (2006).

101. Lee, I., Joo, J.B., Yin, Y. & Zaera, F. A Yolk@Shell Nanoarchitecture for Au/TiO2 Catalysts. *Angew. Chem. Int. Ed.* **50**, 10208-10211 (2011).

102. Joo, S.H., Park, J.Y., Tsung, C.-K., Yamada, Y., Yang, P. & Somorjai, G.A. Thermally stable Pt/mesoporous silica core-shell nanocatalysts for high-temperature reactions. *Nat. Mater.* **8**, 126-131 (2009).

103. Ikeda, S., Ishino, S., Harada, T., Okamoto, N., Sakata, T., Mori, H., Kuwabata, S., Torimoto, T. & Matsumura, M. Ligand-Free Platinum Nanoparticles Encapsulated in a Hollow Porous Carbon Shell as a Highly Active Heterogeneous Hydrogenation Catalyst. *Angew. Chem. Int. Ed.* **45**, 7063-7066 (2006).

104. Wu, C., Lim, Z.-Y., Zhou, C., Wang, W.G., Zhou, S., Yin, H. & Zhu, Y. A soft-templated method to synthesize sintering-resistant Au-mesoporous-silica core-shell nanocatalysts with sub-5 nm single-cores. *Chem. Commun.* **49**, 3215-3217 (2013).

105. Qi, J., Chen, J., Li, G., Li, S., Gao, Y. & Tang, Z. Facile synthesis of core-shell Au@CeO2 nanocomposites with remarkably enhanced catalytic activity for CO oxidation. *Energy & Environmental Science* **5**, 8937-8941 (2012).

106. Güttel, R., Paul, M. & Schüth, F. Activity improvement of gold yolk–shell catalysts for CO oxidation by doping with TiO2. *Catalysis Science & Technology* **1**, 65-68 (2011).

107. Yin, Y., Chen, M., Zhou, S. & Wu, L. A general and feasible method for the fabrication of functional nanoparticles in mesoporous silica hollow composite spheres. *J. Mater. Chem.* **22**, 11245-11251 (2012).

108. Lin, C.-H., Liu, X., Wu, S.-H., Liu, K.-H. & Mou, C.-Y. Corking and Uncorking a Catalytic Yolk-Shell Nanoreactor: Stable Gold Catalyst in Hollow Silica Nanosphere. *J. Phys. Chem. Lett.* **2**, 2984-2988 (2011).

109. Galeano, C., Güttel, R., Paul, M., Arnal, P., Lu, A.H. & Schüth, F. Yolk-Shell Gold Nanoparticles as Model Materials for Support-Effect Studies in Heterogeneous Catalysis: Au,@ C and Au,@ ZrO2 for CO Oxidation as an Example. *Chem. Eur. J.* **17**, 8434-8439 (2011).

110. Liu, R., Mahurin, S.M., Li, C., Unocic, R.R., Idrobo, J.C., Gao, H., Pennycook, S.J. & Dai, S. Dopamine as a Carbon Source: The Controlled Synthesis of Hollow Carbon Spheres and Yolk-Structured Carbon Nanocomposites. *Angew. Chem. Int. Ed.* **50**, 6799-6802 (2011).

111. Stöber, W., Fink, A. & Bohn, E. Controlled growth of monodisperse silica spheres in the micron size range. *J. Colloid Interface Sci.* **26**, 62-69 (1968).

112. Shevchenko, E.V., Bodnarchuk, M.I., Kovalenko, M.V., Talapin, D.V., Smith, R.K., Aloni, S., Heiss, W. & Alivisatos, A.P. Gold/Iron Oxide Core/Hollow-Shell Nanoparticles. *Adv. Mater.* **20**, 4323-4329 (2008).

113. Liang, X., Li, J., Joo, J.B., Gutiérrez, A., Tillekaratne, A., Lee, I., Yin, Y. & Zaera, F. Diffusion through the Shells of Yolk–Shell and Core–Shell Nanostructures in the Liquid Phase. *Angew. Chem. Int. Ed.* **51**, 8034-8036 (2012).

114. Chen, C., Fang, X., Wu, B., Huang, L. & Zheng, N. A Multi-Yolk–Shell Structured Nanocatalyst Containing Sub-10 nm Pd Nanoparticles in Porous CeO2. *ChemCatChem* **4**, 1578-1586 (2012).

115. Wei, Z., Zhou, Z., Yang, M., Lin, C., Zhao, Z., Huang, D., Chen, Z. & Gao, J. Multifunctional Ag@Fe2O3 yolk-shell nanoparticles for simultaneous capture, kill, and removal of pathogen. *J. Mater. Chem.* **21**, 16344-16348 (2011).

116. Chen, Z., Cui, Z.-M., Li, P., Cao, C.-Y., Hong, Y.-L., Wu, Z.-y. & Song, W.-G. Diffusion Induced Reactant Shape Selectivity Inside Mesoporous Pores of Pd@meso-SiO2 Nanoreactor in Suzuki Coupling Reactions. *The Journal of Physical Chemistry C* **116**, 14986-14991 (2012).

117. Barrer, R. 33. Synthesis of a zeolitic mineral with chabazite-like sorptive properties. *J. Chem. Soc.*, 127-132 (1948).

118. Corma, A. From Microporous to Mesoporous Molecular Sieve Materials and Their Use in Catalysis. *Chem. Rev.* **97**, 2373-2420 (1997).

119. Iler, R.K. The chemistry of silica: Solubility, polymerization, colloid and surface properties, and biochemistry. (1979).

120. Navrotsky, A., Trofymluk, O. & Levchenko, A.A. Thermochemistry of Microporous and Mesoporous Materials. *Chem. Rev.* **109**, 3885-3902 (2009).

121. Weitkamp, J. Zeolites and catalysis. *Solid State Ionics* **131**, 175-188 (2000).

122. Nishiyama, N., Miyamoto, M., Egashira, Y. & Ueyama, K. Zeolite membrane on catalyst particles for selective formation of -xylene in the disproportionation of toluene. *Chem. Commun.* **0**, 1746-1747 (2001).

123. Chen, N.Y. & Garwood, W.E. Industrial application of shape-selective catalysis. *Catal. Rev.; Sci. Eng.* **28**, 185-264 (1986).

124. Olsbye, U., Svelle, S., Bjørgen, M., Beato, P., Janssens, T.V.W., Joensen, F., Bordiga, S. & Lillerud, K.P. Conversion of methanol to hydrocarbons: how zeolite cavity and pore size controls product selectivity. *Angew. Chem. Int. Ed.* **51**, 5810-5831 (2012).

125. Habib, E., Zhao, X., Yaluris, G., Cheng, W., Boock, L. & Gilson, J. Advances in fluid catalytic cracking. *Catalytic Science Series* **3**, 105-130 (2002).

126. Weisz, P.B., Frilette, V.J., Maatman, R.W. & Mower, E.B. Catalysis by Crystalline Aluminosilicates Molecular-Shape Selective Reactions. *J. Catal.* **1**, 307-312 (1962).

127. Csicsery, S.M. Shape-Selective Catalysis in Zeolite. *Zeolites* **4**, 202-213 (1984).

128. Verheyen, E., Jo, C., Kurttepeli, M., Vanbutsele, G., Gobechiya, E., Korányi, T.I., Bals, S., Van Tendeloo, G., Ryoo, R., Kirschhock, C.E.A. & Martens, J.A. Molecular shape-selectivity of MFI zeolite nanosheets in n-decane isomerization and hydrocracking. *J. Catal.* **300**, 70-80 (2013).

129. Marcilly, C. Acido-basic catalysis: application to refining and petrochemistry, Vol. 2. (Technip Ophrys Editions, 2006).

130. Corma, A. & García, H. Lewis Acids: From Conventional Homogeneous to Green Homogeneous and Heterogeneous Catalysis. *Chem. Rev.* **103**, 4307-4366 (2003).

131. Altwasser, S., Glaeser, R. & Weitkamp, J. Ruthenium-containing small-pore zeolites for shape-selective catalysis. *Microporous Mesoporous Mater.* **104**, 281-288 (2007).

132. Goel, S., Wu, Z., Zones, S.I. & Iglesia, E. Synthesis and Catalytic Properties of Metal Clusters Encapsulated within Small-Pore (SOD, GIS, ANA) Zeolites. *J. Am. Chem. Soc.* **134**, 17688-17695 (2012).

133. Laursen, A.B., Hojholt, K.T., Lundegaard, L.F., Simonsen, S.B., Helveg, S., Schueth, F., Paul, M., Grunwaldt, J.-D., Kegnoes, S., Christensen, C.H. & Egeblad, K. Substrate Size-Selective Catalysis with Zeolite-Encapsulated Gold Nanoparticles. *Angew. Chem. Int. Ed.* **49**, 3504-3507 (2010).

134. Collier, P., Golunski, S., Malde, C., Breen, J. & Burch, R. Active-site coating for molecular discrimination in heterogeneous catalysis. *J. Am. Chem. Soc.* **125**, 12414-12415 (2003).

135. Hashimoto, S., Uwada, T., Masuhara, H. & Asahi, T. Fabrication of gold nanoparticle-doped zeolite L crystals and characterization by optical microscopy: Laser ablation- and crystallization inclusion-based approach. *J. Phys. Chem. C* **112**, 15089-15093 (2008).

136. Wu, Z., Goel, S., Choi, M. & Iglesia, E. Hydrothermal synthesis of LTA-encapsulated metal clusters and consequences for catalyst stability, reactivity, and selectivity. *J. Catal.* **311**, 458-468 (2014).

137. Hojholt, K.T., Laursen, A.B., Kegnaes, S. & Christensen, C.H. Size-Selective Oxidation of Aldehydes with Zeolite Encapsulated Gold Nanoparticles. *Top. Catal.* **54**, 1026-1033 (2011).

138. Cai, J., Ma, H., Zhang, J., Song, Q., Du, Z., Huang, Y. & Xu, J. Gold Nanoclusters Confined in a Supercage of Y Zeolite for Aerobic Oxidation of HMF under Mild Conditions. *Chem. Eur. J.* **19**, 14215-14223 (2013).

139. Tang, Q., Zhang, Q., Wang, P., Wang, Y. & Wan, H. Characterizations of Cobalt Oxide Nanoparticles within Faujasite Zeolites and the Formation of Metallic Cobalt. *Chem. Mater.* **16**, 1967-1976 (2004).

140. van den Broek, A.C.M., van Grondelle, J. & van Santen, R.A. Preparation of Highly Dispersed Platinum Particles in HZSM-5 Zeolite: A Study of the Pretreatment Process of [Pt(NH3)4]2+. *J. Catal.* **167**, 417-424 (1997).

141. Philippaerts, A., Paulussen, S., Breesch, A., Turner, S., Lebedev, O.I., Van Tendeloo, G., Sels, B. & Jacobs, P. Unprecedented Shape Selectivity in Hydrogenation of Triacylglycerol Molecules with Pt/ZSM-5 Zeolite. *Angew. Chem. Int. Ed.* **50**, 3947-3949 (2011).

142. Fierro-Gonzalez, J.C., Hao, Y. & Gates, B.C. Gold nanoclusters entrapped in the alpha-cages of Y zeolites: Structural characterization by X-ray absorption spectroscopy. *J. Phys. Chem. C* **111**, 6645-6651 (2007).

143. Schwarz, J.A., Contescu, C. & Contescu, A. Methods for Preparation of Catalytic Materials. *Chem. Rev.* **95**, 477-510 (1995).

144. Yang, G., Tsubaki, N., Shamoto, J., Yoneyama, Y. & Zhang, Y. Confinement effect and synergistic function of H-ZSM-5/Cu-ZnO-Al2O3 capsule catalyst for one-step controlled synthesis. *J. Am. Chem. Soc.* **132**, 8129-8136 (2010).

145. Nishiyama, N., Ichioka, K., Park, D.-H., Egashira, Y., Ueyama, K., Gora, L., Zhu, W., Kapteijn, F. & Moulijn, J.A. Reactant-Selective Hydrogenation over Composite Silicalite-1-Coated Pt/TiO2Particles. *Ind. Eng. Chem. Res.* **43**, 1211-1215 (2004).

146. Miyamoto, M., Kamei, T., Nishiyama, N., Egashira, Y. & Ueyama, K. Single Crystals of ZSM-5/Silicalite Composites. *Adv. Mater.* **17**, 1985-1988 (2005).

147. Nishiyama, N., Ichioka, K., Park, D.-H., Egashira, Y., Ueyama, K., Gora, L., Zhu, W., Kapteijn, F. & Moulijn, J.A. Reactant-Selective Hydrogenation over Composite Silicalite-1-Coated Pt/TiO2 Particles. *Ind. Eng. Chem. Res.* **43**, 1211-1215 (2004).

148. van der Puil, N., Janto-Saputro, I.B., van Bekkum, H. & Jansen, J.C. in Studies in Surface Science and Catalysis, Vol. Volume 105. (eds. S.-K.I. Hakze Chon & U. Young Sun) 1341-1348 (Elsevier, 1997).

149. van der Puil, N., Dautzenberg, F.M., van Bekkum, H. & Jansen, J.C. Preparation and catalytic testing of zeolite coatings on preshaped alumina supports. *Microporous Mesoporous Mater.* **27**, 95-106 (1999).

150. van der puil, N., Creyghton, E.J., Rodenburg, E.C., Sie, T.S., van Bekkum, H. & Jansen, J.C. Catalytic testing of TiO2/platinum/silicalite-1 composites. *J. Chem. Soc., Faraday Trans.* **92**, 4609-4615 (1996).

151. He, J., Yoneyama, Y., Xu, B., Nishiyama, N. & Tsubaki, N. Designing a capsule catalyst and its application for direct synthesis of middle isoparaffins. *Langmuir* **21**, 1699-1702 (2005).

152. Sartipi, S., van Dijk, J.E., Gascon, J. & Kapteijn, F. Toward bifunctional catalysts for the direct conversion of syngas to gasoline range hydrocarbons: H-ZSM-5 coated Co versus H-ZSM-5 supported Co. *Appl. Catal., A* **456**, 11-22 (2013).

153. Sartipi, S., Makkee, M., Kapteijn, F. & Gascon, J. Catalysis engineering of bifunctional solids for the one-step synthesis of liquid fuels from syngas: a review. *Catal. Sci. Technol.* **4**, 893-907 (2014).

154. He, J., Liu, Z., Yoneyama, Y., Nishiyama, N. & Tsubaki, N. Multiple-Functional Capsule Catalysts: A Tailor-Made Confined Reaction Environment for the Direct Synthesis of Middle Isoparaffins from Syngas. *Chemistry – A European Journal* **12**, 8296-8304 (2006).

155. Li, X., He, J., Meng, M., Yoneyama, Y. & Tsubaki, N. One-step synthesis of H–β zeolite-enwrapped Co/Al2O3 Fischer–Tropsch catalyst with high spatial selectivity. *J. Catal.* **265**, 26-34 (2009).

156. Devi, R.N., Meunier, F.C., Le Goaziou, T., Hardacre, C., Collier, P.J., Golunski, S.E., Gladden, L.F. & Mantle, M.D. Modulating the Selectivity for CO and Butane Oxidation over Heterogeneous Catalysis through Amorphous Catalyst Coatings. *J. Phys. Chem. C* **112**, 10968-10975 (2008).

157. Baur, R. & Krishna, R. The effectiveness factor for zeolite catalysed reactions. *Catal. Today* **105**, 173-179 (2005).

158. Sun, J., Bonneau, C., Cantín, Á., Corma, A., Díaz-Cabañas, M.J., Moliner, M., Zhang, D., Li, M. & Zou, X. The ITQ-37 mesoporous chiral zeolite. *Nature* **458**, 1154-1157 (2009).

159. Perez-Ramirez, J., Christensen, C.H., Egeblad, K., Christensen, C.H. & Groen, J.C. Hierarchical zeolites: enhanced utilisation of microporous crystals in catalysis by advances in materials design. *Chem. Soc. Rev.* **37**, 2530-2542 (2008).

160. Egeblad, K., Christensen, C.H., Kustova, M. & Christensen, C.H. Templating Mesoporous Zeolites†. *Chem. Mater.* **20**, 946-960 (2007).

161. Larsen, S.C. Nanocrystalline zeolites and zeolite structures: Synthesis, characterization, and applications. *J. Phys. Chem. C* **111**, 18464-18474 (2007).

162. Camblor, M.A., Corma, A. & Valencia, S. Characterization of nanocrystalline zeolite Beta. *Microporous Mesoporous Mater.* **25**, 59-74 (1998).

163. Egeblad, K., Christensen, C.H., Kustova, M. & Christensen, C.H. Templating mesoporous zeolites. *Chem. Mater.* **20**, 946-960 (2008).

164. Madsen, C., Madsen, C. & J. H. Jacobsen, C. Nanosized zeolite crystals-convenient control of crystal size distribution by confined space synthesis. *Chem. Commun.*, 673-674 (1999).

165. Jacobsen, C.J.H., Madsen, C., Janssens, T.V.W., Jakobsen, H.J. & Skibsted, J. Zeolites by confined space synthesis - characterization of the acid sites in nanosized ZSM-5 by ammonia desorption and Al-27/Si-29-MAS NMR spectroscopy. *Microporous Mesoporous Mater.* **39**, 393-401 (2000).

166. Choi, M., Na, K., Kim, J., Sakamoto, Y., Terasaki, O. & Ryoo, R. Stable single-unit-cell nanosheets of zeolite MFI as active and long-lived catalysts. *Nature* **461**, 246-249 (2009).

167. Koekkoek, A.J.J., Kim, W., Degirmenci, V., Xin, H., Ryoo, R. & Hensen, E.J.M. Catalytic performance of sheet-like Fe/ZSM-5 zeolites for the selective oxidation of benzene with nitrous oxide. *J. Catal.* **299**, 81-89 (2013).

168. Kim, J., Kim, W., Seo, Y., Kim, J.-C. & Ryoo, R. n-Heptane hydroisomerization over Pt/MFI zeolite nanosheets: Effects of zeolite crystal thickness and platinum location. *J. Catal.* **301**, 187-197 (2013).

169. Liu, Y., Zhang, W.Z. & Pinnavaia, T.J. Steam-stable aluminosilicate mesostructures assembled from zeolite type Y seeds. *J. Am. Chem. Soc.* **122**, 8791-8792 (2000).

170. Kloetstra, K.R., Zandbergen, H.W., Jansen, J.C. & vanBekkum, H. Overgrowth of mesoporous MCM-41 on faujasite. *Microporous Mater.* **6**, 287-293 (1996).

171. Trong On, D. & Kaliaguine, S. Large-Pore Mesoporous Materials with Semi-Crystalline Zeolitic Frameworks. *Angew. Chem. Int. Ed.* **40**, 3248-3251 (2001).

172. Jacobsen, C.J.H., Madsen, C., Houzvicka, J., Schmidt, I. & Carlsson, A. Mesoporous zeolite single crystals. *J. Am. Chem. Soc.* **122**, 7116-7117 (2000).

173. Christensen, C.H., Johannsen, K., Schmidt, I. & Christensen, C.H. Catalytic benzene alkylation over mesoporous zeolite single crystals: Improving activity and selectivity with a new family of porous materials. *J. Am. Chem. Soc.* **125**, 13370-13371 (2003).

174. Tao, Y.S., Kanoh, H., Abrams, L. & Kaneko, K. Mesopore-modified zeolites: Preparation, characterization, and applications. *Chem. Rev.* **106**, 896-910 (2006).

175. Dessau, R.M., Valyocsik, E.W. & Goeke, N.H. Aluminum zoning in ZSM-5 as revealed by selective silica removal. *Zeolites* **12**, 776-779 (1992).

176. Groen, J.C., Peffer, L.A.A., Moulijn, J.A. & Perez-Ramirez, J. Mechanism of hierarchical porosity development in MFI zeolites by desilication: The role of aluminium as a pore-directing agent. *Chem. Eur. J.* **11**, 4983-4994 (2005).

177. Groen, J.C., Jansen, J.C., Moulijn, J.A. & Pérez-Ramírez, J. Optimal Aluminum-Assisted Mesoporosity Development in MFI Zeolites by Desilication. *The Journal of Physical Chemistry B* **108**, 13062-13065 (2004).

178. Groen, J.C., Peffer, L.A.A., Moulijn, J.A. & Pérez-Ramírez, J. Mesoporosity development in ZSM-5 zeolite upon optimized desilication conditions in alkaline medium. *Colloids and Surfaces A: Physicochemical and Engineering Aspects* **241**, 53-58 (2004).

179. Groen, J.C., Bach, T., Ziese, U., Donk, A., de Jong, K.P., Moulijn, J.A. & Perez-Ramirez, J. Creation of hollow zeolite architectures by controlled desilication of Al-zoned ZSM-5 crystals. *J. Am. Chem. Soc.* **127**, 10792-10793 (2005).

180. Schmidt, W. Solid catalysts on the nanoscale: design of complex morphologies and pore structures. *ChemCatChem* **1**, 53-67 (2009).

181. Mei, C., Wen, P., Liu, Z., Liu, H., Wang, Y., Yang, W., Xie, Z., Hua, W. & Gao, Z. Selective production of propylene from methanol: Mesoporosity development in high silica HZSM-5. *J. Catal.* **258**, 243-249 (2008).

182. Bjørgen, M., Joensen, F., Holm, M.S., Olsbye, U., Lillerud, K.-P. & Svelle, S. Methanol to gasoline over zeolite H-ZSM-5: Improved catalyst performance by treatment with NaOH. *Appl. Catal., A* **345**, 43-50 (2008).

183. Groen, J.C., Abello, S., Villaescusa, L.A. & Perez-Ramirez, J. Mesoporous beta zeolite obtained by desilication. *Microporous Mesoporous Mater.* **114**, 93-102 (2008).

184. Gopalakrishnan, S., Zampieri, A. & Schwieger, W. Mesoporous ZSM-5 zeolites via alkali treatment for the direct hydroxylation of benzene to phenol with N2O. *J. Catal.* **260**, 193-197 (2008).

185. Cheng, K., Kang, J., Huang, S., You, Z., Zhang, Q., Ding, J., Hua, W., Lou, Y., Deng, W. & Wang, Y. Mesoporous Beta Zeolite-Supported Ruthenium Nanoparticles for Selective Conversion of Synthesis Gas to C5–C11 Isoparaffins. *ACS Catalysis* **2**, 441-449 (2012).

186. Sartipi, S., Parashar, K., Valero-Romero, M.J., Santos, V.P., van der Linden, B., Makkee, M., Kapteijn, F. & Gascon, J. Hierarchical H-ZSM-5-supported cobalt for the direct synthesis of gasoline-range hydrocarbons from syngas: Advantages, limitations, and mechanistic insight. *J. Catal.* **305**, 179-190 (2013).

187. Sartipi, S., Parashar, K., Makkee, M., Gascon, J. & Kapteijn, F. Breaking the Fischer-Tropsch synthesis selectivity: direct conversion of syngas to gasoline over hierarchical Co/H-ZSM-5 catalysts. *Catal. Sci. Technol.* **3**, 572-575 (2013).

188. Sartipi, S., Alberts, M., Santos, V.P., Nasalevich, M., Gascon, J. & Kapteijn, F. Insights into the Catalytic Performance of Mesoporous H-ZSM-5-Supported Cobalt in Fischer–Tropsch Synthesis. *ChemCatChem* **6**, 142-151 (2014).

189. Kang, J., Cheng, K., Zhang, L., Zhang, Q., Ding, J., Hua, W., Lou, Y., Zhai, Q. & Wang, Y. Mesoporous Zeolite-Supported Ruthenium Nanoparticles as Highly Selective Fischer–Tropsch Catalysts for the Production of C5–C11 Isoparaffins. *Angew. Chem. Int. Ed.* **50**, 5200-5203 (2011).

190. Mielby, J., Abildstrøm, J.O., Wang, F., Kasama, T., Weidenthaler, C. & Kegnæs, S. Oxidation of Bioethanol using Zeolite-Encapsulated Gold Nanoparticles. *Angewandte Chemie* **126**, 12721-12724 (2014).

191. Wang, X.D., Yang, W.L., Tang, Y., Wang, Y.J., Fu, S.K. & Gao, Z. Fabrication of hollow zeolite spheres. *Chem. Commun.* **0**, 2161-2162 (2000).

192. Dong, A., Ren, N., Yang, W., Wang, Y., Zhang, Y., Wang, D., Hu, J., Gao, Z. & Tang, Y. Preparation of Hollow Zeolite Spheres and Three-Dimensionally Ordered Macroporous Zeolite Monoliths with Functionalized Interiors. *Adv. Funct. Mater.* **13**, 943-948 (2003).

193. Dong, A.G., Wang, Y.J., Wang, D.J., Yang, W.L., Zhang, Y.H., Ren, N., Gao, Z. & Tang, Y. Fabrication of hollow zeolite microcapsules with tailored shapes and functionalized interiors. *Microporous Mesoporous Mater.* **64**, 69-81 (2003).

194. Ren, N., Yang, Y.-H., Shen, J., Zhang, Y.-H., Xu, H.-L., Gao, Z. & Tang, Y. Novel, efficient hollow zeolitically microcapsulized noble metal catalysts. *J. Catal.* **251**, 182-188 (2007).

195. Dong, A., Wang, Y., Tang, Y., Ren, N., Zhang, Y. & Gao, Z. Hollow Zeolite Capsules: A Novel Approach for Fabrication and Guest Encapsulation. *Chem. Mater.* **14**, 3217-3219 (2002).

196. Fodor, D., Pacosova, L., Krumeich, F. & van Bokhoven, J.A. Facile synthesis of nano-sized hollow single crystal zeolites under mild conditions. *Chem. Commun.* **50**, 76-78 (2014).

197. Mei, C., Liu, Z., Wen, P., Xie, Z., Hua, W. & Gao, Z. Regular HZSM-5 microboxes prepared via a mild alkaline treatment. *J. Mater. Chem.* **18**, 3496-3500 (2008).

198. Wang, Y., Lin, M. & Tuel, A. Hollow TS-1 crystals formed via a dissolution-recrystallization process. *Microporous Mesoporous Mater.* **102**, 80-85 (2007).

199. Burel, L. & Tuel, A. Nanozeolites: New strategies for designing ultra small silicalite crystals with very few framework defects. *Microporous Mesoporous Mater.* **174**, 90-99 (2013).

200. Anderson, M.W., Agger, J.R., Hanif, N. & Terasaki, O. Growth models in microporous materials. *Microporous Mesoporous Mater.* **48**, 1-9 (2001).

201. Agger, J.R., Hanif, N. & Anderson, M.W. Fundamental Zeolite Crystal Growth Rates from Simulation of Atomic Force Micrographs. *Angew. Chem. Int. Ed.* **40**, 4065-4067 (2001).

202. Wang, Y. & Tuel, A. Nanoporous zeolite single crystals: ZSM-5 nanoboxes with uniform intracrystalline hollow structures. *Microporous Mesoporous Mater.* **113**, 286-295 (2008).

Experimental procedures

I. Material preparation

I.1. Chemicals

All chemicals were used as received without any further purification

Aluminum nitrate, $Al(NO_3)_3 \cdot 9H_2O$, (Aldrich, >98%)

Chloroauric acid, $HAuCl_4 \cdot 3H_2O$, (Aldrich, 99.999%)

Cobalt nitrate, $Co(NO_3)_2 \cdot 6H_2O$, (Aldrich, 99.8%)

Copper nitrate, $Cu(NO_3)_2 \cdot 3H_2O$, (Aldrich, 99.999%)

Hexadecyl trimethyl ammonium bromide, $CH_3(CH_2)_{15}N(Br)(CH_3)_3$, CTAB, (Aldrich, 99.999%)

Hydrochloric acid, HCl, (Aldrich, 37%)

Methylbenzene, Toluene, C_7H_8, (Aldrich, 99.9%)

Nickel nitrate, $Ni(NO_3)_2 \cdot 6H_2O$, (Aldrich, 99.999%)

Silver nitrate, $AgNO_3$, (Alfa Aesar, 99%)

Silver oxide, Ag_2O, (Alfa Aesar, 99.99%)

Sodium aluminate, $NaAlO_2$, (Strem Chemicals, 99.9%)

Sodium borohydride, $NaBH_4$, (Aldrich, 99%)

Sodium carbonate, Na_2CO_3, (Alfa Aesar, 99%)

Sodium silicate solution, $(NaOH)_x(Na_2SiO_3)_z \cdot H_2O$, (Aldrich, ≥27% SiO_2 basis)

Sodium tetrachloropalladate Na_2PdCl_4, (Aldrich, 99.99%)

Tetraamine platinum nitrate, $(NH_3)_4Pt(NO_3)_2$, (Aldrich, 99.995%)

Tetrabutylphosphonium hydroxide, $P(C_4H_9)_4OH$, TBPOH, (Aldrich, 40 wt. % in H_2O)

Tetraethyl orthosilicate, $Si(OC_2H_5)_4$, TEOS, (Aldrich, 98%)

Tetraethylphosphonium bromide, $P(C_2H_5)_4Br$, TEPBr, (Aldrich, 98%)

Tetrapropylammonium bromide, $N(C_3H_7)_4Br$, TPABr, (Aldrich, 99%)

1,3,5-trimethylbenzene, mesitylene, C_9H_{12}, (Aldrich, 99%)

I.2. Synthesis of zeolites

I.2.1. Synthesis of silicalite-1 nanocrystals

Silicalite-1 is synthesized from the crystallization of gels containing TEOS, 1M TPAOH solutions and water. TPAOH solution with a concentration of 1 M/L is prepared from TPABr solution by exchange with Ag_2O for 5 minutes in the absence of light and then precipitated AgBr is removed by filtration. In a typical synthesis, 0.2mol TEOS is first hydrolyzed in 80ml TPAOH solution (with a concentration of 1 M/L) at room temperature, then 80ml water is added and the mixture is heated at 75°C for 3 hours under stirring. Then the resulting gel with the composition in mole: SiO_2-0.4TPAOH-35H_2O is transferred into a Teflon-lined autoclave and heated under static conditions at 170°C for 3 days. The autoclave is then cooled and the solid is recovered by centrifugation, washed with water for several times and then dried overnight at 110°C. It is finally calcined at 525°C in air for 12 hours to remove organic templates. Generally, approximately 12g of product can be obtained for one synthesis. Samples are denoted Sil-1 (silicalite-1) for short.

I.2.2. Synthesis of large silicalite-1 crystals

Large silicalite-1 crystals are prepared following the same recipe as for nanocrystals but using a mixture of TBP^+ and TEP^+ cations with a ratio of TBP/TEP=3 instead of TPAOH as template. TEPOH was prepared from the corresponding bromide by ion exchange with Ag_2O, as previously mentioned the preparation of TPAOH. The mixture of phosphonium templates leads to large silcalite-1 crystals, typically 1-2 µm. The hydrolyzed TEOS solution was transferred into a Teflon-lined autoclave with the gel composition: SiO_2-0.3TBPOH-0.1TEPOH-35H_2O. The crystallization conditions (170°C, 3 days) and the treatments after crystallization such as washing, drying and calcination are the same as those used for nanocrystals. Samples are denoted L-Sil-1 (large silicalite-1) for short.

I.2.3. Synthesis of ZSM-5 crystals

ZSM-5 is synthesized following a published recipe with minor modifications (1.7 times more water in our recipe than the literature one).[1] Typically, a gel containing TEOS, 1M/L TPAOH solution and $NaAlO_2$ with a composition of 140SiO_2-Al_2O_3-30TPAOH-1240H_2O is stirred at room temperature for 7 hours, transferred into a Teflon-lined autoclave and heated under static conditions at 180°C for 7 days. After crystallization, the autoclave is cooled and the solid is recovered by centrifugation, washed with water and dried overnight at 110°C. The resulting ZSM-5 is then washed with a 5M HCl solution at 90°C for 5 hours to remove of the non-reacted aluminum species, and then centrifuged, washed until pH 7 and finally dried at 110°C in air. The resulting solid is calcined for 12 hours at 525°C

in air yielding ZSM-5 microporous crystals that are characterized by a Si/Al ratio in the range from 80 to 100 detected by ICP. Generally, the synthesis started with 0.1 moles TESO gave approximately 6 g of ZSM-5 zeolites.

ZSM-5 zeolites with different Al contents are also prepared by varying the amount of $NaAlO_2$ in the crystallization gel. Na^+ cations in the as prepared ZSM-5 can be exchanged by treatment with NH_4NO_3 solutions. The solid is dispersed in a NH_4NO_3 solution, stirred at 90°C for 3 hours and washed. The treatment is performed for 3 times, after which the solid is dried and calcined. The resulting acidic zeolite is denoted H-ZSM-5.

I.3. Impregnation of metal precursor(s) into zeolite

I.3.1. Incipient wetness impregnation (IWI) method

Gold impregnation into zeolite (hollow and bulk) is performed by using the so-called incipient wetness impregnation (IWI) method. The zeolite is first desorbed under vacuum at 300°C, purged with argon, and then impregnated with an aqueous solution of $HAuCl_4$ with a volume corresponding to the pore volume of the zeolite (approx. 0.23 ml for 1 g of zeolite). The concentration of the gold solution is estimated by the theoretical Au loading in the zeolite. The mixture is stirred at 50°C overnight until complete evaporation of the liquid and then dried at 110°C. Finally, the solid is reduced under H_2 at 350°C for 2 hours.

I.3.2. General wetness impregnation

Except Au, the pre-degassed zeolites (silicalite-1 and ZSM-5) are impregnated with excess aqueous solutions of corresponding metal salts, $(NH_3)_4Pt(NO_3)_2$ for Pt, Na_2PdCl_4 for Pd and the corresponding nitrates for Ag, Co, Ni and Cu. In a typical wet impregnation, 1 gram of zeolite is impregnated by 2mL of aqueous solution. The mixture is then stirred at 50°C until complete evaporation of water. A series of samples with different metal loadings was obtained by using metal solutions of various concentrations, typically from 0.026 to 1.23 mol/L. In the case of alloy particles (AgPt, AgPd, AuAg and PtPd) in zeolite, a mixture of the two metal solutions is used for the impregnation.

I.4. Formation of metal particles in hollow zeolites

I.4.1. Dissolution/recrystallization process

The dissolution/recrystallization process is achieved by treating metal impregnated zeolite (silicalite-1 and large silicalite-1) crystals (1g) in the presence of TPAOH (7.5 ml; 0.55M) in a Teflon-lined autoclave at 170°C for 24 hours. Then the autoclave is cooled, the solids are washed with water, dried and calcined in air at 525°C for 6 hours. After calcination, solids are reduced under H_2 (details will be given in 1.4.4) and denoted w-metal@Sil-1 or w-metal@L-Sil-1 depending on the nature of the starting zeolites, where w is the metal loading (wt. %) detected by ICP. In the case of alloy particles encapsulated in hollow zeolites, samples are denoted A_xB_y@Sil-1 where x and y are the loadings of metal A and B (wt. %) detected by ICP, respectively.

Regular ZSM-5 hollow crystals can be obtained by treating ZSM-5 with TPAOH under the same hydrothermal conditions of those for silicalite-1. Hollow ZSM-5 prepared by this route is denoted ZSM-5-DR (DR for Directly dissolution/Recrystallization from ZSM-5). Metal particles encapsulated in hollow ZSM-5 prepared by treating metal impregnated ZSM-5 are denoted w-metal@ZSM-5-DR or A_xB_y@ZSM-5-DR in the case of alloys, where w, x and y are the metal loadings given by ICP-OES.

I.4.2. Dissolution/recrystallization with aluminum source

Metal nanoparticles encapsulated in hollow ZSM-5 can also be prepared by adding aluminum source (aluminum nitrate) into TPAOH solution during the dissolution-recrystallization step and followed the same washing, drying, calcination and reduction procedures as presented in 1.4.1 for metal nanoparticle in hollow silicalite-1.

The dissolved silicon species recrystallized in the presence of aluminum to form hollow ZSM-5 zeolites with an Al gradient (Al rich on the zeolite surface). The obtained hollow ZSM-5 is named as ZSM-5-PA (PA for Post Aluminum adding). Hollow ZSM-5 with desirable Al loading can be prepared by varying the amount of aluminum in the TPAOH solution. The corresponding metal encapsulated samples are denoted w-metal@ZSM-5-PA, where w is representing the metal loading (wt. %) detected by ICP.

I.4.3. Desilication using Na_2CO_3

Another series of metal nanoparticles in hollow ZSM-5 is obtained by desilication treatment carried out by dispersing metal impregnated ZSM-5 into a Na_2CO_3 solution with the concentration in the range of 0.6M-1M. Typically, 1 gram ZSM-5 is dispersed in 50ml solution, the mixture is stirred for 12

hours at 80°C, and then the solid is centrifuged, washed by H_2O until pH=7 and dried at 110°C. After reduction under H_2, the obtained samples are denoted w-metal@ZSM-5-DS or A_xB_y@ZSM-5-DS for alloy ones (DS for DeSilication), where w, x and y are representing the metal loadings (wt. %) detected by ICP.

I.4.4. Reduction procedures

All metal containing hollow zeolites are further reduced under hydrogen to get metallic particles, the general reduction conditions are given in Table 1. 20ml/min hydrogen is used as reduction atmosphere, other reduction conditions and further ones for sinter tests are given individually in the corresponding chapter.

Table 1: Reduction conditions for metal nanoparticle in hollow zeolite materials (20ml/min of pure H_2 for all the reductions)

Metal content	Reduction temperature (°C)	Ramp (°C/min)	Redution time (hours)
Au	350	1	2
Pt	600	1	2
Pd	350	1	2
Co	750	2	3
Cu	750	2	3
Fe	750	2	3
Ni	750	2	3
Pt Ag	600	2	5
Pt Pd	600	2	5
Pd Ag	600	2	5
Au Ag	600	2	5

I.5. The preparation and treatments of reference catalysts

I.5.1. The preparation of Pt supported on zeolite catalysts

Pt supported on silicalite-1 (Pt/Sil-1 for short) with 0.9 wt. % Pt loading detected by ICP-OES was prepared by reducing directly Pt impregnated silicalite-1 powder in H_2 600°C for 2 h with a heating rate 5°C/min. Similarly, Pt supported on ZSM-5 (Pt/ZSM-5 for short) was prepared by reducing the Pt impregnated ZSM-5 under hydrogen at 500°C for 2 hours with a heating rate 1°C/min.

I.5.2. The treatments of Pt/SiO_2 catalyst (commercial)

A commercial catalyst of Pt/SiO_2 from Sigma-Aldrich is used as a reference catalyst denoted Pt/SiO_2-C (C for Commercial). The material contains 0.71% Pt as determined by ICP analysis and Pt particle mean size of 7.5 nm estimated from TEM images. The sample is pre-reduced under hydrogen at 600°C for 2 h to get metallic particles under the same reduction conditions as those used for Pt zeolite materials.

I.5.3. Pt/SiO_2 catalyst (prepared)

Another Pt/SiO_2 material with 0.5 wt. % Pt loading is prepared by incipient wetness impregnation method following a literature recipe.[2] A commercial silica gel (Aldrich, Davisil grade 643, S_{BET} = 300m^2 g^{-1}, V_{pore} = 1.15 mL g^{-1}) was impregnated by a H_2PtCl_6 aqueous solution via incipient wetness impregnation (IWI) method. The solution was added progressively to the support under continuous mechanical stirring. The solid was dried overnight at 85 °C. Finally, the dried catalyst was reduced under hydrogen flow at 500°C for 2 hours. The sample is denoted Pt/SiO_2-P (P for as Prepared).

I.5.4. AuAg/MCM-41 materials

An AuAg alloy particle supported on mesoporous MCM-41 material has been prepared followed a literature recipe.[3] First, 5.5 g of sodium silicate was added to a mixture of 1.6 g of hexadecyl trimethyl ammonium bromide (CTAB), and water. The solution is stirred for 1 h at 45°C and then transferred to an autoclave and heated at 100°C for 24 h. Finally, after filtration, washing, and drying processes, as synthesized MCM-41 was obtained.

The obtained MCM-41 was first functionalized with 3-aminopropyltrimethoxysilane (APTS) in an ethanol solution for 12 hours, and then washed 3 times and re-dispersed in water. A $HAuCl_4$ aqueous solution was added into the MCM-41 solution for 20 min, which was reduced subsequently by a $NaBH_4$ aqueous solution (0.1 M). Then the obtained Au/MCM-41 material was washed 3 times and re-dispersed in water. An $AgNO_3$ solution was subsequently added stirred for 20 min and reduced with $NaBH_4$, similar procedures as the reduction of Au. The whole loading amount of metal was

controlled to 5 wt. % with a ratio of Au/Ag=8 in weight. The materials were finally calcined at 560°C in air for 6 h and denoted AuAg/MCM-41.

II. Characterization techniques

II.1. Elementary analysis (ICP-OES)

Elementary analysis is carried out by Inductively-Coupled Plasma Optical Emission Spectroscopy (HORIBA Jobin Yvon Activa ICP-OES). The samples are first dissolved in an acid solution (mixture of HF and HCl solutions; mixture of HF, H_2SO_4 and HNO_3 solutions for Ag) which is then introduced into the spectrometer. Excited atoms and ions produced from each element emit a characteristic radiation whose intensity is measured. This intensity is then correlated to the amount of each element.

ICP technique is used for detecting the metal, aluminum and sodium (ZSM-5 samples) contents in the metal nanoparticle hollow zeolite materials. However, in the case of bimetallic particles, the particle dissolution is not perfectly achieved in acid solutions, which may affect the accuracy of the results.

II.2. Solid Nuclear Magnetic Resonance (NMR)

Solid NMR spectra are obtained on a Bruker DSX 400 spectrometer equipped with a double-bearing probe-head. Samples are spun at 10 kHz in 4 mm zirconia rotors. ^{27}Al NMR spectra are recorded with a pulse length of 0.6 µs (π/12) and a recycle delay of 500 ms. Chemical shifts are referred as $Al(H_2O)_6^{3+}$. NMR is used for characterizing the presence of framework and non-framework Al in hollow ZSM-5 crystals to further determine the evolution of structural aluminum during the zeolite post treatment.

II.3. Powder X-Ray Diffraction (XRD)

X-ray diffraction (XRD) patterns of the solid are recorded on a Bruker (Siemens) D5005 diffractometer using CuKα radiation. Diffractograms are collected between 4 and 80° (2Θ) with steps of 0.02° and 1 s per step. This technique is used to verify the crystallinity of zeolite related materials and estimate the metal particle size if possible.

In this thesis, Co particle sizes of Co@ZSM-5-DS samples have been measured due to the high metal loading and the formation of ultra-thin zeolite shell. The crystallite sizes of cobalt are estimated from peak half-widths by using Scherrer's equation (Eq.1) with corrections for instrumental line broadening.

$$d = \frac{0.89\,\lambda}{\beta \cos\Theta} \times \frac{180°}{\pi} \qquad \text{Eq. 1}$$

where d is the average size of the crystalline grains, λ is the wavelength of incident x-ray, and β is the full width at half maximum of the highly diffraction peak, Θ is the Bragg angle.

II.4. X-ray photoelectron microscopy (XPS)

XPS measurements are carried out on a Kratos AXIS Ultra DLD spectrometer with an Al Kα (1486.6 eV) X-ray source. The analyzed sample area is 300 x 700 microns and the analysis energy of 160 eV is used. XPS is a surface sensitive technique, in which the detectable emergent electrons can be only approximately from 1 to 8 nm under the surface, and this fact has been usually used to estimate the concentration with depth in materials. The thickness of the hollow zeolite is generally around 20nm (dissolution recrystallization route), thus, XPS technique can be used to evaluate the success of metal encapsulation in hollow zeolites. In the case of ultra-thin hollow zeolite (produced by desilication route) metals can be easily detected but their location has to be confirmed using TEM. For the quantitative analysis, the binding energies of all the peaks are referenced to the C 1s peak at 284.7 eV, the relative density is calculated for the metal contents using intensity of Al or Si as reference.

II.5. N_2 adsorption/desorption

N_2 adsorption isotherms are measured on an ASAP 2020 (Micromeritics) sorption apparatus. Approx. 100 mg of sample is degassed in a cell at 350°C for 3 hours prior to adsorption. Apparent surface area is calculated using the BET method and the microporous volume estimated from the t-plot curve.

From isotherms of hollow zeolites, the hysteresis loop with an abrupt closure at p/p_0 around 0.45 characterizes internal porosity connected to outer surface via entrances smaller than 4nm. Conversely, the presence of a hysteresis loop is generally taken as an indication for the presence of cavities in the crystals. The y-intercept of the extrapolation of the t-plots curves to x = 0 is used to determine the presence of micropores and/or mesopores in the materials.

II.6. Scanning Electronic Microscopy (SEM)

SEM images are taken on a JEOL 5800 LV microscope equipped with an Oxford Isis 300 analytical system. This technique is used to characterize the morphology of the large silicalite-1 crystals (1 to 2 µm in size).

II.7. Transmission Electronic Microscopy (TEM)

TEM images of metal nanoparticle in hollow zeolites and reference catalysts are obtained on a Jeol 2010 LaB_6 microscope operating at 200 kV. The resolution of electronic microscopy is much higher than the optical ones due to the very short De Broglie wavelength of electrons (resolution of 0.19 nm in Jeol 2010 microscopy).

II.7.1. Sample preparation for TEM observation

Sample preparation involves grinding of a catalyst in ethanol in a mortar and depositing a drop of the suspension on a Cu TEM grid. This procedure allows a very thin layer of the sample deposit on the grid, avoiding overlap between catalyst particles and making it easier to image the metal particles in thin hollow zeolite or on the support.

II.7.2. TEM apparatus

The photo and schema of the TEM equipment is showed in Fig. 1. An electron beam is emitted by an electron gun containing an emission source (LaB_6 single crystal in JEOL 2010) connected to a high voltage source (200Kv in JEOL 2010) under vacuum. The beam is converged by the different electromagnetic lenses of the TEM, typically the condenser, objective and projector lenses. The condenser lenses are responsible for primary beam formation and focus the beam on the sample. When passing through the sample, electrons are scattered due to collisions with the atoms in the sample and the beam is focused by the objective lenses to form the image of the sample. The projector lenses magnify the image and project them on an imaging device (a CCD camera in the case of JEOL 2010). The images are then recorded using Digital Micrograph software.

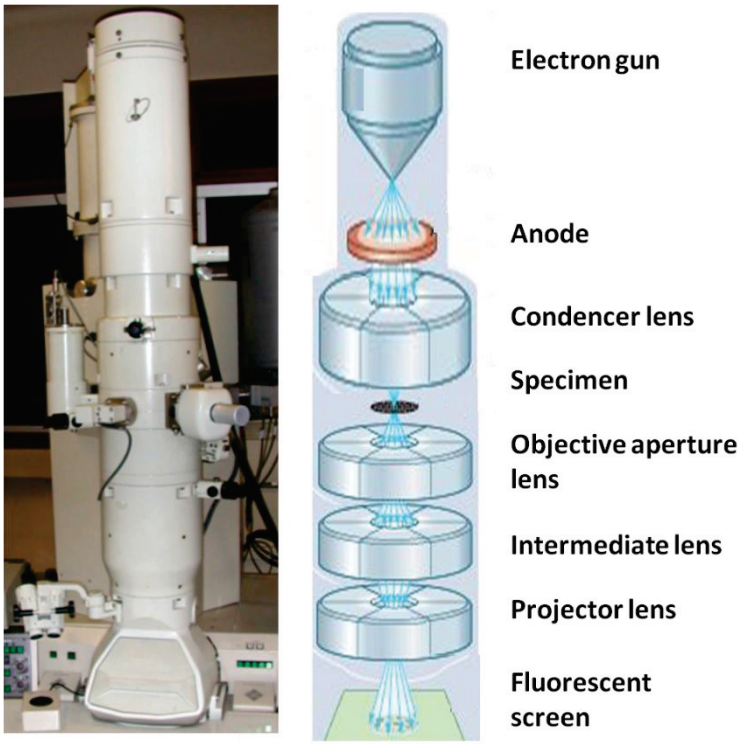

Figure 1: Photo (left) and scheme (right) of JEOL-2010 TEM apparatus.

The resolution of the TEM is determined by the speed and wavelength of the electrons. The magnification of the TEM is determined by the ratio of the distances between the specimen and the

image plane of the objective lens; the contrast is due to the absorption of electrons by the solid depending on the thickness and composition of the material.

In this thesis, this technique has been frequently used for the characterization of the particular structure of yolk-shell materials in the nanometer range. Moreover, TEM images have been used to evaluate particle size distribution, which is an important parameter for the nanosized materials, using Image J software.

II.7.3. Statistical study of nanoparticles based on TEM images

From TEM images, the particle size distributions (for metal containing samples) were obtained by counting around 400 particles using Image J software. The diameter d_{30} (defined as $\sum n_i d_i^3 / \sum n_i)^{1/3}$, where n_i is the number of particles with diameter d_i, corresponding to the diameter of an hypothetical particle having the volume (or the mass if all particles have the same density) of the average volume (or mass) of the true distribution is estimated from the size distribution. This d_i is also the diameter of a mono-disperse distribution which has the same number of particles and the same total volume (or mass) than the true distribution.[4] The dispersion of metal nanoparticles was estimated from the size distribution using a cub-octahedral model and a calculation method according to Van Hardeveld and Hartog.[5] This model is used to evaluate the dispersion by considering the percentage of surface atoms among the overall atoms in each metal particle.

II.7.4. Energy Dispersive *X*-Ray Spectroscopy (EDX) measurement

The microscope (Jeol 2010) is also equipped with an EDX Link ISIS analyzer from Oxford Instruments.

It is possible to identify the elements present in the sample by performing EDX. When the electron beam passes through the sample, X-ray can be generated and emitted from the sample. Thus, X-ray escaping from the sample can be detected and measured from the characteristic spectrum of each element. In addition, the number of photons emitted by a chemical species in the analyzed material is proportional to the mass concentration of this species.

In this study EDX analysis has been used to analyze the dispersion of particular elements in the samples. Especially, in the characterization of phyllosilicates and alloy particles, EDX provide very precise constitution of each area or particle. However, this technique provides the results in the range of nanometer, which should be considered with other techniques detecting the overall composition of materials such as ICP-OES.

II.7.5. High-Resolution Transmission Electron Microscopy (HRTEM)

HRTEM pictures were also taken on the Jeol 2010 apparatus in the high resolution mode, the image formation is based on a different principle than conventional ones. Both the transmitted and the scattered beams were used to create a HRTEM interference image. The contrast of a HRTEM image

arises from the interference of the electron wave with itself in the image plane which is a phase contrast. The outgoing modulated electron waves at very low angles interfere with themselves during propagation through the objective lens. All electrons emerging from the specimen are combined at a point in the image plane.

Here, HRTEM has been used for analyzing crystal structure of zeolite and nanoparticles at an atomic resolution scale.

II.7.6. Environmental transmission Electron Microscopy (ETEM)

The ETEM analysis of Ag zeolite sample was carried out on a Cs-corrected Titan ETEM G2 FEI microscope (operating between 80-300 kV) which allows measurement under gas pressure below 20 mbar and heating until 1000°C.

The principle of ETEM is to use differentially individual evacuating vacuum stages in the microscope column separated by additional small pumping apertures. This allows large pressure differences between the specimen area and electron source area which requires high vacuum conditions with an otherwise free 'line of sight' for the electron beam. Fig. 2 shows the photo and scheme of different pumped stages of ETEM (Cs-corrected Titan ETEM G2 FEI).

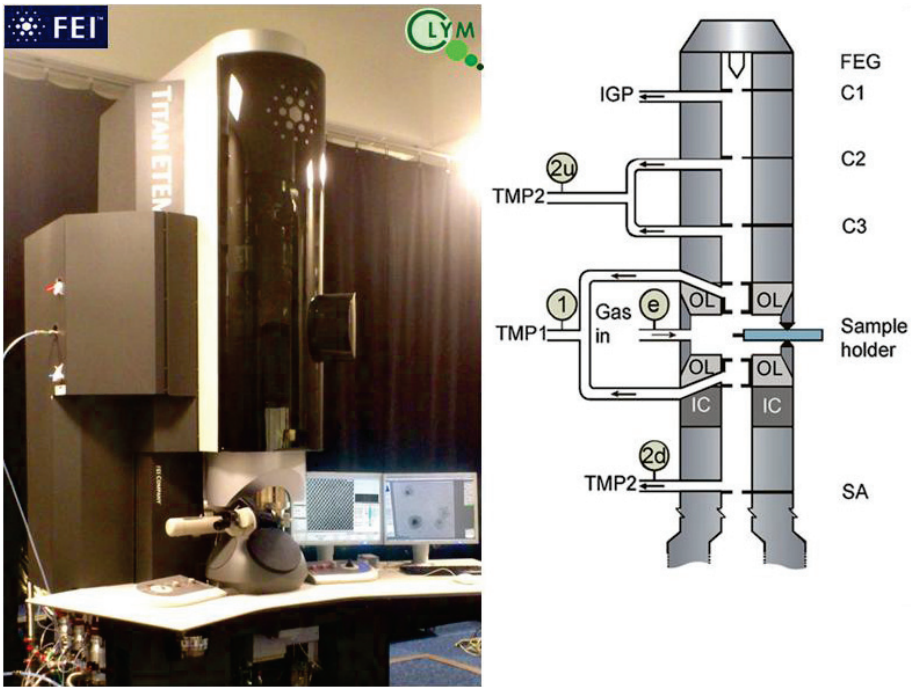

Figure 2: The photo (left) and sketch of the vacuum system(right) of the ETEM apparatus. vacuum system highlighting the pressure-limiting apertures at the stages of the objective lens (OL), the condenser lenses (first (C1), second (C2) and third (C3)) and the selected area (SA) aperture.[6]

This ETEM is also equipped with a mass spectrometer to determine gas composition either in the gas inlet system or on the specimen area. A built-in plasma cleaner allows for cleaning of the specimen area after using a gas. Furthermore, the single-tilt tomography can be carried out under vacuum or

gas pressure and under in-situ heating with a continuous tilting series from 78°to -38.5° (limited by the grid shadowing). In the thesis, single-tilt tomographies have been performed on Pt@ZSM-5-DS under vacuum and Ag@Sil-1 under vacuum and an oxygen pressure of 1 mbar.

II.7.7. Scanning Transmission Electron Microscopy (STEM)

The STEM mode can be operated on Titan ETEM G2 FEI equipment using objective lenses above the sample to make the incident electron beam convergent. The incident electrons are then optically focused and scanned across the sample rather than focused into a narrow spot as in the case of conventional mode. Under this ETEM mode, ETEM is suitable for analysis such as mapping EDX, electron energy loss spectroscopy (EELS) and high angle annular dark field (HAADF). The HAADF images are taken under the STEM mode by collecting electrons which are not Bragg-scattered using a HAADF detector. As the HAADF images show little or no diffraction effects, their intensity is approximately proportional to Z^2. This imaging technique is particularly adapted to tomography reconstruction as it generates strong contrast between heavy metal particles and inorganic supports.

II.8. Thermogravimetric analysis (TGA)

Thermal analysis data were collected on a SETSYS Evolution-1200 apparatus from SETARAM. Approx. 20 mg of sample were heated from room temperature to 900 °C in 5%H_2/Ar at a heating rate of 10 °C/min. Due to the particular properties of the phyllosilicates formed with transition metal (Fe, Co, and Ni) encapsulated in hollow zeolites samples; TGA is used for detecting the reduction temperature of these samples.

II.9. Temperature Programmed Reduction (TPR)

Temperature-programmed reduction of Co-containing hollow zeolite was performed on a BELCAT-B catalyst analyzer. The zeolite was preheated at 200°C/Ar and then treated under 5%H_2/Ar up to 1000°C using a rate of 10°C/min. This technique is used for analyzing the reduction temperature of phyllosilicates formed in the transition metal (Fe, Co, and Ni) encapsulated in hollow zeolites samples. The results are then compared with those obtained by TGA analysis carried out under hydrogen atmospheres.

II.10. Magnetic measurements

Magnetic measurements were carried out at room temperature in a magnetometer (fields up to 21 kOe) using the Weiss extraction method: the in-situ reduced sample is placed in a quartz tube which is moved up and down in the uniform magnetic field induced by the two electromagnets (from -0.1 to 2T). An electrical voltage is created and measured in an integrated measuring coil. The reduction degree of the in-situ reduced sample (under a given condition such as temperature, ramp and reduction time) is determined from the amount of metallic cobalt given by the saturation magnetization of the samples. Thus, by varying the adding magnetic field between 2T and -0,1T, the degree of reduction of the sample can be estimated according to Eq.2

$$\%_{red} = \frac{100 M_S}{M_M \times m_M} \quad \text{Eq.2}$$

where $\%_{red}$ is the reduction percentage, M_S is the saturation magnetization (emu), M_M is the specific magnetization of the metal M (emu/g) and m_M is the cobalt mass in the sample (g).

Herein, the cobalt hollow silicalite-1 sample is analyzed to check the reduction degree of cobalt under reduction conditions given in Table 1.

II.11. Adsorption measurements and modeling

The adsorption of toluene and mesitylene over the silicate-1 hollow boxes (free of metal) was measured over a BelSorp Max apparatus (Bel Japan) at 30°C.

CO and C_3H_6 adsorption isotherms were recorded at 30°C from 10 to 1000 kPa on a BelSorp HP system (Bel Japan). The adsorption isotherms are fitted by a Langmuir model for the estimation of adsorption parameters, using literature results as first estimates. Langmuir equation is given as Eq.3

$$\Theta = \frac{q_i}{q_{sat}} = \frac{K_i \times p_i}{1 + \sum_{n=1}^{n} (K_j \times p_j)} \qquad i, j = 1,2, \dots, n. \qquad Eq.3$$

Θ is the fraction of the adsorption sites occupied, q_i is the adsorbed amount of i species, q_{sat} the saturation capacity. For species i, K_i is the adsorption constant and p_i is the partial pressure.

For CO and propylene mono-adsorbate system, the adsorption isotherm is obtained by simplifying the Langmuir equation as

$$q_i = \frac{q_{sat}\, K_i \times p_i}{1 + K_i \times p_i} \qquad Eq.4$$

Where q_{sat} is amount of CO or propylene adsorbed at saturation obtained from experimental isotherms, p_i is the partial pressure of each gas (from 1 to the maximum saturation pressure at 30°C; 1000 kPa and 100 kPa for CO and C_3H_6, respectively) and the adsorption constant is calculated by the Eq.5

$$K = e^{-\frac{\Delta H^0}{RT}+\frac{\Delta S^0}{R}} \qquad \text{Eq. 5}$$

Where ΔH^0 (isosteric heat) and ΔS^0 (enthalpy) are from literature results, and q_{sat}, ΔH^0 and ΔS^0 are constants for each adsorbent/adsorbate pair. Thus, the isotherms of CO and C_3H_6 at different temperatures (523 K, 573 K and 623K) on hollow silicalite-1 can be obtained from Eq.4 and Eq.5.

II.12. Diffusion and modeling

Adsorption kinetic data were measured on a BelSorp HP system. The presented plots are obtained at 10% coverage. The effective mass transfer coefficient (Kap) has been fitted using the Linear Driving Force Model (LDF) model.[7]

III.Catalytic reactions

III.1. CO oxidation

III.1.1. CO oxidation in the presence of hydrogen

The activities of Au particle and AuAg alloy particle in hollow silicalite-1 catalysts in the oxidation of CO (in the absence and in the presence of hydrogen) and the oxidation of hydrogen were measured in a continuous flow fixed bed reactor at atmospheric pressure at variable temperature. Typically, 50 mg of catalyst is mixed with 750 mg of alumina and placed in a quartz tube reactor. The reactant gases were mixed using mass flow controllers (Brooks Instrument) and sent through the reactor at a total flow rate of 50 mL min^{-1}. The outlet gases were analyzed with an online Varian-Micro GC (Gas chromatography, CP2003) equipped with a TCD detector. Two columns were used in parallel: a Molsieve 5A column (Ar as carrier gas) and a poraPLOT Q column (He as carrier gas).

The gas mixtures consisted of:

CO oxidation: CO (2%) + O_2 (2%), balanced in helium;

CO oxidation in the presence of hydrogen: CO (2%) + O_2 (2%) + H_2 (48%), balanced in helium;

H_2 oxidation: O_2 (2%) + H_2 (48%), balanced in helium.

The reaction was temperature-programmed between ambient and 300 °C -400°C with a heating rate of 1 min^{-1}. Two thermocouples located in the furnace and inside the catalytic bed allowed control of the furnace heating power and acquisition of the reaction temperature that is used to plot the catalytic activities, respectively. Two reaction cycles, each consisting of a heating and a cooling period, were recorded. The data corresponding to the second cooling step are plotted and used for discussion.

III.1.2. CO oxidation in the absence or in the presence of propylene

Typically, 50 mg of catalyst (Pt-zeolite and Pt/SiO_2 catalysts) was mixed with 50 mg of alumina, and placed in a quartz U-Type reactor. The catalyst was activated under hydrogen at 350°C for 2 hours with a heating rate of 1°C min^{-1}.

The gas mixtures consisted of:

CO oxidation: CO (2%) + O_2 (2%), balanced in N_2;

CO oxidation with propylene: CO (2%) + C_3H_6 (2%) + O_2 (2%), balanced in N_2;

To study the effect of catalyst mass on the CO conversion, four different amounts (from 5 mg to 50 mg) of catalysts have been tested. Different amounts of diluents (Al_2O_3) was adjusted so as to ensure that the catalyst bed height (and hence GHSV) remained constant.

Constants: Total catalytic bed height 1.4 cm / Total volume 0.135 cm^3 / Gas flow 50 $ml.min^{-1}$ (3000 $ml.h^{-1}$) / GHSV 22272 h^{-1}

III.1.3. Catalytic activities

The conversion (C %) is the fraction (in %) of a molecule that has reacted; for a reactant i is thus calculated by

$$C_i\% = \frac{n_{i0} - n_{it}}{n_{i0}} \times 100 \qquad \text{Eq. 6}$$

where n_{i0} and n_{it} are the number of moles of the reactant at the beginning and after a certain time (t) of reaction, respectively.

The reaction rate (r) of reactant i is calculated by:

$$r_i = \frac{C_i\% \times f_i}{m_a} \qquad \text{Eq. 7}$$

where $C_i\%$ is the conversion of the reactant i, m_a is the mass of active element in the catalyst (for example, mass of Au element used in Au@Silicalite-1 sample) and f_i is the flow of reactant i in mol/s in the gas phase. Here, the gas is considered as an ideal gas, whereas 1mol gas equals to 22.4 liters. Therefore, in the CO oxidation reactions, the partial flow for a reactant i is

$$f_i = \frac{1000 \times vol_i.\% \times f_{total}}{22.4 \times 60} \frac{mol}{s} \qquad \text{Eq. 8}$$

where $vol_i.\%$ is the volume percentage of the reactant i in the mixture gas and f_{total} is the total flow of gas phase.

TOF is expressed as the number of molecules of CO converted per second per surface Au atoms, which is calculated by the equation

$$TOF = \frac{r_{co} \times M_{metal}}{D} \qquad \text{Eq. 9}$$

Where r is the reaction rate of CO, M_{metal} is the molecular weight of the active metal and D is the dispersion of the metal particles.

The carbon balance is the percentage of carbon-containing products and non-reacted molecules compared to the initial carbon-containing reactant concentration; it is estimated by the equation

$$Carbon\ balance = \frac{n_r(out) + x n_p(out)}{n_r(in)} \times 100 \quad \text{Eq. 10}$$

Where $n_r(out)$ is the mole number of the non-reacted carbon-containing molecules, $n_p(out)$ is that of the carbon-containing products and $n_r(in)$ is the initial mole number of carbon-containing reactants.

Additionally, x is the coefficient from chemical equation balance. This parameter was mainly used to evaluate the mass balance in oxidation reactions.

III.2. Hydrogenation catalytic tests

Toluene and mesitylene hydrogenation reactions were carried out using two kinds of reactors

1) A tubular quartz plug flow reactor placed in a tubular furnace. 20 ± 0.1 mg of catalysts were used, held between quartz wool plugs, this reactor is used in the Chapter 3.
2) A diffuse reflectance FT-IR (DRIFTS) reaction cell. The reaction bed of the DRIFTS cell was made of a ceramic crucible. A mass of sample precisely weighted around 10 mg was deposited on top of a SiC layer filling up the crucible, this reactor is used in the Chapter 4 and 5.

The system is always operated at ambient pressure and the samples are reduced at 450°C in pure H_2 for 90 min before the catalytic tests. Each aromatic was fed separately using a saturator kept at 0°C, leading to partial pressures of 910 Pa and 59 Pa for toluene and mesitylene, respectively. 20 mL/min of pure hydrogen was used as carrier gas and fed through one saturator at a time. The reactor effluent was then diluted with 380 mL/min of Ar before reaching a 2 m path-length gas cell fitted in a Thermo FT-IR spectrophotometer. The proportion of the reactant and the corresponding saturated product were determined through integration of two zones in to the C-H stretching spectral region. In the case of toluene, methylcyclohexane was the only product observed, while trimethylcyclohexane was the only product obtained in the case of using mesitylene.

The reaction rate for each reaction is calculated by Eq.7 and turn-over frequencies (TOFs, expressed as molecules of toluene converted per second per surface Pt atoms) were calculated by Eq.9.

Furthermore the activation energy is calculated by Arrhenius equation

$$\ln r = \frac{-\mathrm{Ea}}{\mathrm{R}}\frac{1}{\mathrm{T}} + \ln \mathrm{A} \qquad \text{Eq. 11}$$

Where *r* is the reaction rate, Ea is the activation energy, R is the universal gas constant, T is the temperature in Kelvin and A is the pre-exponential factor. The TOF is used instead of *r* for the calculation; therefore the activation energy is calculated from the slope of the linear relationship between ln (TOF) and 1/T.

Bibliography

1. Mei, C., Liu, Z., Wen, P., Xie, Z., Hua, W. & Gao, Z. Regular HZSM-5 microboxes prepared via a mild alkaline treatment. *J. Mater. Chem.* **18**, 3496-3500 (2008).

2. Corvaisier, F., Schuurman, Y., Fecant, A., Thomazeau, C., Raybaud, P., Toulhoat, H. & Farrusseng, D. Periodic trends in the selective hydrogenation of styrene over silica supported metal catalysts. *J. Catal.* **307**, 352-361 (2013).

3. Yen, C.-W., Lin, M.-L., Wang, A., Chen, S.-A., Chen, J.-M. & Mou, C.-Y. CO Oxidation Catalyzed by Au−Ag Bimetallic Nanoparticles Supported in Mesoporous Silica. *The Journal of Physical Chemistry C* **113**, 17831-17839 (2009).

4. Allen, T. Particle Size Measurement, Powder sampling and particle size measurement, Vol. 1, Edn. Fifth (1968).

5. Van Hardeveld, R. & Hartog, F. The statistics of surface atoms and surface sites on metal crystals. *Surf. Sci.* **15**, 189-230 (1969).

6. Jinschek, J.R. & Helveg, S. Image resolution and sensitivity in an environmental transmission electron microscope. *Micron* **43**, 1156-1168 (2012).

7. Sircar, S. & Hufton, J. Why does the linear driving force model for adsorption kinetics work? *Adsorption* **6**, 137-147 (2000).

Noble metal particles in hollow silicalite-1 zeolites

I. Introduction

Gold nanoparticles display unique properties in catalysis.[1-5] Although supported gold nanoparticles can be prepared using many chemical and physical methods, they are not thermodynamically stable upon heating and particle sintering leads to larger particles with a boarder size distribution.[6] On silica, Oswald ripening of gold nanoparticles (diameter approx. 6nm) takes place at 550°C.[7] The functionalization of porous silica surface (MCM-41, SBA-15) by amine groups enhances the sintering resistance and allows the synthesis of gold nanoparticles of 4-8 nm. Nevertheless, the dimension of gold particles cannot be tailored by using this synthesis pathway.[8] Higher stabilities are observed when silica is functionalized with thiol groups; Au particles with a diameter of 2 nm can be obtained upon heating in air at 550°C but the size grows very rapidly at higher temperatures.[9]

The so-called "yolk-shell" and "core-shell" catalyst design is an alternative solution which prevents particle growth by sintering. Yolk-shell catalysts are a class of specific materials in which the yolk is a catalytic particle and the shell is a thin mesoporous layer, generally an inorganic oxide (ZrO_2, TiO_2 and SiO_2) or carbon.[10-14] Very few groups have been working on yolk shell materials with a microporous zeolite shell. Meanwhile, several groups have reported the synthesis of core-shell catalysts in which a macroscopic zeolite layer is coated on metal/SiO_2 grains and the activity is given by the metal particles underneath the membrane.[15-20] However, the thickness of the zeolite shell is usually from 200 nm up to several microns [15, 21] which eventually limits the overall reaction rates due to diffusion transport limitations.[15]

Herein, we have extended the concept of yolk-shell materials to noble metal nanoparticles encapsulated in single-crystal hollow zeolite shells, in which the thin hollow shell protects metal particles from sintering and also serves as molecular sieve.

The topic of chapter 3 is dealing with the development of an original and scalable synthesis pathway for noble metal nanoparticles with controlled size from 2 to 15nm encapsulated in hollow zeolite single crystals. The synthesis method will then extend to other noble metals.

The effects of encapsulation of the catalyst will be first evaluated on CO oxidation in the presence of hydrogen over Au@Sil-1 (Sil-1 for silicalite-1). It is known that carbon monoxide and alkenes strongly compete for adsorption on noble metal surfaces.[22] The presence of a very small concentration of CO decreases the activity in the hydrogenation of ethylene by several orders of magnitude.[23] Conversely,

the process of selective CO oxidation in the presence of alkenes for purification purposes is also a scientific and technical challenge.[22, 24, 25] Then the influence of the encapsulating zeolite membrane in yolk-shell materials was evaluated over Pt@Sil-1 in the selective CO oxidation in the presence of propylene. Additionally, the molecular sieving at sub-manometer scale was evidenced in the hydrogenation of light substituted aromatics (toluene and mesitylene) over Pt@Sil-1.

II. Results and discussion

II.1. The preparation of Au particles encapsulated in hollow silicalite-1 material (Au@Sil-1)

II.1.1. Post-impregnation method

We have impregnated hollow silicalite-1 with an Au aqueous solution and then reduced the solid under H_2. The corresponding final material was denoted 0.38-Au@Sil-1-PI (for post impregnation, 0.38 represents Au loading detected by ICP). TEM image and particle size distribution of the catalyst are given in Fig. 1; they clearly show that Au particles are not homogeneously distributed, with sizes from 2 to 30 nm. Moreover, only a few of them are inside zeolite cavities, most of them being large and outside the crystals. Then the post-impregnation method was not further studied.

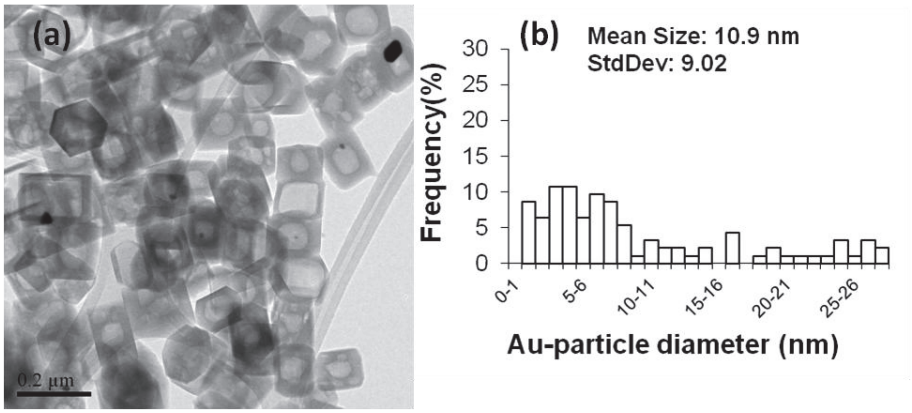

Figure 1: TEM image (a) and particle size distribution (b) of Au@Sil-1-PI sample.

II.1.2. Impregnation followed by the formation of hollow structures method

Later on, another synthesis method to prepare Au@Sil-1 has been developed which consists of three steps (synthesis details in chapter 2; the recipe is given for a particular concentration, yielding a final material with 0.52 wt. % Au):

1) Impregnation of bulk silicalite-1 crystals with Au aqueous solution followed by a reduction under H_2

Fig. 2-b shows that after the incipient wetness impregnation (IWI) and reduction, gold nanoparticles around 1-2nm in size are located in the centre of the crystals, where the density of framework defects is maximum.[26, 27]

2) Hollow zeolites are then formed by a dissolution-recrystallization process in the presence of TPAOH at 170°C as previously described elsewhere.[28, 29]

During this process, the highly defective core of the zeolite crystal is preferentially dissolved and silica species recrystallize on the outer surface in the presence of TPA^+ cations. Tuel et al. estimated that approx. 50% of the original crystals were dissolved and recrystallized during the process.[28, 29] Since gold nanoparticles are too big to migrate through the microporous zeolite walls, they remain trapped in the cavity and sinter together into a unique larger particle following an Ostwald ripening process. At this point, each hollow crystal contains one gold nanoparticle which is usually located at an inner-edge of the hollow zeolite (Fig. 2-c).

3) 0.52-Au@Sil-1 composite is calcined at 525°C in order to remove the template and organic residues, yielding a light pink powder (Fig. 2-d).

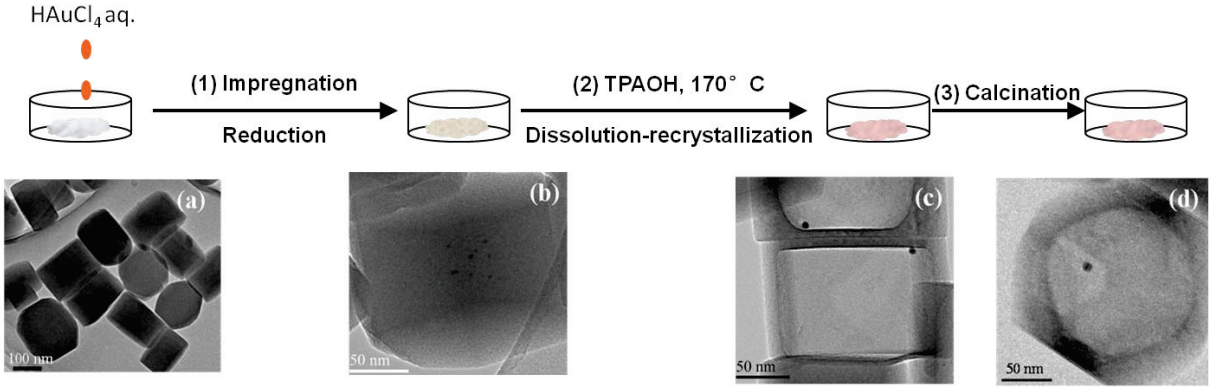

Figure 2: The synthesis process of Au@Sil-1 yolk-shell materials and TEM images of materials at different synthesis steps of 0.52-Au@Sil-1: silicalite-1(a), Au-impregnated silicalite-1(b), 0.52-Au@Sil-1 before(c) and after (d) calcination.

High Resolution TEM pictures clearly show the single crystalline nature of hollow silicalite-1 without apparent crystalline defects such as twinning planes, grain boundary zones or pinholes (Fig. 3). We can see that a gold particle around 7nm in size was encapsulated in the hollow silicalite-1 crystal with wall thickness around 20 to 30 nm.

II.1.3. Control of Au particle size encapsulated in hollow silicalite-1

The relationship between the particle size and the initial amount of Au precursor was studied on four Au@Sil-1 samples with different Au loadings. These samples were prepared by varying the concentration of the $HAuCl_4$ solution (from 0.05M to 0.44M) used for the impregnation step. The samples are designated as w-Au@Sil-1, where (w) is the Au loading (wt %) determined by ICP-OES (see Table 1).

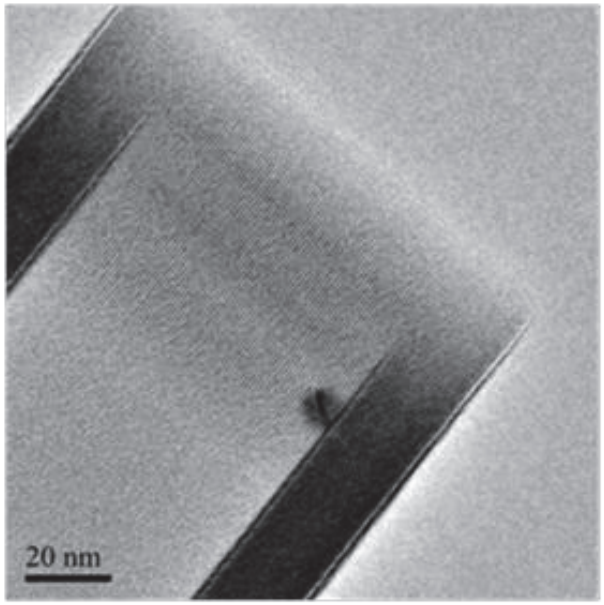

Figure 3: HRTEM picture of 0.52-Au@Sil-1 material.

II.1.4. ICP-OES analysis of Au@Sil-1 samples

As shown in Table 1, the Au loadings in final materials are approximately proportional to the concentration of the $HAuCl_4$ solution used in IWI process (Fig. 4). This linear relationship will be particular useful to find the relationship between the mean particle size and $HAuCl_4$ concentrations (see below for details). However, Au loadings in the final Au@Sil-1 samples are approximately half of the expected value, suggesting a significant loss of Au during washing steps of the synthesis process.

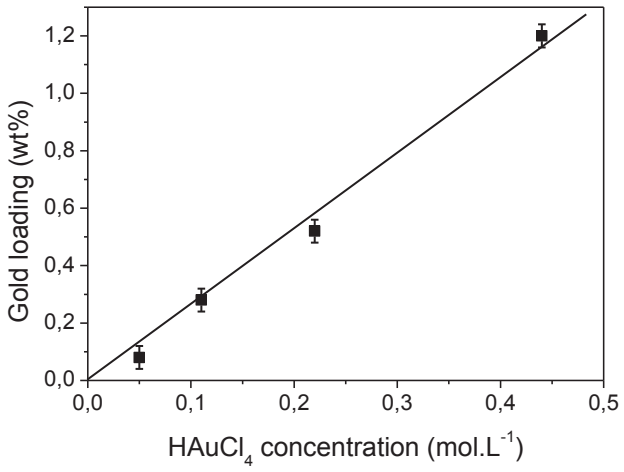

Figure 4: Gold loading wt% (w-Au@Sil-1) as function of $HAuCl_4$ concentration for the impregnation.

II.1.5. Relationship between Au particle size and loading

As shown in Fig.5, in all the four Au@Sil-1 samples, almost each hollow zeolite contains one Au particle. Average gold particle diameters have been estimated from the size distribution of a population of 400 particles measured on TEM images, the histograms are shown in Fig. 6. Particle

size distributions are relatively narrow for all samples as indicated by the standard variation indicators. For example, more than 50% of particles possess a diameter between 1.5 and 2.5nm for 0.08-Au@Sil-1. The particle dispersions are also estimated from the size distribution using a cub-octahedral model and a calculation method according to Van Hardeveld and Hartog.[30] The gold contents and Au particle dispersions of these four Au@Sil-1 samples are given in Table 1.

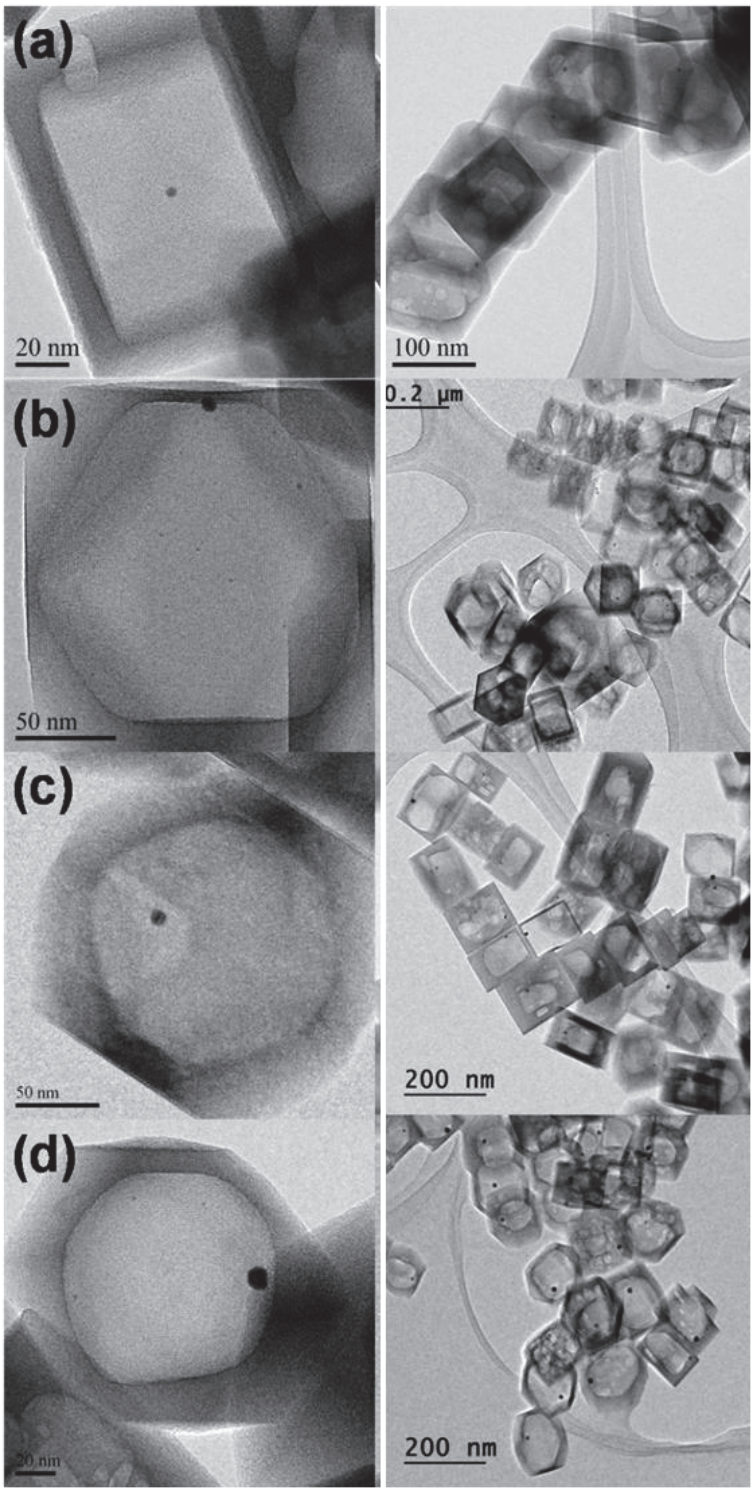

Figure 5: TEM images of 0.08-Au@Sil-1 (a), 0.28-Au@Sil-1 (b), 0.52-Au@Sil-1 (c) and 1.2-Au@Sil-1(d) materials.

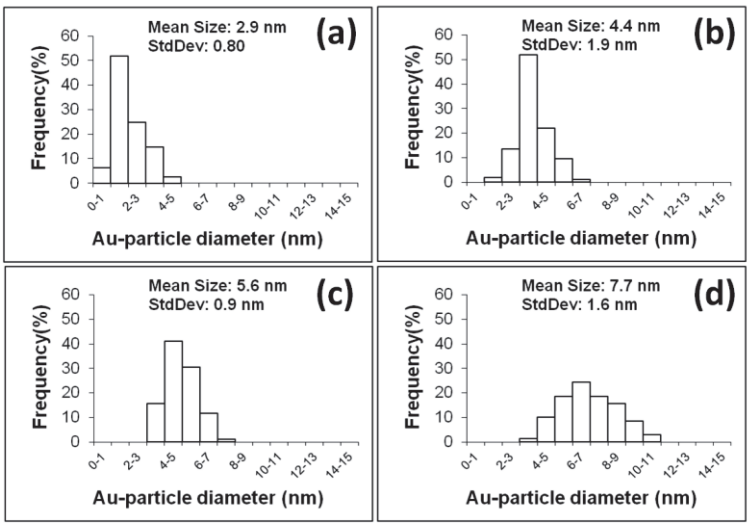

Figure 6: Gold particle size distributions for (a) 0.08-, (b) 0.28-, (c) 0.52- and (d) 1.2-Au@Sil-1 samples.

Table 1: Gold contents and dispersions of Au@Sil-1 samples.

Sample Name	$HAuCl_4$ concentration (mol/L)	Au loading (wt%)	Dispersion (%)
0.08-Au@Sil-1	0.05	0.08	38.2
0.28-Au@Sil-1	0.11	0.28	28.3
0.52-Au@Sil-1	0.22	0.52	24.5
1.2-Au@Sil-1	0.44	1.20	17.7
0.38-Au@Sil-1-PI	0.22	0.38	7.3

PI: Post-Impregnated

The Au loading w (expressed as wt. %) is defined as:

$w = m_{Au}/(m_{zeolite} + m_{Au})$ where m_{Au} and $m_{zeolite}$ are the masses of zeolite and gold, respectively,

assuming that $m_{zeolite} >> m_{Au}$, the above equation can be simplified as:

$$m_{Au}/m_{zeolite} = w/(1-w) \approx w$$

On the other hand the mass corresponding to a population of monodispersed gold spheres with diameter d_{30} can be expressed as:

$$m_{Au} = n \cdot \rho \cdot f \cdot d^3$$

where n is the number of particles in the sample, ρ the density of gold and f a shape factor (π/6 for spherical particles); the term $\rho.f.d_{30}^3$ represents the mass of a single metal particle.

Therefore, if we assume that the gold loading is low, the combination of the above equation gives:

$$w = n\rho f \cdot d_{30}^3 \qquad \text{(Eq.1)}$$

Eq.1 establishes that the particle volume d_{30}^3 varies linearly with the metal loading, at least when the latter is negligible compared to the mass of zeolite. As all samples are made of spherical gold particles, ρ and f are constant. Assuming that the number of gold particles (n) per gram of sample does not vary from sample to sample (we assume that each hollow crystal contains 1 Au particle), a linear relationship is obtained experimentally between d_{30}^3 and the gold content (w) for the four Au@Sil-1 samples (Fig.7). Clearly, experimental observations follow the theoretical linear relationship within experimental errors.

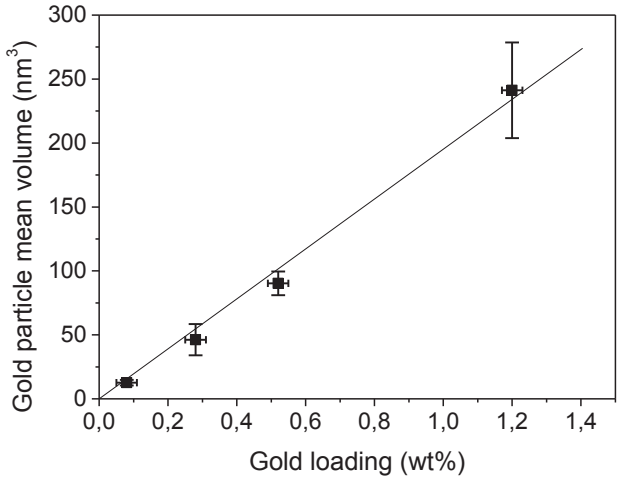

Figure 7: Mean volume of gold particles measured by TEM as a function of gold loading (w). Experimental data (dots) obtained from 0.08-, 0.28-, 0.52- and 1.2-Au@Sil-1 samples. The straight line is the fitting of Eq. 1.

The knowledge of this linear relationship makes possible to synthesize a batch of gold nanoparticles with a targeted size. For example, to synthesize 1g of zeolite with gold particles of 5 nm in diameter (d_{30}) (which corresponds to a volume of 65 nm^3), the gold loading should be equal to 33 mg (0.33 wt %) (Fig.7). This can be readily achieved in practice by adjusting the $HAuCl_4$ concentration. In the IWI process, the volume of $HAuCl_4$ solution is fixed by the total porous volume of the zeolite (0.23 ml/g of starting silicalite-1). Hence the gold loading (w) is proportional to the $HAuCl_4$ concentration (Table 1 and Fig.4) and particles of 5nm will be obtained with an estimated $HAuCl_4$ concentration of 0.13 M.

II.1.6. Nitrogen physisorption at 77K

Nitrogen physisorption results (at 77 K) on 0.52-Au@Sil-1 and 0.38-Au@Sil-1-PI samples are similar to those previously reported for metal-free hollow silicalite-1 (see Fig. 8).[28] A H2 hysteresis loop with an abrupt closure at $p/p_0 \approx 0.45$ characterizes internal porosity connected to outer surface via entrances smaller than 4nm.[31-33]

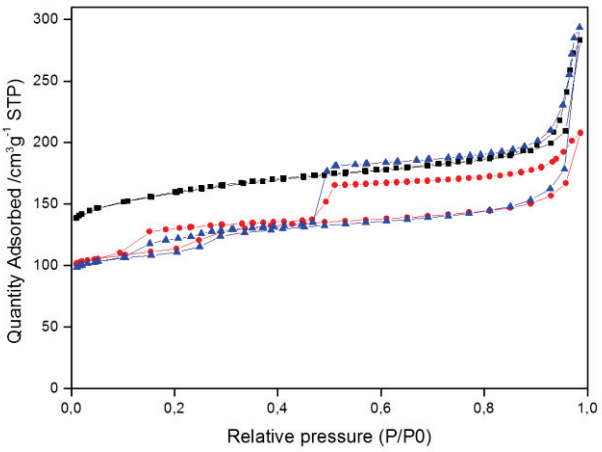

Figure 8: N_2 adsorption/desorption isotherms on Silicalite-1 (■), 0.52-Au@Sil-1 (●) and 0.38-Au@Sil-1 PI (▲), the isotherms of Silicalite-1 have been shifted upwards 40cm^3 for comparison.

II.1.7. XRD analysis

XRD patterns show that the zeolite structure is unchanged after Au impregnation and TPAOH treatment (Fig. 9). In contrast to conventional desilication or dealumination which usually leads to the formation of amorphous structures, the dissolution-recrystallization method allows the generation of highly crystalline hollow zeolites. Diffraction peaks at 38.3°, 44.7° which are assigned to (111) and (200) planes of face-centered cubic (fcc) Au particles, are not observed due to the low Au loading in Au containing samples.

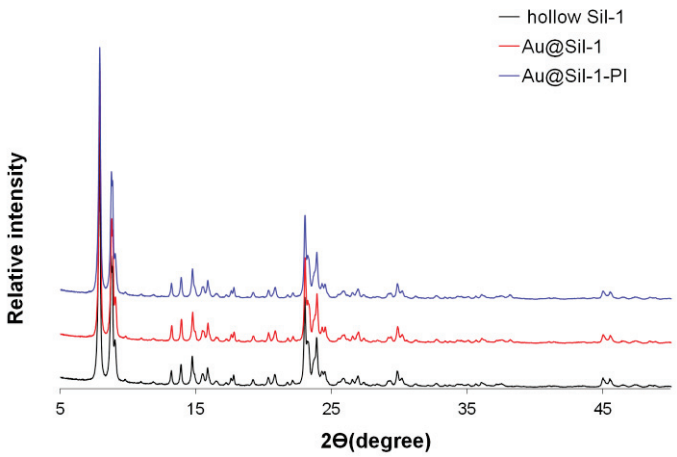

Figure 9: XRD patterns of 0.38-Au@Sil-1-PI (blue); 0.52-Au@Sil-1(red); and hollow silicalite-1 crystals (black).

II.2. The extension of the preparation method to other noble metals

II.2.1. The synthesis of Pt particles in hollow silicailte-1 material (Pt@Sil-1)

0.9-Pt@Sil-1 was obtained following a method similar to that previously used for Au but Pt impregnated silicalite-1 was not reduced prior to treatment in TPAOH at 170°C (synthesis details given in the experimental chapter). A general wet impregnation method is used instead of incipient wetness impregnation (IWI). As shown in Fig. 10, Pt particles with relatively narrow particle size distribution are individually encapsulated in each hollow zeolite.[34] More than 50% of the particles are between 10 nm to 12 nm in diameter.

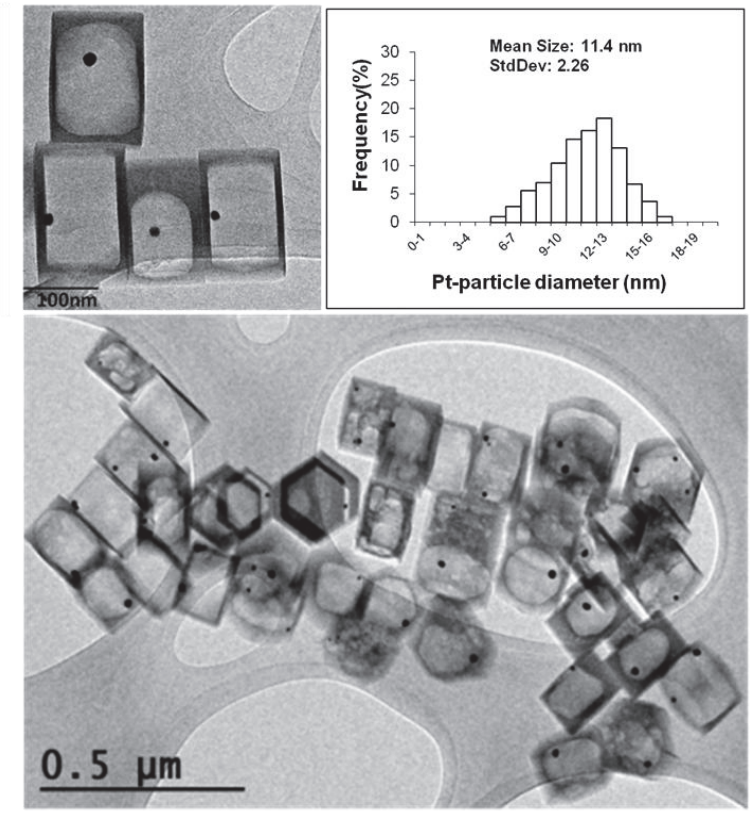

Figure 10: TEM images of 0.9-Pt@Sil-1 and Pt particle size distribution.

Nitrogen physisorption measurements (at 77 K, Fig.11) are similar to those previously reported for Pt-free hollow silicalite-1 and Au@Sil-1 (see Fig. 8), and show a similar hysteresis loop which is closed at P/P_0 around 0.45 resulting from the presence of the internal cavity.[28]

Later on, the synthesis method of Pt@Sil-1 has also been extened to Pd and Ag using Na_2PdCl_4 and $AgNO_3$ as metal precusors, respectively.

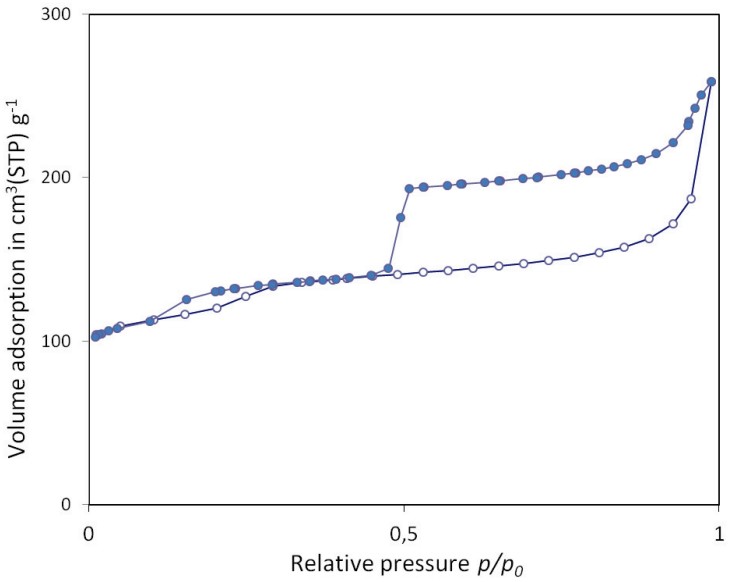

Figure 11: N_2 adsorption/desorption isotherms of 0.9-Pt@Sil-1 sample.

II.2.2. The synthesis of Pd particles in hollow silicailte-1 material (Pd@Sil-1)

II.2.2.1. TEM analysis

Three samples have been prepared with different Pd loadings in the range of 0.14 to 0.48 wt. %, the TEM images and particle size distributions are given in Fig.12. Pd@Sil-1 materials look very similar to Au@Sil-1 and Pt@Sil-1; in particular we can observe that there is generally one Pd particle per hollow silicalite-1 crystal. Pd particle size distributions are relatively narrow for these three samples.

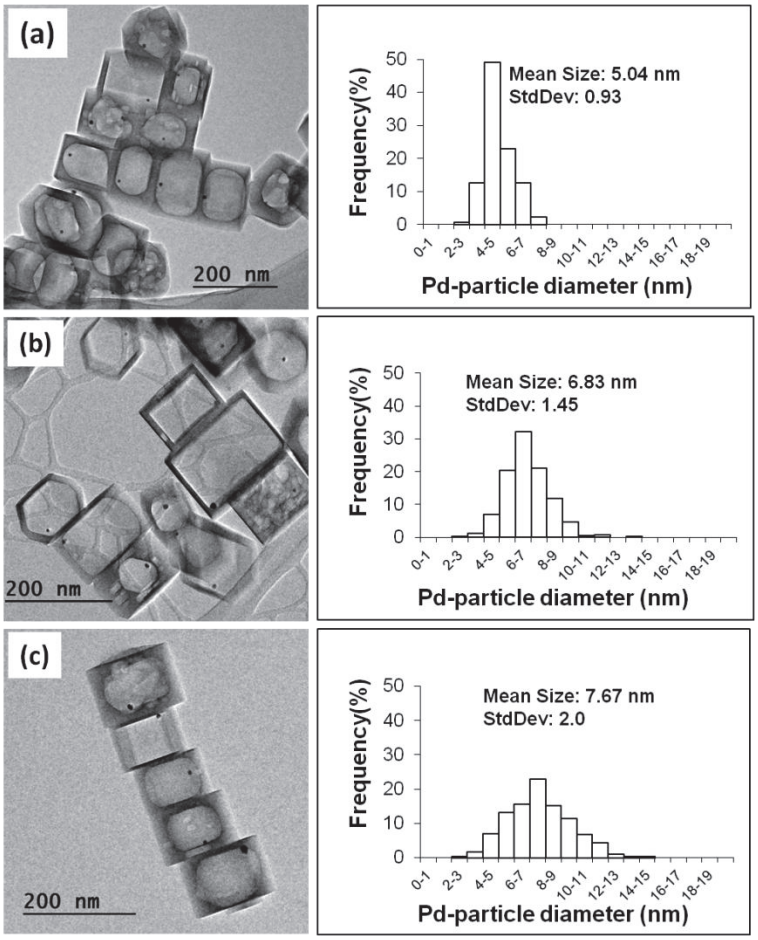

Figure 12: TEM images of 0.14-Pd@Sil-1(a), 0.45-Pd@Sil-1(b), 0.48-Pd@Sil-1 with corresponding Pt particle size distributions on the right.

II.2.2.2. Relationship between metal particle size and metal molar loading

For Au@silcalite-1 samples, we have shown that the metal loading was proportional to the particle volume d_{30}^3 (see Eq.1). The factor of proportionality involves the metal density, which means that slopes will be different from a metal to another (for example, the density of gold is approx. twice that

of silver). All metals studied here crystallize in the same face-centered cubic (fcc) system with approximately the same unit cell (0.4±0.05 nm), which suggests that for a given particle size, the number of moles is also the same for all metals providing that the particles size is unchanged. If the mass w in Eq.1 is replaced by the number of moles (mol. %), then equation 1 becomes:

$$\text{mol. \%} = w/A = n\rho f \cdot (d_{30})^3/A \quad \text{(Eq.2)}$$

where A represents the molar weight of the metal. From the TEM observations, it is clear that metal particles in Au@Sil-1 and Pd@Sil-1 are spherical and that the form factor f is the same for both samples. Under such conditions, in Eq.2 ρ/A is a constant for each kind of metal which are very similar in the studied metals. As a consequence, if d_{30}^3 is corrected by ρ/A for each metal, the coefficient of proportionality between the corrected particle volume d_{30}^3 and the number of moles of metal present in the zeolite will not depend on the nature of the metal. This linear relationship was confirmed experimentally for Au and Pd (Fig. 13). It is very useful because it allows a direct estimation of the particle size from the metal loading and shows the generality of our synthesis strategy. Of course, this relationship is valid only if hollow crystals contain one (and only one) particle, which is not always the case as it will be discussed later.

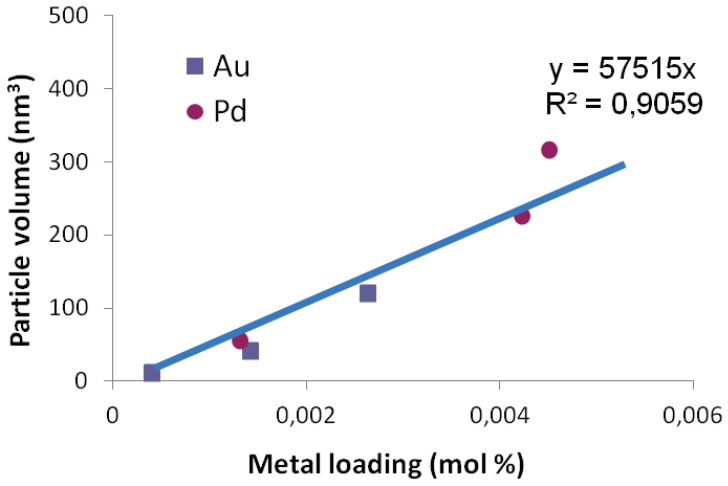

Figure 13: Pd and Au particle volume as a function of metal loading mol % in hollow silicalite-1.

II.2.3. The synthesis of Ag particles in hollow silicailte-1 material (Ag@Sil-1)

II.2.3.1. TEM analysis

Sliver behaves differently from the other noble metals. After TPAOH treatment, each hollow crystal contains several particles (Fig.14-left), contrasting with Au, Pt and Pd for which there are only one particle per cavity. More surprisingly, almost all the particles are outside the crystals after calcination (Fig.14-right), suggesting that they could pass through the zeolite shell at high temperature.

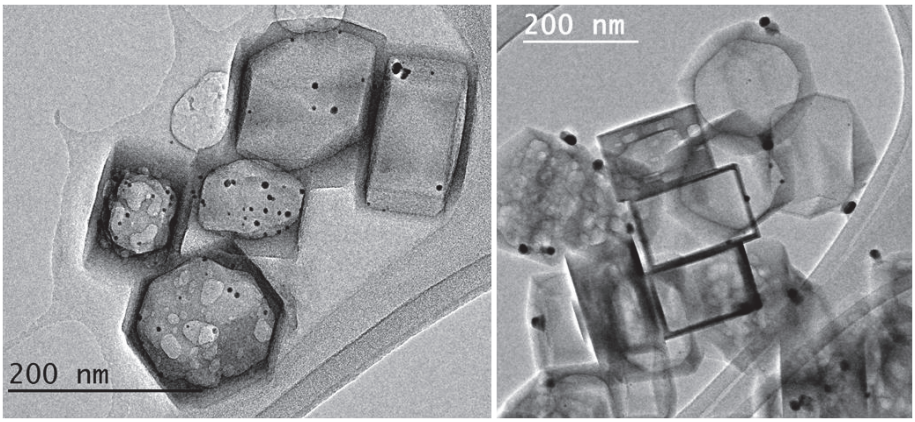

Figure 14: TEM images of 1-Ag@Sil-1 before (left) and after (right) calcination in air at 525°C for 6 hours.

To investigate this phenomenon and obtain a three-dimensional information on the evolution of the sample with temperature, an 'operando' tomography was performed of non-calcined 1-Ag@Sil-1 material during its evolution with temperature and gas conditions in a dedicated Environmental Transmission Electron Microscope (Cs-corrected TITAN ETEM G2 FEI, 80-300 kV).

II.2.3.2. Tomography analysis

A tomography of the non-calcined 1-Ag@Sil-1 was first carried out under vacuum. A continuous tilted series from 78 to -38.5° (limited by the grid shadowing) was acquired in bright field within less than 4 minutes using a rapid and continuous video-recording sequence, instead of the 'step-by-step' usual method. This fast acquisition method preserves the integrity of sample under exposure to the electron beam (microscopy operating at 300 KV). Video frames of the sample under high vacuum at 20°C are shown in Fig.15-a and b. In the four observed crystals, only 2 among the 56 visible Ag particles are outside the cages (less than 4%). The surface rendering of these four cages obtained from TOMO video reconstruction shows that most of the Ag particles are located on the inter-surface of the cavities (Fig.15-c). A mean particle size about 5.8nm is estimated from size distribution (Fig.15-

d). The ultra thin zeolitic walls indicated by the arrows in Fig.15-c are deliberately removed in the TOMO reconstruction process to have a better view of the particles inside the hollow zeolite.

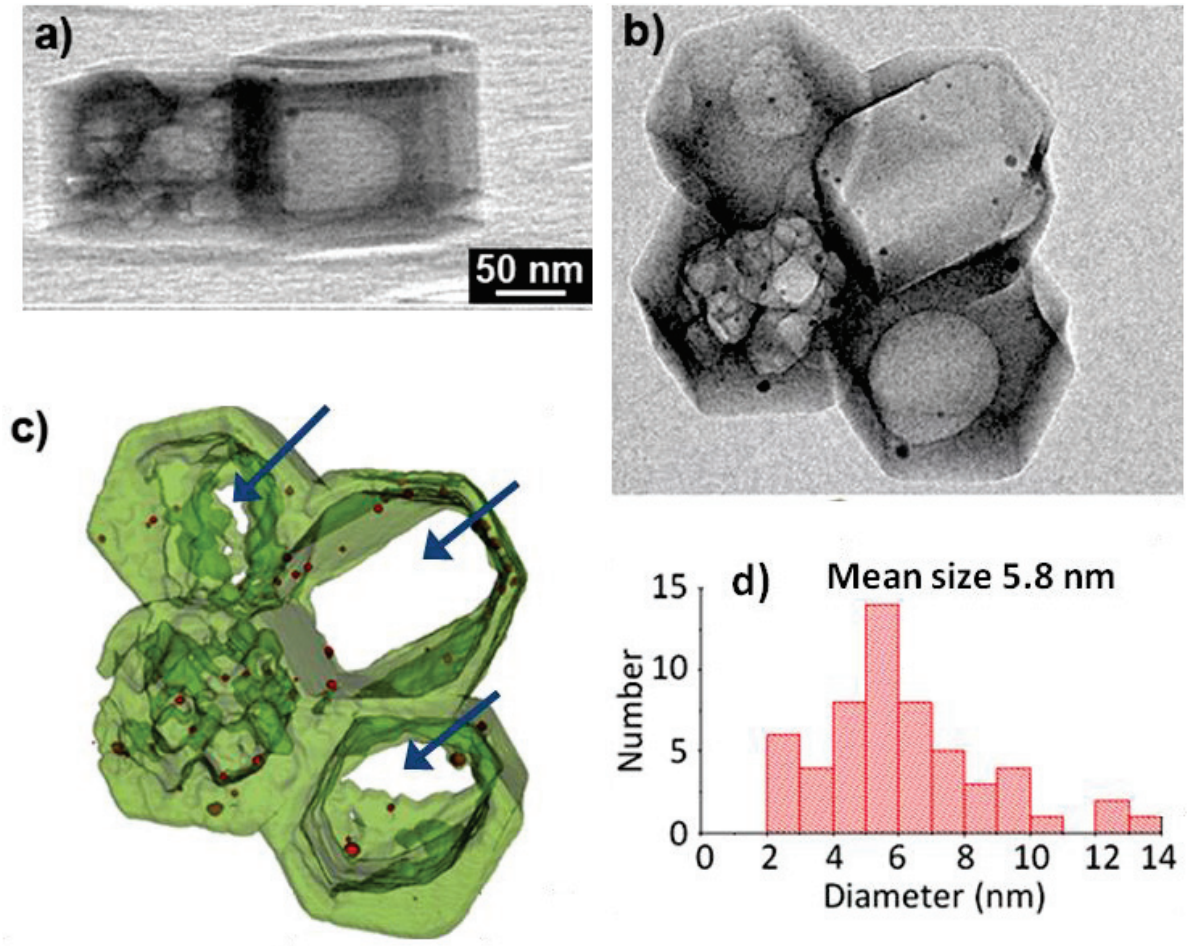

Figure 15: Video frames of fast single-tilt tomography on 1-Ag@Sil-1 (a, b) (the limits of a continuous tilting series acquired in bright field in less than 4 minutes from 78°to -38.5° under high vacuum at 20°C and 300 KV); surface rendering obtained by reconstruction from the tomography video (c) and size histogram of Ag NPs (d).

II.2.3.3. Environmental Transmission Electron Microscopy

The evolution of the non-calcined Ag@Sil-1 with temperature was followed by Environmental Transmission Electron Microscope (ETEM) under vacuum and oxygen flux at different temperatures. Images of some zeolite crystals before and after heating in-situ at 700°C under vacuum are shown in Fig.16-a and b. Ag particles are slightly larger than those at 20°C due to Ostwald ripening but all of them are still inside hollow crystals indicating that they are thermally stable under vacuum. Another image of the sample heated at 450°C under 1 mbar of oxygen shows that some of Ag nanoparticles have been expelled from the cages and spread on the carbon support (Fig.16-c).

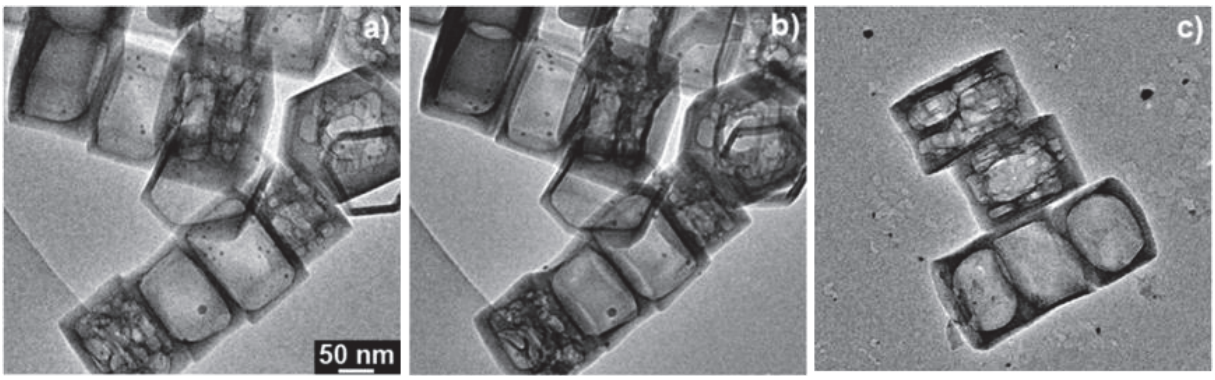

Figure 16: TEM images of Ag@Sil-1 at 20°C under high vacuum (a); the same area at 700°C under high vacuum (b) and another area at 450°C under 1 mbar of O_2 (c).

HAADF (High Angle Annular Dark Field) images of the non-calcined 1-Ag@Sil-1 were taken at different temperatures during in-situ heating under 1 mbar oxygen pressure (Fig. 17). We found that, Ag particles are still inside zeolite cavities at 350°C (Fig.17-a), but not at 450°C, a temperature for which some of the particles are visible outside zeolite crystals (indicated by arrows in Fig. 17-b).

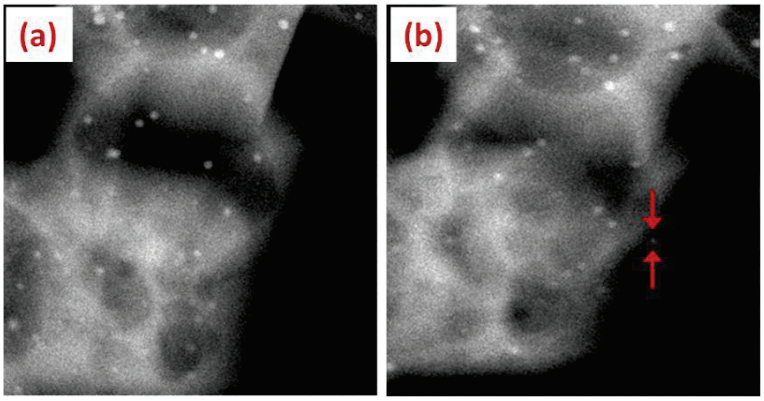

Figure 17: HAADF images of Ag@Sil-1 at 350°C (a) and 450°C (b) under 1 mbar of O_2, (images taken from the same area).

As temperature increased, particles grew continuously both inside and outside zeolite cavities (Fig. 18-a) until 800°C, all particles were outside (indicated by circles in Fig. 18-b).

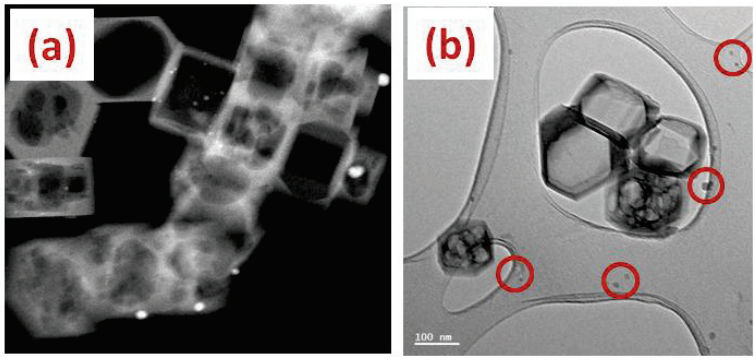

Figure 18: HAADF (a) and TEM (b) images of Ag@Sil-1 under 1 mbar of O_2 at 500°C (a) and 800°C (b).

It is known that the template (TPA^+ cations) inside the zeolite pores is burned at temperatures around 450°C under oxygen. At higher temperatures, micropores are free from organics and oxygen can

easily diffuse inside the zeolite cavity and oxidize Ag particles to form silver oxide particles. However, silver oxide is not stable at these temperatures (the sublimation temperature of silver oxide is about 280°C), which can explain why the particles are expelled from the cavity through the zeolite around 450°C. Similar observations have also been reported by Massiani et al. on the Ag nanoparticles dispersed on NaX zeolite materials.[35]

II.3. The synthesis of Au and Pt particles in large hollow silicailte-1

Large silicalite-1 (further denoted L-Sil-1) crystals were synthesized according to a published procedure using a mixture of tetrabutylphosphonium and tetraethylphosphonium cations (TBP^+/TEP^+ = 3) as template (details in experimental chapter).[36] SEM image of the prepared zeolite shows that crystal dimensions are about 1 µm x 0.5 µm x 0.5 µm, which is approximately 60 times larger in volume than nanocrystals (0.20 µm x 0.15 µm x 0.14 µm), as shown in (Fig.19).

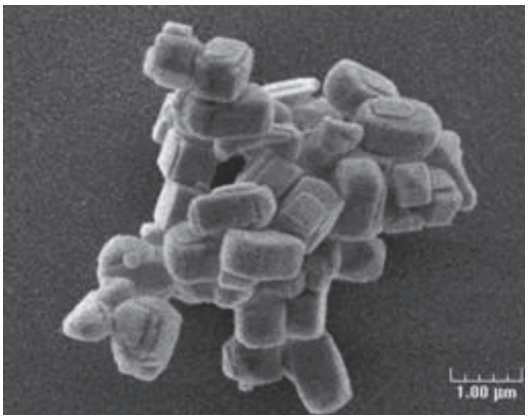

Figure 19: SEM image of calcined Large silicalite-1 crystals.

The XRD pattern of L-Sil-1 is strictly identical to that obtained on nanocrystals, with characteristic intense diffraction peaks of a highly crystalline solid (Fig.20).

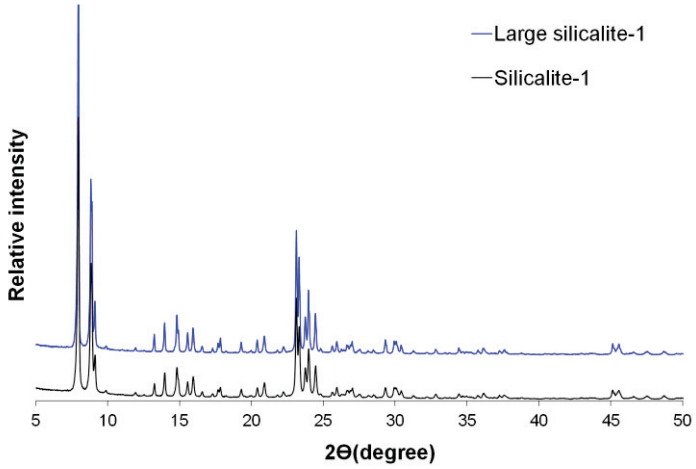

Figure 20: XRD patterns of calcined Large silicalite-1 crystals (in blue) and calcined silicalite-1 crystals (in black).

Metal containing materials with two different loadings were synthesized from large silicalite-1 crystals following the same receipt as that used or nanocrystals. In contrast to nanocrystals, the treatment did not form a single large hole but many internal small cavities. TEM images of 0.5-Pt@L-Sil-1 (Fig.21) and 0.5-Au@L-Sil-1 (Fig.22) show that metal particles with particle size mainly between 4 to 6 nm are individually encapsulated in different cavities, however, some particles about 15nm in size are also present in the crystals which lead to a broader particle size distribution. This strategy increases the metal particle density per zeolite volume by approximately 10 times (estimated from TEM image) compared to that of nanocrystals, which may be of practical interest for reducing the catalyst volume in large-scale applications.

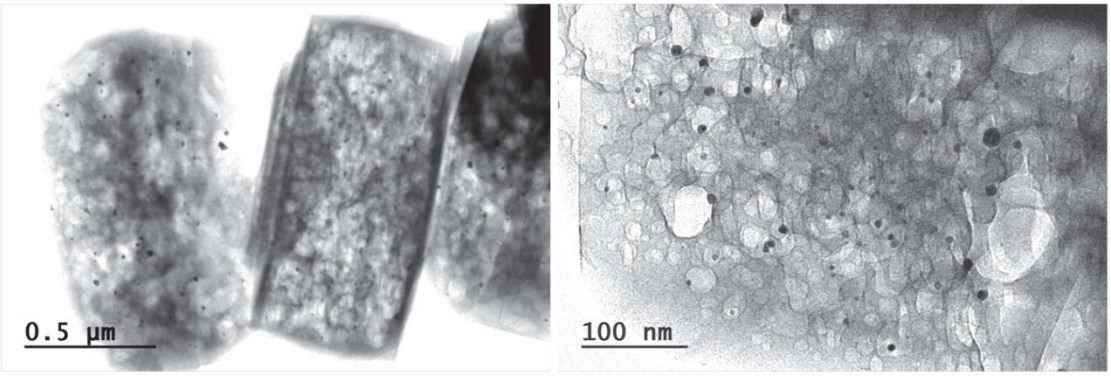

Figure 21: TEM images of 0.5-Pt@L-Sil-1 sample.

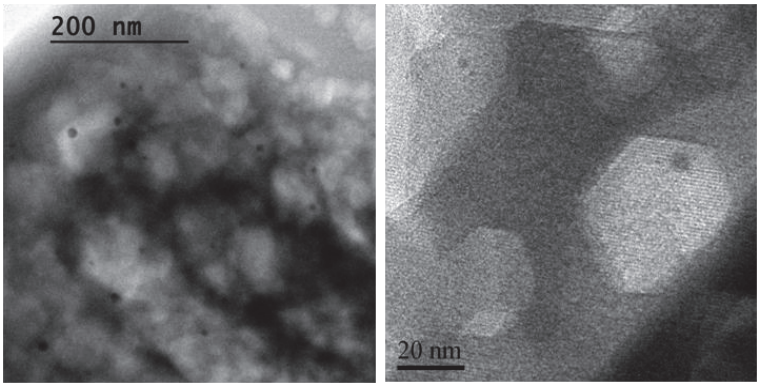

Figure 22: TEM images of 0.5-Au@L-Sil-1 sample.

II.4. Study of the particle sintering as function of temperature

Pt particles with diameter below 15 nm are known to migrate and coalesce under H_2 at temperatures between 600 and 700 °C over supported catalysts.[37] 0.7-Pt@Sil-1 has been tested for Pt particle stability under heating at 600°C and 750°C in H_2 for 12 hours, respectively. A Pt/SiO_2-C (C for commercial) catalyst (Pt loading at 0.71 wt. % with a mean particle size of 7.5nm) was also tested for comparison. Between these two temperatures, the mean particle size is almost unchanged over Pt@Sil-1 material, while the particle size distribution slightly broadens, probably due to Ostwald ripening (Fig. 23-a and b). In contrast to Pt encapsulated zeolites sample, the mean size of Pt particles in Pt/SiO_2 increased by a factor of 1.7 from 7.5 nm to 12.8nm (Fig23-c and d). Therefore, we can conclude that due to the zeolite shell protection, the Pt@Sil-1 material is sinter-resistant at 750 °C under hydrogen.

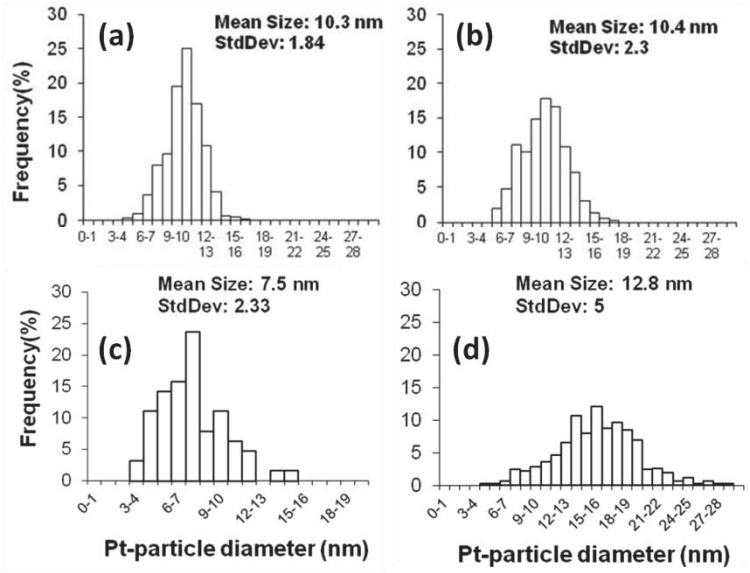

Figure 23. Pt particle size distribution on 0.7-Pt@Sil-1(a ,b) and 0.71/SiO_2-C (c,d) after reduction in H_2 at 600 (a,c) and 750°C (b,d).

II.5. Catalytic tests

II.5.1. Catalytic evaluation of Au@Sil-1 materials

Herein, 0.28-Au@Sil-1 and 0.38-Au@Sil-1-PI (PI for Post Impregnation) were tested for CO oxidation in presence of H_2 (PrOx reaction) and H_2 oxidation (see Fig.24 and 25).[38]

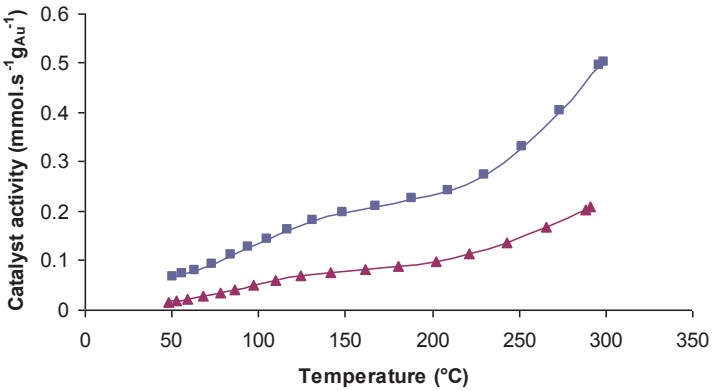

Figure 24: CO oxidation rates as function of temperature over 0.28-Au@Sil-1 (■) and 0.38-Au@Sil-1-PI (▲) catalysts in PrOx reaction (2%CO+2%O_2+48%H_2 in He).

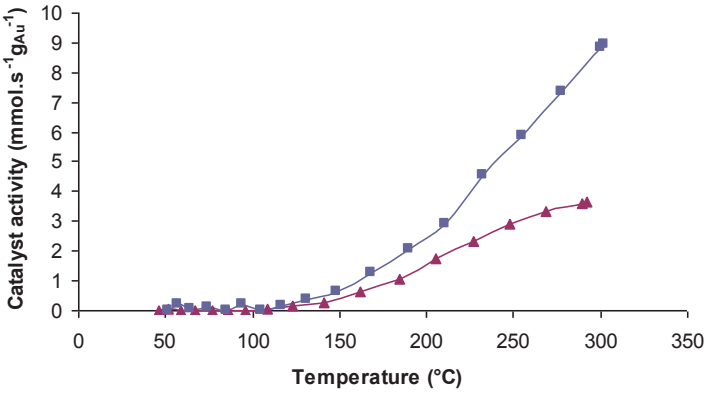

Figure 25: H_2 oxidation rates as function of temperature over 0.28-Au@Sil-1 (■) and 0.38-Au@Sil-1-PI (▲) catalysts in PrOx reaction (2%CO+2%O_2+48%H_2 in He).

For both CO and H_2 oxidation reactions, the activity is much higher over 0.28-Au@Sil-1 than 0.38-Au@Sil-1-PI. The difference in activity increases with temperature and reaches a factor of approximately 3 at 300°C. This different observed between the two catalysts is actually in good agreement with the metal dispersion ratio (see Table 1).

For both reactions, the profiles of the light-off curves and activity levels are similar to those obtained in the literature over Au/Al_2O_3 and Au/silicalite-1 supported catalysts.[31, 32] This also confirms that the very thin microporous zeolite shell does not limit the activity of the catalyst.

II.5.2. Selective CO oxidation over Pt@Sil-1

One of the objectives in WP2 of CARENA project (details in chapter 1) is to develop catalysts for the selective CO removal in propylene and propane gas mixture. Herein, 0.9-Pt@Sil-1 (Fig.10) has been tested in the catalytic CO oxidation in the absence and in the presence of propylene. Catalytic data are compared with those obtained on the other two catalysts: 0.90 wt. % Pt supported silicalite-1 (Pt/S-1) and a commercially available catalyst Pt/SiO_2.

II.5.2.1. Textural properties of reference Pt-supported catalysts

Pt/Sil-1 is prepared by directly reducing Pt-impregnated zeolite crystals at 600°C (with a heating ramp 5°C/min) under H_2 (details in experimental chapter). TEM images show that a significant proportion of Pt particles are on the external surface of zeolite crystals; a possible reason may be that during heat treatment Pt atoms and/or cluster diffuse to the surface through the zeolite channels and grow in size (Fig. 26). However, a small percentage of Pt particles is inside zeolite crystals with a diameter between 1 to 2 nm (indicated by the star in the distribution histogram), as already observed for Au-containing samples. However, Au samples were gently reduced in H_2 (at 350°C with a heating ramp 1°C/min) to keep most of the Au particles inside the crystals.

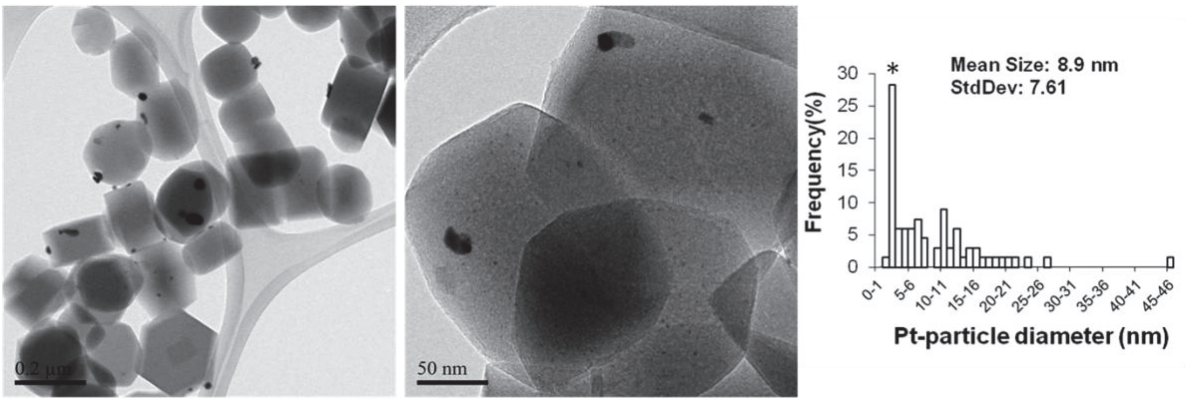

Figure 26: TEM images and particle size distribution of Pt/Sil-1 catalyst, * in the particle size distribution indicating the particles embedded in zeolite crystals.

A commercial Pt/SiO_2-C (C for commercial) supported catalyst obtained from Sigma-Aldrich (0.71 wt. % Pt, Fig. 27) has been used as a second reference catalyst.

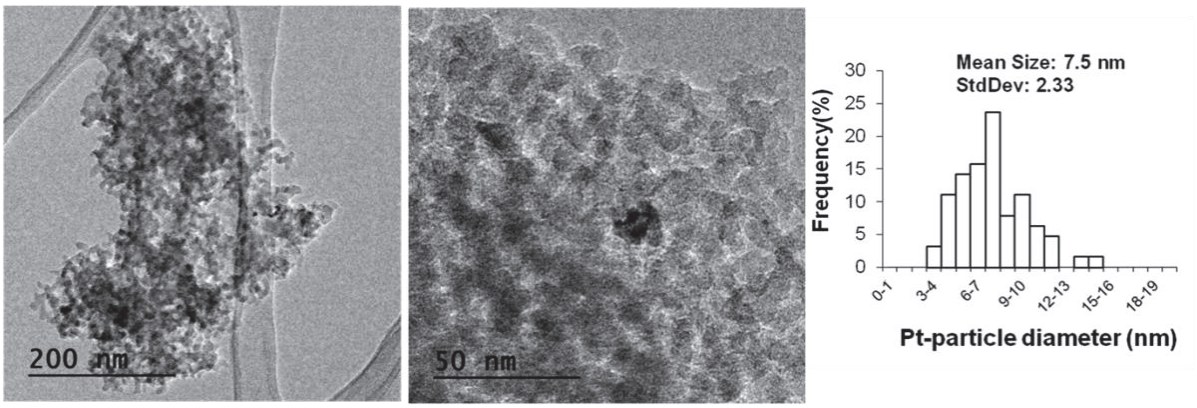

Figure 27: TEM images and particle size distribution of Pt/SiO_2-C catalyst.

The three catalysts are quite similar in terms of Pt loading and mean Pt particle sizes which are 11.4 nm, 8.9 nm and 7.5 nm for Pt@Sil-1, Pt/Sil-1 and Pt/SiO_2-C, respectively (Table 2). They differ mainly on the location of the Pt nanoparticles. In Pt@Sil-1, Pt particles are encapsulated inside a hollow silicalite-1 shells whereas in the other two reference catalysts, most of the particles are on the outer surface of the supports and then directly accessible to the gas phase.

Table 2: Characterization of the metallic phases of Pt zeolites and Pt/SiO_2-C samples.

Sample Name	Pt loading (wt. %)	Particle size (nm)	Metal dispersion (%)
Pt@Sil-1	0.88	11.4	11.4
Pt/S-1	0.90	8.9	10.5*
Pt/SiO_2-C	0.71	7.5	15.2

***Distribution is not homogeneous due to two different populations of particles (see Fig. 26).**

II.5.2.2. CO oxidation over three Pt based catalysts

CO oxidation was carried out in a fixed bed reactor with stream compositions (vol. %) 2% CO, 2% O_2 and balance of N_2. As a consequence, O_2 is in excess since the theoretical O_2 conversion is only 50% compared to CO ($2CO + O_2 \rightarrow 2CO_2$). The catalysts mass was fixed at 50 mg for the three Pt based catalysts. All catalysts fully convert CO at high temperature (Fig. 28) with light-off temperatures (temperature at which conversion is 50% of the maximum conversion) between 270 and 310°C, in

good agreement with data from the literature.[39] Meanwhile O_2 conversions reach a plateau at 50%, in agreement with stoichiometry of the reaction (Fig. 28).

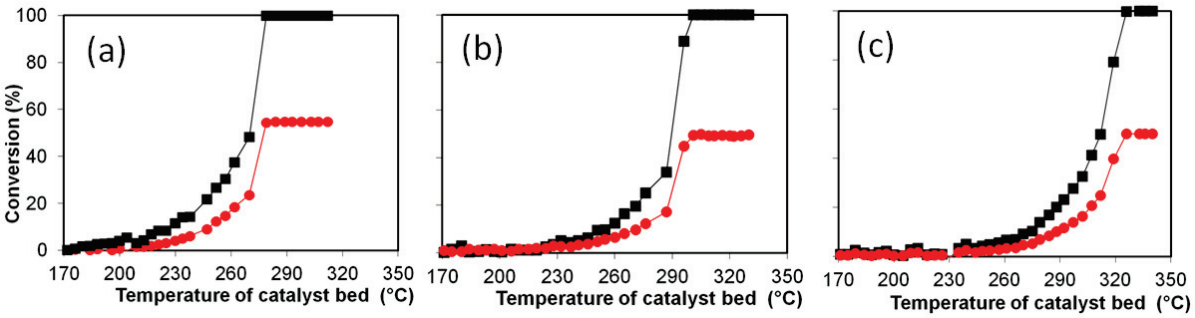

Figure 28: Reactant conversions as function of catalyst bed temperature over 0.9-Pt@Sil-1 (a), Pt/S-1(b) and Pt/SiO_2-C (c); symbols represented :(■) CO conversion, (●) O_2 conversion in CO oxidation.

Light-off temperatures increase in the order: Pt@Sil-1 ‹ Pt/Sil-1 ‹ Pt/SiO_2-C (see Fig. 28 and Table 3).

Table 3: Light-off temperatures of CO oxidation over Pt zeolites and Pt/SiO_2-C catalysts

Catalyst	Mass of Pt (mg)	T(°C)
Pt@Sil-1	0.44	270
Pt/S-1	0.45	290
Pt/SiO_2-C	0.35	310

The origin of the small variation of the light-off temperature observed for the three samples may be due to the slightly different Pt loading used in the tests, i.e. 0.44 mg, 0.45 mg, 0.35 mg for Pt@Sil-1, Pt/Sil-1 and Pt/SiO_2-C, respectively (Table 3). Thus, CO oxidations catalyzed by different amounts of 0.9-Pt@Sil-1 Pt were carried out to evaluate the influence of Pt loading on reactant conversion.

II.5.2.3. CO oxidation over different amounts of 0.9-Pt@Sil-1 catalyst

CO conversion curves show that the light-off temperature decreases when the mass of metal increases from 0.05 mg to 0.43 mg (Fig. 29, Table 4). A similar trend was observed for the temperature at which CO is fully converted. The larger the amount of catalyst used, the lower the temperature to reach complete CO conversion, thus, confirmed the small variation of the light-off temperature observed over the three samples in CO oxidation reactions (Table 3).

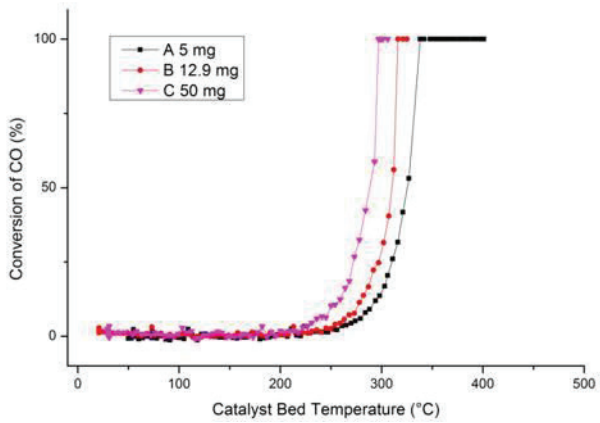

Figure 29: Oxidation of CO over different amounts of 0.9-Pt@Sil-1 catalyst.

Table 4: The light-off and full conversion temperatures over different amounts of 0.9-Pt@Sil-1 catalysts

Catalyst mass (mg)	Mass of Pt (mg)	Light off temperature (°C)	Full CO conversion (°C)
5.4	0.05	325	338
12.9	0.11	310	315
50	0.43	276	297

II.5.2.4. CO oxidation in the presence of propylene over three Pt based catalysts

CO oxidation over Pt catalysts was performed subsequently in the presence of propylene; the compositions (vol. %) of the stream was 2% CO, 2% C_3H_6, 2% O_2 and balance of N_2. Under such conditions, there is not enough oxygen to fully oxidize CO and propylene since the combustion of one mole of propylene necessitates 4.5 moles of oxygen ($C_3H_6 + CO + 5O_2 \rightarrow 4CO_2 + 3H_2O$).

Reactant conversions as function of catalyst bed temperature are given in Fig. 30. Light-off temperatures were all moved to higher temperatures by approx. 40°C as compared to reactions performed in the absence of propylene (Fig. 30, Table 5). The catalyst 0.9-Pt@Sil-1 remains very active with a maximum CO conversion of 92% at 360°C. However, maximum CO conversions reach only 35-40% at 370°C over Pt/Sil-1 and Pt/SiO_2-C catalysts with light-off temperatures of ca. 340°C. Pt/Sil-1 and Pt/SiO_2-C catalysts both exhibit very similar results with a significant deactivation for CO oxidation in the presence of propylene. Voltz et al. have reported that propylene partially prevents the adsorption of CO on Pt particles and acts as a surface reversible poison for CO oxidation.[22] For

Pt/SiO_2-C, all Pt particles are directly accessible to the gas phase and therefore subject to propylene poisoning. The same applies for Pt/S-1, in which most of the Pt particles are located on the external surfaces of zeolite crystal, activities of the very small particle encapsulated in the zeolite being probably limited by diffusion limitations. Therefore, 92% CO conversion observe over 0.9-Pt@Sil-1 is approximately twice that obtained over reference catalysts.

For all three catalysts, the propylene conversion is very small at 350°C, with values of 2.4%, 4% and 1.3% over Pt@Sil-1, Pt/Sil-1 and Pt/SiO_2-C catalysts, respectively (Fig. 30). Moreover, we do not observe any change in the color of the catalyst before and after reaction. The carbon balance for each reaction is generally above 98% (details in experimental chapter), which suggests that the amount of coke formed is negligible.

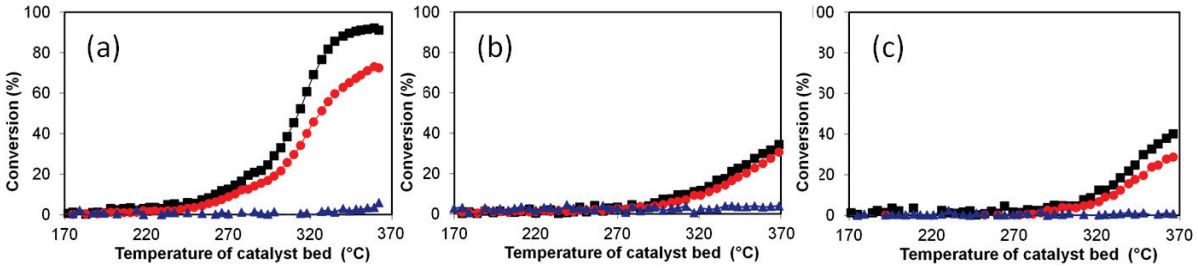

Figure 30: Reactant conversions as function of catalyst bed temperature over 0.9-Pt@Sil-1 (a), Pt/S-1(b) and Pt/SiO_2-C (c) (■) CO conversion, (●) O_2 conversion, (▲) C_3H_6 conversion in CO oxidation in the presence of propylene.

Table 5: Light-off temperatures and TOFs for CO oxidation in the presence of C_3H_6 over Pt-zeolites and Pt/SiO_2-C catalysts

Catalyst	Mass of Pt (mg)	T(°C)	ΔT[a]	TOFs (280°C)
Pt@Sil-1	0.44	310	40	2314
Pt/S-1	0.45	336	46	307
Pt/SiO_2-C	0.35	340	40	134

a: ΔT represents the difference in light-off temperatures between CO oxidation in the presence and in the absence of propylene over these three catalysts.

At 280°C, TOF of 0.9-Pt@Sil-1 is approximately 8 and 12 times higher than those of Pt/Sil-1 and Pt/SiO_2-C (Table 5). The relatively higher activity of Pt/Sil-1 compared to Pt/SiO_2-C may result from the slightly greater Pt loading and the presence of small particles in the zeolite crystals which access is limited by diffusion in the micropores (Fig.26, Table 3). In contrast to supported catalysts, 0.9-Pt@Sil-1 shows a high CO conversion, indicating that the zeolite shells limit Pt poisoning by propylene while maintaining a high accessibility to carbon monoxide.

The kinetic diameters of CO (0.376 nm) and C_3H_6 (0.45 nm) are both smaller than the pore size of silicalite-1 (0.51 nm x 0.55 nm). Hence catalytic results cannot be explained by steric exclusion of the molecules by the micropores of the zeolite but rather by differences in adsorption and diffusion properties between the molecules in the zeolite shell. This was supported by the studies adsorption and diffusion of CO and propylene through hollow silicalite-1 crystals.

For a silicalite-1 membrane, it is generally accepted that the separation mechanism of a mixture of substrates depends first on coverage concentrations of the different species.[40, 41] At high coverage, the most strongly adsorbed substrate prevents other substrates from adsorption and thus diffusion.

II.5.2.5. Adsorption study of CO and C_3H_6 through hollow silicalite-1

CO and propylene adsorption isotherms in hollow silicalite-1 were measured at 30°C (Fig. 31) and fitted by a Langmuir model (black square in Fig. 31) for the estimation of adsorption parameters.[42] The isosteric heat (ΔH^0) used to build the Langmuir model and the saturation capacity (q_{sat}) measured by the adsorption isotherms are similar to those in the literature (shown in Table 6).

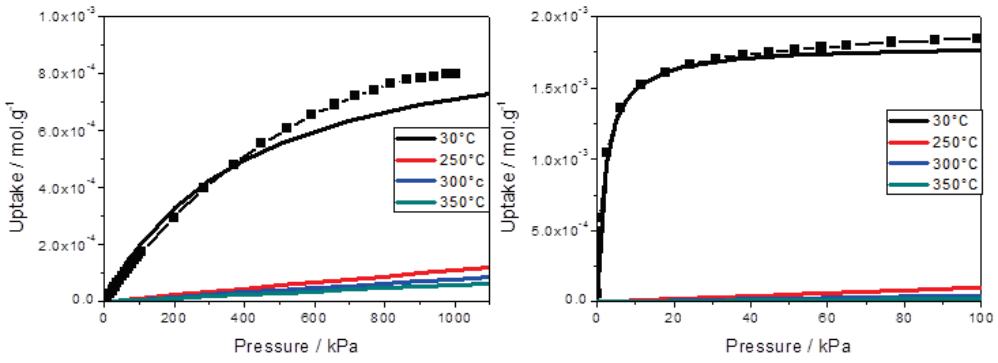

Figure 31: CO (left) and C_3H_6 (right) adsorption isotherms over hollow silicalite-1. Experimental data at 30°C (full line), fitted data at 30°C (black square) and simulated data at 250, 300 and 350°C.

Then adsorption isotherms of reaction at higher temperatures (250, 300 and 350°C) were estimated from Langmuir models (Fig. 31, calculation details in experimental chapter). CO and propylene coverages (the fraction of adsorption sites occupied) were estimated at reaction conditions, for which they are all lower than 1% (Table 7). As a consequence, competitive adsorption can be ruled out for the limitation of the transport of propylene into hollow silicalite-1.

Table 6: Parameter estimations of the Langmuir models obtained by fitting experimental isotherms.

Parameter	Δ H	q_{sat}	Ref
Unit	kJ.mol^{-1}	mmol.g^{-1}	-
CO	-18.0	1.0	this study
	-18.0	2.0	Ref [40]
C_3H_6	-40.0	1.8	this study
	-37.8	1.2	Ref [41]

Table 7: Coverage estimations at room temperature and reaction conditions for a partial pressures of 2 kPa for both CO and propylene.

Temperature	30°C	250°C	300°C	350°C
Coverage	%	%	%	%
CO	<1	<1	<1	<1
C_3H_6	90.4	1.2	<1	<1

II.5.2.6. Diffusion study of CO and C_3H_6 through hollow silicalite-1

The second mechanism of membrane permselectivity is driven by differences in diffusion rates which are mainly governed by the size of the substrate.[40, 42] The effective mass transfer coefficients (Kap) of CO and propylene were measured at low coverage in hollow silicalite-1 in a volumetric measurement system by applying the Linear Driving Force Model (LDF) (Fig. 32).[43] The estimated Kap was 200 times greater for CO (1.41) than for propylene (6.61×10^{-3}) over hollow silicalite-1, indicating that at room temperature C_3H_6 diffuses more than 200 times slower than CO. Even though calculations were not performed at the reaction temperature, we may assume that the difference between Kap values still exists at higher reaction temperature, which could explain the permselective mechanism of the zeolite shell and the resistance of the 0.9-Pt@Sil-1 catalyst towards poisoning.

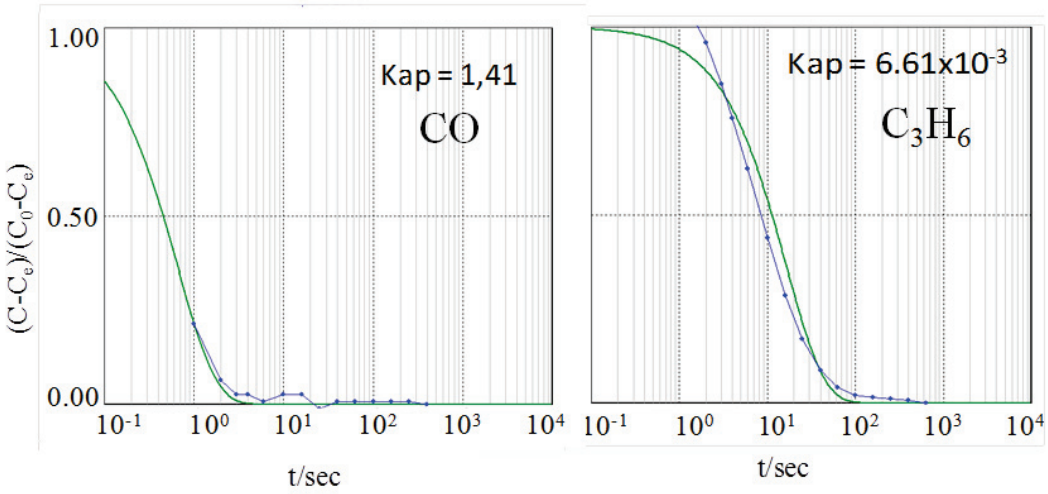

Figure 32: Relaxation pressure in the adsorption of CO (left) and C_3H_6 (right) at 30°C of experimental data (blue squares) and LDF model fit (green line), (corresponding at coverage of 10%).

Since C_3H_6 (kinetic diameter: 0.45 nm) can diffuse through the silicalite-1 membrane (pore size approx. 0.55 nm) it constitutes a potential poison for platinum particles. By contrast to CO which is depleted by oxidation; the concentration of C_3H_6 increases with time inside the hollow zeolite. However, the evolution with time of the partial pressure of C_3H_6 and other components along the reaction in the zeolite cavity would require the modeling of the catalytic process and all transport phenomena including CO, CO_2 and C_3H_6 diffusion as well as CO_2 retro-diffusion. Such a complex simulation was not carried out during this PhD work.

II.5.3. Shape-selective hydrogenation of substituted aromatics

Reactant size selectivity of metal nanoparticle in hollow zeolite yolk-shell catalyst was estimated in the hydrogenation of toluene (methylbenzene) and mesitylene (1, 3, 5- trimethylbenzene), two substituted aromatics with kinetic diameters of 0.61 and 0.87 nm, respectively.

II.5.3.1. Prepared Pt/SiO_2-P reference catalyst

0.9-Pt@Sil-1 was used as catalyst and the catalytic performance was compared to that of a conventional Pt sample supported on high surface area silica (denoted Pt/SiO_2-P, P for prepared). The conventional catalyst, which preparation details are given in the experimental chapter, was synthesized by impregnation followed a reduction process. TEM image shows uniform Pt particles on the surface of SiO_2 with an average diameter of about 3 nm and a quite narrow particle size distribution (Fig. 33). The dispersion of Pt particles is estimated to 20% using a cub-octahedral model and a calculation method according to Van Hardeveld and Hartog.[30]

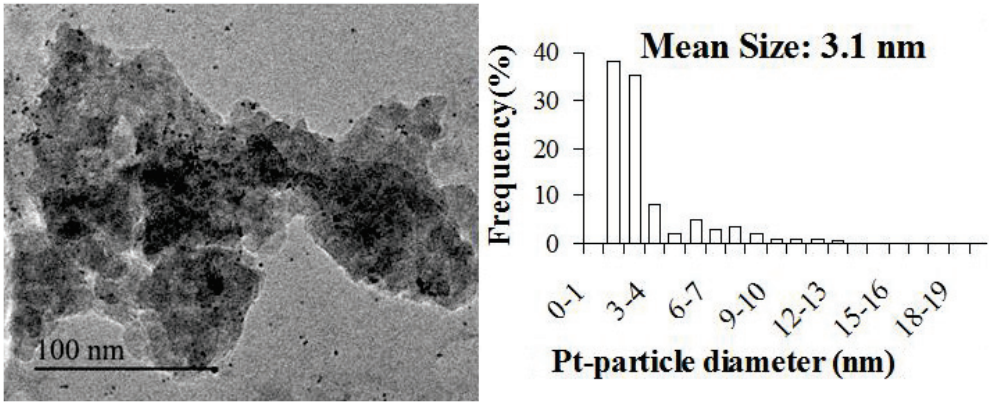

Figure 33: TEM image and particle size distribution of Pt/SiO_2-P catalyst.

II.5.3.2. Analysis methods of hydrogenation reactions

Toluene and mesitylene hydrogenations were carried out using a tubular quartz plug flow reactor placed in a tubular furnace. The reactor effluent was then diluted and analyzed by Thermo FT-IR spectrophotometer (details in experimental chapter). The proportion of reactants and corresponding saturated products was determined through integration of two zones in the C-H stretching spectral region (Fig 34). For example the characteristic spectral region for toluene is 3150-2990cm^{-1}, while it is only 2905-2820 cm^{-1} for methylcyclohexane (Fig.34-a).

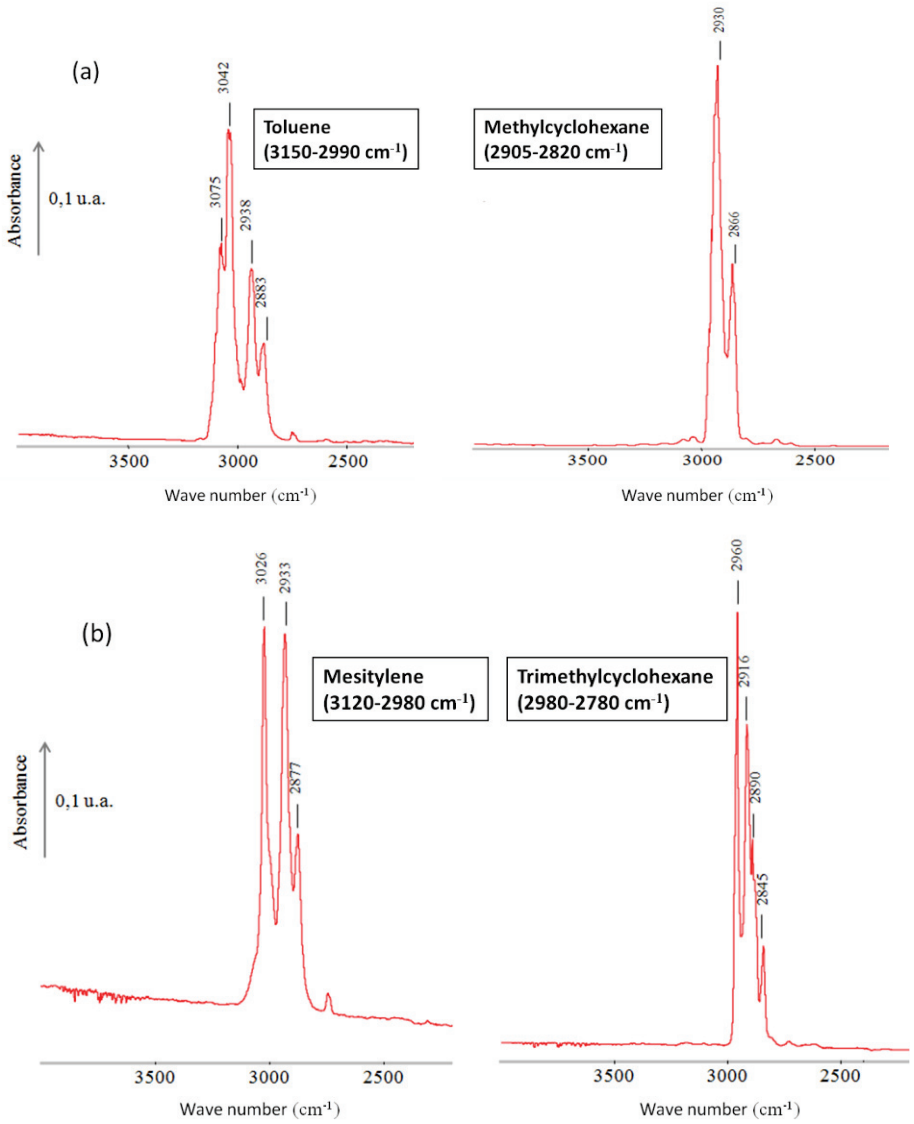

Figure 34: Gas phase FT-IR spectra of aromatics (left) and their corresponding saturated products (right) of toluene (a) and mesitylene (b).

Methylcyclohexane and trimethylcyclohexane were the only products detected during the hydrogenation of toluene and mesitylene. Thus, in the reaction mixture which contains both toluene and methylcyclohexane, part of toluene peaks which overlap with the products region can be calculated from the proportional relationship between the non-overlapped area and the overlapped region from the spectrum of pure toluene on Fig. 34-a.

II.5.3.3. Hydrogenation results over Pt catalysts

The hydrogenation of toluene and mesitylene were first tested over Pt/SiO_2-P catalyst. The FTIR spectra observed at 50 °C are essentially those of aromatic molecules while signals corresponding to saturated molecules are superimposed at higher temperatures (Fig. 35).

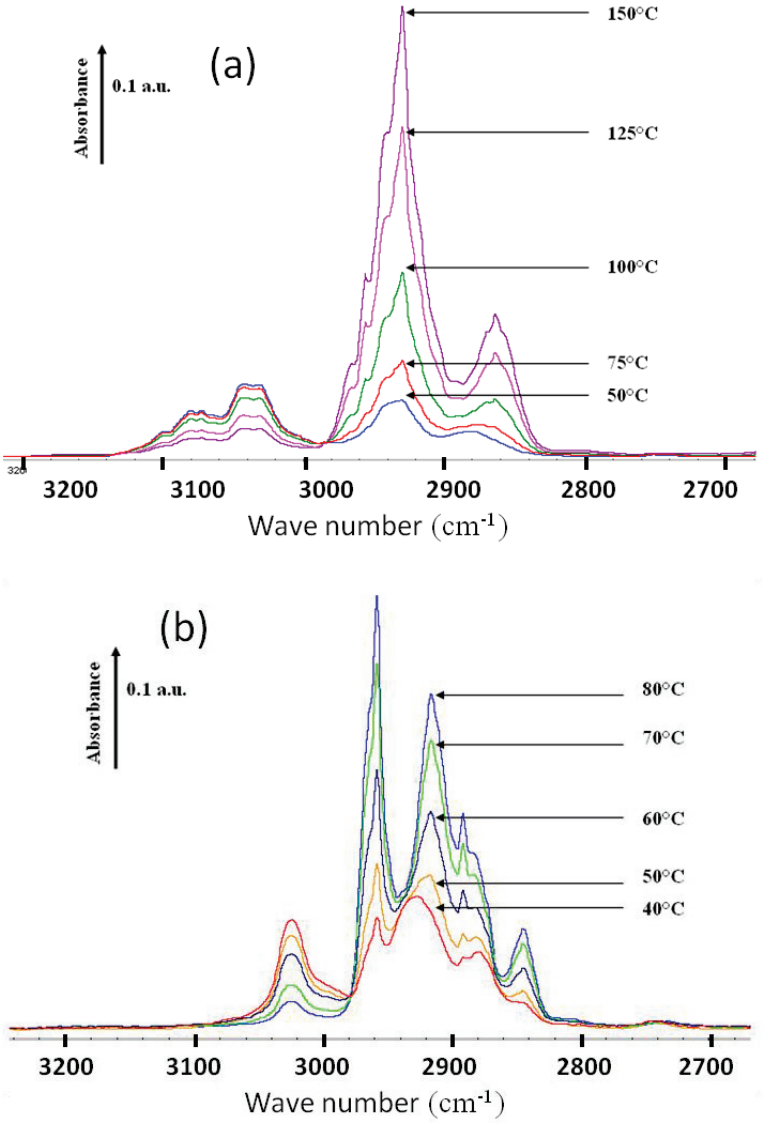

Figure 35: FT-IR spectra obtained at various temperatures of the reactor during the hydrogenation of toluene (a) and mesitylene (b) over the 0.5%-Pt/SiO_2-P catalyst.

The hydrogenation of toluene and mesitylene were also evaluated over 0.9-Pt@Sil-1. Conversions obtained over these two catalysts are plotted in Fig. 36 as a function of temperature.

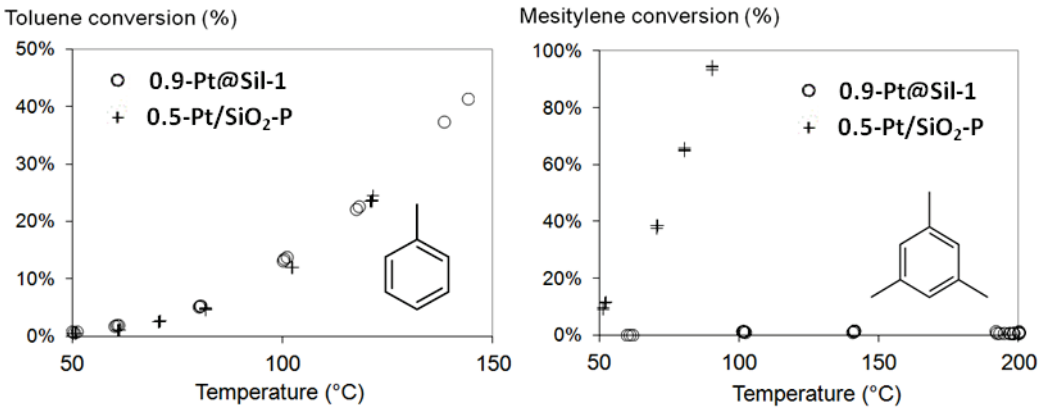

Figure 36: Conversion of toluene (left) and mesitylene (right) over 0.9-Pt@Sil-1 (o) and Pt/SiO_2-P (+) catalysts. Toluene pressure = 903 Pa, balance H_2; Mesitylene pressure = 61 Pa, balance H_2.

Fig. 36-left shows that 0.9-Pt@Sil-1 and Pt/SiO_2-P convert toluene in a very similar way. Indeed, the effect of a higher Pt loading on the 0.9-Pt@Sil-1 (about twice that of Pt/SiO_2-P) is neutralized by a lower dispersion (approximately half that of Pt/SiO_2-P), and identical turn-over frequencies TOFs (turn-over frequencies, expressed as molecules of toluene converted per second per surface Pt atoms, calculation details in experimental part) were obtained for these two catalysts in the hydrogenation of toluene (Fig. 37). The values of turnover frequencies (e.g. 6×10^{-2} s^{-1} at 80 °C) are consistent with those obtained for toluene hydrogenation on other Pt-based catalysts under similar experimental conditions.[44,45]

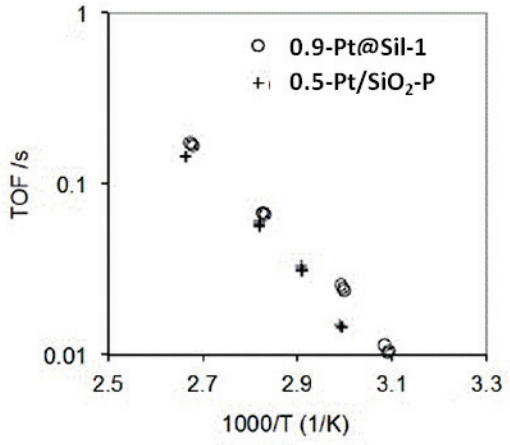

Figure 37 : TOF versus reciprocal temperature for toluene hydrogenation at various temperatures over 0.9-Pt@Sil-1 (o) and Pt/SiO_2-P (+)catalysts.

Similarly, the apparent activation energies measured here (55 ±3 kJ mol^{-1}, Fig. 38) are similar to those reported in the literature.[45] These data indicate that the silicate-1 hollow box does not significantly hinder either the transport of toluene or that of the reaction product methylcyclohexane.

The case of mesitylene was dramatically different. Mesitylene was readily fully hydrogenated to trimethylcyclohexane over the conventional silica-supported Pt sample, while the conversion was negligible over 0.9-Pt@Sil-1 (Fig. 36- right).

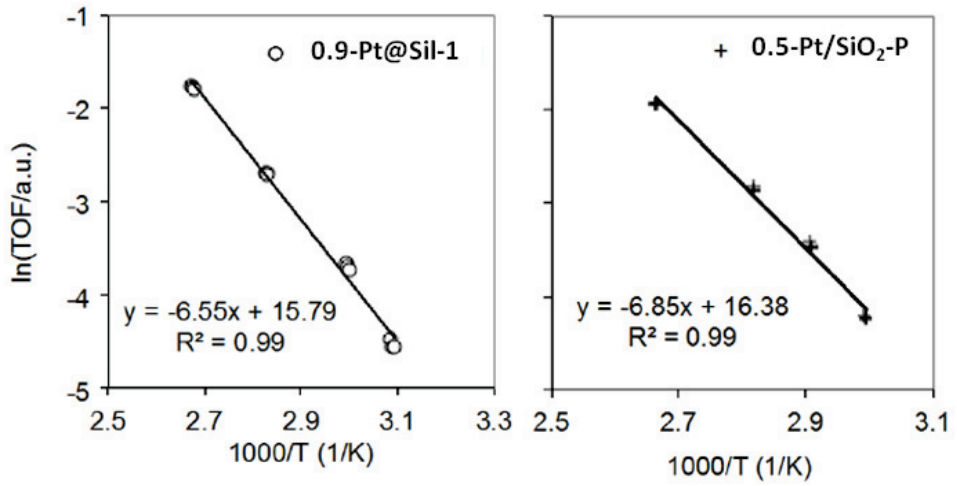

Figure 38: Arrhenius-type plot relating the logarithm of TOF versus the reciprocal temperature for the hydrogenation of toluene over the 0.9-Pt@Sil-1(left) and 0.5-Pt/SiO_2-P (right). The corresponding apparent activation energy is 54 kJ mol^{-1} and 57 kJ mol^{-1}, respectively.

TOFs obtained in the mesitylene hydrogenation over Pt/SiO_2-P were estimated to be 7.6×10^{-3} s^{-1}at 41 °C. Over Pt/SiO_2-P for toluene hydrogenation, TOF would be expected to be around 4×10^{-3} s^{-1} at 41 °C, suggesting that TOFs for hydrogenation of toluene and mesitylene on the Pt/SiO_2-P were of the same order of magnitude. All the TOFs discussed here were measured for conversions lower than 15%.

The above results indicate that the rate of mesitylene hydrogenation over 0.9-Pt@Sil-1 was at least two orders of magnitude lower than that on Pt/SiO_2-P. We can therefore conclude that the vast majority (at least 99%) of the observed Pt particles were indeed inside the microporous hollow boxes and inaccessible to the bulky molecules.

II.5.3.4. Adsorption isotherms of toluene and mesitylene on hollow silicalite-1

The origin of the above size selectivity is due to the fact that mesitylene is too large to penetrate the zeolite micropores. N_2 physisorption isotherms and the corresponding t-plots revealed that hollow zeolites are free of cracks and mesoporous pinholes.[9] The channel dimensions of silicalite-1 are about 0.56 x 0.53 nm and toluene can enter them while mesitylene is too large and is therefore excluded from the micropores. This was confirmed by adsorption isotherms of both molecules on Pt-free silicalite-1 hollow crystals (Fig. 39). The uptake of toluene and the size exclusion of the mesitylene

confirm that each hollow box entirely consists of microporous zeolite, without any significant mesoporosity.

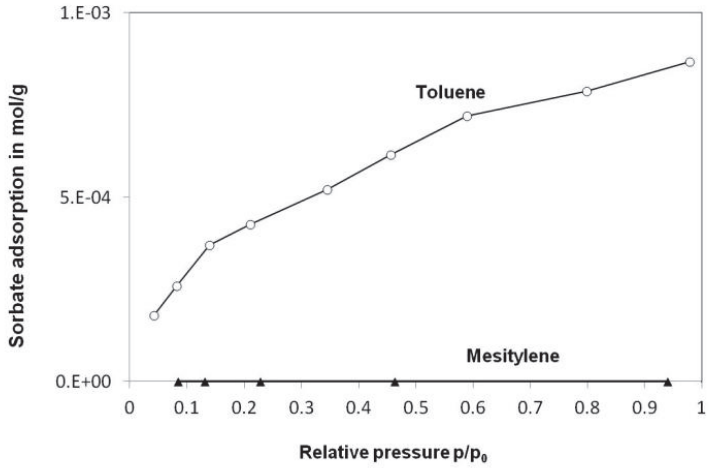

Figure 39: Adsorption isotherms of toluene and mesitylene on the silicalite-1 hollow crystals at 30°C.

Furthermore, it is known that p-xylene (kinetic diameter= 0.58 nm) can readily diffuse in MFI-type materials while the bulker o- and m-xylene isomers (ca. 0.68 nm) are greatly hindered to structure of MFI zeolites.[44, 46] Therefore, we propose that the hollow zeolite crystal operates as a zeolite oriented membrane with a cut-off at about 0.7 nm, corresponding to the maximum size to access the embedded Pt.

III.Conclusion

The original ship-in-a-bottle type synthesis enabled us to prepare isolated gold nanoparticles with size control below 10 nm and narrow particle size distributions. The desired particle size could be obtained by readily adjusting the concentration of the starting gold solution. This pathway is straightforward since the preparation does not require the synthesis of gold colloids and/or core-shell gold precursors.[47] In addition, our novel method is scalable unlike physical methods such as laser ablation.[48, 49]

By modifying the synthesis protocol it was possible to form many cavities in large zeolites crystals (0.5-1 µm) and to encapsulate hundreds of Au and Pt nanoparticles isolated from each other by zeolite walls. The synthesis method could be easily extended to other kinds of noble metal such as Pt, Pd and Ag.

A fast acquisition EMTE technique has been applied in Ag@Sil-1 material. The TOMO film and reconstruction structures provided the 3D yolk-shell morphology of the material, confirming that less than 4% of Ag particles were detected outside zeolite cavities. Additionally, the particle sintering process has been observed by in-situ heating under O_2 atmosphere and a mechanism has been proposed.

In the case of Pt@Sil-1 materials, we have shown that a single crystal zeolite shell can act as a permselective membrane which prevents the encapsulated metal nanoparticles from poisoning. In the case of CO oxidation in presence of propylene, the separation mechanism is driven by the difference in the diffusion rates between CO and propylene in zeolite micropores, the latter diffusing 200 times slower at room temperature. Furthermore, a molecular sieving driven selectivity could also be observed on Pt@Sili-1 with a cut-off of 0.7 nm in the hydrogenation reactions.

This series of well controlled nanosized noble particles encapsulated in microporous hollow silicalite-1 opens new perspectives in catalysis since they can be used in harsh conditions without the issues of growth and leaching. They could also be applied as shape and/or size selective catalysts in a wide range of catalytic systems.

Bibliography

1. Bell, A.T. The impact of nanoscience on heterogeneous catalysis. *Science* **299**, 1688-1691 (2003).

2. Bond, G.C. The Origins of Particle-Size Effects in Heterogeneous Catalysis. *Surf. Sci.* **156**, 966-981 (1985).

3. M. Boudart Catalysis by Supported Metals, Vol. 20. (1969).

4. Haruta, M. Size- and support-dependency in the catalysis of gold. *Catal. Today* **36**, 153-166 (1997).

5. Hashmi, A.S.K. & Hutchings, G.J. Gold catalysis. *Angew. Chem. Int. Ed.* **45**, 7896-7936 (2006).

6. Corma, A. & Garcia, H. Supported gold nanoparticles as catalysts for organic reactions. *Chem. Soc. Rev.* **37**, 2096-2126 (2008).

7. Wu, C., Lim, Z.-Y., Zhou, C., Wang, W.G., Zhou, S., Yin, H. & Zhu, Y. A soft-templated method to synthesize sintering-resistant Au-mesoporous-silica core-shell nanocatalysts with sub-5 nm single-cores. *Chem. Commun.* **49**, 3215-3217 (2013).

8. Chi, Y.S., Lin, H.P. & Mou, C.Y. CO oxidation over gold nanocatalyst confined in mesoporous silica. *Appl. Catal., A* **284**, 199-206 (2005).

9. Kerdi, F., Caps, V. & Tuel, A. Mesostructured Au/C materials obtained by replication of functionalized SBA-15 silica containing highly dispersed gold nanoparticles. *Microporous Mesoporous Mater.* **140**, 89-96 (2011).

10. Arnal, P.M., Comotti, M. & Schüth, F. High-temperature-stable catalysts by hollow sphere encapsulation. *Angew. Chem. Int. Ed.* **45**, 8224-8227 (2006).

11. Lee, I., Joo, J.B., Yin, Y. & Zaera, F. A Yolk@Shell Nanoarchitecture for Au/TiO2 Catalysts. *Angew. Chem. Int. Ed.* **50**, 10208-10211 (2011).

12. Joo, S.H., Park, J.Y., Tsung, C.-K., Yamada, Y., Yang, P. & Somorjai, G.A. Thermally stable Pt/mesoporous silica core-shell nanocatalysts for high-temperature reactions. *Nat. Mater.* **8**, 126-131 (2009).

13. Galeano, C., Guettel, R., Paul, M., Arnal, P., Lu, A.-H. & Schüth, F. Yolk-Shell Gold Nanoparticles as Model Materials for Support-Effect Studies in Heterogeneous Catalysis: Au, @C and Au, @ZrO2 for CO Oxidation as an Example. *Chem. Eur. J.* **17**, 8434-8439 (2011).

14. Ikeda, S., Ishino, S., Harada, T., Okamoto, N., Sakata, T., Mori, H., Kuwabata, S., Torimoto, T. & Matsumura, M. Ligand-Free Platinum Nanoparticles Encapsulated in a Hollow Porous Carbon Shell as a Highly Active Heterogeneous Hydrogenation Catalyst. *Angew. Chem. Int. Ed.* **45**, 7063-7066 (2006).

15. Miyamoto, M., Kamei, T., Nishiyama, N., Egashira, Y. & Ueyama, K. Single Crystals of ZSM-5/Silicalite Composites. *Adv. Mater.* **17**, 1985-1988 (2005).

16. Nishiyama, N., Ichioka, K., Park, D.-H., Egashira, Y., Ueyama, K., Gora, L., Zhu, W., Kapteijn, F. & Moulijn, J.A. Reactant-Selective Hydrogenation over Composite Silicalite-1-Coated Pt/TiO2 Particles. *Ind. Eng. Chem. Res.* **43**, 1211-1215 (2004).

17. He, J., Yoneyama, Y., Xu, B., Nishiyama, N. & Tsubaki, N. Designing a capsule catalyst and its application for direct synthesis of middle isoparaffins. *Langmuir* **21**, 1699-1702 (2005).

18. Sartipi, S., van Dijk, J.E., Gascon, J. & Kapteijn, F. Toward bifunctional catalysts for the direct conversion of syngas to gasoline range hydrocarbons: H-ZSM-5 coated Co versus H-ZSM-5 supported Co. *Appl. Catal., A* **456**, 11-22 (2013).

19. Sartipi, S., Makkee, M., Kapteijn, F. & Gascon, J. Catalysis engineering of bifunctional solids for the one-step synthesis of liquid fuels from syngas: a review. *Catal. Sci. Technol.* **4**, 893-907 (2014).

20. Collier, P., Golunski, S., Malde, C., Breen, J. & Burch, R. Active-site coating for molecular discrimination in heterogeneous catalysis. *J. Am. Chem. Soc.* **125**, 12414-12415 (2003).

21. Devi, R.N., Meunier, F.C., Le Goaziou, T., Hardacre, C., Collier, P.J., Golunski, S.E., Gladden, L.F. & Mantle, M.D. Modulating the Selectivity for CO and Butane Oxidation over Heterogeneous Catalysis through Amorphous Catalyst Coatings. *J. Phys. Chem. C* **112**, 10968-10975 (2008).

22. Voltz, S.E., Morgan, C.R., Liederman, D. & Jacob, S.M. Kinetic study of carbon monoxide and propylene oxidation on platinum catalysts. *Ind. Eng. Chem. Prod. Res. Dev* **12**, 294-301 (1973).

23. Rioux, R.M., Komor, R., Song, H., Hoefelmeyer, J.D., Grass, M., Niesz, K., Yang, P. & Somorjai, G.A. Kinetics and mechanism of ethylene hydrogenation poisoned by CO on silica-supported monodisperse Pt nanoparticles. *J. Catal.* **254**, 1-11 (2008).

24. Patience, G.S., Benamer, A., Chiron, F.X., Shekari, A. & Dubois, J.L. Selectively combusting CO in the presence of propylene. *Chem. Eng. Process. Process Intensif.* **70**, 162-168 (2013).

25. Koermer, G.S. & Hratko, L., Vol. US 6,548,446/B1 **2003**).

26. Anderson, M.W., Agger, J.R., Hanif, N. & Terasaki, O. Growth models in microporous materials. *Microporous Mesoporous Mater.* **48**, 1-9 (2001).

27. Agger, J.R., Hanif, N. & Anderson, M.W. Fundamental Zeolite Crystal Growth Rates from Simulation of Atomic Force Micrographs. *Angew. Chem. Int. Ed.* **40**, 4065-4067 (2001).

28. Wang, Y. & Tuel, A. Nanoporous zeolite single crystals: ZSM-5 nanoboxes with uniform intracrystalline hollow structures. *Microporous Mesoporous Mater.* **113**, 286-295 (2008).

29. Wang, Y., Lin, M. & Tuel, A. Hollow TS-1 crystals formed via a dissolution-recrystallization process. *Microporous Mesoporous Mater.* **102**, 80-85 (2007).

30. Van Hardeveld, R. & Hartog, F. The statistics of surface atoms and surface sites on metal crystals. *Surf. Sci.* **15**, 189-230 (1969).

31. Groen, J.C. & Perez-Ramirez, J. Critical appraisal of mesopore characterization by adsorption analysis. *Appl. Catal., A* **268**, 121-125 (2004).

32. Kang, Y.J., Shan, W., Wu, J.Y., Zhang, Y.H., Wang, X.Y., Yang, W.L. & Tang, Y. Uniform nanozeolite microspheres with large secondary pore architecture. *Chem. Mater.* **18**, 1861-1866 (2006).

33. Dong, A.G., Wang, Y.J., Wang, D.J., Yang, W.L., Zhang, Y.H., Ren, N., Gao, Z. & Tang, Y. Fabrication of hollow zeolite microcapsules with tailored shapes and functionalized interiors. *Microporous Mesoporous Mater.* **64**, 69-81 (2003).

34. Quinet, E., Morfin, F., Diehl, F., Avenier, P., Caps, V. & Rousset, J.-L. Hydrogen effect on the preferential oxidation of carbon monoxide over alumina-supported gold nanoparticles. *Appl. Catal., B* **80**, 195-201 (2008).

35. Sayah, E., Brouri, D. & Massiani, P. A comparative in situ TEM and UV–visible spectroscopic study of the thermal evolution of Ag species dispersed on Al2O3 and NaX zeolite supports. *Catal. Today* **218–219**, 10-17 (2013).

36. Tuel, A. & Taarit, Y.B. Synthesis and characterization of titanium silicalite TS-1 prepared using phosphonium ions. *Zeolites* **14**, 272-281 (1994).

37. Datye, A.K., Xu, Q., Kharas, K.C. & McCarty, J.M. Particle size distributions in heterogeneous catalysts: What do they tell us about the sintering mechanism? *Catal. Today* **111**, 59-67 (2006).

38. Quinet, E., Piccolo, L., Morfin, F., Avenier, P., Diehl, F., Caps, V. & Rousset, J.-L. On the mechanism of hydrogen-promoted gold-catalyzed CO oxidation. *J. Catal.* **268**, 384-389 (2009).

39. Alayon, E.M.C., Singh, J., Nachtegaal, M., Harfouche, M. & Van Bokhoven, J.A. On highly active partially oxidized platinum in carbon monoxide oxidation over supported platinum catalysts. *J. Catal.* **263**, 228-238 (2009).

40. Savitz, S., Myers, A.L. & Gorte, R.J. Calorimetric Investigation of CO and N2 for Characterization of Acidity in Zeolite H-MFI. *J. Phys. Chem. B* **103**, 3687-3690 (1999).

41. Hampson, J.A. & Rees, L.V.C. Adsorption of ethane and propane in silicalite-1 and zeolite NaY: determination of single components, mixture and partial adsorption data using an isosteric system. *J. Chem. Soc., Faraday Trans.* **89**, 3169-3176 (1993).

42. van de Graaf, J.M., Kapteijn, F. & Moulijn, J.A. Modeling permeation of binary mixtures through zeolite membranes. *AIChE J.* **45**, 497-511 (1999).

43. Sircar, S. & Hufton, J. Why does the linear driving force model for adsorption kinetics work? *Adsorption* **6**, 137-147 (2000).

44. Meunier, F.C., Verboekend, D., Gilson, J.-P., Groen, J.C. & Perez-Ramirez, J. Influence of crystal size and probe molecule on diffusion in hierarchical ZSM-5 zeolites prepared by desilication. *Microporous Mesoporous Mater.* **148**, 115-121 (2012).

45. Rousset, J.L., Stievano, L., Aires, F., Geantet, C., Renouprez, A.J. & Pellarin, M. Hydrogenation of toluene over gamma-Al2O3-supported Pt, Pd, and Pd-Pt model catalysts obtained by laser vaporization of bulk metals. *J. Catal.* **197**, 335-343 (2001).

46. Garcia, S.F. & Weisz, P.B. Effective Diffusivities in Zeolites Aromatics in ZSM-5 Crystals. *J. Catal.* **121**, 294-311 (1990).

47. Guettel, R., Paul, M. & Schüth, F. Ex-post size control of high-temperature-stable yolk-shell Au, @ ZrO2 catalysts. *Chem. Commun.* **46**, 895-897 (2010).

48. Hashimoto, S., Uwada, T., Masuhara, H. & Asahi, T. Fabrication of gold nanoparticle-doped zeolite L crystals and characterization by optical microscopy: Laser ablation- and crystallization inclusion-based approach. *J. Phys. Chem. C* **112**, 15089-15093 (2008).

49. Arrii, S., Morfin, F., Renouprez, A.J. & Rousset, J.L. Oxidation of CO on gold supported catalysts prepared by laser vaporization: Direct evidence of support contribution. *J. Am. Chem. Soc.* **126**, 1199-1205 (2004).

Transition metal particles in hollow zeolites:

I. Introduction

In this chapter, we extend the synthesis of such nano-designed catalysts to the particular case of transition metals (Co, Ni, and Cu), which significantly differs from that of noble metal systems. Instead of particles, phyllosilicates were formed during the dissolution-recrystallization step and particles encapsulated in hollow silicalite-1 were only obtained after reduction at higher temperature, typically 750°C.

In addition, bifunctional yolk-shell materials displaying excellent metal nanoparticles dispersion inside ZSM-5 hollow crystals were also prepared. Regular ZSM-5 hollow crystals could be obtained by treating hydrothermally particular ZSM-5 crystals having a non-uniform composition, with an Al-rich periphery and a Si-rich core. The formation of internal cavities involved the preferential desilication of Si-rich domains of the crystals followed by a recrystallization process, resulting in hollow ZSM-5 with the same overall composition as the parent zeolite. The molecular sieving effect of the zeolite shell was evaluated in the hydrogenation of substituted aromatics over Ni particles encapsulated in hollow silicalite-1 materials.

II. Results and discussion

II.1. Cobalt nanoparticles in hollow silicalite-1 (Co@Sil-1)

The silicalite-1 was first impregnated by a cobalt aqueous solution via a wet impregnation method, and then the solid was treated by TPAOH to form hollow structures, following our previous protocol developed for noble metals. However, contrary to noble metals (discussed in chapter 3), cobalt-containing hollow silicalite-1 did not yield nanoparticles after the TPAOH treatment. The color of the sample was gray, indicating the presence of Co species in the crystals but TEM pictures revealed only the presence of dark long fibers covering the internal surface of the cavities (arrows in Fig.1). As previously, samples are further denoted w-metal@Sil-1, w is representing the metal loading (wt. %) detected by ICP.

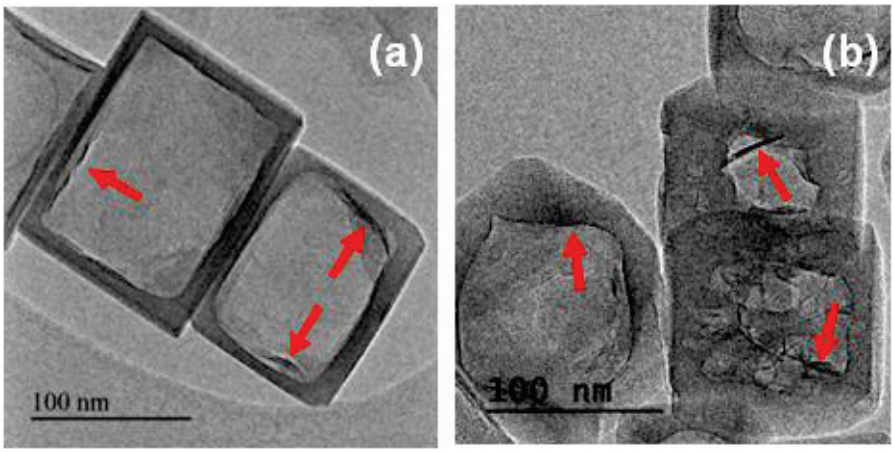

Figure 1: TEM images of 2.5-Co@Sil-1 before reduction. Arrows indicate cobalt phyllosilicates.

This type of fibrous structure is often found in Co/SiO_2 catalysts and corresponds to cobalt phyllosilicates.[1-3] In order to characterize these fibers, EDX and high resolution TEM measurements were carried out on the sample with the highest Co loading (8-Co@Sil-1, Fig.2 and 3) before reduction. In this sample, Co is not only located inside the cavities but also on the external surface of the zeolite crystals (Fig. 2-a). The cobalt phyllosilicate structure was confirmed by the interlayer distance of ca. 0.9-0.95 nm (Fig. 2-b), corresponding to the value generally observed in these structures.[4] EDX spectrum of these fibers (measured area is indicated by the red circle in Fig.2-a) given in Fig.3-b, leads to 26 wt. % Co, 24.5 wt. % Si and 49.5 wt. % O (Table 1), corresponding to the chemical formula $CoSi_2O_5.2H_2O$. The $Si_2O_5^{2-}$ stoichiometry is characteristic of phyllosilicates according to the Nickel-Strunz classification.[5] In addition, we did not observe Co in the zeolite walls (blue circle in Fig.2-a is the EDX detecting area) by EDX analysis (Fig.3-a and Table 1) which suggests that all Co atoms are in the form of Co phyllosilicates.

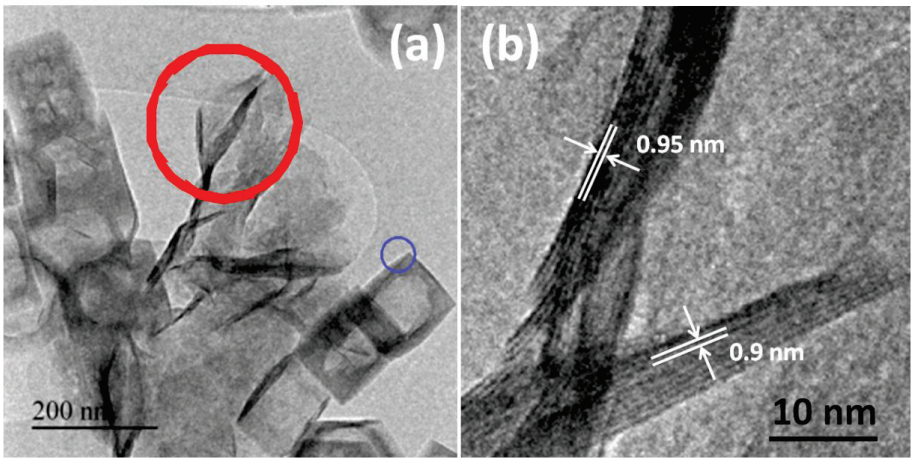

Figure 2: TEM images of cobalt-loaded hollow silicalite-1 with highest Co content (8-Co@Sil-1) before calcination showing Co phyllosilicates formed outside zeolite boxes. EDX analysis was performed in the areas indicated by the two circles in (a); white lines in (b) indicate the layers used for interlayer space distance determination.

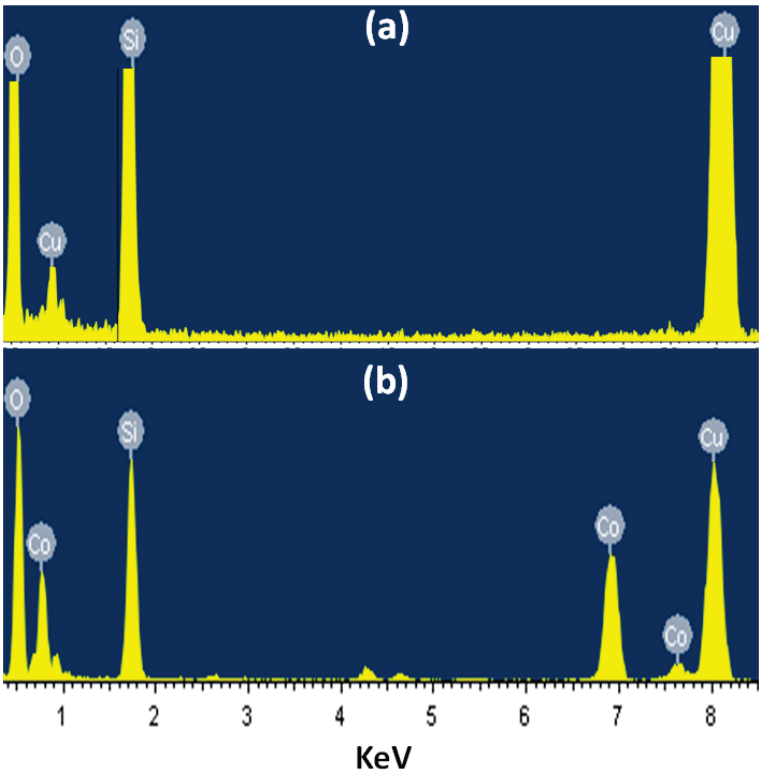

Figure 3: EDX spectra of the zeolite wall (a) (analyzed area indicated in Fig.2-a by a blue circle) and the Co phyllosilicates (indicated by the red circle in Fig.2-a) in 8-Co@Sil-1 sample, Cu peaks in the spectra are from the Cu grid used as the sample holder in TEM measurement.

Table 1: Elemental analysis deduced from EDX spectra in Fig.3

Spectrum	O(wt. %)	Si(wt. %)	Co(wt. %)
a	58.8	41.2	0
b	49.5	24.5	26

As those fibers were not observed in the absence of Co, we assumed that they were formed during the TPAOH treatment when partial dissolution of the zeolite occurs. The reduction of Co phyllosilicates to Co nanoparticles was monitored by Temperature Program Reduction (TPR) and thermal gravimetric analysis (TGA) under hydrogen flow (Figs.4 and 5).

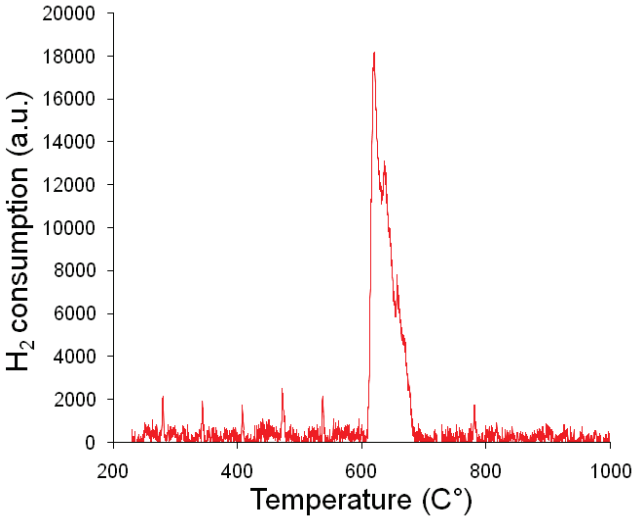

Figure 4: TPR profile of 2.5-Co@Sil-1 sample before reduction under hydrogen atmosphere (5%H_2 in Ar).

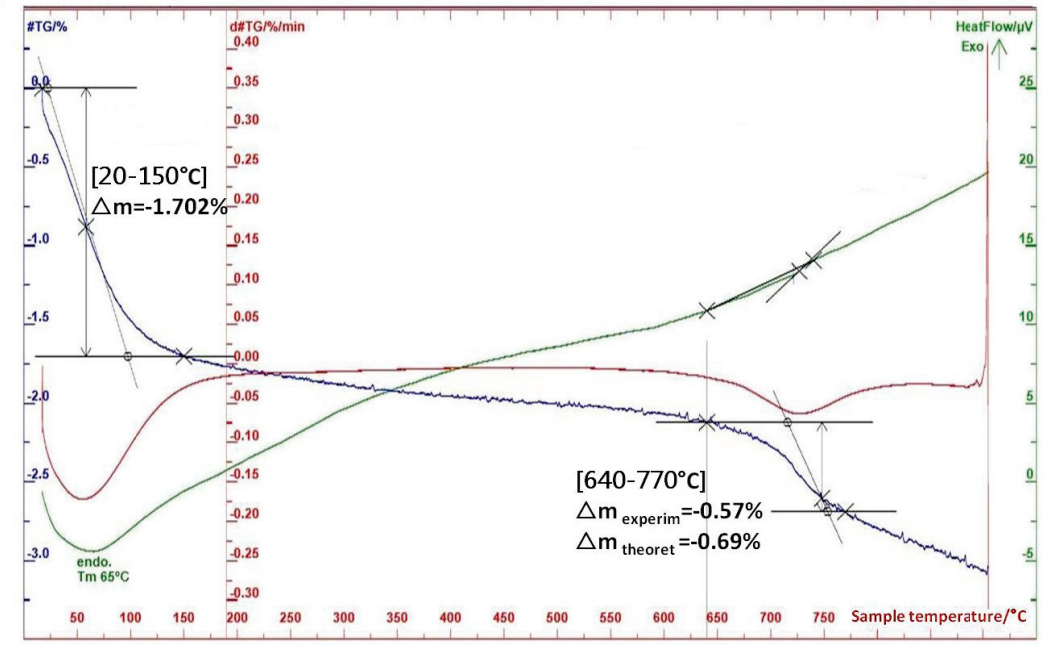

Figure 5: Thermal gravimetric profile of 2.5-Co@Sil-1 sample (before reduction) under hydrogen atmosphere (5%H_2 in Ar).

Both techniques indicate that phyllosilicates start to be reduced around 630°C in agreement with literature data for similar compounds.[6] Indeed, TEM pictures of solids reduced at 500°C under H2 did not show any change with respect to freshly prepared compounds, thus confirming that Co-phyllosilicates were not reduced at this temperature. In TGA curve, the mass loss observed before 150°C results from the removal of water molecules adsorbed in the zeolite pores. A second endothermic phenomenon is observed at 640°C and is associated with a mass loss of ca. 0.57 wt. %, which could correspond to the reduction of ca. 82% of Co^{2+} to Co^0 (see Fig. 5).

The Co-containing hollow zeolite sample was then set to 750°C for 10 h in 10% H_2 atmosphere to ensure complete reduction and then subjected to magnetic measurements (details in experimental chapter). The reduction degree of 2.5-Co@Sil-1 sample is estimated to 85%, in excellent agreement with TGA results.[6] For a reduction temperature of 750°C, TEM images showed the appearance of particles inside hollow crystals, supporting the transformation of phyllosilicates into metallic cobalt particles upon high temperature reduction (Fig. 6-a,b). TEM pictures of 2.5-Co@Sil-1 also revealed the presence of very minor amounts of fibrous species (not shown), in agreement with the incomplete reduction of Co^{2+} species measured by magnetic measurements. In the case of noble metals in hollow silicalite-1 with comparable metal loading, materials showed a single particle inside the big cavity of the crystal. In contrast, many particles are observed in the internal cavities for Co containing hollow zeolite samples (Fig. 6-a, b). The particle size distribution is quite narrow with a mean size of 3.2 nm (Fig. 6-c).

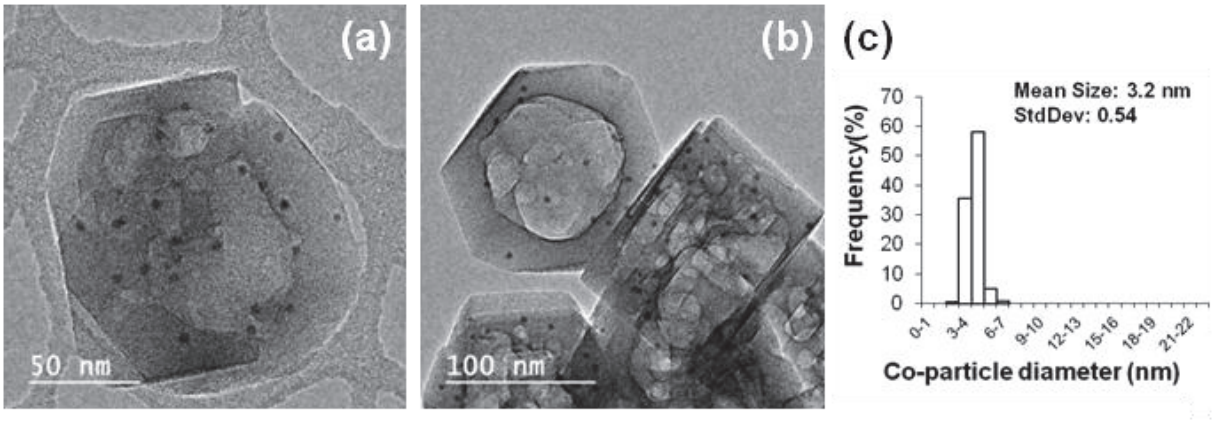

Figure 6: TEM images (a and b) and Co particle size distribution (c) of 2.5-Co@Sil-1 after reduction in hydrogen at 750°C.

Another significant difference with noble metals in hollow silicalite-1 is that a fraction of the Co particles is occluded in the zeolite walls (Fig. 6-a, b). We can propose that these differences with respect to noble metals arise from the formation of the phyllosilicates during the treatment with TPAOH. The Co precursor impregnation of bulk crystals likely leads to the dispersion of Co^{2+} species throughout the crystals. When Co-phyllosilicates crystallize, a chemical bond is formed with silica species and the observed fibers are strongly attached to the silica walls. By contrast to noble species those are weakly interacting with the zeolite and are free to move sintering in the internal cavity, phyllosilicates are hardly mobile and they remain dispersed inside the zeolite walls during recrystallization. In addition, the presence of phyllosilicates on the zeolite walls certainly affects the dissolution process which could explain the formation of several internal cavities (Fig. 6-a, b) instead of one unique cavity in the case of noble metal.

Increasing Co loading up to 3.1 wt. % led to a solid similar to the previous one except that Co particles are less regular in size with large particles (5-11 nm) coexisting with a population of smaller particles (3.7 nm) (Fig. 7).

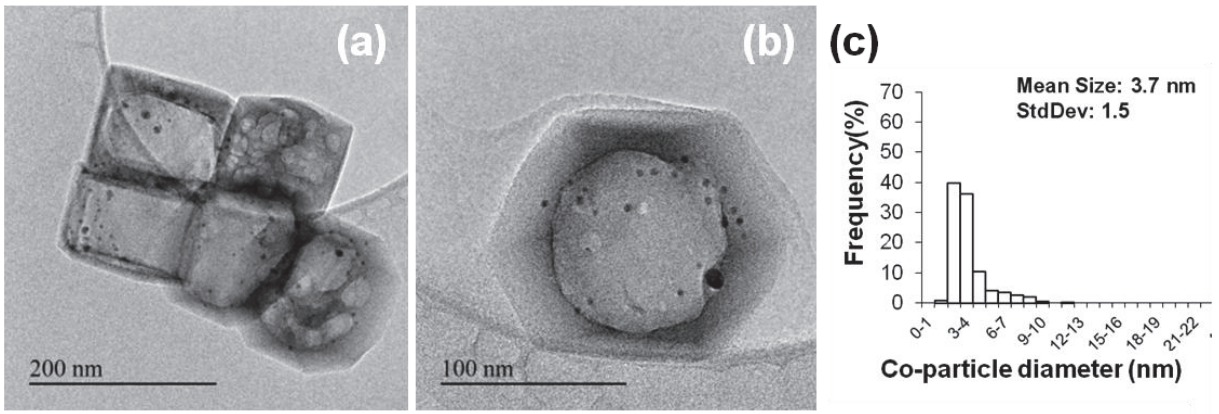

Figure 7: TEM images (a and b) and Co particle size distribution (c) of 3.1-Co@Sil-1 sample after reduction.

For a much higher Co content of 8 wt. % (8-Co@Sil-1), we have previously reported that a significant proportion of Co phyllosilicates was found outside zeolite crystals (Fig. 2), which eventually led to external particles after reduction (Fig. 8). The presence of particles outside hollow crystals for samples with high Co loadings suggests that the maximum incorporation level of Co species inside silicalite-1 does not exceed a few percent.

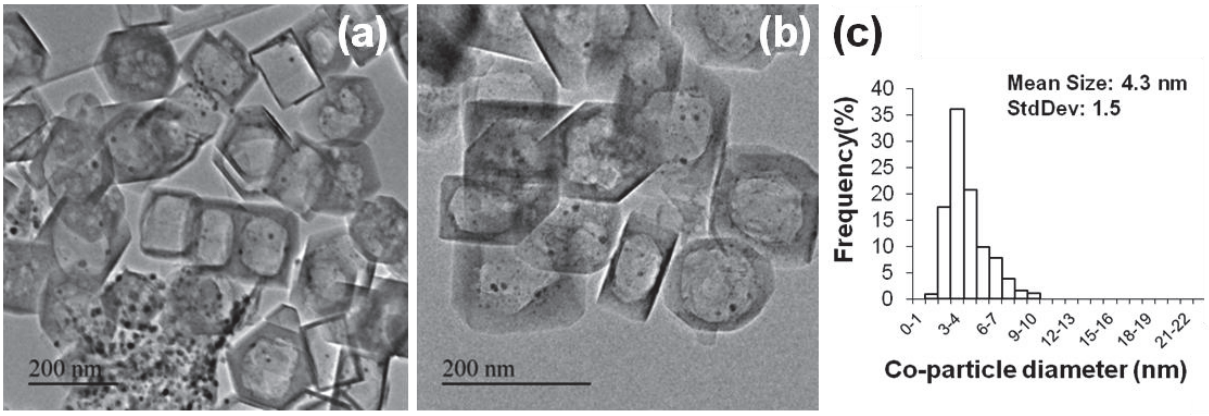

Figure 8: TEM images (a and b) and Co particle size distribution (c) of 8-Co@Sil-1 sample after reduction. Only the particles encapsulated in the zeolites are measured for the particle size distribution.

From these three cobalt samples, we could observe that increasing Co loading mainly affects the mean particle size but not the average number of particles per cavity. Indeed, we could estimate that each hollow crystal contains between 9 to 10 particles, whatever the Co loading (2.5%, 3.1% or 8%).

For example, when the loading increased by a factor of 1.2 from 2.5 to 3.1 wt. %, the particle volume increased by a factor of 1.5 (the mean particle size changed from 3.2 to 3.7 nm) (Figs. 6 and 7 and Table 2). It should be noted that the slight difference between the two factors obviously results from the presence of bigger particles at higher loading (approximately 13% particle with a diameter above 5 nm in the 3.1-Co@Sil-1 sample).

Table 2: Mean particle sizes in various transition metals in hollow silicalite-1 samples

Sample	Mean particle size (nm)
2.5-Co@Sil-1	3.2±0.5
3.1-Co@Sil-1	3.7±1.5
8-Co@Sil-1	4.3±1.5
1-Ni@Sil-1	2.7±0.5
2.5-Ni@Sil-1	3.5±0.8
2.8-Cu@Sil-1	9.8±2.2(1.5)[a]

[a]Values in parentheses correspond to the average particle size for a second population of particles

II.2. Nickel and copper particles in hollow silicalite-1

Nickel and copper-containing hollow zeolites were prepared following the same procedure as that used for cobalt materials. For both metals, the formation mechanisms were similar to that previously described for cobalt. In particular, Ni and Cu phyllosilicates (Fig.9-a and 11-a) were formed during the dissolution/recrystallization step in the presence of TPAOH and were then converted into metal nanoparticles upon reduction at high temperature, yielding yolk-shell type materials. TEM images of 1-Ni@Sil-1 before and after reduction (Fig.9-a and b) are quite similar to those obtained with cobalt (Fig. 1 and 6) but a main difference is that the average number of particles per hollow crystal after reduction is approximately 4 times larger. Indeed, each cavity contains approx. 40 particles (Fig. 9-a and b) and the difference with Co likely from intrinsic properties of metals and the corresponding phyllosilicates. The particle size distribution is quite narrow with a mean diameter of 2.7 nm.

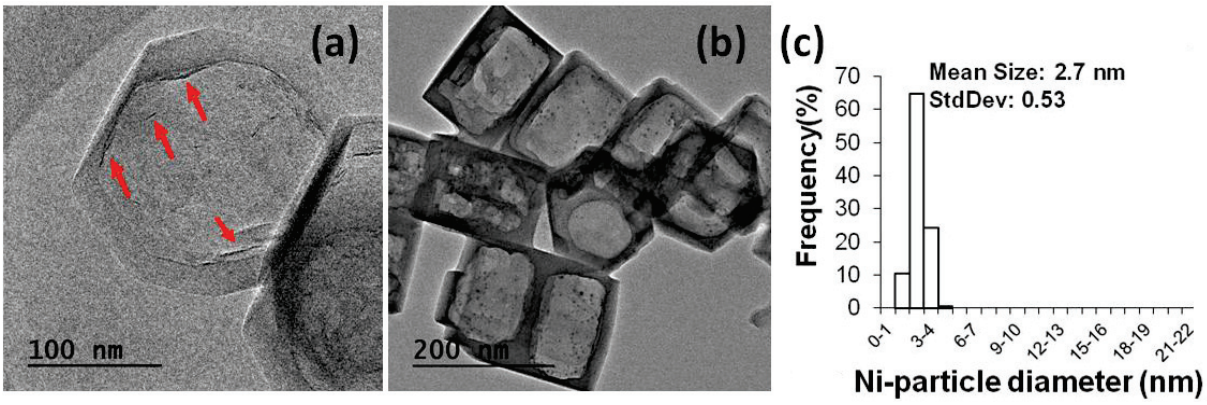

Figure 9: TEM images of 1-Ni@Sil-1 sample before (a), after (b) reduction and Ni particle size distribution (c), phyllosilicates indicated by the red arrows in (a).

Increasing Ni loading to 2.5 wt. % leads to a slight increase in the particle size while the average number of particles per hollow zeolite crystal remains almost constant (Fig. 10). As for Co, the average volume of Ni particles varied proportionally to the Ni content: when the loading increased from 1 to 2.5 wt. %, the mean particle volume increased by a factor of 2.4 (diameter from 2.7 to 3.5 nm, Table 2).

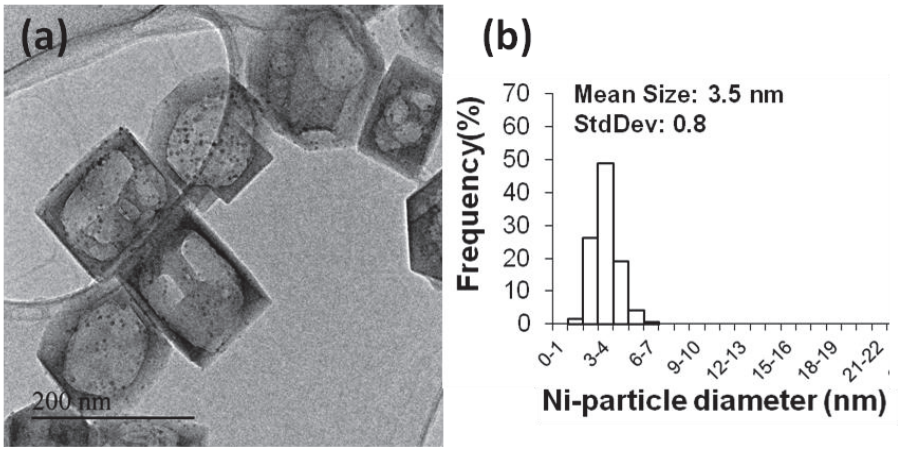

Figure 10: TEM images and Ni particle size distribution (b) of 2.5-Ni@Sil-1 (a) sample.

Though similar to Co and Ni-containing zeolites after TPAOH treatment (Fig.11-a, phyllosilicates indicated by red arrows), copper-containing silicalite-1 materials were somewhat different in terms of particle size distribution after reduction under hydrogen. Indeed, most of hollow silicalite-1 crystals contained a bimodal population of Cu particles, with one or two large particles coexisting with very small particles inside the same cavity (Fig.11-b). The smaller particles are approximately 1.5 nm in size, while the bigger ones possess a mean diameter of 9.8 nm estimated from the histogram of the particle distribution (Fig 11-c).

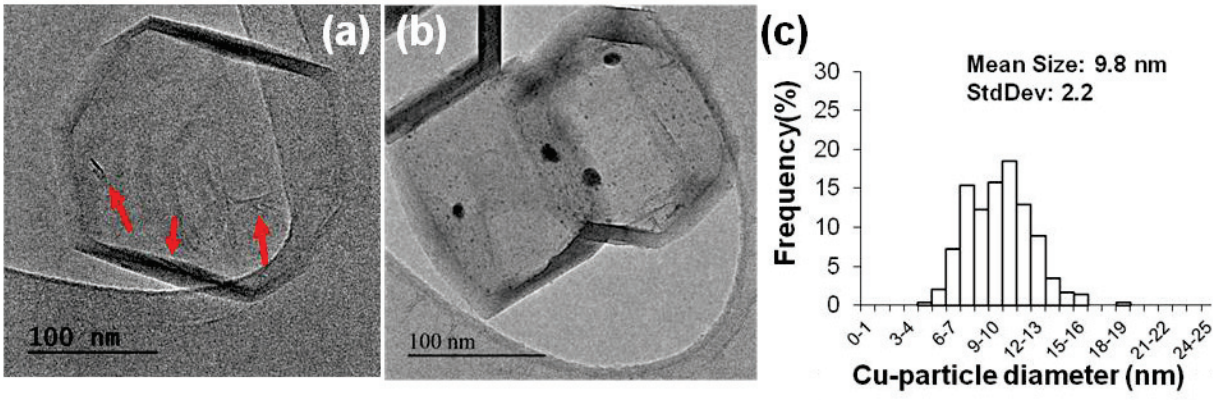

Figure 11: TEM images of 2.8-Cu@Sil-1 before (a) and after (b) reduction and Cu particle size distribution (c), the distribution is only given by the bigger particles.

II.3. Cobalt particles in hollow ZSM-5

The synthesis of Co-containing yolk-shell materials was extended to the preparation of cobalt particles in hollow ZSM-5 materials. The dissolution process is different when Al^{3+} is present in the zeolite structure. For silicalite-1, the creation of hollow structures in the presence of TPAOH was attributed to the preferential dissolution of the core area of the crystals, a region with a high density of defects compared to surface layer of the crystals. In the case of ZSM-5 crystals, if aluminum is homogeneously distributed, treatment with TPAOH does not form regular hollow structures, and partial dissolution occurs throughout the crystals.[7, 8] Therefore, suitable ZSM-5 crystals must show a gradient of composition with a Si-rich core which can be referentially dissolved in alkaline media compared to the Al-rich periphery.[9]

Desilication is generally performed using inorganic bases such as NaOH[10, 11] or Na_2CO_3[12, 13] which leads to a significant loss of matter and non-uniform structures in the final crystals. [Na]ZSM-5 nanocrystals with an Al gradient were prepared following a literature method with minor modifications (1.7 times more water in our crystallization gel than the literature one, synthesis details in experimental chapter).[14] Then this as-prepared ZSM-5 zeolites was treated by TPAOH under the same dissolution recrystallization conditions as those for silicalite-1 materials (details in experimental chapter). TEM image of the materials after TPAOH treatment is given in Fig. 12 which shows that hollow ZSM-5 zeolites are obtained with a wall thickness similar to that observed on silicalite-1, suggesting the completely re-crystallization of ZSM-5 in the presence of TPAOH via the dissolution recrystallization process. In contrast to inorganic bases, recrystallization of the dissolved silicon species in the presence of TPAOH leads to the identical overall Si/Al ratio in the parent ZSM-5 and the hollow ones (Si/Al=100 in bulk and hollow ZSM-5 detected by ICP-OES). The obtained hollow

ZSM-5 is denoted as ZSM-5-DR (DR for Directly dissolution Recrystallization from ZSM-5 zeolites) if necessary, when the discussion involves hollow ZSM-5 synthesis by other routes in the following chapters.

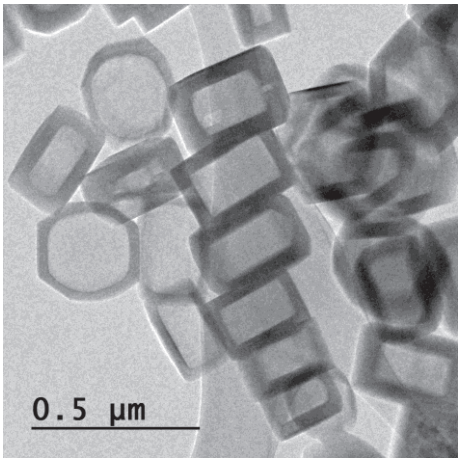

Figure 12: TEM image of hollow ZSM-5 synthesized by directly dissolution recrystallization process in the presence of TPAOH starting with ZSM-5 crystals.

X-ray diffraction and nitrogen physisorption measurements show that the characteristics of hollow ZSM-5 are similar to those previously reported of hollow silicalite-1 (Fig. 13, 14).

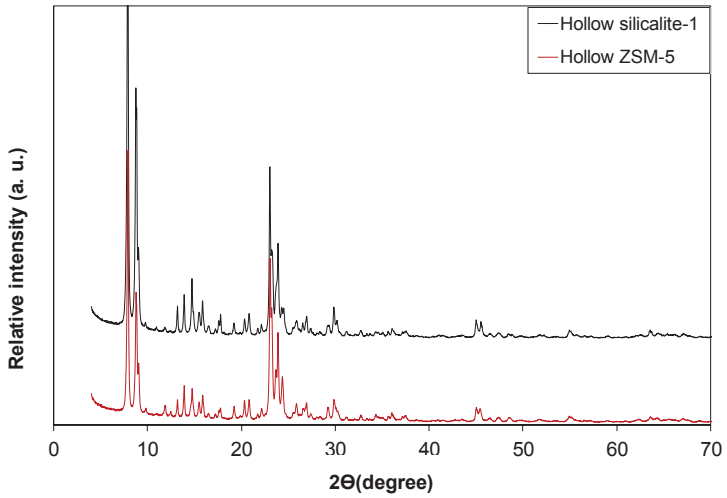

Figure 13: XRD patterns of hollow silicalite-1 (top) and hollow ZSM-5 (bottom).

In particular, the presence of a hysteresis loop in the isotherm confirms the presence of the inner cavity. Moreover, the t-plot curve indicates that the ZSM-5 walls are perfectly closed and contain exclusively micropores.

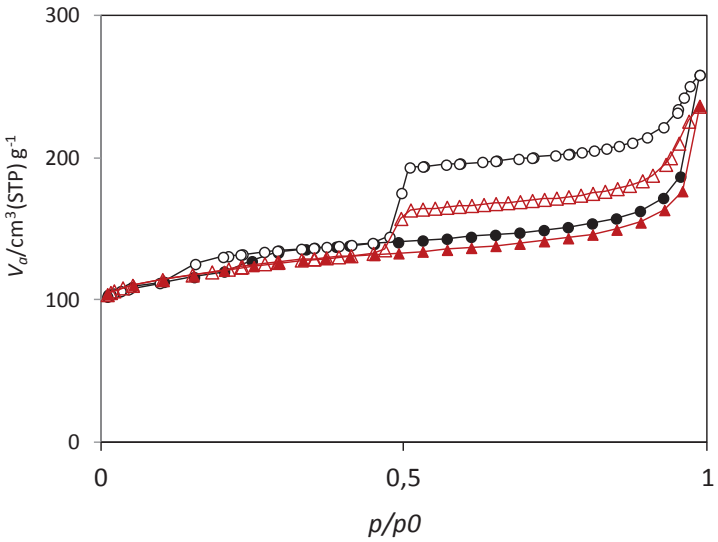

Figure 14: N_2 adsorption/desorption isotherms of hollow silicalite-1(○) and hollow ZSM-5-DR (△) at 77K.

The ^{27}Al NMR spectra of hollow ZSM-5 before and after calcination are both composed a major resonance at ca. 50 ppm, characteristic of AlO_4 tetrahedra in the silica framework, which confirms that most of Al species remain at framework positions during the formation of hollow structures and subsequent calcination (Fig. 15). A weaker resonance at around 0 ppm suggests the existence of a small amount of extra framework aluminum atoms in hollow ZSM-5 before and after calcination. As can be seen in the figure, the amount of extra-framework Al species slightly increases after calcination of hollow zeolites, due to the partial exchange of Na^+ cations by protons upon treatment with TPAOH. The signal at ca. -42ppm in the spectrum of the calcined zeolite (right) is a pinning sideband resulting from the spinning of the sample during measurement.

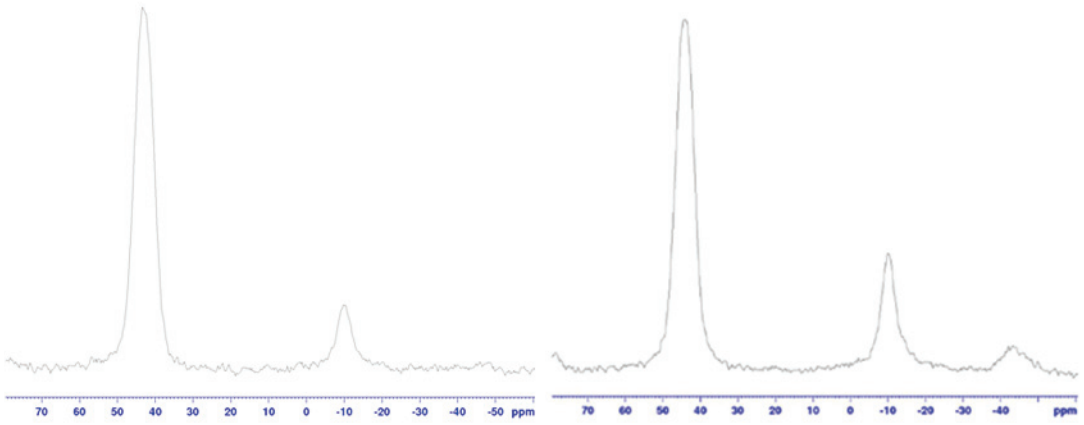

Figure 15: ^{27}Al NMR spectra of hollow ZSM-5 before (left) and after (right) calcination.

On the basis of these observations, TPAOH treatments were performed on ZSM-5 impregnated with three transition metal (Co, Ni and Cu) solutions. All metal-containing samples were characterized by

TEM and ICP-OES; the average metal particle sizes and aluminum contents in the various samples are given in Table 3.

Table 3: Mean particle size in the various transition metal in hollow ZSM-5 samples

Sample	Si/Al ratio	Average particle size (nm)
2.2-Co@ZSM-5	102	15.1±4.1
7.4-Co@ZSM-5	104	18.8±4.8
2.6-Ni@ZSM-5	101	11.2±3.2
7.7-Ni@ZSM-5	105	14.5
3-Cu@ZSM-5	102	15-100(2.5)[a]

[a]The population of large particles was very inhomogeneous

For cobalt containing samples, the presence of Co species did not alter the dissolution/re-crystallization process and the morphology of hollow Co@ZSM-5-DR samples (Fig. 16) is similar to that of Co-free materials (Fig. 12). After hydrothermal treatment in TPAOH, fibrous phyllosilicates were also observed, indicating by the red arrows in Fig.16-a. In contrast to silicalite-1, phyllosilicates were scarce in ZSM-5 and generally formed a thin layer on the internal surface of the cavities. After reduction in H_2 at 750°C, Co particles were located only inside the cavity (Fig. 16), which contrasts with silicalite-1 for which particles were also detected inside the zeolite walls (Fig. 6). Another difference with Co@Sil-1 samples is the average number of particles per hollow zeolites. In the two samples containing a comparable amount of cobalt, 2.2-Co@ZSM-5-DR and 2.5-Co@Sil-1, the number of particles is generally limited to 2 or 3 per hollow ZSM-5 compared to 9 to 10 in the case of silicalite-1, as a result, Co particles are 5 times bigger in hollow ZSM-5 (15.1 nm) than those in hollow silicalite-1 (3.2 nm) (Figure 6 and 16).

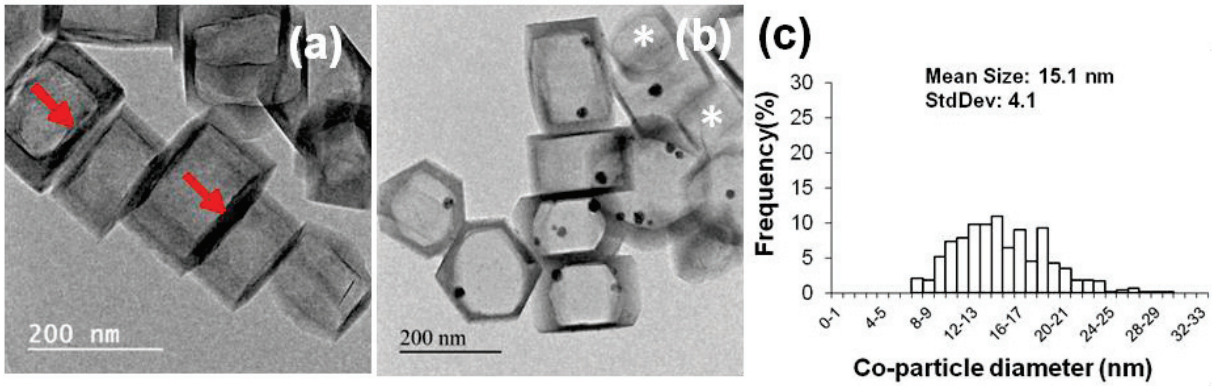

Figure 16: TEM pictures of 2.2-Co@ZSM-5-DR before (a) and after (b) reduction at 750°C and corresponding Co particle size distribution(c). Arrows in (a) point out phyllosilicate layers on the internal surface of zeolite nanoboxes, stars in (b) indicate empty nanoboxes.

The origin of such differences is not clear but we assumed that the presence of Al^{3+} in the zeolite could affect the formation of Co phyllosilicates, especially in the zeolite matrix. Since Co particles are not entrapped in the zeolite walls, they are free to move into the cavities during reduction and thus to grow by Ostwald ripening and coalescence. By contrast to Co@Sil-1 materials, high Co loadings of 7.4 wt. % (7.4-Co@ZSM-5-DR) did not yield particles outside the hollow crystals. More than 95% of hollow zeolites contained at least one Co particle as shown in Fig. 17. We can note that increasing the loading by a factor of 3.4 from 2.2 to 7.4 wt. % led to an increase of mean particle size from 15 nm to 19 nm(Fig. 16, 17 and Table 3), which corresponded to a 2-fold increase in volume. This difference can be partly explained by the fact that ca. 16% of hollow zeolites in 2.2-Co@ZSM-5-DR did not contain Co particles (see Fig. 16 for evidence of empty shells).

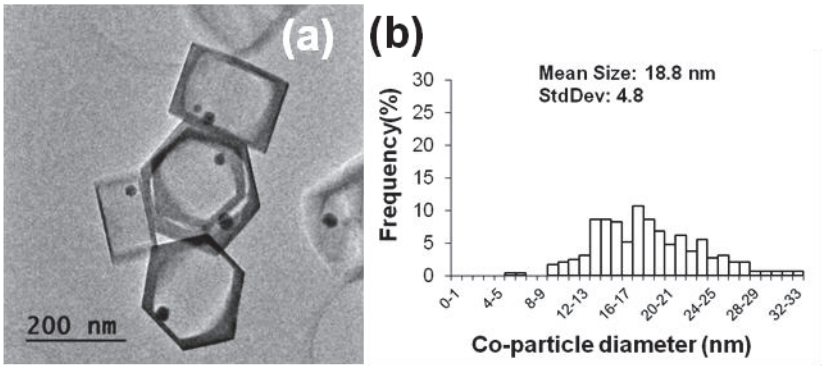

Figure 17: TEM image (a)and Co particle size distribution (b) of 7.4-Co@ZSM-5-DR sample after reduction at 750°C.

Successive oxidation/reduction cycles were performed on 7.4-Co@ZSM-5-DR sample to evaluate the stability of the solid against sintering during regeneration. Moreover, oxidation/reduction cycles are often used to re-disperse transition metal nanoparticles on different supports.[15] The evolution of the morphology of the particles in 7.4-Co@ZSM-5-DR sample during oxidation/reduction cycles were followed by TEM (Fig. 18). After calcination at 250°C in air for 2 hours, a major modification on the shape of Co particles was noted, characterized by a hollow morphology with an irregular shape (Fig. 18-a and b). The formation of these structures has already been reported for transition metal nanoparticles and it has been attributed to a nanoscale Kirkendall effect, arising from a difference in diffusion rates between anions and cations.[16] A thin layer of oxide is first formed on the surface of the metal particle, and then an electron field is formed between the metal and the oxide layer.

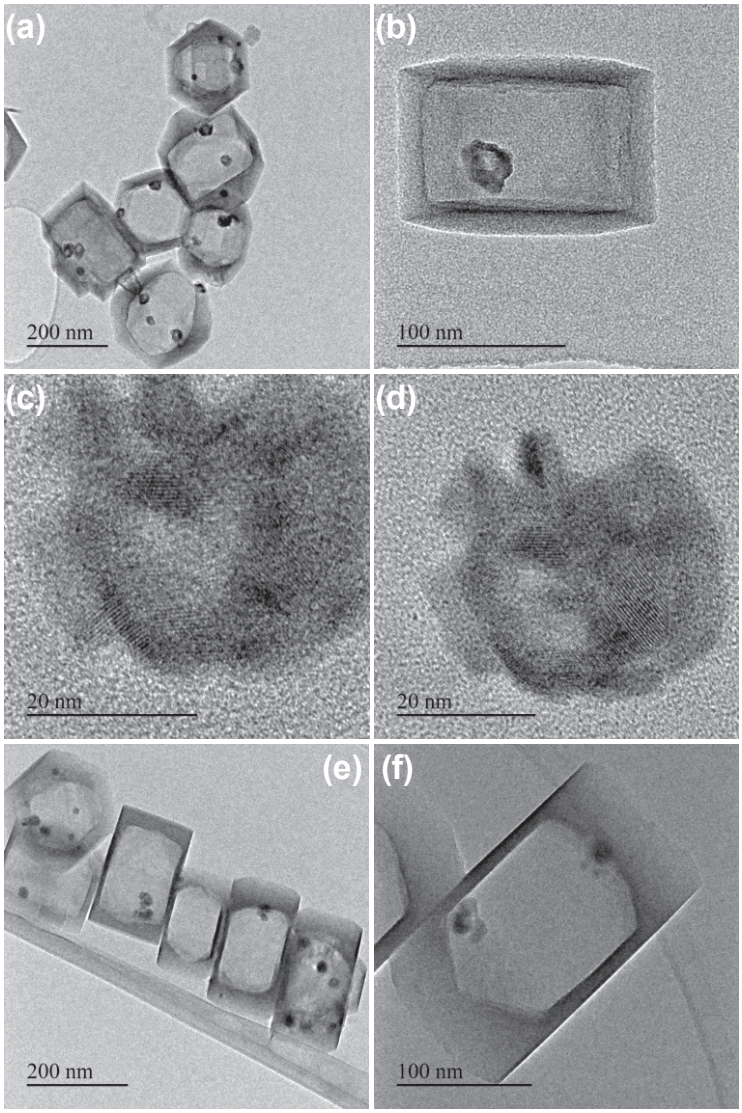

Figure 18: TEM pictures of 7.4-Co@ZSM-5-DR after re-oxidation at 250°C (from a to d) and subsequent reduction at 500°C (e and f). Polycrystalline nature of Co-oxide hollow particles are clearly showed in (c) and (d).

Thus, the different diffusion rates between metal cations and ionized oxygen lead to the formation of hollow structure.[17] TEM pictures at high magnification clearly revealed the polycrystalline nature of the cobalt oxide shells, with individual particle size of ca. 3-5 nm (Fig. 18-c and d). When the oxidized 7.4-Co@ZSM-5-DR was reduced under H_2, two populations of Co particles could be observed: large particles with a size similar to that observed on freshly reduced solids and small ones formed by fragmentation and re-dispersion of the cobalt oxides as already reported in many studies (Fig. 18-e and f).[15] Actually, the presence of oxide nanocrystals in the shell favors the presence of nuclear sites for reduction and the contraction in volume from hollow oxide shell to cobalt particles leads to breaking of the shells. Moreover, grain boundaries can significantly accelerate the diffusion rate of ionized oxygen into the metal and further the re-dispersion to smaller particles upon reduction conditions.

II.4. Nickel and Copper particles in hollow ZSM-5

Nickel in hollow ZSM-5 was prepared following the same procedure as cobalt ones. The formation mechanisms were similar to that for cobalt; the corresponding phyllosilicates were formed and reduced at 750°C in hydrogen. TEM pictures of 2.6-Ni@ZSM-5-DR shows that particles are obviously located in the cavities of hollow crystals with the average number ca. 5 per crystal (Fig.19). For a similar Ni content, particles are much larger in hollow ZSM-5(11.2 nm) than in silicalite-1(3.6 nm) (Fig.19 and 10), which is consistent with previous observation on Co-based solids.

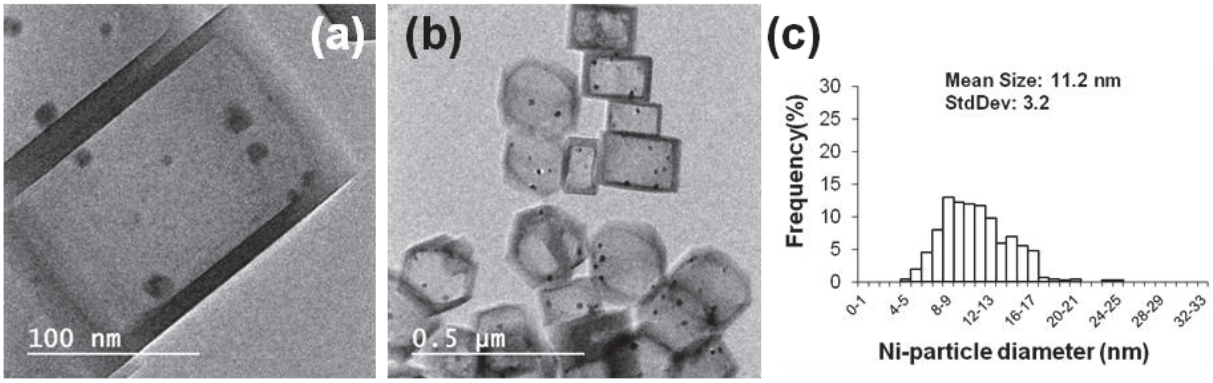

Figure 19: TEM images (a and b) and Ni particle size distribution (c) of 2.6-Ni@ZSM-5-DR sample after reduction at 750°C.

Another Ni containing hollow ZSM-5 was prepared with a higher metal loading (7.7 wt. %). TEM images of 7.7-Ni@ZSM-5-DR (Fig.20) show much larger particles were formed with well-defined crystallographic shapes, likely due to metal crystallization conditions. The particles size was estimated to 14.5nm for qualitative comparison (the histogram of particle size distribution could not be calculated due to the presence of non-spherical particles).

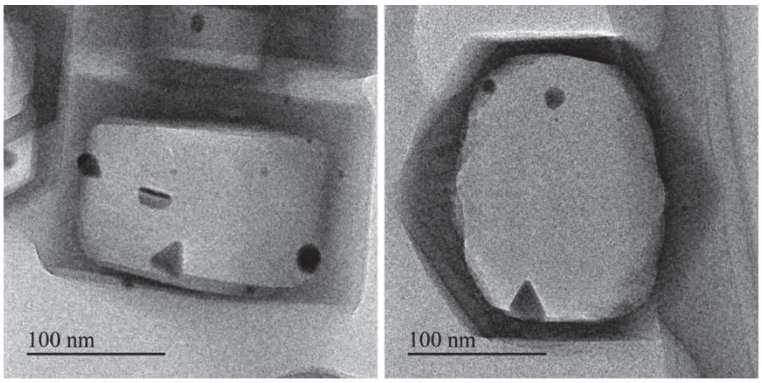

Figure 20: TEM images of 7.7-Ni@ZSM-5-DR sample.

ZSM-5 crystals containing Cu particles clearly exhibited two distinct populations in the same box: one big particle with a size of about 30 nm surrounded by many nanoparticles of ca. 1-2 nm (Fig.21-a and b) suggesting that the aggregation mechanism was not complete even after reduction at 750°C. In contrast to Cu@Sil-1, we could estimate that only half of the hollow zeolite crystals contained a large particle. However, these crystals were not Cu-free and TEM images revealed that they still contained fibrous matter similar to phyllosilicates observed before reduction. Their presence in samples reduced at 750°C suggests that Cu phyllosilicates are much more difficult to reduce than Ni and Co analogs. The reduction was more effective in silicalite-1, in which Cu phyllosilicates were only detected at trace levels after treatment at 750°C.

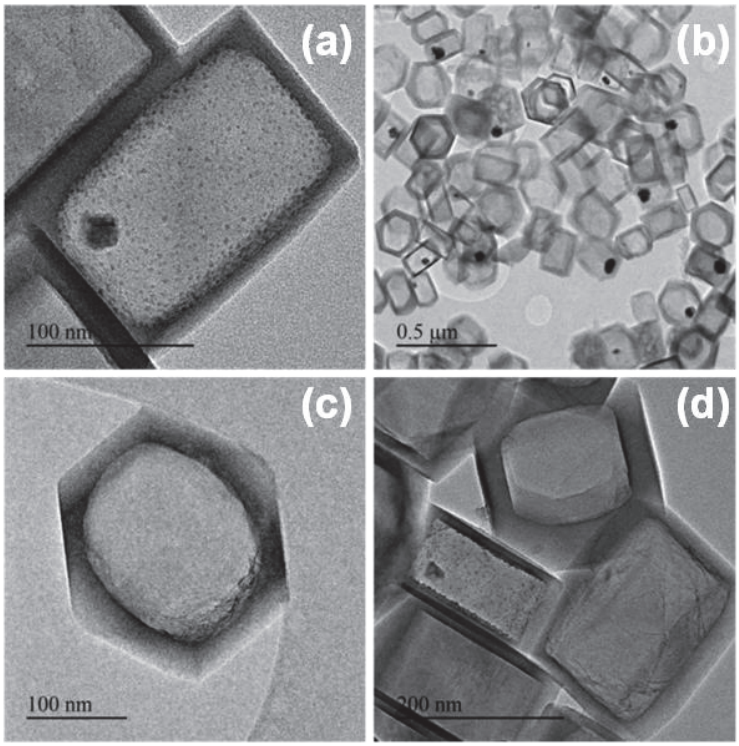

Figure 21: TEM images of 3-Cu@ZSM-5-DR hollow crystals reduced at 750°C in H_2, showing boxes with large and small Cu particles (a and b) and others with silicate fibres (c and d).

II.5. Catalytic evaluation of 1-Ni@Sil-1

1-Ni@Sil-1 was evaluated in the catalytic hydrogenation of substituted aromatics and its catalytic performance was compared to that of a traditional supported Ni-based catalyst: 35-Ni/Ca-Al_2O_3 (35 wt. % of Ni loading detected by ICP-OES, catalyst from Johnson Matthey). The conversion of toluene and mesitylene (i.e. 1, 3, 5-trimethylbenzene) were both significant over the supported Ni catalyst (Fig. 22). In contrast, the conversion of mesitylene was essentially negligible over the 1-Ni@Sil-1, while this sample was still able to convert toluene. Similarly to the case of Pt@Sil-1 discussed in Chapter 3,[18] indicating that the transport of the bulkier mesitylene was suppressed through the zeolite layer.

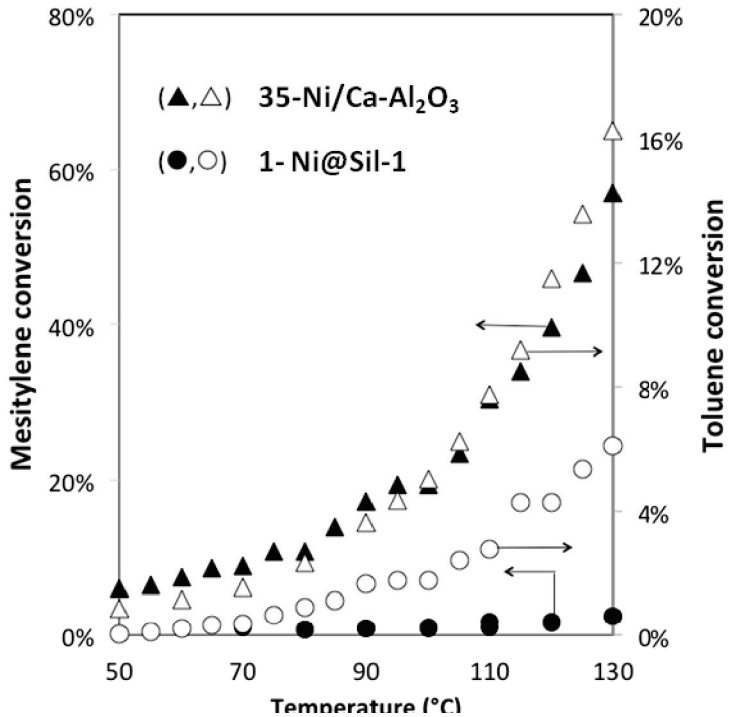

Figure 22: Conversion of toluene (open symbols) and mesitylene (full symbols) at various temperatures over 9.4 mg of 1-Ni@Sil-1 (●,○) and 14.2 mg of 35-Ni/Ca-Al_2O_3 commercial catalyst (▲,△).

The kinetic diameter of mesitylene is significantly larger than the pore size of silicalite-1, while toluene can readily diffuse into this microporous solid. These data can therefore be rationalized by proposing that the zeolite shell surrounding the Ni particles is essentially free of mesoporous defects and acts as a near-ideal membrane permeable to toluene but not to mesitylene. Moreover, it also supports the absence of particles on the outer surface of the nanoboxes, in agreement with the TEM analysis presented above. The molecular sieving properties of these transition metal-based catalysts mirror those obtained over Pt nanoparticles occluded inside hollow silicalite-1 single crystals.[26]

III. Conclusions

In this chapter we have optimized a method for preparing hollow ZSM-5 single crystals by dissolution-recrystallization of bulk ZSM-5 crystals in the presence of TPAOH. Dissolution mainly occurs at the Si-rich core occurs and it is followed by a recrystallization on the outer surface of the crystals. The obtained hollow structures are similar to those obtained with silicalite-1, with regular microporous walls of ca. 20 nm thick. The presence of trivalent sites in hollow ZSM-5 was confirmed by ^{27}Al NMR.

A series of novel hollow silicalite-1 and ZSM-5 single crystals containing uniform transition metal particles were prepared. The synthesis involves the desilication-recrystallization of bulk crystals previously impregnated with the corresponding nitrate solutions. In contrast to noble metals (Au, Pt, Pd and Ag)@Sil-1, all solids were obtained by reduction of fibrous phyllosilicates which are formed inside the cavities by the reaction between silicate and metal species at high pH values and temperature (corresponds to TPAOH treatment). For hollow silicalite-1 systems at low loading, the mean particle sizes were 3.5 ± 0.3 and 3.1 ± 0.5 nm for Co and Ni, respectively. Larger loading could be obtained in ZSM-5, with mean particle sizes of 17 ± 2 nm for Co and 13 ± 2 nm for Ni. Upon oxidation, Co particles adopted a polycrystalline hollow morphology, resulting from a nanoscale Kirkendall effect.

The molecular sieving of the zeolite shell was demonstrated by the difference in hydrogenation conversions between toluene and mesitylene, the latter being too bulky to pass through the zeolite membrane and reach the nanoparticles. We believe that this new family of bifunctional catalysts showing well-controlled particle size and location opens new exciting perspectives in size-selective and bi-functional catalysis.

Bibliography

1. Kababji, A.H., Joseph, B. & Wolan, J.T. Silica-Supported Cobalt Catalysts for Fischer–Tropsch Synthesis: Effects of Calcination Temperature and Support Surface Area on Cobalt Silicate Formation. *Catal. Lett.* **130**, 72-78 (2009).

2. Puskas, I., Fleisch, T.H., Full, P.R., Kaduk, J.A., Marshall, C.L. & Meyers, B.L. Novel aspects of the physical chemistry of Co/SiO2 Fischer–Tropsch catalyst preparations: The chemistry of cobalt silicate formation during catalyst preparation or hydrogenation. *Appl. Catal., A* **311**, 146-154 (2006).

3. Grams, J., Ura, A. & Kwapiński, W. ToF-SIMS as a versatile tool to study the surface properties of silica supported cobalt catalyst for Fischer–Tropsch synthesis. *Fuel* **122**, 301-309 (2014).

4. Jabłoński, J.M., Wołcyrz, M. & Krajczyk, L. On Cobalt Silicate Formation during High-Temperature Calcination of Impregnated Cobalt/Silica Catalysts. *J. Catal.* **173**, 530-534 (1998).

5. Strunz, H.N., E.H. Strunz Mineralogical Tables: Chemical-Structural Mineral Classification System, 9th Edition. (Stuttgart Ed., Schweizerbart; 2001).

6. Lim, S., Ciuparu, D., Chen, Y., Pfefferle, L. & Haller, G.L. Effect of Co-MCM-41 Conversion to Cobalt Silicate for Catalytic Growth of Single Wall Carbon Nanotubes. *J.Phys.Chem.B* **108**, 20095-20101 (2004).

7. Wang, Y. & Tuel, A. Nanoporous zeolite single crystals: ZSM-5 nanoboxes with uniform intracrystalline hollow structures. *Microporous Mesoporous Mater.* **113**, 286-295 (2008).

8. Burel, L. & Tuel, A. Nanozeolites: New strategies for designing ultra small silicalite crystals with very few framework defects. *Microporous Mesoporous Mater.* **174**, 90-99 (2013).

9. Fodor, D., Pacosova, L., Krumeich, F. & van Bokhoven, J.A. Facile synthesis of nano-sized hollow single crystal zeolites under mild conditions. *Chem. Commun.* **50**, 76-78 (2014).

10. Groen, J.C., Peffer, L.A.A., Moulijn, J.A., Pérez, R., amp, x & rez, J. On the introduction of intracrystalline mesoporosity in zeolites upon desilication in alkaline medium. *Microporous Mesoporous Mater.* **69**, 29-34 (2004).

11. Li, J., Li, X., Zhou, G., Wang, W., Wang, C., Komarneni, S. & Wang, Y. Catalytic fast pyrolysis of biomass with mesoporous ZSM-5 zeolites prepared by desilication with NaOH solutions. *Appl. Catal., A* **470**, 115-122 (2014).

12. Kim, Y.H., Lee, K.H., Nam, C.-M. & Lee, J.S. Formation of Hierarchical Pore Structures in Zn/ZSM-5 to Improve the Catalyst Stability in the Aromatization of Branched Olefins. *ChemCatChem* **4**, 1143-1153 (2012).

13. Fathi, S., Sohrabi, M. & Falamaki, C. Improvement of HZSM-5 performance by alkaline treatments: Comparative catalytic study in the MTG reactions. *Fuel* **116**, 529-537 (2014).

14. Mei, C., Liu, Z., Wen, P., Xie, Z., Hua, W. & Gao, Z. Regular HZSM-5 microboxes prepared via a mild alkaline treatment. *J. Mater. Chem.* **18**, 3496-3500 (2008).

15. Sadasivan, S., Bellabarba, R.M. & Tooze, R.P. Size dependent reduction-oxidation-reduction behaviour of cobalt oxide nanocrystals. *Nanoscale* **5**, 11139-11146 (2013).

16. Yang, Z., Yang, J., Bergstrom, J., Khazen, K. & Pileni, M.-P. Crystal polymorphism: dependence of oxygen diffusion through 2D ordered Co nanocrystals. *Phys. Chem. Chem. Phys.* **16**, 9791-9796 (2014).

17. Cabrera, N. & Mott, N. REP PROG PHYS. *Rep. Prog. Phys.* **12**, 163 (1948).

18. Li, S., Boucheron, T., Tuel, A., Farrusseng, D. & Meunier, F. Size-selective hydrogenation at the subnanometer scale over platinum nanoparticles encapsulated in silicalite-1 single crystal hollow shells. *Chem. Commun.* **50**, 1824-1826 (2014).

Metal particles in hollow ZSM-5 zeolites

I. Introduction

In chapter 3, we have discussed the dissolution-recrystallization method to synthesize noble nanoparticles encapsulated in hollow silicalite-1 by treating the corresponding metal containing silicalite-1 crystals.[1, 2] ZSM-5, which is the analog of silicalite-1 with aluminum content, is highly used in catalytic processes such as industrial Fluid Catalytic Cracking (FCC) and isomerization due to its acidic properties.[3, 4] In this chapter, the dissolution-recrystallization method has been extended to prepare metal nanoparticles encapsulated in hollow ZSM-5 materials starting with either silicalite-1 or ZSM-5 crystals. This method allowed the synthesis of yolk-shell material with a unique particle per hollow shell, in which the particle size was only dictated by the metal content.

Another simple and more scalable desilication strategy was developed to prepare larger amount of highly-dispersed metal nanoparticles (Pt, Co and Ni) encapsulated in hollow ZSM-5 with walls thickness down to 10 nm.

This series of ZSM-5 based samples prepared via different routes were characterized by XRD, N_2 physisorption, NMR, ICP-OES and TEM. Furthermore, the sintering test and hydrogenation of light aromatics have been carried out over the Pt containing hollow ZSM-5 samples.

II. Results and discussion

II.1. Dissolution recrystallization route for preparing hollow ZSM-5

II.1.1. Dissolution recrystallization route with TPAOH by starting with silicalite-1

Hollow ZSM-5 can be synthesized by introducing aluminum during TPAOH treatment (synthesis details in experimental chapter). The metal containing silicalite-1 has been treated by this method, resulting in metal nanoparticles encapsulated in hollow ZSM-5 materials denoted w-metal@ZSM-5-PA (w for metal loading in wt. % detected by ICP and PA for Post Al adding). TEM image of 0.45-Pd@ZSM-5-PA exhibits the yolk-shell structure with almost one metal nanoparticle per hollow shell, the irregular form of metal species (Fig.1-left) changed to spherical particles (Fig.1-right) after reduction which due to the instinct properties of Pd metal. Crystals exhibit cavities with regular hexagonal shapes similar to those observed on silicalite-1 but with relatively rough surfaces, suggesting a difference in composition between the inner and outer parts of the crystals. Indeed, in

the presence of Al the dissolved silicon species crystallized in the presence of TPAOH, resulting in a layer of ZSM-5 on the surface of parent silicalite-1 crystals. Thus, an Al gradient exists in those hollow ZSM-5 shells with an increase of Al content from inside to outside of the hollow shells.

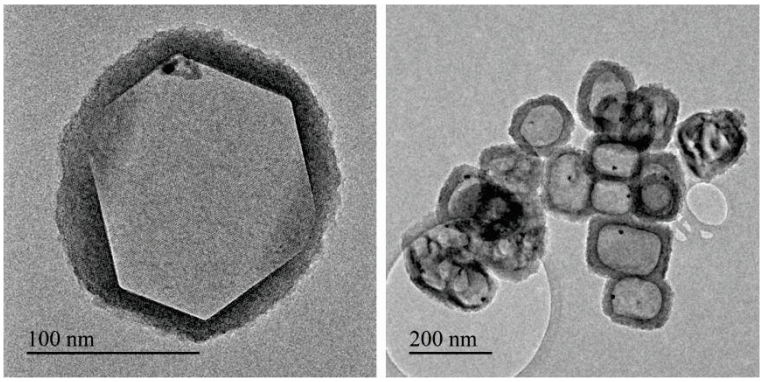

Figure 1: TEM pictures of 0.45-Pd@ZSM-5-PA with Si/Al=45 before (left) and after (right) reduction.

Moreover, it is possible to modify the chemical composition of the zeolite without modifying the geometry of the crystal and the particles. Au particles encapsulated in hollow ZSM-5 with different Si/Al ratios have been prepared by modifying the amount of aluminum in the TPAOH solution (Fig.2).

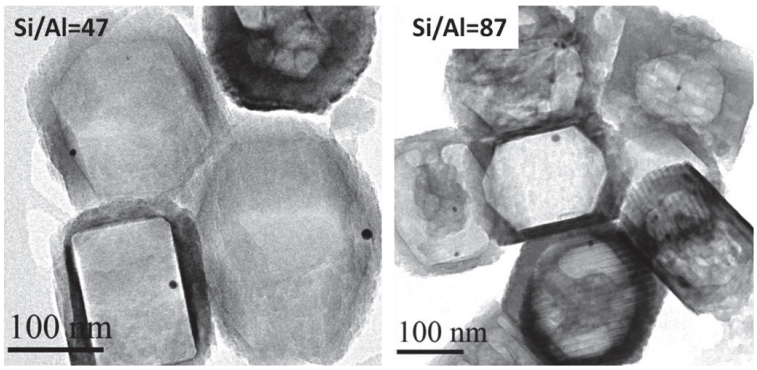

Figure 2: TEM pictures of 0.5-Au@ZSM-5-PA with different Si/Al ratios, Si/Al=47 on the left and Si/Al=87 on the right, indicating on the upper left of the images. Theoretical Si/Al ratios are 50 (left) and 100 (right), respectively.

Furthermore, a non-metal containing slilicalie-1 has been treated by TPAOH containing aluminum corresponding to Si/Al ratio 25, where Si is representing all the silica species in bulk zeolite crystals. However, the final hollow ZSM-5 zeolite possessed a Si/Al around 70. This has been previously reported by Tuel et al.[5] The possible reason is that aluminum is in excess compared to the dissolved silicon species for the recrystallization. Approximately 50% of the original zeolites are dissolved in the gel, leading to a local Si/Al ration of 12.5 at the zeolite surface. The recrystallization is likely limited by high Al concentration in the gel. Thus, the crystallization kinetics as well as zeolite yield are strongly affected, and the overall Al content in hollow zeolites is low.

Here in, the Si/Al ratio of hollow ZSM-5 prepared by post aluminum adding is generally in the range from 100 to 50, more Al containing samples being relatively difficult to obtain.

II.1.2. Dissolution recrystallization route with TPAOH by starting with with ZSM-5

As it has been discussed previously in chapter 4 taht transition metal nanoparticles encapsulated in hollow ZSM-5 can be achieved by treating metal containing ZSM-5 crystals having a gradient of composition (a Si-rich core and an Al-rich periphery, synthesis details in experimental chapter) with TPAOH. In this chapter, this synthesis method is also extended to Pt encapsulated hollow ZSM-5. To distinguish this sample, it is denoted w-Pt@ZSM-5-DR (w for metal loading in wt. % detected by ICP and DR for Directly dissolution/Recrystallization). TEM images of 1.02-Pt@ZSM-5-DR are shown in Fig. 3. The zeolites were completely re-crystallized in the presence of TPAOH with regular cavities; each cavity contains one particle separately with a relatively narrow Pt particle size distribution (more than 50% particles are between 10 to 13nm in size). In contrast to the post Al adding method, the dissolved core of the zeolite crystals contains less aluminum than the surface. Upon recrystallization in the presence of TPAOH, the surface of hollow crystals is enriched in silicon resulting in crystals with more aluminum on the inner surface. Since the Al content is not as high as for samples prepared by post Al addition, the surface of hollow crystals is flat and does not exhibit roughness. Herein, the recrystallization is performed without adding Al in TPAOH so the overall Si/Al ratio remains almost constant (Si/Al ratio of 75 in the parent ZSM-5 and 70 in 1.02-Pt@ZSM-5-DR).

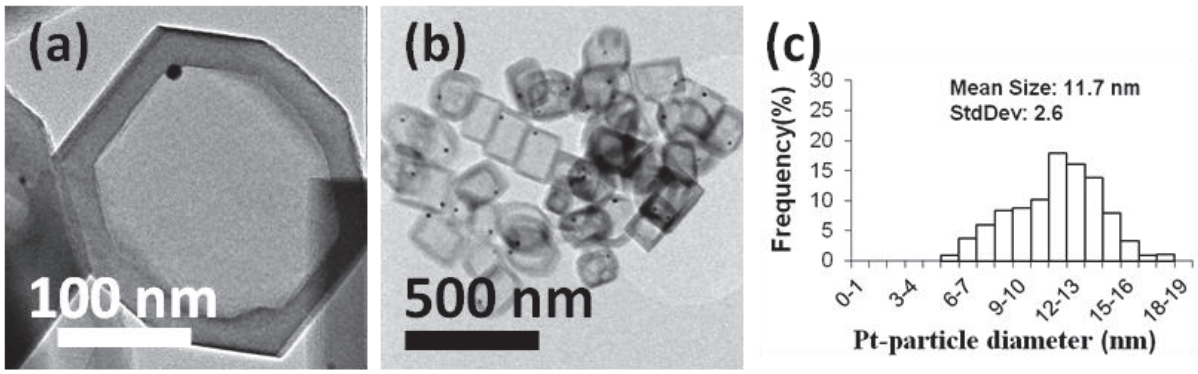

Figure 3: TEM images (a and b) and Pt particle size distribution (c) of 1.02-Pt@ZSM-5-DR, Si/Al=70 detected by ICP-OES.

However, through this synthesis method, some of the metal species are introduced into ZSM-5 by ion exchange; this difference somehow limits the extension to anionic metal precursors in solution, as it is the case for Au ($AuCl_4^-$ in the aqueous solution). Indeed, 0.62-Au@ZSM-5-DR sample prepared following the same recipe did not show Au particles encapsulated in ZSM-5 but exclusively very big Au particles outside hollow ZSM-5 crystals (Fig.4).

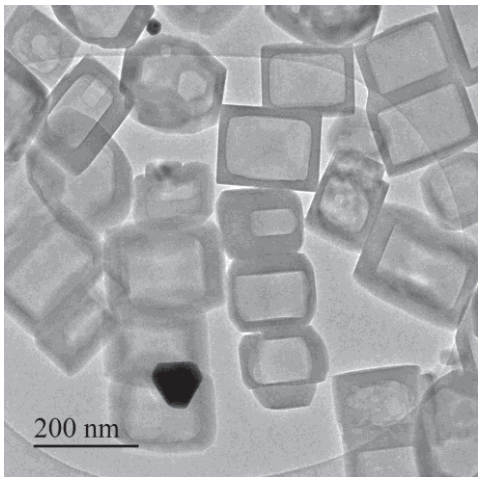

Figure 4: TEM image of 0.62-Au@ZSM-5-DR.

Herein, hollow ZSM-5 prepared by these two methods which involve a dissolution recrystallization mechanism exhibit opposite Al distributions in the shell, the PA method being more general for introducing metals into the starting zeolites.

II.2. Desilicalition route (DS) with Na_2CO_3 for preparing hollow ZSM-5

Though the synthesis of hollow ZSM-5 by treating ZSM-5 crystals using Na_2CO_3 solution have been previously reported by other groups,[6, 7] most of the parameters to control synthesis processes have not been studied in details. Herein, we have first studied the influences of the concentration of Na_2CO_3 and Si/Al ratio of parent ZSM-5 on the formation of hollow ZSM-5. Then metal nanoparticles encapsulated in hollow ZSM-5 were obtained through this desilicalition route.

II.2.1. Influence of Na_2CO_3 concentration

First, ZSM-5 nanocrystals with pronounced Al zoning were prepared. Similar to dissolution recrystallization with TPAOH, this condition is necessary to get hollow ZSM-5 structures upon preferential desilication of the silica-rich core with respect to the Al-rich outer surface. Typically, the calcined ZSM-5 zeolites were treated with a Na_2CO_3 solution for 12 hours at 80°C (details in experimental chapter). In order to investigate the influence of Na_2CO_3 concentration on the characteristics of ZSM-5, the concentration of the Na_2CO_3 solutions was modified from 0.6M to 1M. To distinguish this sample, it is denoted ZSM-5-DS-x (DS for desilication, x is the concentration of Na_2CO_3 solution with the unit of mole/L). The shell thickness of the resulting zeolites was tunable from 30nm to 6nm when the concentration of Na_2CO_3 solution increased from 0.6 to 1 mol/L (see Fig. 5). At lower Na_2CO_3 concentration, the center of the crystals looks very porous, which confirms that the desilication first occurs at the center of the crystals (Fig. 5-b). When 0.8 mole/L Na_2CO_3 solution is used, the resulting zeolites possess a regular hollow shape with a wall thickness of approximately 20 nm (Fig. 5-c). Moreover, the wall thickness can be decreased down to 10 nm by

treating ZSM-5 with 1 mole/L Na_2CO_3, nevertheless, very thin walls make zeolites fragile and some of the shells appear broken (Fig. 5-d). Such a thin zeolite will be definitely useful in catalysis due to the significantly reduced mass transfer limitation.

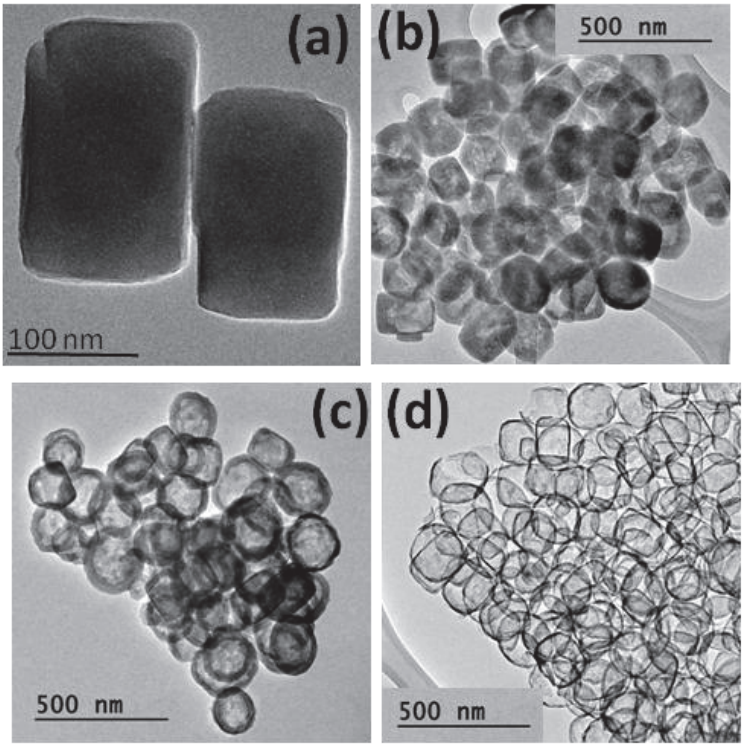

Figure 5: TEM images of calcined ZSM-5 crystals (a), hollow ZSM-5-DS treated by 0.6M Na_2CO_3 (b), 0.8M Na_2CO_3 (c), 1M Na_2CO_3 (d).

Meanwhile, as the concentration of Na_2CO_3 for desilication increased, the x-ray diffraction peaks of the corresponding hollow zeolites became broader, (see Fig. 6). The XRD patterns of ZSM-5-DS-0.6 show relatively narrow characteristic diffraction peaks of ZSM-5, while those of ZSM-5-DS-0.8 and ZSM-5-DS-1 exhibit significant broader peaks, consistent with small coherent domains within the shell, as already observed in the case of MFI nanosheets.[8]

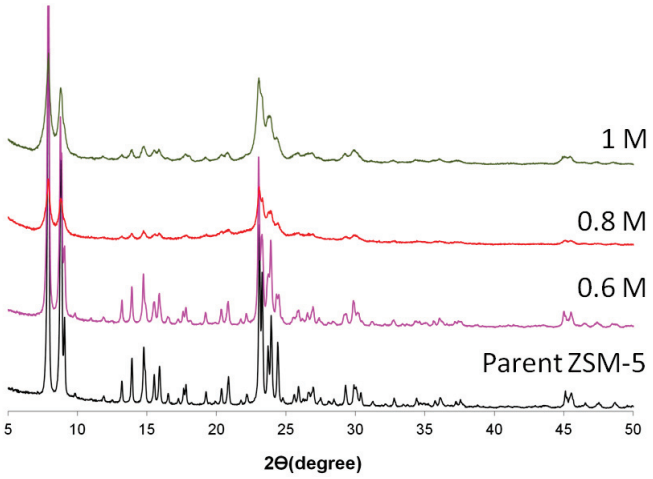

Figure 6: XRD patterns of parent ZSM-5 and ZSM-5-DS treated by 0.6M, 0.8M and 1M Na_2CO_3.

N_2 adsorption/desorption isotherms of ZSM-5-DS-0.6 showed a hysteresis loop with closure at P/P_0=0.45, characteristic of fully closed structures accessible by pores smaller than 4 nm. While at higher concentration (1M), the hysteresis disappeared (Fig. 7), suggesting that the hollow shells were broken and contained many macroscopic defects in agreement with TEM observations (Fig. 5). The corresponding porous properties of these ZSM-5 materials are given in Table 1, which shows a significant increase in total pore volume in the sample treated by higher concentration of Na_2CO_3 solutions. This corresponds to inter-particular mesoporosity resulting from the disordered stacking of nanoshells.

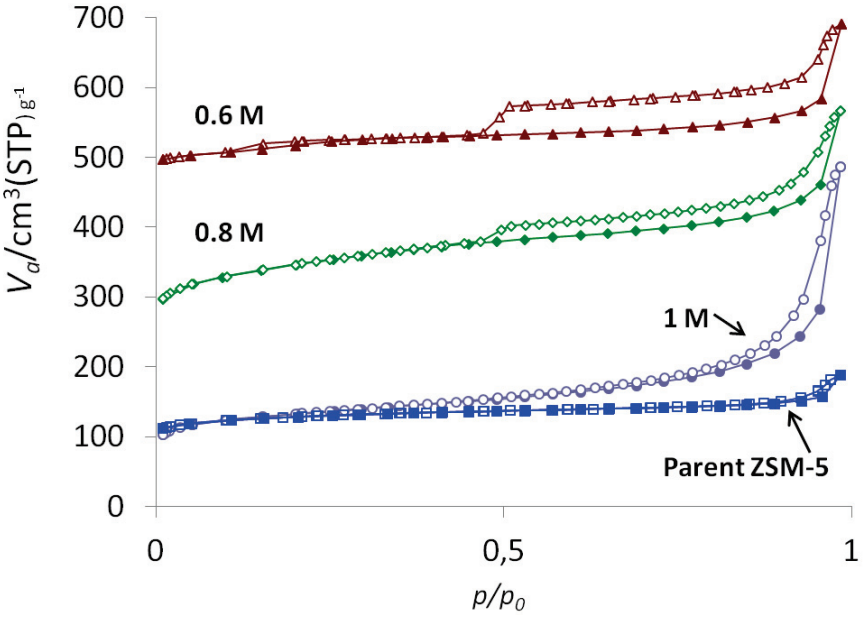

Figure 7: N_2 adsorption/desorption isotherms of (top-down order) hollow ZSM-5-DS treated by different concentration of Na_2CO_3 solutions and bulk ZSM-5, the isotherms of 0.8M and 0.6M shift upwards 200cm^3 and 400cm^3 for comparison.

Additionally, Al contents of the parent ZSM-5 and the three hollow ZSM-5-DS samples were detected by ICP-OES; the thickness of the hollow ZSM-5-DS was estimated from 40 different crystals in TEM images (Table 1). The thickness is decreasing from 31 to 6 nm, while the Si/Al ration varies from 84 to 24, as compared to 103 in the original ZSM-5. These results further confirm that the desilication process is achieved by partial removal of Si-rich regions of the crystals. Moreover, this desilication method usually leads to an increase amount of Na cations in the prepared hollow ZSM-5 shells (0.28wt. % Na in parent ZSM-5 increase to 1.6% in ZSM-5-DS-1), as it is known that sodium is a catalyst poison for some reactions such as Fisher-Tropsch synthesis. An ion exchange process has been carried out over ZSM-5-DS-1 sample in a NH_4NO_3 solutions at 90°C, after 3 times repetition of exchanging with NH_4NO_3 solution followed by washing with water (details in experimental chapter), the resulting hollow ZSM-5 shell contains very small amount (ppm level) of Na.

Table 1: Textural properties of parent ZSM-5 and hollow ZSM-5-DS obtained by different concentration of Na_2CO_3

Sample	Si/Al[a]	Thickness (nm)	S_{BET} cm^3/g	V_{micro} cm^3/g [b]	V_{meso} cm^3/g[c]	V_{total} cm^3/g
ZSM-5-parent	103	-	417	0.16	0.11	0.29
ZSM-5-DS-0.6	84	31	397	0.12	0.32	0.45
ZSM-5-DS-0.8	53	14	504	0.10	0.42	0.57
ZSM-5-DS-1	24	6	439	0.13	0.61	0.75

[a] Determined by ICP-OES, [b] Determined by t-plot method, [c] Determined by BJH method.

II.2.2. Influence of aluminum containing in parent ZSM-5

Two other parent ZSM-5 zeolites were prepared similarly but with lower Al contents (Si/Al= 280 and 493, respectively). Considering that lower Al content may reduce the stability of the zeolite upon the alkaline treatment, the desilication treatments have been carried out with 0.6 mole/L Na_2CO_3 solutions at 80°C for 12 hours. The TEM images of the obtained hollow ZSM-5 are given in Fig. 8. In contrast to hollow ZSM-5 obtained by treating parent ZSM-5 with Si/Al=103 (Fig.5b), hollow ZSM-5 shells obtained by treating parent ZSM-5 with Si/Al=280 possess very thin and partially broken walls with some amorphous material both inside and outside of the crystals (Fig.8-a and b). The N_2 adsorption/desorption isotherms confirm the destruction of the hollow shells and the partial amorphization of the structure, with a BET surface area of 327 m^2/g compared to 417 m^2/g for the parent zeolite (Fig. 9). In the case of treating parent ZSM-5 with Si/Al=493, the obtained hollow ZSM-5 are significantly destroyed due to a lack of aluminum and desilication throughout the crystals (Fig8.-c and d).

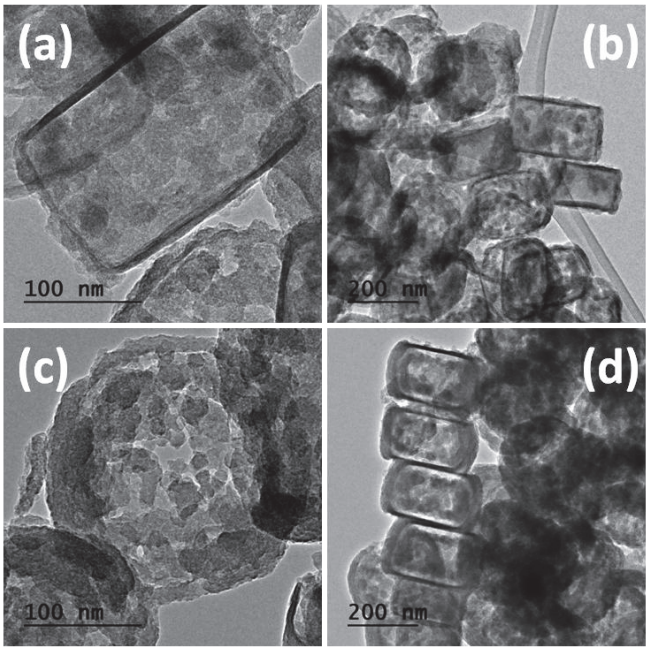

Figure 8: TEM images of hollow ZSM-5 obtained by treating parent ZSM-5 with different Si/Al, 280 (a and b) and 493 (c and d) with 0.6 M Na_2CO_3 solution at 80°C for 12 hours.

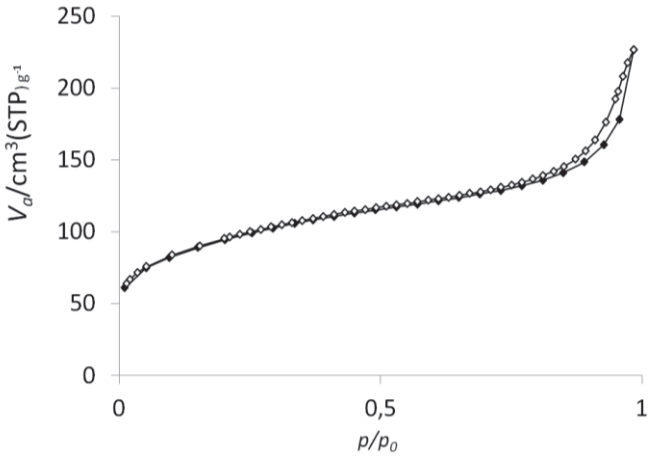

Figure 9 : N_2 adsorption/desorption isotherms of hollow ZSM-5 obtained by treating parent ZSM-5 with Si/Al=280 with 0.6M Na_2CO_3 at 80°C for 12hours.

The aluminium in ZSM-5 structure plays a key role in the desilication process, which can stabilize the zeolite structure against collapse under alkaline treatment and determine the morphology of the resulting hollow ZSM-5 shell. Thus, from the above observations and discussion, the parent ZSM-5 with Si/Al around 100 seems to be preferred for the synthesis of hollow shells with tunable thickness even down to 10 nm, which will be used in the synthesis of metal nanoparticle encapsulated in hollow ZSM-5.

II.3. Synthesis of metal particles in hollow ZSM-5 by desilication method

II.3.1. Pt@ZSM-5-DS

Pt encapsulated in hollow ZSM-5-DS (hollow ZSM-5 is obtained through desilication route) is prepared by treating Pt containing ZSM-5 crystals with 1M Na_2CO_3 solution (synthesis details in experimental chapter). By contrast to silicalite-1 crystals, Pt^{2+} cations were also introduced into ZSM-5 by ion-exchange of Na^+ cations in the channel. Most of the Pt species were retained in hollow structures since they were originally located in the Al-rich outer region of the ZSM-5 crystals through the ion-exchange process. At this stage, TEM image clearly shows that Pt particles around 1 nm in size formed inside an approx.12nm thick ZSM-5 shell (Fig.10-a; HRTEM image in upper left corner).

After reduction at 500°C under H_2, Pt particles sintered and grew from 1nm to a mean size of 2.6nm with a narrow particle size distribution and a total absence of particles larger than 4.5 nm (see Fig. 10-b, c and d). The sample is named as 1.5-Pt@ZSM-5-DS (1.5 wt. % Pt detected by ICP-OES). In contrast to Pt@Sil-1 materials[1] (details in chapter 3) obtained by dissolution recrystallization with TPAOH, of which Pt was confined and sintered into a unique particle inside each shell; for 1.5-Pt@ZSM-5-DS sample, TEM and HAADF images clearly show hundreds of Pt particles with a diameter of 2 to 3nm dispersed throughout the hollow shells, most of them being located in the walls or near the inner-surface of the shell. Those small particles were very stable and they did not merge upon reduction at 500°C, probably because of the strong interaction between Pt particles and the zeolite.

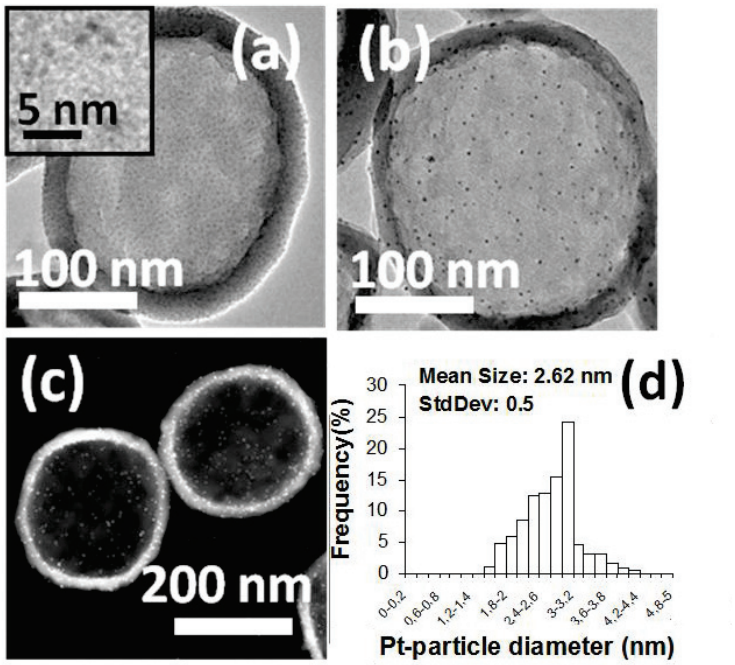

Figure 10: TEM images of 1.5-Pt@ZSM-5-DS before reduction(a), reduced at 500°C (b), STEM HAADF image of 1.5-Pt@ZSM-5-DS reduced at 500°C(c) and Pt particle size distribution (d).

Single-tilt tomography (from 78°to -38.5°, limited by the grid shadowing) of 1.5-Pt@ZSM-5-DS was also performed on an ETEM (Cs-corrected Titan ETEM G2 FEI microscope) to get 3-dimensional information for further identifying the location of Pt particles in the hollow shells. Fig. 11 is the video frames of the continuous tilting series, the red arrows indicating the fragmentation of the hollow ZSM-5 shells which has been previously reported for the non-metal containing shells obtained under similar conditions. And the blue ones show the rough inner-surface of hollow ZSM-5 shell which can be distinguished for particular sample positions in single titled tomography.

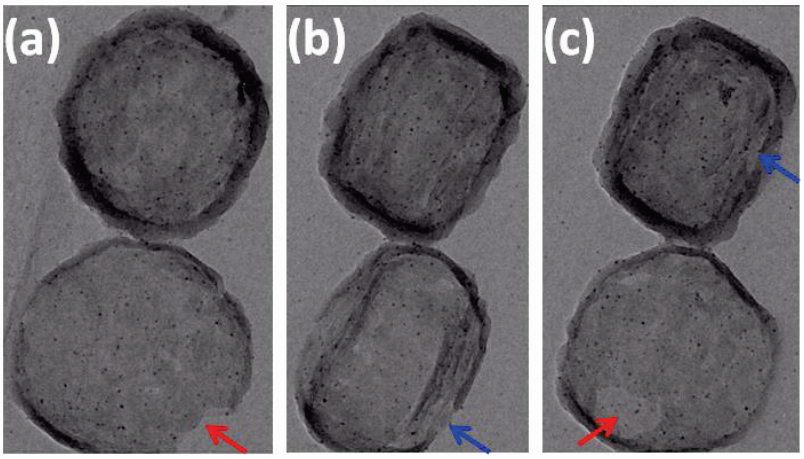

Figure 11: video frames of single-tilt tomography of 1.5-Pt@ZSM-5-DS sample. The limits of a continuous tilting series acquired in bright field in less than 4 minutes from 78°to -38.5°, limited by the grid shadowing.

Thus, the stability of the Pt particles in hollow ZSM-5 shell could result from a highly rough internal surface of hollow structures, which significantly reduces the aggregation of atoms and thus prevents sintering at high temperature.

High resolution HAADF image of 1.5-Pt@ZSM-5-DS sample taken from a broken shell shows Pt particle (the bright spot on the upper right in Fig.12) supported on zeolite. The zeolite structure is resolved at the atomic scale with silicon atoms appearing as the bright points surrounded black holes which correspond to the channels of the zeolite. The black rectangle represents the framework of MFI zeolite and the ball-and-stick structure is the theoretical one for MFI zeolite (blue balls represent Si atoms and red balls for O atoms). As we can see both theoretical illustrations fit our HAADF observations perfectly, supporting the ultra-thin and highly crystalline of the ZSM-5 shell.

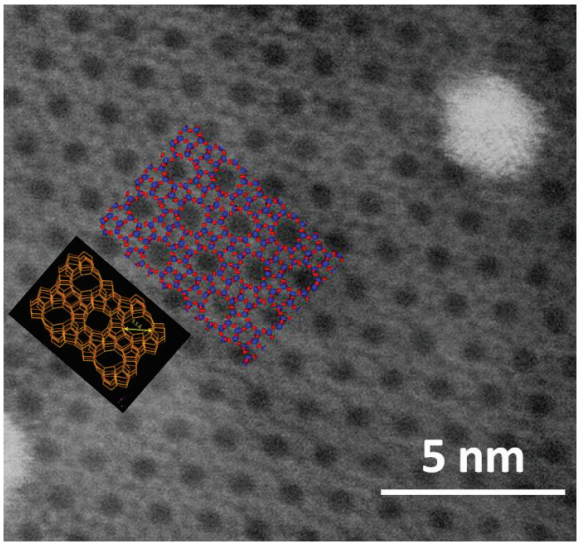

Figure 12: High resolution HAADF image of 1.5-Pt@ZSM-5-DS sample, the black rectangular is the theoretical channel of MFI zeolite, the ball-stick structure is to emphases the Si (blue balls) and O (red balls) atoms in the image, the bright particle on the upper right is a Pt particle.

Another 0.34-Pt@ZSM-5-DS sample was also prepared by treating ZSM-5 crystals with lower Pt loading by Na_2CO_3 solutions; TEM images and particles size distribution are given in Fig. 13. In contrast to the dissolution recrystallization route in which the particle size was depending on the metal content, the particle size is almost identical in both materials obtained by desilication method (Fig. 10 and 13).

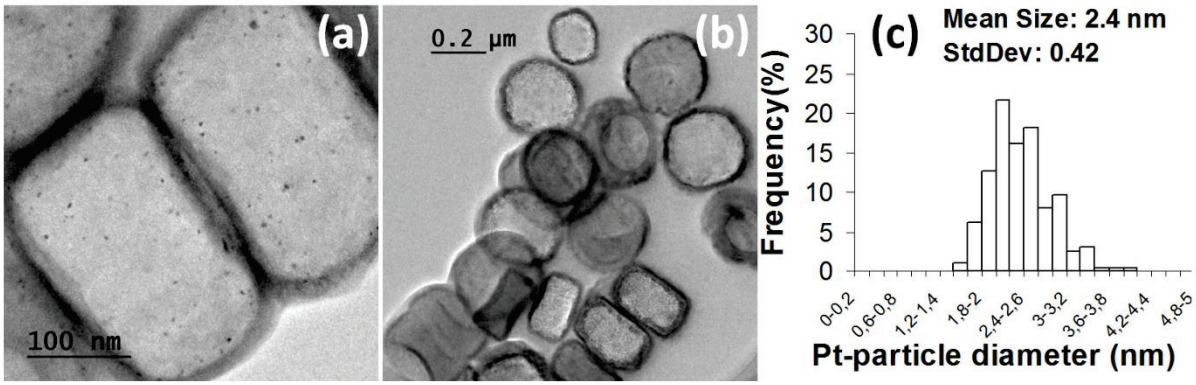

Figure 13: TEM images of 0.34-Pt@ZSM-5-DS (a and b) and Pt particle size distribution (c).

II.3.2. Co@ZSM-5-DS and Ni@ZSM-5-DS

Taking into account the significant increase of Al content in the hollow ZSM-5 shells compared to that of parent ZSM-5 (Table 1), hollow ZSM-5 crystals prepared by desilication method may be a promising catalyst for acid-catalysed reactions such as Fluid Catalytic Cracking (FCC) reactions.[9] Meanwhile, Fischer-Tropsch synthesis (FTS) is one of the most investigated catalytic processes which produce liquid fuels from syngas (mixture of CO and H_2). The products of FTS synthesis are normal hydrocarbons, while short-chain isoparaffins and alkylates with high octane numbers are preferential products as liquid fuels. An ideal catalyst for FTS is a bifunctional catalyst[10], in which acid sites catalyze the (hydro) cracking and (hydro) isomerization while hydrogenation and hydrogenolysis occur on metal sites, typically group-VIII metals such as Fe, Co or Ni.

Herein, Co and Ni encapsulated in hollow ZSM-5 materials have been prepared by desilication of ZSM-5 using 1 M Na_2CO_3 solutions. Compared to ZSM-5 crystals treated by TPAOH, more cobalt phyllosilicates are formed in the hollow ZSM-5 shell, which thickness is between 10 to 15 nm after desilication (see Fig. 14-a and b, red arrows indicate cobalt phyllosilicates) suggesting higher Co loading in the sample. A cobalt content of 18.5 % is detected by ICP-OES, which is more than twice that of Co@ZSM-5 obtained by TPAOH treatment (7.4% Co). The majority of the hollow crystals are covered with cobalt phyllosilicates which may lead to changes in the shell morphology during the reduction.

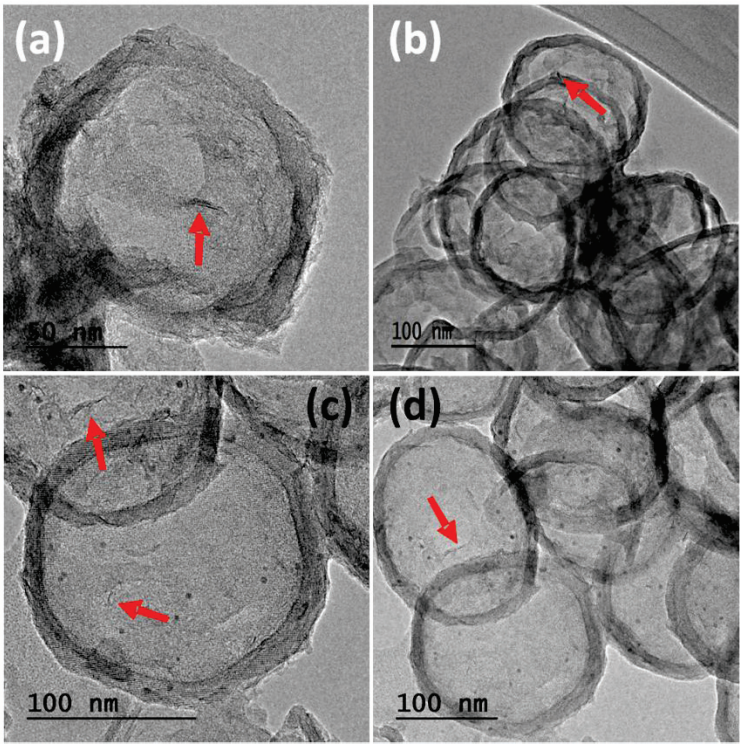

Figure 14: TEM images of 18.5-Co@ZSM-5-DS sample before reduction (a and b) and after the reduction at 500°C for 10 hours (c and d). Arrows indicate cobalt phyllosilicates.

Considering the high Co loading in the desilicated sample, the reduction is carried out first at 500°C under H_2 for 10 hours. Co particles with diameters approximately 3 nm co-exist with cobalt phyllosilicates in hollow ZSM-5 crystals (see Fig. 14-c and d), indicating that a higher reduction temperature is needed to get complete reduction of Co species.

After reduction at 750°C, most of the cobalt phyllosilicates have been reduced and Co particles with a mean diameter of 9.2 nm were formed (Fig.15). TEM images clearly show that most of Co particles are located near the zeolite shells, some of them seem to be in the shell or protected by a layer of zeolite-like material. The zeolite shells seem more destroyed after the reduction and a Si/Al ratio of 44 given by ICP-OES. Here, we can propose that during the reduction step the highly dispersed Co phyllosilicates are reduced under hydrogen, the great changes in volume from cobalt phyllosilicates to cobalt particles lead to the fragmentation of the ultra thin zeolite shell, and then Co particles grow by sintering with the particles nearby.

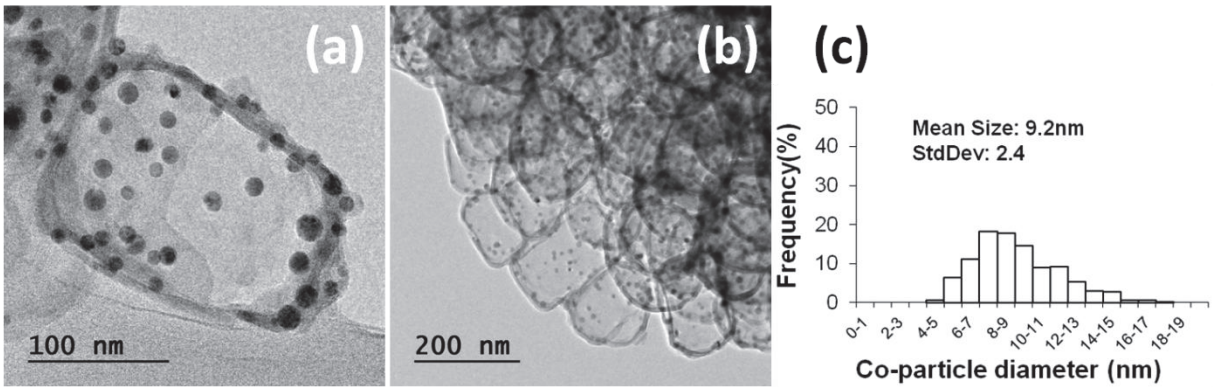

Figure 15: TEM images (a,b)and Co particle size distribution (c) of 18.5-Co@ZSM-5-DS sample, obtained by desilication with 1M Na_2CO_3 then reduced at 750°C for 3 hours.

Herein, lower concentrations of Na_2CO_3 have been used for the desilication of Co containing ZSM-5 crystals. In the case of 0.8 M Na_2CO_3, the majority of the shells are still broken and the wall thickness remains relatively constant (approx. 10 to 15 nm for each, Fig. 16). However, the mean particle size decreased from 9.2 to 7.1 nm by using 0.8 M Na_2CO_3 solution instead of 1M, suggesting the improved sinter stability of the Co particle by using 0.8M Na_2CO_3.

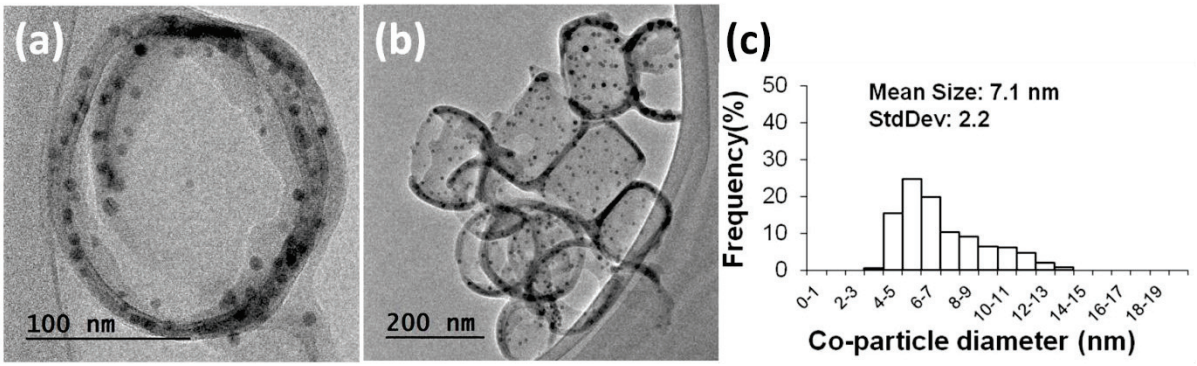

Figure 16: TEM images (a,b)and Co particle size distribution (c) of 18.5-Co@ZSM-5-DS sample, obtained by desilication with 0.8M Na_2CO_3 then reduced at 750°C for 3 hours.

As previously discussed, Co particles are likely formed through reduction and sintering processes. In the sintering step, the morphology of the inner surface of the zeolite shell can limit the particle sintering, a mechanism similar to that observed on Pt@ZSM-5-DS samples.

In the case of 0.6M, the hollow ZSM-5 shells seem intact with wall thickness very similar to those obtained by 0.8 and 1 M Na_2CO_3 solutions (Fig.17). The Co particles with a mean size of 4.5 nm (more than 90% of the Co particles are between 3 to 6 nm) are dispersed throughout ZSM-5 hollow shell. This is confirmed by our previous proposition that the morphology of the hollow zeolite shell affects the particle sintering process, thus resulting in a particular particle size under the corresponding desilication treatment.

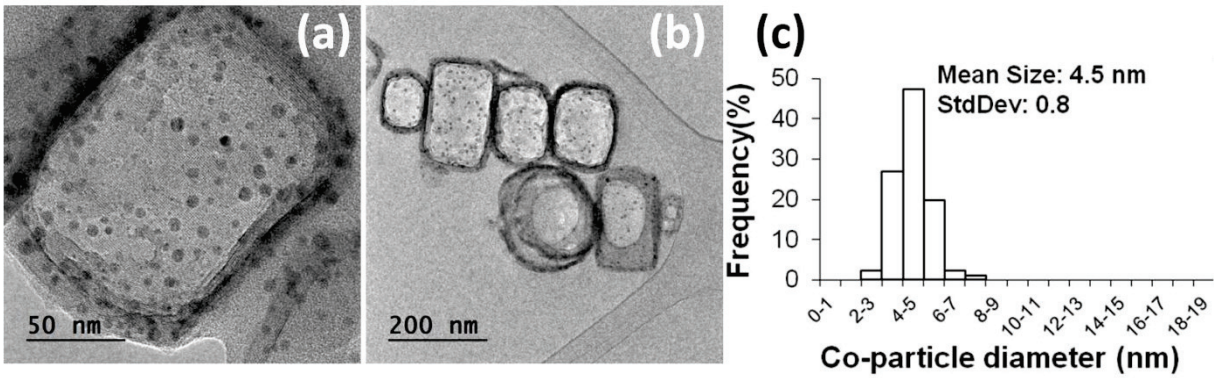

Figure 17: TEM images (a,b)and Co particle size distribution (c) of 18.5-Co@ZSM-5-DS sample, obtained by desilication with 0.6M Na_2CO_3 then reduced at 750°C for 3 hours.

Si/Al ratios of 18.5-Co@ZSM-5-DS materials treated by 1M and 0.6 M Na_2CO_3 solution are 45 and 77, respectively (given by ICP-OES), suggesting more integrity of the hollow shell at lower Na_2CO_3 concentration treatment. Herein, the reducing fragments of zeolite shell obtained by lower concentration of Na_2CO_3 solution leads to a smaller Co particle size upon reduction at 750°C. Furthermore, similar as Pt@ZSM-5-DS samples, Co particles are preferentially located near the zeolite shell as shown in Fig.17.

Since the same Co containing ZSM-5 crystals were used for these three treatments, and TEM images of the hollow samples show similar constitutions, Co percentages are expected to be 18% for the samples obtained by 0.8 and 0.6 M Na_2CO_3. The shell thickness of hollow ZSM-5 shown in Fig.17 is between those of cobalt-free zeolites treated with 0.8 and 1M solutions (Fig. 5-c, d). This difference may be due to the formation of cobalt phyllosilicates simultaneously to desilication, which are both silica consuming. Thus, thinner hollow shell is obtained under the same desilication treatment when cobalt is present, which is also confirmed by TEM (Fig. 17-b and Fig. 5-b).

The HRTEM image and the corresponding Fast Fourier Transform (FFT) diffraction patterns of a Co particle from 18.5-Co@ZSM-5-DS sample obtained by 0.6M Na_2CO_3 treatment are given in Fig. 18. The interplanar angles along (-101), (101) and (002) planes are measured from the diffraction

patterns and the corresponding interplanar spacings are given in Fig. 18 (a) and Table 2. The interplanar lattice spacing along *a* axis are 1.96, 1.94 and 2.04 A° respectively which is consistent with the unit cell parameter of hexagonal metallic cobalt particles along *a*-axis (*a* = 1.915, 1.915 and 2.035, see Table 2). [0-20] is the axis perpendicular to the image planar, which is calculated from the 3 known plans on the image.

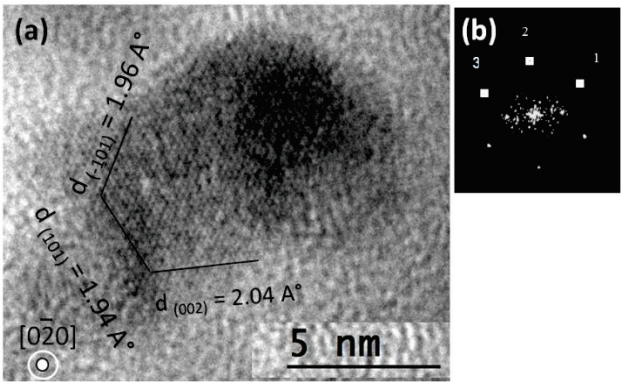

Figure 18: HRTEM picture (a) and corresponding Fast Fourier Transform (FFT) diffraction patterns (b) of a cobalt particle from 18.5-Co@ZSM-5-DS treated by 0.6M Na_2CO_3 reduced at 750°C for 3 hours sample.

Table 2: The experimental and theoretical of interplanar spacings and interplanar angles of cobalt metallic particle

Spot	Observed d-Spacing (*a*) (Å)	Measured angles to spot 1(°)	Theoritical d-Spacing (*a*)[1] (Å)	Theoritical angle between plans[1] (°)	HKL
1	1.94	0	1.915	0	101
2	2.04	61.13	2.035	61.94	002
3	1.96	122.98	1.915	123.88	-101

[1] Theoritical data from International Centre for Diffraction Datametallic (ICDD), file number: 89-4308, hexagonal metallic cobalt

The XRD patterns of parent ZSM-5 and Co containing hollow ZSM-5 materials are given in Fig. 19. Compared to XRD patterns of Co-free samples (Fig. 6), diffraction peaks are significantly broader and their intensity is considerably reduced, suggesting that the shell thickness is not the only parameter that affects the patterns. Indeed, even at the lowest concentration (0.6 M), the XRD patterns shows only broad reflections around 8 and 23°, and these peaks almost completely disappear when the concentration reaches 1M. The decrease in intensity may result from a partial collapse of the zeolite structure in the presence of high Co loading. Indeed, the appearance of a very broad signal between 20 and 30° supports a significant loss of crystallinity, which will be confirmed later by N_2 adsorption measurements. However, fluorescence due to the very high Co content also certainly modifies the

intensity of the signal. Meanwhile, all of the three Co hollow ZSM-5 samples show the characteristic diffraction peaks of metallic cobalt indicated by the peaks between 40 and 50° which can be assigned to both the hexagonal (JCPDS 05-727) and cfc cubic (JCPDS 015-806) lattices. Co particle sizes are estimated by using Scherrer's equation (details in experimental chapter) on the peak around 44.5° indicating by the red square in Fig. 19 which is the characteristic diffraction peak of both cubic and hexagonal metallic cobalt. The results are given in Table 3, which are consistent with those obtained by TEM observations. Thus, cobalt particles with different diameters can be encapsulated in hollow ZSM-5 shells with similar thickness by treating the zeolite by Na_2CO_3 solutions with various concentrations.

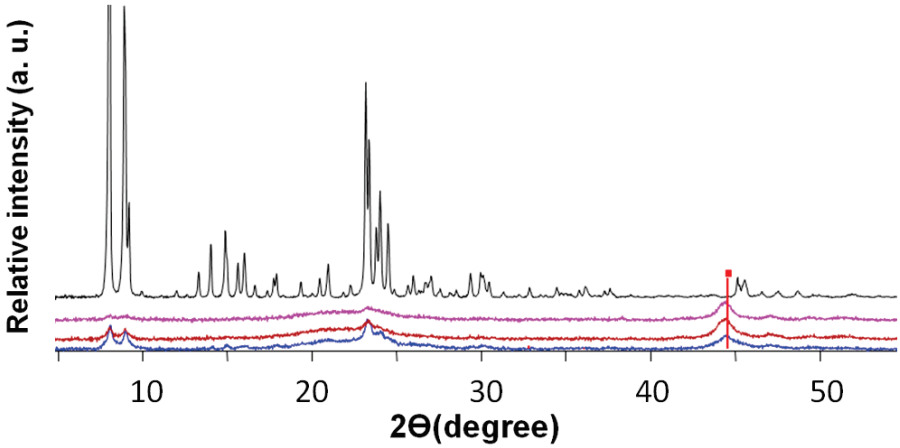

Figure 19: XRD patterns of parent ZSM-5(black line), 18.5-Co@ZSM-5-DS treated by 1M Na_2CO_3 (pink line); 0.8M Na_2CO_3 (red line) and 0.6M Na2CO3 (blue line). Red squares indicating the characteristic diffraction peak used for cobalt particle size estimation using Scherrer's equation, which belongs to both cubic and hexagonal metallic cobalt.

Table 3: Si/Al ratio and Co particle size of 18.5-Co@ZSM-5-DS samples prepared by zeolite desilication with different concentration of Na_2CO_3 solutions. Particle sizes are obtained from Scherrer's equation using XRD patterns and TEM observations.

C_{Na2CO3}[a]	Si/Al[b]	XRD	TEM
0.6	77	5 nm	4.5±0.8 nm
0.8	-	7.3 nm	7.1±2.2 nm
1.0	44	9.1 nm	9.2±2.4 nm

[a]: C_{Na2CO3} representing concentration of Na_2CO_3 solution in mole/L; [b] detected by ICP-OES.

N_2 adsorption/desorption isotherm of 18.5-Co-ZSM-5-DS obtained by treating the zeolite with 0.6 M Na_2CO_3 (Fig. 20) is quite different from that obtained in the absence of cobalt (Fig. 7). First, the BET surface area is significantly lower (224 m^2/g), thus confirming the decrease of crystallinity observed by XRD. Also, the hysteresis loop with closure at P/P_0=0.45 is small compared to that of the Co-free

ZSM-5-DS-0.6 (Fig.7), suggesting that part of the hollow shells are broken and contain many macroscopic defects. The broken crystals are also likely responsible for the huge N_2 uptake at $p/p_0 >$ 0.9.

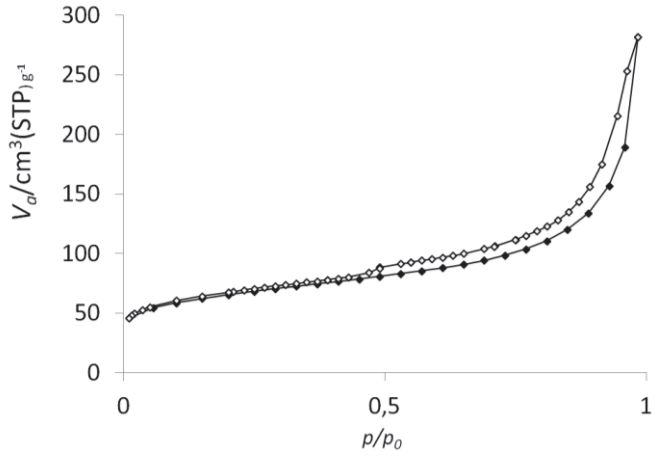

Figure 20 : N_2 adsorption/desorption isotherms of Co@ZSM-5-DS obtained by desilication with 0.6M Na_2CO_3 then reduced at 750°C for 3 hours.

Another sample with 3% Co loading was prepared by using a 0.6 M Na_2CO_3 solution for desilication; TEM images and Co particle size distribution are given in Fig. 21. Under similar treatment conditions, decreasing the cobalt loading results in a decrease in the number of particles per hollow shell, while keeping the size constant around 5 nm (Fig.17 and 21).

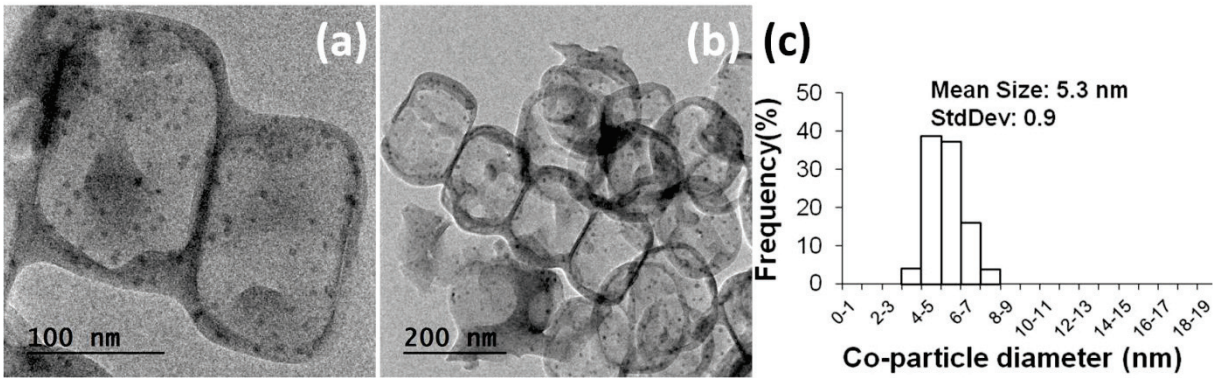

Figure 21: TEM images (a,b) and Co particle size distribution (c) of 3-Co@ZSM-5-DS, obtained by desilication with 0.6M Na_2CO_3 then reduced at 750°C for 3 hours.

This synthesis method is also extented to Ni encapsulated in hollow ZSM-5 materials. Similar to Co samples, Ni particles with diameter around 10 nm are encapsulated in hollow ZSM-5 shells with thickness of approximately 10 nm. Most of the shells are broken after the desilication in a 1M Na_2CO_3 solution, shown in Fig.22. A Ni loading of 21 wt. % and a Si/Al ratio of 40 are detected by ICP-OES, similar to those values obtained on cobalt containing samples. Thus, this desilication method to prepare metal particles encapsulated in hollow ZSM-5 shell is relatively reproducible. Materials

obtained by this method also possess significantly more metal sites per volume of catalyst as compared to those prepared using TPAOH.

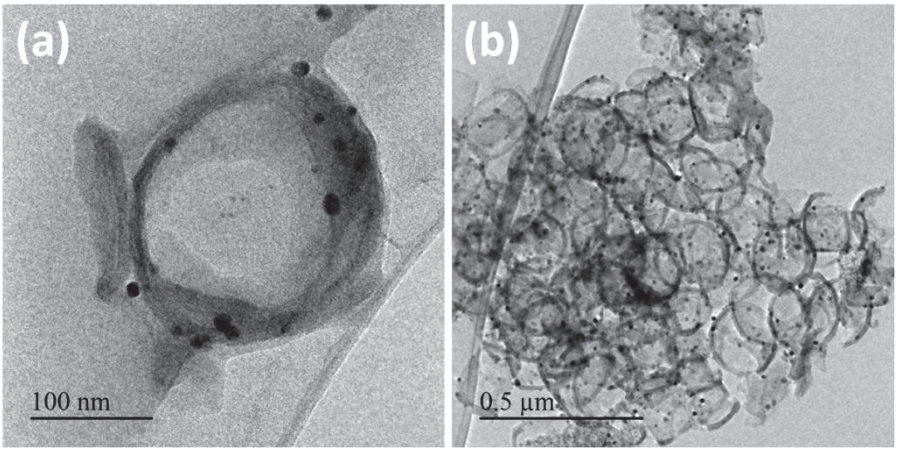

Figure 22: TEM pictures of 21-Ni@ZSM-5-DS, obtained by desilication with 1 M Na_2CO_3 then reduced at 750°C for 3 hours.

II.4. Sintering tests over Pt@ZSM-5-DS materials

To further study the thermal stability of Pt particles in hollow ZSM-5 shells, sintering tests have been carried out on 1.5-Pt@ZSM-5-DS sample under different conditions.

II.4.1. Sintering tests under hydrogen

1.5-Pt@ZSM-5-DS sample (2.62±0.5 nm, Fig. 10) previously reduced at 500°C was reduced again under hydrogen at 750°C for 3 hours. TEM images and Pt particle size distribution of the sample after 2nd time reduction at 750°C are given in Fig. 23. As we can see, neither the morphology nor the particle size significantly changed with temperature, supporting the high thermal stability of Pt particles under hydrogen. This particularly high stability results from an excellent dispersion of the particles, mainly due to a strong interaction with the inner surface of the shells, as previous discussed.

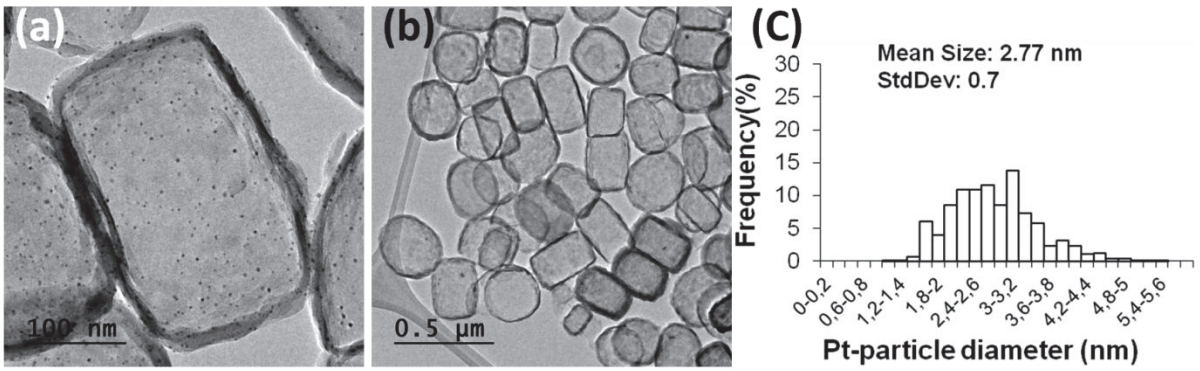

Figure 23: TEM images (a,b) and Pt particle size distribution (c) of 1.5-Pt@ZSM-5-DS reduced in H_2 at 750°C for 3 hours.

II.4.2. Sintering test under oxygen

Later on, the same compound (1.5-Pt@ZSM-5-DS; 2.62±0.5 nm; Fig. 10) was heated at 750°C for 2 hours in air. TEM images of the resulting material are given in Fig. 24. The extremely harsh conditions led to Pt sintering and the formation of a single large Pt particle with a size around 15 nm in each hollow crystal. The empty shells visible in Fig. 24-b correspond to broken crystals after desilication, in which Pt may sinter outside the shell.

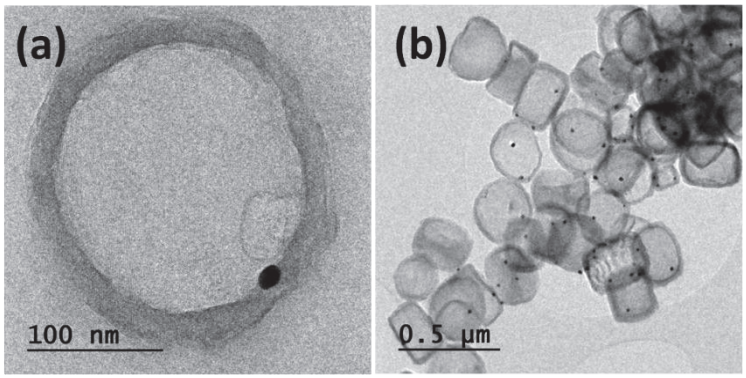

Figure 24: TEM images of 1.5-Pt@ZSM-5-DS calcined in air at 750°C for 2 hours.

II.5. Hydrogenation tests over Pt catalysts

The catalytic properties of metal nanoparticles encapsulated in hollow ZSM-5 materials prepared by dissolution recrystallization (1.02-Pt@ZSM-5-DR) and desilication (1.5-Pt@ZSM-5-DS) methods have been tested in the toluene and mesitylene hydrogenation reactions.

A Pt supported on ZSM-5 reference catalyst (0.98-Pt/ZSM-5 for short, 0.98 wt. % Pt content detected by ICP-OES, synthesis details in experimental chapter) was prepared by directly reducing Pt containing ZSM-5 crystals under the same conditions as those for Pt encapsulated samples. Due to the microporosity of ZSM-5, two populations of Pt particles were observed (see Fig. 25). A small fraction of Pt particles below 2 nm were located inside ZSM-5 crystals while the majority was located on the outer surface of the crystals with a board particle size distribution from 3 to 14nm.

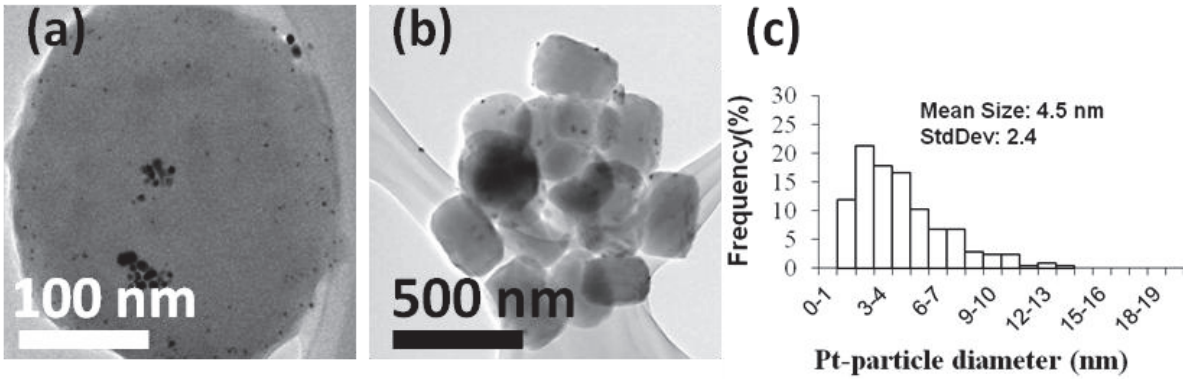

Figure 25: TEM images (a,b) and Pt particle size distribution (c) of 0.98-Pt/ZSM-5 sample.

Pt supported SiO_2 catalyst 0.5-Pt/SiO_2-P (0.5 % wt. Pt loading detected by ICP-OES) prepared by impregnation method (synthesis details in chapter 2 and characterizations in chapter 3) was also used as a reference catalyst.

N_2 adsorption desorption isotherms of 1.02-Pt@ZSM-5-DR, 1.5-Pt@ZSM-5-DS and 0.98-Pt/ZSM-5 samples are given in Fig. 26. As expected the micropore volume of these three Pt zeolite catalysts is exactly the same, which suggests that both dissolution-recrystallization and desilication processes do not change the microporosity of the zeolite (see also Table 4). Moreover, the appearance of a hysteresis at P/P_0 around 0.45 in 1.02-Pt@ZSM-5-DR material suggests the presence of closed cavities with entrance smaller than 4 nm, in contract to 1.5-Pt@ZSM-5-DS material for which hollow shells are completely destroyed, as previously discussed.

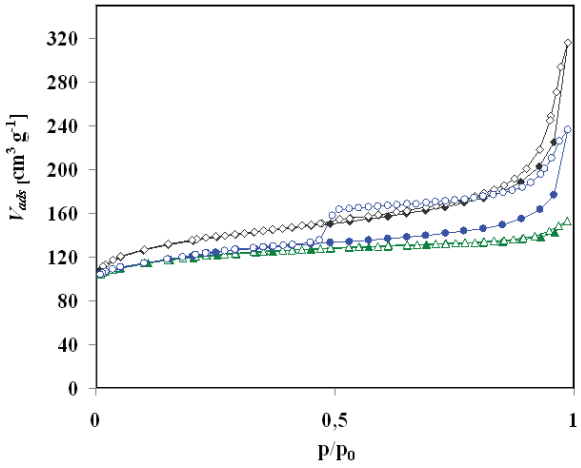

Figure 26: N_2 adsorption/desorption isotherms of (top-down order) 1.5-Pt@ZSM-5-DS (◆), 1.02-Pt@ZSM-5-DR (●) and 0.98-Pt/ZSM-5 (▲).

Table 4 depicts the main characteristics of the four catalysts. All zeolite-based catalysts possessed similar Pt loadings (0.98 - 1.50 wt. %) and very similar BET surface areas (from 388 to 444m^2g^{-1}).

Table 4. Characteristics of Pt zeolites and Pt supported SiO_2 catalysts

Catalyst	Pt diameter (nm)[a]	Dispersion (%)[b]	BET surface (m^2 g^{-1})	V_{micro} (cm^3 g^{-1}) [c]
1.02-Pt@ZSM-5-DR	11.7	11	397	0.15
1.5-Pt@ZSM-5-DS	2.6	42	444	0.15
0.98-Pt/ZSM-5	4.5	19	388	0.15
0.5-Pt/SiO_2-P	3.1	18	300	0

[a] Calculated by counting a minimum of 400 particles in TEM images; [b]Calculated assuming a cub-octahedral model [11]; [c]Determined by t-plot method.

This series of catalysts have been tested in gas phase hydrogenation of toluene and mesitylene as model reactions. The hydrogenation products were the corresponding saturated compounds. The proportion of reactant and product were determined through integration of two zones of C-H stretching spectral region in FT-IR spectrum (details in chapter 3).

The conversion curves of the four Pt based catalysts are given in Fig. 27. In toluene hydrogenation reactions, 1.5-Pt@ZSM-5-DS is 7 times more active than the 0.5-Pt/SiO_2-P reference catalyst at 100°C (Table 5) due to higher dispersed Pt particles as shown in Table 4, the TOF (turnover frequency expressed as molecules of reactant converted per second per surface Pt atoms) is even 137 times larger than for 0.98-Pt/ZSM-5 reference catalyst. A similar trend was also observed in the case of mesitylene hydrogenation. The hydrogenation rate over 1.5-Pt@ZSM-5-DS catalyst was 7 times higher than that of 0.5-Pt/SiO_2-P and 45 times higher than that of 0.98-Pt/ZSM-5 catalyst at 60°C.

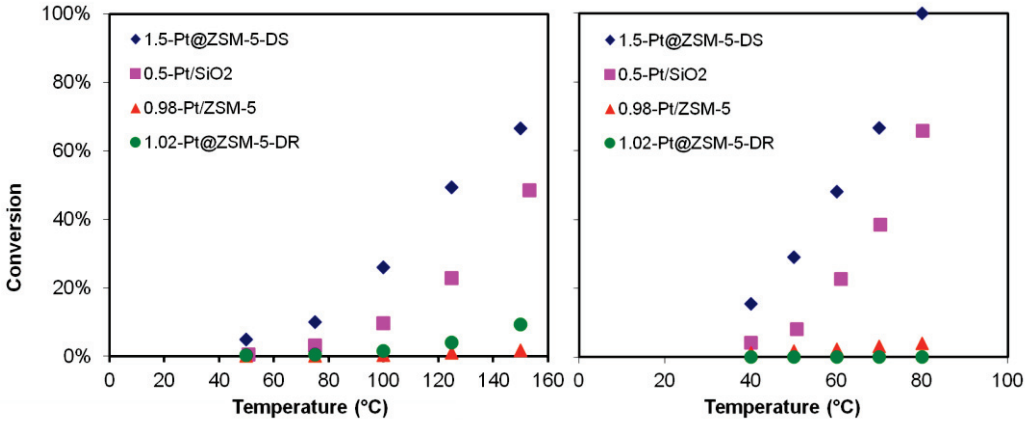

Figure 27: Conversion of toluene (left) and mesitylene (right) over 1.5-Pt@ZSM-5-DS, 0.5-Pt/SiO_2-P, 0.98-Pt/ZSM-5 and 1.02-Pt@ZSM-5-DR.

Table 5. Catalytic performance of Pt zeolites and Pt supported SiO_2 catalyst in toluene and mesitylene hydrogenations (Tol and Mes in the table for short)

Catalyst	Tol hydrogenation at 100°C		Mes hydrogenation at 60°C	
	Rate[1] (µmol $s^{-1}g^{-1}$)	TOF (s^{-1})	Rate[1] (µmol $s^{-1}g^{-1}$)	TOF (s^{-1})
1.5-Pt@ZSM-5-DS	4.10	0.13	0.68	0.021
0.5-Pt/SiO_2-P	0.60	0.13	0.078	0.017
1.02-Pt@ZSM-5-DR	0.18	0.03	0	0
0.98-Pt/ZSM-5	0.03	0.003	0.015	0.0016

[1]: Reaction rates expressed as molecules of reactant converted per second per gram of catalyst.

In the case of 1.02-Pt@ZSM-5-DR for which cavities are completely closed, mesitylene (kinetic diameter 0.87 nm) was not converted because it is too large to penetrate the zeolite pores (0.55 nm). Such size selectivity was also reported for xylene isomers: p-xylene (kinetic diameter 0.585 nm) was able to access the micropores of MFI type zeolite, whereas o- and m-xylene (kinetic diameters 0.68 nm) [12, 13] were not. Mesitylene conversions obtained on 1.5-Pt@ZSM-5-DS support the presence of macroporous defects in zeolite shells, as already evidenced by TEM and N_2 adsorption. The TOFs on 1.5-Pt@ZSM-5-DS, 0.5-Pt/SiO_2-P and 1.02-Pt@ZSM-5-DR are similar for both reactions, and at least one order of magnitude higher than for bulk 0.98-Pt/ZSM-5 catalyst. Activation energies of toluene hydrogenation were in the range of 31-47 kJ mol^{-1} for the four catalysts (see Fig. 28). TOFs and activation energies in this work were consistent with other Pt supported catalysts under similar experimental conditions.[14, 15]

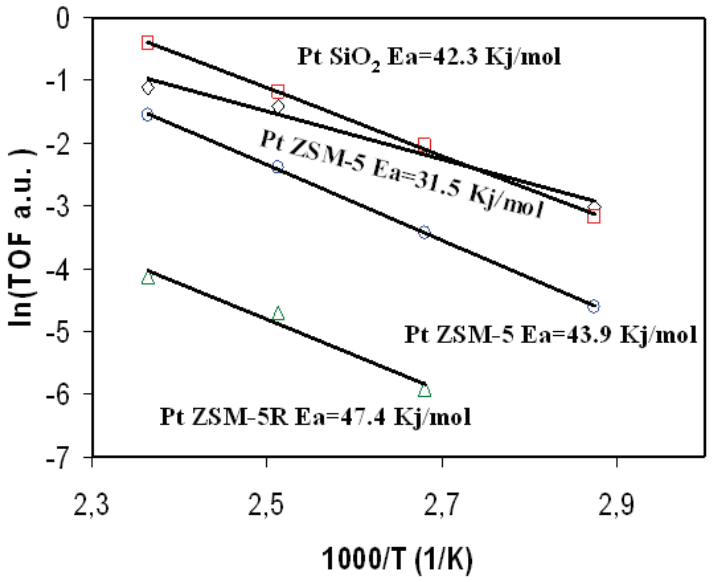

Figure 28: Arrhenius plots for toluene hydrogenation over Pt zeolite catalyst and 0.5-Pt/SiO2-P catalysts.

Data obtained on 1.02-Pt@ZSM-5-DR demonstrated the molecular sieving properties of the zeolite hollow shell similar to Pt@Sil-1 materials. The highly active 1.5-Pt@ZSM-5-DS catalyst confirms that all Pt particles are highly accessible to small gas molecules, which is crucial for applications in heterogeneous catalysis. The reference catalysts showed much less efficient, due to either diffusion limitations in zeolite pores or broader particle size distributions.

III.Conclusion

In conclusion, hollow ZSM-5 has been prepared by disolution recrystallization and desilication methods.

Through dissolution recrystallization method, hollow ZSM-5 can be obtained by starting either directly from ZSM-5 crystals (ZSM-5-DR, directly dissolution recrystallization) or from silicalite-1 in the presence of aluminum source (ZSM-5-PA, post aluminum adding). The obtained holllow ZSM-5 exhibit an Al distribution in the shell and the Si/Al ratio is limited to 50 due to the limited amount of dissolved silicon species from the parent zeolites. Metal nanoparticles encapsulated in hollow ZSM-5 have been prepared, resulting in a conventional yolk shell structure. The PA method is more general for introducing metals into the starting zeolites compared to DR route. The molecular sieving capacity has been demonstrated over 1.02@ZSM-5-DR material in the hydrogenation of toluene and mesitylene reactions; where toluene was the only molecule converted, mesitylene being too bulky to penetrate the zeolite micropores.

Regarding on zeolite desilication to create hollow zeolite, an easy, scalable and affordable method has been developed by using Na_2CO_3 as the alkaline agent for zeolite desilication. By modifying the synthesis process, the thickness of the ZSM-5 shell could be adjusted down to 10 nm, with Si/Al ratio as low as 24. Later, Pt particles encapsulated in hollow ZSM-5 has been synthesized, in which hundreds of Pt particles of approximately 2 to 3 nm in size are thermally stable even at high reduction temperatures (750°C), due to particle isolation by the rough inner surface of the zeolite shell. The method can be extended to other metals (Co and Ni) and the particle size can be easily adjusted by using different concentrations of Na_2CO_3 solutions without changing the thickness of the shell. These prepared bi-functional catalysts which combine the properties of metal particles with the acidity of the zeolite shell will be promising candidates in catalysis.

By contrast to TPAOH, the thin shells obtained with Na_2CO_3 were fragile and easily breakable, thus facilitating the accessibility of gas molecules to Pt particles. Catalysts prepared through this desilication method can not only minimize diffusion limitations through the zeolite shell but they are also thermally stable to 750°C in H_2 and show much higher reaction rates than standard supported catalysts in hydrogenation reactions.

Bibliography

1. Li, S., Burel, L., Aquino, C., Tuel, A., Morfin, F., Rousset, J.-L. & Farrusseng, D. Ultimate size control of encapsulated gold nanoparticles. *Chem. Commun.* **49**, 8507-8509 (2013).

2. Li, S., Boucheron, T., Tuel, A., Farrusseng, D. & Meunier, F. Size-selective hydrogenation at the subnanometer scale over platinum nanoparticles encapsulated in silicalite-1 single crystal hollow shells. *Chem. Commun.* **50**, 1824-1826 (2014).

3. Marcilly, C. Acido-basic catalysis: application to refining and petrochemistry, Vol. 2. (Technip Ophrys Editions, 2006).

4. Corma, A. & García, H. Lewis Acids: From Conventional Homogeneous to Green Homogeneous and Heterogeneous Catalysis. *Chem. Rev.* **103**, 4307-4366 (2003).

5. Wang, Y. & Tuel, A. Nanoporous zeolite single crystals: ZSM-5 nanoboxes with uniform intracrystalline hollow structures. *Microporous Mesoporous Mater.* **113**, 286-295 (2008).

6. Dessau, R.M., Valyocsik, E.W. & Goeke, N.H. Aluminum zoning in ZSM-5 as revealed by selective silica removal. *Zeolites* **12**, 776-779 (1992).

7. Mei, C., Liu, Z., Wen, P., Xie, Z., Hua, W. & Gao, Z. Regular HZSM-5 microboxes prepared via a mild alkaline treatment. *J. Mater. Chem.* **18**, 3496-3500 (2008).

8. Choi, M., Na, K., Kim, J., Sakamoto, Y., Terasaki, O. & Ryoo, R. Stable single-unit-cell nanosheets of zeolite MFI as active and long-lived catalysts. *Nature* **461**, 246-249 (2009).

9. Corma, A. Inorganic Solid Acids and Their Use in Acid-Catalyzed Hydrocarbon Reactions. *Chem. Rev.* **95**, 559-614 (1995).

10. He, J., Yoneyama, Y., Xu, B., Nishiyama, N. & Tsubaki, N. Designing a capsule catalyst and its application for direct synthesis of middle isoparaffins. *Langmuir* **21**, 1699-1702 (2005).

11. Van Hardeveld, R. & Hartog, F. The statistics of surface atoms and surface sites on metal crystals. *Surf. Sci.* **15**, 189-230 (1969).

12. Garcia, S.F. & Weisz, P.B. Effective diffusivities in zeolites 1. Aromatics in ZSM-5 crystals. *J. Catal.* **121**, 294-311 (1990).

13. Meunier, F.C., Verboekend, D., Gilson, J.-P., Groen, J.C. & Perez-Ramirez, J. Influence of crystal size and probe molecule on diffusion in hierarchical ZSM-5 zeolites prepared by desilication. *Microporous Mesoporous Mater.* **148**, 115-121 (2012).

14. Rousset, J.L., Stievano, L., Aires, F.J.C.S., Geantet, C., Renouprez, A.J. & Pellarin, M. Hydrogenation of Toluene over γ-Al2O3-Supported Pt, Pd, and Pd–Pt Model Catalysts Obtained by Laser Vaporization of Bulk Metals. *J. Catal.* **197**, 335-343 (2001).

15. Taimoor, A.A., Pitault, I. & Meunier, F.C. Correlation between deactivation and Pt-carbonyl formation during toluene hydrogenation using a H2 CO2 mixture. *J. Catal.* **278**, 153-161 (2011).

Alloy particles in hollow zeolites:

I. Introduction

Supported metal catalyst is a cornerstone of the fuel and chemical industries and of many pollution abatement technologies.[1] Suitable bimetallic catalysts provide enhanced activity, selectivity and/or stability compared to monometallic systems, while relieving the pressure on scarce and expensive noble metal resources.[2, 3] Various chemical and physical synthesis methods are available for controlling the size and surface compositions of bimetallic nanoparticles, which are factors that ultimately determine the material catalytic properties. However, the supported metal catalysts are generally synthesized by directly metal deposition on the support, and small particles tend to sinter under temperature treatments, which lead to thermal catalyst deactivation. One of the solutions to prevent sintering is to encapsulate alloy nanoparticles into shells or matrices. G.Veser et al. have reported the synthesis of PtRh alloy encapsulated in BHA (barium hexa-aluminate) matrices, which showed exceptional thermal stability.[4] However, the alloy particles are limited by the type of metals (metals possess higher melting point such as Rh are necessary) and the thermal stability of alloy particles critically depends on the metal ratios between the two metal in the alloy particles, the most thermal stable alloy material is with a Pt: Rh ratio of 1:1. More recently, F.Schüch et al. developed a new strategy to synthesize PtCo alloys embedded in mesoporous carbon and the obtained materials showed improved stability and catalytic activities in the synthesis of 2, 5-dimethylfuran (DMF) reaction.[5] So far, there is no efficient and general approach which has been reported to deal with general and well defined alloy encapsulated in microporous porous matrices.

In this chapter, we have extended the synthesis method of mono-metallic nanoparticles in hollow zeolites to bimetallic systems. The different preparation methods have been carried out and different bimetallic systems such as PtPd, PtAg, PdAg and AuAg have been prepared and characterized by TEM, EDX, ICP-OES and XPS techniques. The thermal stability of AuAg@Sil-1 (Sil-1 for silicalite-1) has been tested under humid conditions and compared to that of conventional supported materials. Finally, the catalytic activity of AuAg@Sil-1 has been tested in CO oxidation in the absence and in the presence of hydrogen, in order to characterize the presence of both Au and Ag on the particle surface.

II. Results and discussion

II.1. Alloy nanoparticles in hollow zeolites with yolk-shell structures

As discussed in chapter 3 and 4, the facile and generic dissolution/recrystallization method enable the synthesis of metal nanoparticles with controllable particle size encapsulated in hollow zeolite single crystals (silicalite-1 and ZSM-5). In this chapter, alloy nanoparticles in hollow zeolites have been obtained using methods developed for monometallic systems by adding a second metal. The two detailed synthesis methods (co-impregnation and successive impregnations) to prepare alloy particles in silicalite-1 or ZSM-5 are illustrated in Fig. 1-(a) and (b), respectively. Generally, there is a dissolution/recrystallization step to create hollow structures and a reduction process which allows particles for alloying.

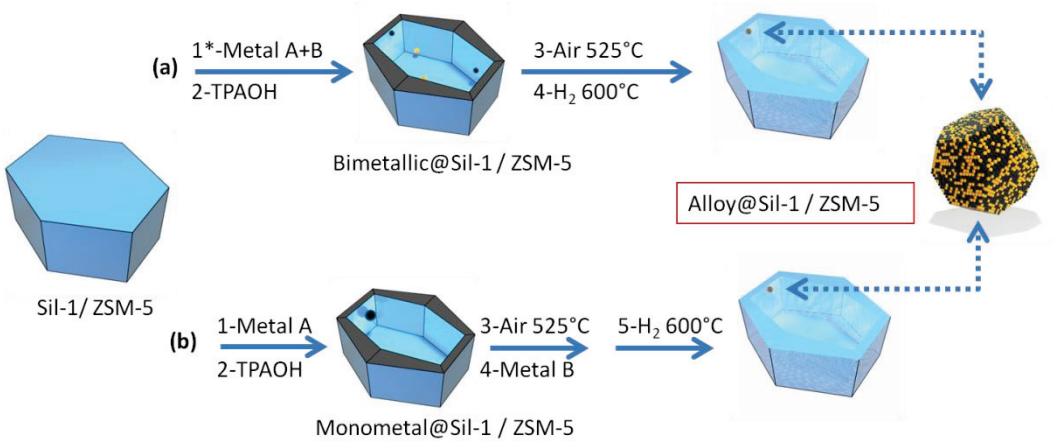

Figure 1: Scheme of two methods to synthesize alloy particles encapsulated in hollow zeolites. (a) co-impregnation method which consists of 4 steps (1: impregnation, 2: TPAOH treatment, 3: calcination, 4: reduction) and (b) successive impregnations method consisting of 5 steps (1: impregnation, 2: TPAOH treatment, 3: calcination, 4: 2nd impregnation, 5: reduction). * indicating the slightly difference in the synthesis of AuAg@Sil-1 material which will be discussed in the following paragraphs.

II.1.1. Alloy particles in hollow silicalite-1 prepared by co-impregnation

II.1.1.1. Alloy particles with different kinds of metals

Silicalite-1 was first impregnated by a mixture of Pt and Pd aqueous solutions with a theoretical Pt/Pd ratio of 1 (in weight) using a wetness impregnation method, then the solid was treated by TPAOH to form hollow structures following our previous protocol (details in experimental chapter). Similar as Pd in hollow zeolite (discussed in chapter 5), metal species with irregular shapes are formed after the TPAOH treatment (Fig. 2), suggesting the presence of Pd in the hollow silicalite-1 shell.

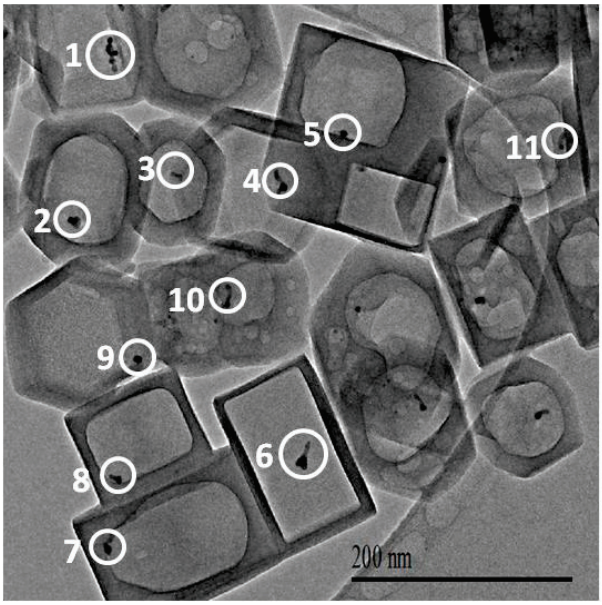

Figure 2: TEM image of $Pt_{0.31}Pd_{0.22}$@Sil-1 sample after TPAOH treatment (the sample after TPAOH treatment-the 2nd step of method (a) in Fig.1). White circles indicate the areas for EDX detection with the corresponding spot numbers on the left.

To further investigate the metal compositions of those metal particles, EDX analysis has been carried out on 11 selected areas indicated by white circles in Fig. 2 with corresponding numbers on the left. EDX results show that all of these 11 areas which are mainly metal species inside hollow zeolites contain both Pt and Pd with an average Pt/Pd mass ratio of 1.28 (Table 1).

Table 1: EDX analysis of areas indicated by corresponding circles in Fig. 2, the identical number in Fig. 2 and Table 1 represents the same area.

Area	O (wt. %)	Si (wt. %)	Pd (wt. %)	Pt (wt. %)	Total	Pt/Pd (wt. %)
1	51.14	43.06	1.76	3.47	100	1.97
2	48.27	37.74	4.38	9.6	100	2.19
3	53.67	41.26	2.67	2.4	100	0.90
4	54.23	42.84	0.89	2.04	100	2.29
5	56.01	39.49	2.94	1.56	100	0.53
6	55.51	39.91	2.93	1.65	100	0.56
7	52.2	40.27	3.34	4.18	100	1.25
8	54.47	40.98	2.45	2.1	100	0.86
9	52.98	42.39	2.26	2.38	100	1.05
10	37.05	40.59	7.38	14.98	100	2.03
11	55.29	41.61	2.08	1.01	100	0.49
Average	51.89	40.83	3.01	4.12	100	1.28/1.41[1]

[1]: 1.41 is the Pt/Pd ratio detected by ICP-OES of the final material in the synthesis pathway given in Fig.1 method (a).

Herein, we conclude that there are probably three possible structures for these two metals in hollow silicalite-1:1): single particles containing both Pd and Pt (Fig. 2 circle 5 and 9); 2): Pt particles linked by Pd species (Fig. 2 circle 1 and 4) and 3): core-shell structures with Pt core and Pd species around (Fig. 2 circle 6).

As previously, the final samples are further denoted A_xB_y@Sil-1, x and y are the loading (wt. %) of metals A and B analyzed by ICP, and Sil-1 for silicalite-1. This material was further calcined in air and characterized by TEM and EDX to follow possible changes in bimetallic particles upon calcination. TEM image of $Pt_{0.31}Pd_{0.22}$@Sil-1 sample after calcination is given in Fig. 3; metal species turned to spherical forms as compared to the previous irregular shapes shown in Fig. 2. However, these particles are not perfectly spherical and they generally possess a rough surface. 14 metal particles have been selected and analyzed by EDX, giving the average metal loadings of 3.89 wt.% Pd and 4.77 wt.% Pt, with a Pt/Pd ratio of 1.34 in weight, consistent with the value before calcination (Pt/Pd = 1.28). So here, PtPd bimetallic species maintain the same metal compositions after calcination in air with a spherical-like structure.

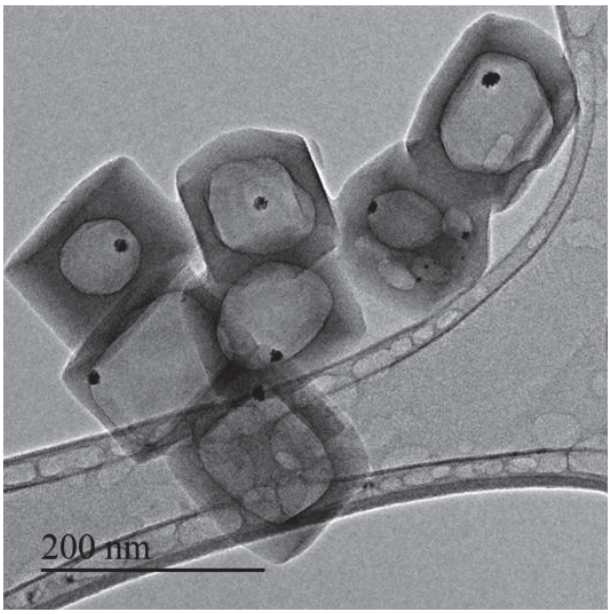

Figure 3: TEM image of $Pt_{0.31}Pd_{0.22}$@Sil-1 sample after calcination (the sample after the 3rd step of method (a) in Fig. 1).

As expected, spherical particles encapsulated individually in each hollow zeolite crystal are formed after reduction under H_2 for 10 hours at 600°C (Fig. 4-left). The particles size distribution is relative narrow with more than 60% of particles with diameter in the range of 8-11 nm.

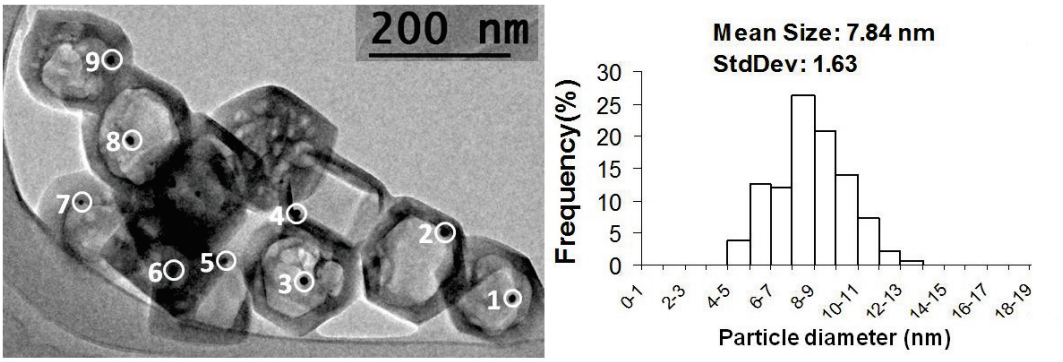

Figure 4: TEM image (left) and particle size distribution (right) of $Pt_{0.31}Pd_{0.22}$@Sil-1 sample after reduction (the final material of method (a) in Fig.1). White circles indicate the EDX detection areas with the corresponding spot numbers on the left.

EDX results (Table 2) on the 9 particles indicated by the circles in Fig. 4 showed that both Pt and Pd are present with a Pt/Pd ratio varying from 0.56 to 2.95. The average percentages for each element from the measurement of 28 particles of this sample are given in Table 2 and the average Pt/Pd ratio of these 28 particles is 1.48 which is also confirmed by ICP-OES analysis of this sample (0.33 wt.% Pt and 0.22 wt.% Pd detected by ICP-OES, which gives a Pt/Pd ratio of 1.41).

Table 2: The corresponding EDX analysis of the areas indicated by the circles in Fig. 4, the identical number in Fig. 4 and Table 2 represents the same area.

Area	O (wt. %)	Si (wt. %)	Pd (wt. %)	Pt (wt. %)	Total	Pt/Pd(wt. %)
1	50.49	40.72	4.16	4.63	100	1.11
2	54.41	42.08	2.19	1.31	100	0.60
3	42.6	43.82	5.24	8.34	100	1.59
4	49.94	43.7	1.61	4.75	100	2.95
5	47.16	46.02	1.94	4.88	100	2.52
6	51.3	43.29	2.82	2.59	100	0.92
7	47.68	41.93	6.64	3.75	100	0.56
8	38.69	38.96	8.01	14.34	100	1.79
9	47.45	43.1	5.43	4.02	100	0.74
Average [1]	49.69	42.93	3.05	4.32	100	1.48/1.41[2]

[1]: Average values are from 28 particle measurements including these 9 results in the table; [2]: 1.41 is the Pt/Pd ratio detected by ICP-OES.

To further investigate more details of the metal dispersion in $Pt_{0.31}Pd_{0.22}$@Sil-1 sample, HRTEM and HAADF-STEM images as well as EDX analysis have been carried out on a Cs-corrected Titan ETEM G2 FEI microscope (Figs. 5 and Table 3).

The HRTEM image and the corresponding diffraction pattern of an area (indicated by the red square in Fig. 5-a) from one particle is given in Fig.5-(a) and the HAADF-STEM image of the same particle is given in Fig.5-b with Pt/Pd ratios detected from different areas (indicated by the circles). The interplanar angles between (220), (022), (-202) and (-4-22) planes have been measured from the diffraction pattern of the selected area (red square in Fig.5-a) and the corresponding d-spacing reported in Table 3 are consistent with those of PtPd alloy particle (ICDD File number: 65-6418, fcc-face cubic centered, PtPd alloy). However, the theoretical d-spacing of fcc Pt, Pd and PtPd are quite similar, for example, the d-spacing of (220) are 1.4036, 1.3788 and 1.377, respectively for Pt, Pd and PtPd alloy. Thus, further characterization is required to confirm the nature of the particles. Then EDX analysis has been carried out on this particle, which shows a Pt/Pd ratio of 0.95 in the area near the core of particle whereas it is 1.03 in the entire particle (shown is Fig.5-b).

Table 3: Experimental and theoretical interplanar spacings and interplanar angles of the PtPd particle in Fig.5-a

Spot	hkl	Observed d-Spacing (Å)	Measured angles to Spot 1	Theoritical d-Spacing [1] (Å)	Theoritical angle between plans [1]
1	2 2 0	1.389	0.00	1.377	0
2	0 2 2	1.419	59.33	1.377	60.00
3	-2 0 2	1.413	120.60	1.377	120.00
4	-4 -2 2	0.806	150.83	0.794	150.00

[1] Theoritical data from International Centre for Diffraction Datametallic (ICDD). File number: 65-6418 which corresponds to fcc PtPd alloy.

Another HAADF-STEM image of $Pt_{0.31}Pd_{0.22}$@Sil-1 taken at larger scale shows the homogeneity of the sample with a yolk-shell structure - one particle per hollow zeolite (Fig. 5-c). Again, one particle (indicated by the red circle in Fig. 5-c) from this image has been analyzed by EDX. The HRTEM image is given in Fig.5-d with two selected areas for EDX analysis. One is near the center of the particle and the other one id near the surface of the particle. Pt and Pd are both found in these two areas with similar Pt/Pd ratios of 2.09 and 2.14, respectively. This figure further confirmed the formation of PtPd alloy particles with relatively homogeneous metal composition in hollow silicalite-1 crystals. Thus, PtPd bimetallic particles are alloy particles with two metals dispersed overall the particles instead of a core shell structure in the sample before calcination and reduction showed in Fig. 2, which is probably formed in the reduction step under hydrogen.

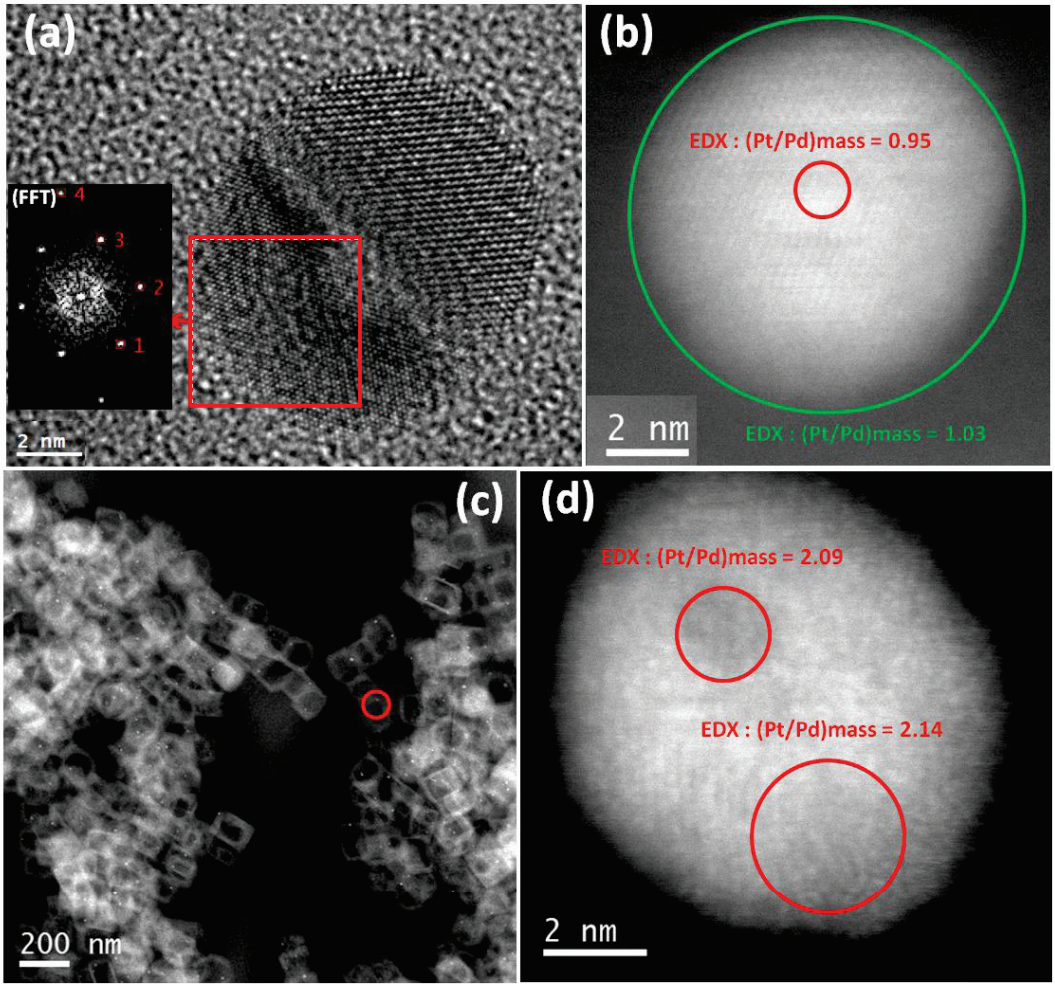

Figure 5: HRTEM image with Fast Fourier Transform (FFT) patterns (a) and STEM-HAADF images (b, c and d) of $Pt_{0.31}Pd_{0.22}$@Sil-1 sample. Images of (a) and (b) are from the same particle, the red square in (a) is the selected area for FFT. The green and red circles in (b) are the EDX detecting areas, the corresponding metal ratios are given in the figure. The particle in (d) are from the one indication by the red circle in (c). The red circles in (d) are the EDX detecting areas, the corresponding metal ratios are given in the figure.

Later on, two other bimetallic systems (PtAg and PdAg) have been encapsulated in hollow silicalite-1 following the same preparation method used for $Pt_{0.31}Pd_{0.22}$@Sil-1 sample.

TEM image and particle size distribution of $Pt_{0.39}Ag_{0.25}$@Sil-1 materials are given in Fig. 6. As previously discussed for PtPd alloys in hollow silicaite-1, the yolk-shell structure is formed and the particle size distribution is quite narrow with a mean particle size of 7.8 nm. However, some particles are observed outside the zeolite crystals indicated by the green circle in Fig. 6.

EDX analysis has been carried out on 35 particles in $Pt_{0.39}Ag_{0.25}$@Sil-1 sample. The average element loadings are given in Table 4 which also shows the compositions of the 16 particles indicated by the white circles in Fig. 6 with identical numbers. We found that Pt/Ag ratio obtained by EDX (1.78) is greater than the one detected by ICP-OES (1.56), which suggests that the particles in hollow shells (EDX analyzed) contain less Ag compared to the bulk materials (ICP-OES analyzed).

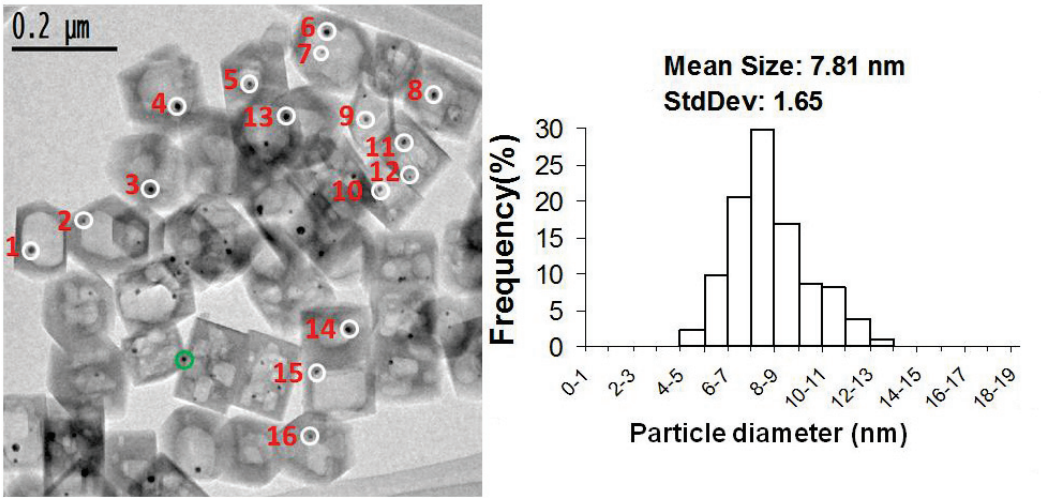

Figure 6: TEM image (left) and particle size distribution (right) of $Pt_{0.39}Ag_{0.25}$@Sil-1 sample (if there is not specially mentioned, the samples are always corresponding those after calcination and reduction-the final materials in Fig. 1). White circles indicate the areas for EDX detection with the corresponding spot number on the left, the green circle indicates one particle outside the hollow zeolite.

Table 4: The corresponding EDX analysis of the areas indicated by the circles in Fig. 6, the identical number in Fig. 6 and Table 4 represents the same area.

Area	O (wt. %)	Si (wt. %)	Ag (wt. %)	Pt (wt. %)	Total	Pt/Ag(wt. %)
1	49.96	39.82	6.46	3.76	100	0.58
2	47.9	45.61	2.60	3.90	100	1.50
3	48.82	42.6	5.97	2.60	100	0.44
4	44.36	45.54	6.13	3.96	100	0.65
5	46.51	46.52	3.22	3.75	100	1.16
6	43.48	40.63	8.35	7.54	100	0.90
7	41.58	48.51	4.71	5.20	100	1.10
8	35.62	45.61	10.07	8.70	100	0.86
9	36.21	55.39	3.44	4.96	100	1.44
10	41.96	52.72	2.42	2.91	100	1.20
11	39.53	51.82	4.41	4.24	100	0.96
12	41.71	55.76	0.53	2.01	100	3.79
13	41.9	45.55	6.12	6.42	100	1.05
14	50.86	42.94	3.07	3.13	100	1.02
15	51.17	43.23	2.24	3.35	100	1.50
16	52.58	44.29	1.13	2.01	100	1.78
Average[1]	46.86	45.01	3.96	4.16	100	1.78/1.56[2]

[1]: Average values are from 35 particles measurments including these 16 results in the table; [2]: 1.56 is the Pt/Ag ratio detected by ICP-OES.

Moreover, a particle outside the shell was characterized as pure Ag by EDX, which could explain why internal particles contain less silver as expected. XPS is a surface characterization technique in which elements are detectable within a zone approximately 10 nm deep from the surface. Since the thickness of the hollow silicalite-1 are estimated from 20 to 30 nm from TEM images, metals will be detected only if they are located on the external surface. XPS spectra of $Pt_{0.39}Ag_{0.25}$@Sil-1 sample show an Ag 3d doublet with binding energies of 369 eV and 374.5 eV, respectively (Fig.7-left). These values suggest that silver is present in the metallic form, indicating the existence of Ag particles outside hollow silicalite-1 crystals. In contrast, the intensity of the Pt 4f spectrum between 70 and 80 eV is very low, indicating that Pt is not present in the first nanometers below the surface of the crystals. Thus XPS characterization further confirmed TEM observations and EDX measurements that some Ag particles are present on the outer surface of hollow zeolites.

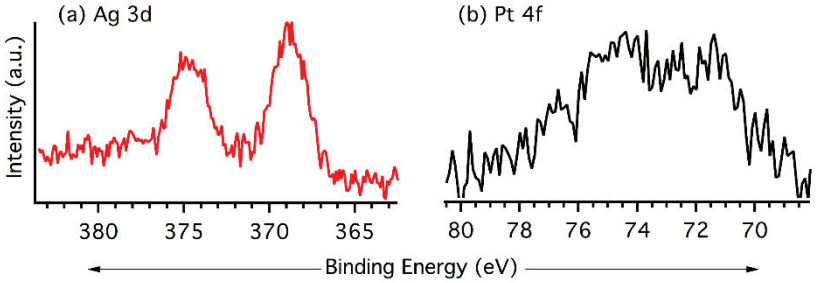

Figure 7: XPS spectra Ag 3d (a) and Pt 4f (b) of $Pt_{0.39}Ag_{0.25}$@Sil-1 sample.

We have previously discussed for mono-metallic Pt and Ag systems (in chapter 3) that spherical particles are both formed after TPAOH treatment, however, Ag particles are oxidized and they thus can be expelled from hollow crystals upon calcination in air.

The HAADF-STEM images of $Pt_{0.39}Ag_{0.25}$@Sil-1 sample are given in Fig. 8. As previously discussed, most of the zeolite crystals possess a yolk-shell structure but one particle outside of the hollow zeolites is again observed, indicated by the green circle.

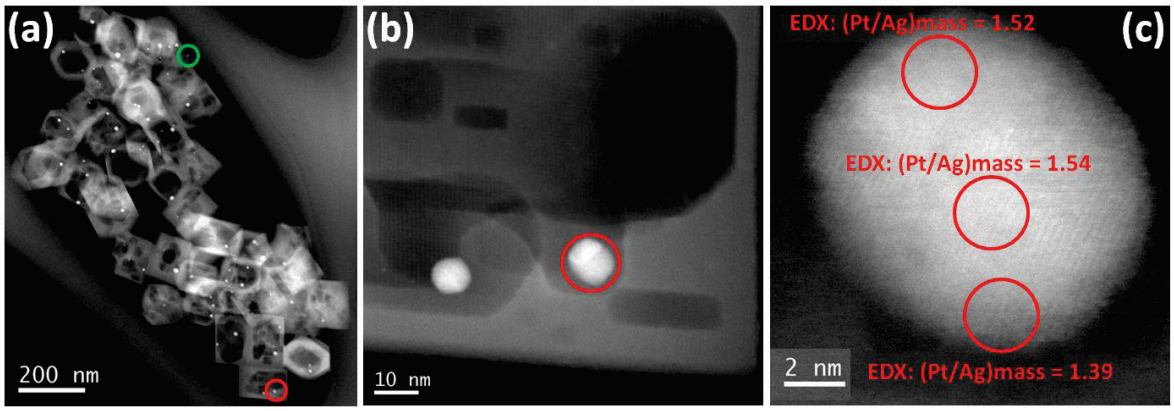

Figure 8: STEM-HAADF images of $Pt_{0.39}Ag_{0.25}$@Sil-1 sample. (c) is the high resolution STEM-HAADF image of the particle indicated by red circle in (a) and (b). Circles in (c) indicate areas for EDX analysis with the corresponding metal ratios. The green circle in (a) indicates the particle outside the hollow zeolite.

Another particle (indicated by the red circle in Fig. 8-a and b) has been observed under greater magnification and selected for EDX analysis. As shown in Fig.8-c, Pt/Ag ratios in three different areas throughout the particle are very similar (the ratio varies from 1.39 to 1.54), supporting the homogeneous composition of the PtAg alloy particle in hollow silicalite-1.

The co-impregnation method has also been used to prepare PdAg bimetallic particle in hollow silicalite-1. TEM image and particle size distribution of the resulting $Pd_{0.21}Ag_{0.14}$@Sil-1 material are given in Fig. 9. As for PtPd@Sil-1, in PdAg@Sil-1 sample each hollow zeolite crystal contains one particle with a mean size of 7.5 nm. In contrast to PtAg@Sil-1 sample, no particle was observed outside hollow shells from TEM observation, which was also confirmed by XPS measurements (Fig. 10). Indeed, intensities of both Ag 3d and Pd 3d XPS spectra are very weak, supporting the absence of external Ag particles and the overall encapsulation of the alloy in the hollow shells.

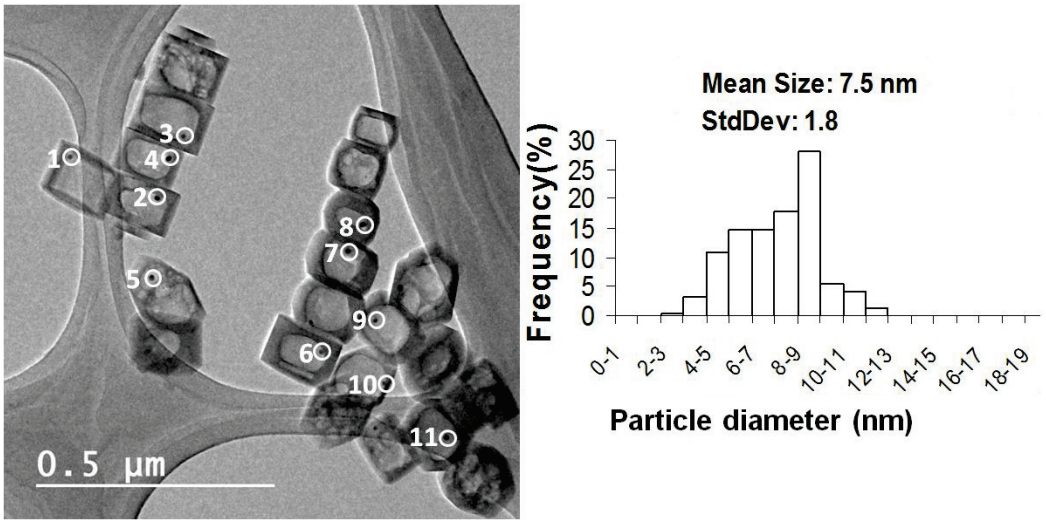

Figure 9: TEM image (left) and particle size distribution (right) of $Pd_{0.21}Ag_{0.14}$@Sil-1. White circles indicate the areas for EDX detection with the corresponding spot numbers on the left.

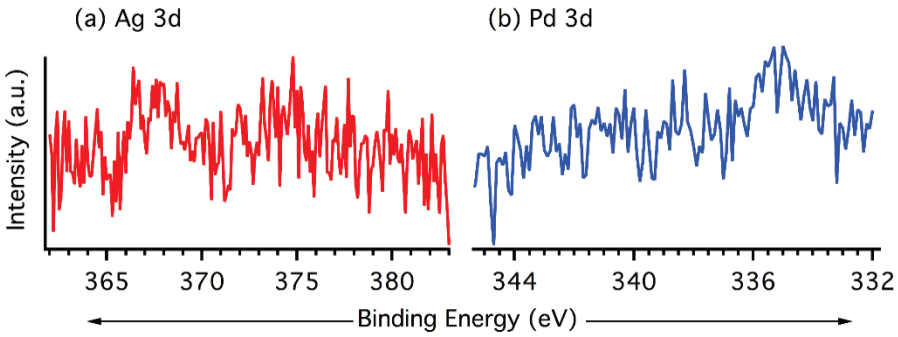

Figure 10: XPS spectra Ag 3d (a) and Pd 3d (b) of $Pd_{0.21}Ag_{0.14}$@Sil-1 sample.

The compositions of the 11 particles indicated by white circles in Fig. 9 are given in Table 5 along with the average values obtained from 30 particles measurements in $Pd_{0.21}Ag_{0.14}$@Sil-1 sample. Note that

Pd/Ag ratios obtained from EDX (1.39) and ICP-OES (1.5) are both in the same range of 1.45±0.5, relatively narrow alloy composition is obtained as previously observed for PtPd@Sil-1 materials.

Table 5: The corresponding EDX analysis of the areas indicated by the circles in Fig. 9, the identical number in Fig. 9 and Table 5 represents the same area.

Area	O (wt. %)	Si (wt. %)	Pd (wt. %)	Ag (wt. %)	Total	Pd/Ag (wt. %)
1	54.90	41.91	2.09	1.09	100	1.92
2	56.61	39.42	2.48	1.49	100	1.66
3	56.70	40.84	1.48	0.98	100	1.51
4	56.19	41.29	1.51	1.01	100	1.50
5	56.66	40.16	2.10	1.08	100	1.94
6	58.06	40.52	0.66	0.76	100	0.87
7	57.99	40.42	0.87	0.72	100	1.21
8	58.11	40.59	0.67	0.63	100	1.06
9	54.90	43.95	0.73	0.42	100	1.74
10	54.60	44.55	0.46	0.39	100	1.18
11	58.98	39.21	0.96	0.85	100	1.13
Average[1]	54.66	41.75	2.07	1.51	100	1.39/1.5[2]

[1]: Average values measured on 30 particles measurments including these 11 results in the table; [2]: 1.5 is the Pd/Ag ratio detected by ICP-OES.

The co-impregnation method has also been applied to the synthesis of AuAg alloy particles in hollow silicalite-1; a TEM image of the resulting material is shown in Fig. 11. In contrast to previous bimetallic systems such as PtPd, PtAg or PdAg, the co-impregnation method led to the formation of large particles essentially located outside the hollow shells with diameters above 20nm.

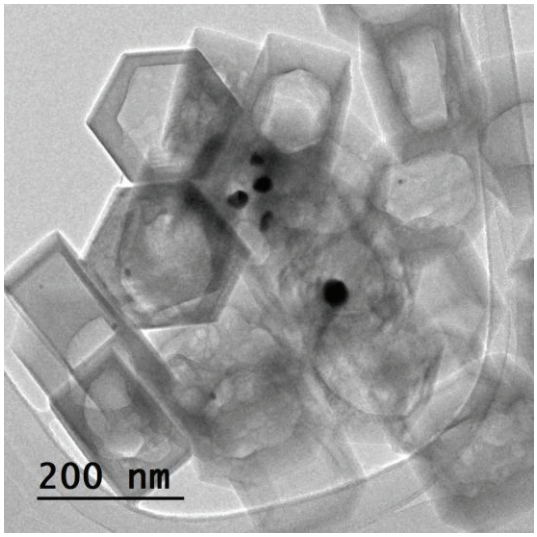

Figure 11: TEM image of AuAg@Sil-1 sample prepared by co-impregnation method (a) in Fig. 1.

Later on, the synthesis method for AuAg@Sil-1 has been modified according to the preparation of Au@Sil-1 material (discussed in Chapter 3). First, silicalite-1 was impregnated with an Au aqueous solution and then the solid was reduced under hydrogen to form Au^0/silicalite-1 composite, which was subsequently impregnated by an Ag precursor solution. The solid thus obtained was treated following steps 2, 3 and 4 of method (a) in Fig. 1, i.e. treatment by TPAOH, calcination and finally reduction at 600°C under hydrogen. This modification of the synthesis protocol led to yolk-shell AuAg@Sil-1 materials with all particles inside hollow zeolite cavities (shown in Fig.12-left). The AuAg bimetallic particle size distribution in Fig.12-right shows that more than 75% of the particles is between 6 to 10 nm in size. Moreover, the metal contents detected by ICP-OES were 0.53% Au and 0.04%Ag (in weight) in the material. Here, the composition of approximately 10%Ag90%Au in alloy particles (in weight) is expected which is known for the synergistic effects of AuAg alloy particles in the CO oxidation in the absence and in the presence of H_2 and will be discussed in the catalytic part of this chapter.

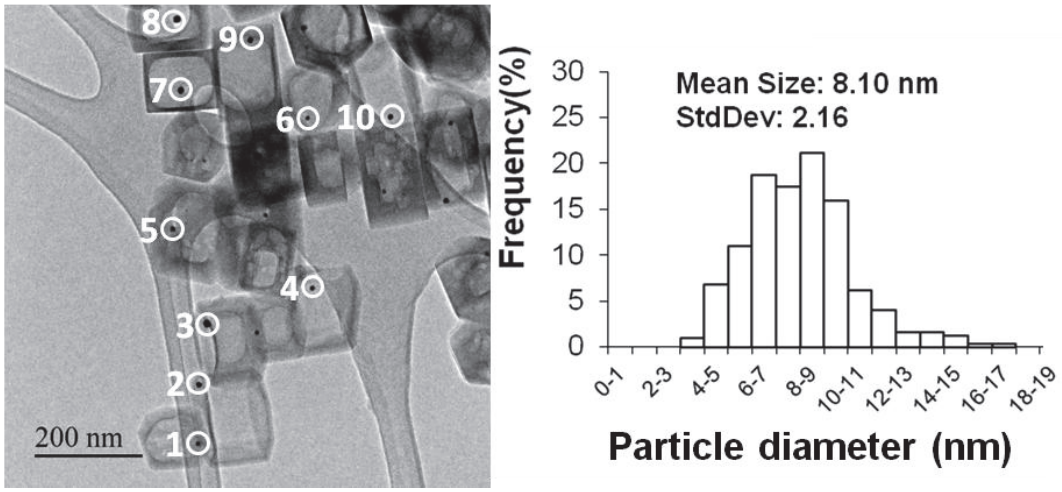

Figure 12: TEM image (left) and particle size distribution (right) of $Au_{0.53}Ag_{0.04}$@Sil-1. White circles indicating the areas for EDX detecting with the corresponding spot number on the left.

EDX analyses have been performed on 15 particles of $Au_{0.53}Ag_{0.04}$@Sil-1 sample, 10 of them being indicated by white circles in the Fig. 12. The corresponding percentages are given in Table 6. All studied particles contain both Au and Ag elements with an average Au/Ag ratio (11.47) quite similar to that obtained by ICP-OES (13.25).

Table 6: EDX analysis of areas indicated by white circles in Fig. 12, the identical number in Fig. 12 and Table 6 represents the same area.

Area	O (wt. %)	Si (wt. %)	Ag (wt. %)	Au (wt. %)	Total	Au/Ag (wt. %)
1	41.61	38.90	2.46	17.03	100	6.92
2	52.06	41.31	0.37	6.26	100	16.92
3	48.23	33.81	1.43	16.53	100	11.56
4	42.60	41.06	2.24	14.09	100	6.29
5	47.84	40.31	1.83	10.02	100	5.48
6	50.47	36.74	1.00	11.78	100	11.78
7	54.79	38.03	0.33	6.84	100	20.73
8	51.11	36.61	0.65	11.63	100	17.89
9	51.39	38.12	0.71	9.78	100	13.77
10	50.78	40.37	0.74	8.11	100	10.96
Average[1]	49.76	38.69	1.11	10.44	100	11.47/13.25[2]

[1]: Average values are from totaly 15 particles measurments including these 10 results in the table; [2]: 13.25 is the Au/Ag ratio detected by ICP-OES.

As a short conclusion, four different alloy systerms (PtPd, PtAg, PdAg and AuAg) have been investigated following a co-impregnation preparation method which consists of impregnation followed by TPAOH treatment, calcination and reduction. Each material processes a yolk-shell nanostructure with well dispersed bimetallic particles. The bimetallic compositions were detected by EDX analysis and the alloy structure was confirmed by the high dispersion of the metals throughout the particles. Later on, PtPd@Sil-1 and PdAg@Sil-1 have been selected to evaluate the possibility of tuning the metal loadings in hollow silicalite-1 by adjusting the concentrations of the impregnation solution.

II.1.1.2. Alloy particles with various metal loadings

Another PdAg@Sil-1 material was synthesized from a higher concentrated metal precursor solution following exactly the same synthesis procedure used for $Pd_{0.21}Ag_{0.14}$@Sil-1. The obtained material contained 0.25 wt. % Pd and 0.19 wt. % Ag, as detected by ICP-OES. A TEM image of $Pd_{0.25}Ag_{0.19}$@Sil-1 and the corresponding particle size distribution are given in Fig. 13. As expected, $Pd_{0.25}Ag_{0.19}$@Sil-1 shows very homogeneous yolk-shell structures with a slightly bigger average particle size (8.73±2.1nm) as compared to $Pd_{0.21}Ag_{0.14}$@Sil-1 (7.5±1.8nm). The bimetallic composition of the particles has been confirmed by EDX measurements. 25 measurements were performed, and 11 of them, corresponding to particles indicated by white circles in Fig. 13, are reported in Table 7.

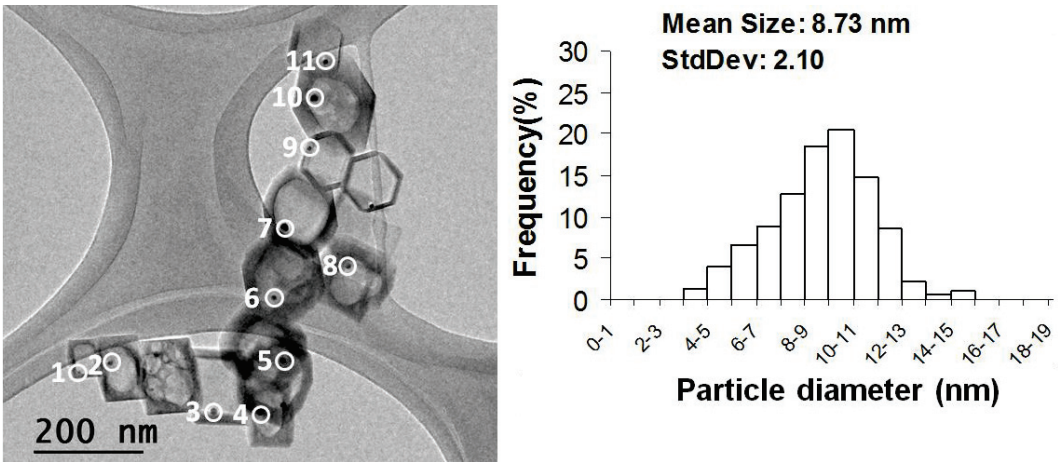

Figure 13: TEM image (left) and particle size distribution (right) of $Pd_{0.25}Ag_{0.19}$@Sil-1. White circles indicate the areas for EDX detection with the corresponding spot numbers on the left.

Data indicate that all particles contain both Pd and Ag, with an average Pd/Ag ratio of 1.25, quite closed to that obtained by ICP-OES (1.32), suggesting the homogeneous overall composition of the sample.

Table 7: EDX analysis of areas indicated by circles in Fig. 13, the identical number in Fig. 13 and Table 7 represents the same area.

Area	O (wt. %)	Si (wt. %)	Pd (wt. %)	Ag (wt. %)	Total	Pd/Ag (wt. %)
1	52.72	44.47	1.43	1.38	100	1.04
2	51.79	40.95	3.46	3.81	100	0.91
3	51.36	41.76	3.92	2.96	100	1.32
4	48.37	47.69	2.13	1.81	100	1.18
5	43.63	53.45	1.72	1.20	100	1.43
6	47.96	48.57	2.23	1.24	100	1.80
7	41.74	53.70	2.12	2.44	100	0.87
8	48.39	50.34	0.80	0.47	100	1.70
9	43.61	49.97	2.86	3.57	100	0.80
10	52.19	46.29	0.80	0.72	100	1.11
11	52.73	45.83	0.60	0.84	100	0.71
Average [1]	47.54	48.78	1.91	1.77	100	1.25/1.32[2]

[1]: Average values are from 28 particles measurements including these 16 results in the table; [2]: 1.32 is the Pd/Ag ratio detected by ICP-OES.

Another PtPd@Sil-1 sample was prepared following the same preparation method described in Fig.1 method (a) but using Pt and Pd impregnating solutions less concentrated than those used for

$Pt_{0.31}Pd_{0.22}$@Sil-1. The obtained material is denoted $Pt_{0.19}Pd_{0.06}$@Sil-1 (0.19 wt. % Pt and 0.06 wt. % Pd detected by ICP-OES). A TEM image and the particle size distribution in Fig.14 show that yolk-shell structures contain particles with a slightly smaller average size (6±1.5 nm) as compared to $Pt_{0.31}Pd_{0.22}$@Sil-1 (7.84±1.63 nm).

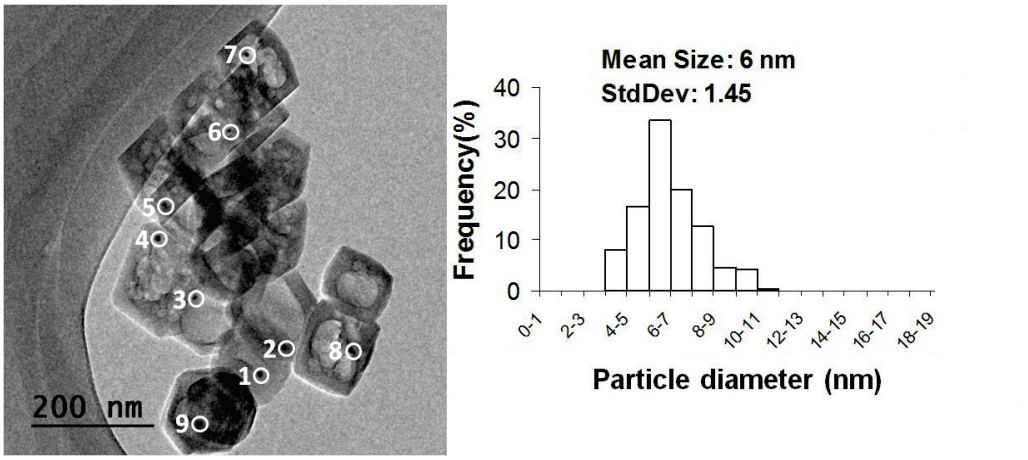

Figure 14: TEM image (left) and particle size distribution (right) of $Pt_{0.19}Pd_{0.06}$@Sil-1 sample. White circles indicate the areas for EDX detection with the corresponding spot numbers on the left.

EDX analyses of 21 particles give an average Pt/Pd ratio of 3.28, a value slightly greater than the one obtained by ICP-OES (3.17). Nine of these EDX analyses corresponding to particles in Fig. 14 are reported in Table 8; they clearly show that the Pt/Pd ratio varies from 1.02 to 6.85, suggesting that particles are less homogeneous in composition than in the sample with higher metal loadings.

Table 8: The corresponding EDX analysis of the areas indicated by the circles in Fig. 14, the identical number in Fig. 14 and Table 8 represents the same area.

Area	O (wt. %)	Si (wt. %)	Pd (wt. %)	Pt (wt. %)	Total	Pt/Pd(wt. %)
1	52.38	42.99	0.59	4.04	100	6.85
2	51.42	46.01	0.81	1.76	100	2.17
3	47.80	49.74	1.04	1.43	100	1.38
4	42.53	45.78	1.55	10.14	100	6.54
5	44.28	52.52	0.55	2.64	100	4.80
6	49.21	49.88	0.33	0.58	100	1.76
7	53.06	45.02	0.54	1.38	100	2.56
8	35.95	45.12	9.36	9.58	100	1.02
9	50.55	47.03	0.85	1.57	100	1.85
Average [1]	47.83	47.45	1.26	3.46	100	3.28/3.17[2]

[1]: The average values are from 21 particle measurements including these 9 results in the table; [2]: 3.17 is the Pt/Pd ratio detected by ICP-OES.

The Pt 4f and Pd 3d XPS spectra of $Pt_{0.19}Pd_{0.06}$@Sil-1 are given in Fig. 15 show that both metals are hardly detected, suggesting the overall metal encapsulation in hollow silicalite-1 crystals.

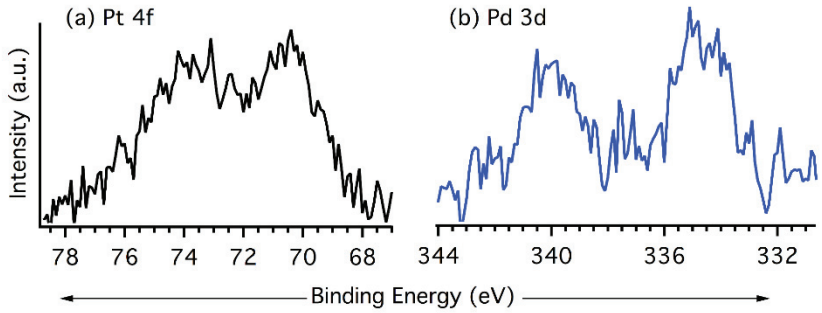

Figure 15: Pt 4f (a) and Pd 3d (b) XPS spectra of $Pt_{0.19}Pd_{0.06}$@Sil-1 sample.

To conclude, different metal loadings and average sizes of alloy particles in hollow silicalite-1 can be prepared by simply adjusting metal concentrations in the impregnation solution. The metal containing is characterized by ICP-OES on the bulk materials as well as EDX analysis on the individually alloy particles, data are shown in Table 14. However, in the case of low metal contents (typically lower than 0.1 wt. %), the composition of alloy particles is less homogeneous than those obtained on materials with higher loadings.

Table 9: The mean size and metal ratios obtained by ICP-OES and EDX techniques of alloy particles in hollow silicalite-1 materials discussed above

A_xB_y@Sil-1 [1]	Mean size (nm) [2]	x/y by ICP-OES	x/y by EDX
$Pt_{0.31}Pd_{0.22}$@Sil-1	7.84 ± 1.63	1.41	1.48
$Pt_{0.39}Ag_{0.25}$@Sil-1	7.81 ± 1.65	1.56	1.78
$Pd_{0.21}Ag_{0.14}$@Sil-1	7.5 ± 1.8	1.5	1.39
$Au_{0.53}Ag_{0.04}$@Sil-1	8.1 ± 2.16	13.25	11.47
$Pd_{0.25}Ag_{0.19}$@Sil-1	8.73 ± 2.1	1.32	1.25
$Pt_{0.19}Pd_{0.06}$@Sil-1	6 ± 1.45	3.17	3.28

[1] A_xB_y@Sil-1 representing metals A and B in hollow silicalite-1 shells with the corresponding loadings (wt. %) of x and y analyzed by ICP. [2]: mean particle size obtained by counting more than 400 particles from TEM images of each sample.

II.1.2. Alloy particles in hollow ZSM-5 prepared by co-impregnation

With the above achievements in the preparation of alloy particles in hollow silicalite-1, the co-impregnation method is then extended to alloy particles in hollow ZSM-5. As previously discussed in chapter 4, hollow ZSM-5 can be prepared from crystals with a gradient of composition (Si-rich core, Al-rich periphery) by direct dissolution/recrystallization in the presence of TPAOH. Following the synthesis route of Fig. 1-a in which the starting silicalite-1 was replaced by ZSM-5 (Si/Al=78 detected by ICP-OES), $Pt_{0.27}Pd_{0.17}$@ZSM-5-DR material was obtained (0.27 wt. %Pt and 0.17 wt. %Pd detected by ICP-OES, DR for Direct dissolution Recrystallization). A TEM image and the particle size distribution, confirming the existence of very regular hollow ZSM-5 shells, are given in Fig. 16.

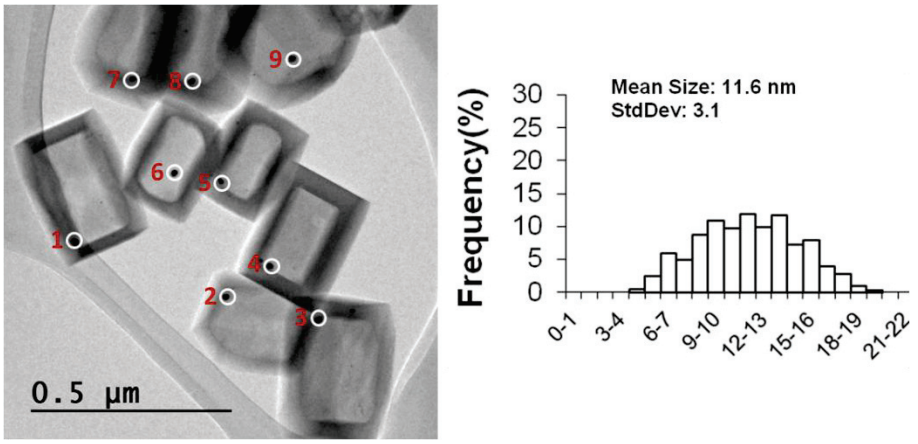

Figure 16: TEM image (left) and particle size distribution (right) of $Pt_{0.27}Pd_{0.17}$@ZSM-5-DR sample. White circles indicate the areas for EDX detection with corresponding spot numbers on the left. Only one of the biggest particle in each shell are counted for the particle size distribution (several small particles with diameter about 2 nm are co-existed in the shell of ZSM-5 which will show in Fig. 17 and will be discussed in the following paragraphs).

The particle size distribution is relatively broad as compared to that measured on the same alloy in hollow silicalite-1. Moreover, despite similar metal contents, the mean particle size (11.6±3.1 nm) is also bigger than that of PtPd@Sil-1 material ($Pt_{0.31}Pd_{0.22}$@Sil-1, 7.84±1.63 nm). This could be due to the presence of empty hollow shells in the sample which was also observed and discussed in the chapter 4. Furthermore, each of the hollow ZSM-5 contains one particle approximately 10 nm in size along with many small particles of ca. 2 nm located inside the zeolite shell was confirmed by a closer examination of TEM pictures (Fig. 17), revealing the presence of many very small particles in the zeolite walls. However, the extremely tiny amount of metal incorporated in the zeolite walls did not permit an analysis by EDX and it was not possible to conclude on the nature of these small particles.

The areas indicated by white circles in Fig. 16 have been analyzed by EDX and the results are given in Table 10. Pt, Pd are all present in these 9 particles with an average Pt/Pd ratio of 2.49 obtained from 13 measurements, quite different from 1.59 given by ICP-OES. This difference between Pt/Pd ratios obtained by ICP-OES and EDX measurements on large particles strongly suggests that those small particles could mainly contain Pd.

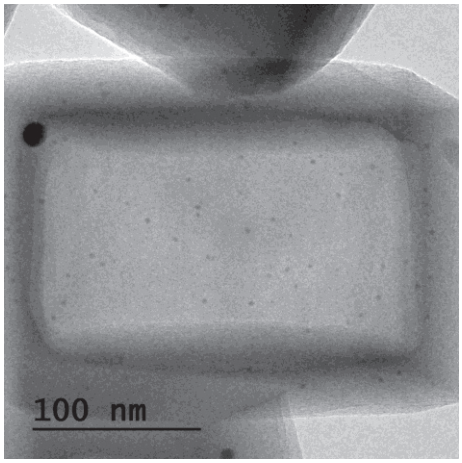

Figure 17: TEM image of $Pt_{0.27}Pd_{0.17}$@ZSM-5-DR sample with higher magnification.

Table 10: The corresponding EDX analysis of the areas indicated by the circles in Fig. 16, the identical number in Fig. 16 and Table 10 represents the same area.

Area	O (wt. %)	Al (wt. %)	Si (wt. %)	Pd (wt. %)	Pt (wt. %)	Total	Pt/Pd(wt. %)
1	49.40	1.10	36.77	3.30	9.44	100	2.86
2	52.45	0.41	44.52	0.51	2.11	100	4.14
3	46.91	0.50	34.80	5.62	7.68	100	1.37
4	49.77	0.35	40.07	3.59	6.22	100	1.73
5	48.43	0.34	37.74	3.69	9.81	100	2.66
6	50.78	0.40	45.94	0.59	2.30	100	3.90
7	42.79	0.45	38.73	7.23	10.79	100	1.49
8	46.52	0.47	41.90	3.30	7.81	100	2.37
9	45.69	0.60	39.13	4.60	9.98	100	2.17
Average [1]	48.28	0.49/0.44[2]	40.50	3.35	7.04	100	2.49/1.59[2]

[1]: Average values are from 13 particle measurements including these results in the table; [2]: value and ratio detected by ICP-OES.

To further characterize those small particles, XPS measurements have been carried out on this sample and the spectra are given in Fig. 18. The presence of Al 2p peak at binding energy of 74.1 eV suggests the small amount of Al in the framework of ZSM-5 shells, confirming the formation of hollow ZSM-5 shells (0.65% Al, detected by ICP-OES). However, at the binding energy between 332 to 344 eV which is typically for Pd 3d doublet, the spectrum is unable to be resolved, indicating that no Pd is present from the sample surface down to approximately 10 nm underneath of the surface. Thus, the small Pd particles are likely to be more deeply in the wall of ZSM-5 shell, which are able to maintain the smaller diameter even after calcination and reduction processes.

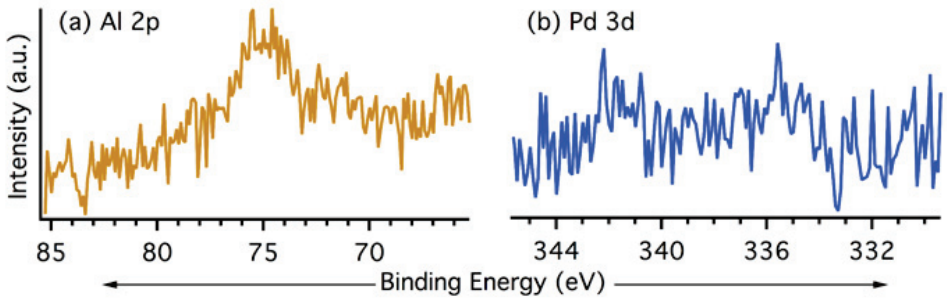

Figure 18: XPS spectra Al 2p (a) and Pd 3d (b) of $Pt_{0.27}Pd_{0.17}$@ZSM-5-DR sample.

II.1.3. Alloy particles in hollow zeolites prepared by successive impregnations

We have shown in chapter 3 that a post-impregnation synthesis method resulted in a very inhomogeneous sample in the case of Au@Sil-1. However, we demonstrate in this chapter that the presence of a second metal can drastically improve the stability of metal particles in hollow zeolites, in the case of Ag. Thus, a single-metal nanoparticle-containing hollow zeolite (1.02-Pt@ZSM-5-DR sample presented in chapter 5) was post-impregnated with a second metal precursor (palladium) solution and the resulting material was subsequently reduced in hydrogen at 600°C for 10 hours (the synthesis process is denoted in Fig.1 as method b). The obtained sample is denoted $Pt_{1.02}Pd_{0.66}$@ZSM-5-PI (1.02 wt. %Pt and 0.66 wt. %Pd detected by ICP-OES, PI for Post Impregnation). TEM images of the starting 1.02-Pt@ZSM-5-DR (1.02 wt. %Pt, Si/Al=70 detected by ICP-OES) and the final $Pt_{1.0}Pd_{0.66}$@ZSM-5-PI materials are given in Fig. 19. Both solids possess a yolk-shell structure, with a unique particle per cavity. The mean particle size in $Pt_{1.0}Pd_{0.66}$@ZSM-5-PI is approximately 15nm, which is significantly larger than that obtained on pure Pt particles in hollow ZSM-5 (11.7 nm). However, some particles outside hollow crystals indicated by the green circles in Fig.19 (b) have been observed and characterized as pure Pd by EDX, indicating the less efficient encapsulation of the post impregnated metal.

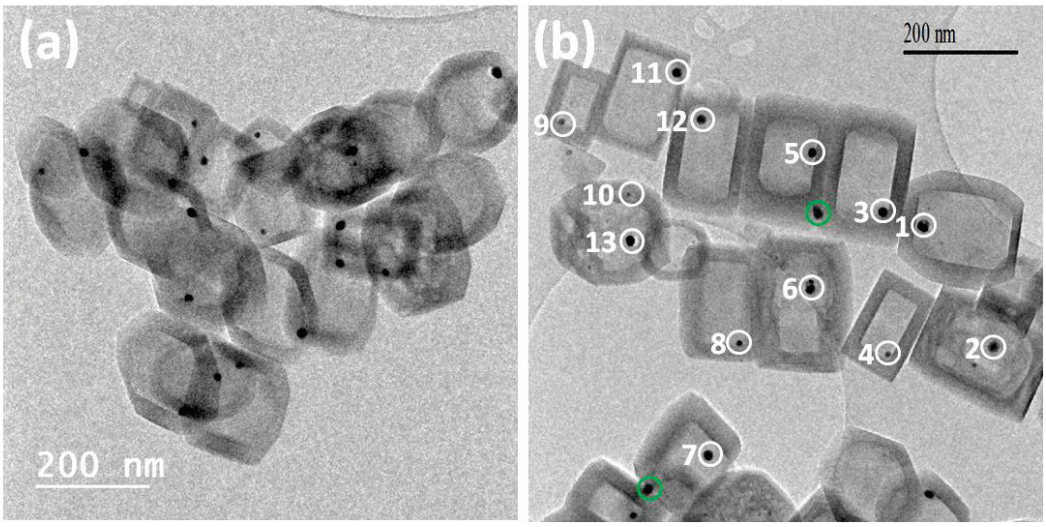

Figure 19: TEM image of $Pt_{1.0}$@ZSM-5 (a) with a mean particle size 11.7±2.6 nm and $Pt_{1.02}Pd_{0.66}$@ZSM-5-PI(b). White circles indicate the areas for EDX detection with corresponding spot numbers on the left. The green circles in (b) indicate the particles outside hollow zeolites.

Particles indicated by white circles in Fig.19 (b) have been analized by EDX and the corresponding results are given in Table 11. Among these 13 particles, two of them contain only Pt (No. 8 and 11), revealing the quite low homogeneity of Pd dispertion throughout the sample.

Table 11: EDX analysis of areas indicated by white circles in Fig. 19, the identical number in Fig. 19 and Table 11 represents the same area.

Area	O (wt. %)	Si (wt. %)	Pd (wt. %)	Pt (wt. %)	Total	Pt/Pd(wt. %)
1	49.75	32.71	4.39	13.15	100	3.00
2	35.71	28.96	10.31	25.02	100	2.43
3	43.52	31.11	6.16	19.21	100	3.12
4	51.66	29.85	7.88	10.61	100	1.35
5	47.49	32.8	3.04	16.68	100	5.49
6	36.88	30.5	5.93	26.69	100	4.50
7	54.93	36.23	3.84	5	100	1.30
8	51.1	38.9	0	10	100	-
9	40.02	23.79	10.21	25.98	100	2.54
10	53.16	34.73	1.88	10.23	100	5.44
11	44.51	34.45	0	21.04	100	-
12	42.4	30.29	5.15	22.16	100	4.30
13	49.7	35.87	3.94	10.5	100	2.66
Average[1]	44.12	34.51	4.82	16.55	100	2.67/1.54[2]

[1]: Average values are from 18 particle measurements including these 13 results in the table; [2]: 1.54 is the Pt/Pd ratio detected by ICP-OES.

The XPS spectra of $Pt_{1.0}Pd_{0.66}$@ZSM-5-PI sample are given in Fig. 20. The Al 2p peak at binding energy of 74 eV suggests the presence of Al in the framework of ZSM-5 shells as previously discussed. The intense Pd 3d doublet with binding energies of 337.8 eV and 343.1 eV (Fig.20-b) indicates that part of Pd particles are located on the outer surface of hollow crystals in agreement with TEM observations. The presence of Pd particles outside hollow zeolites could also explain the huge difference in Pt/Pd ratios obtained by chemical analysis and EDX. In contrast, Pt was not detected, thus confirming its complete encapsulation in hollow crystals (Table 12). Note that the carbon content reported in Table 11 likely results from a sample surface contamination with CO_2 from air.

The incorporation of metals by successive impregnations is then an alternative method to prepare alloy particles in hollow zeolites but the composition of particles is less homogenous than that of materials synthesized by co-impregnation. Improvements such as repeated impregnations followed by selective removal of external particles may somehow increase the homogeneity of the material prepared by this process.

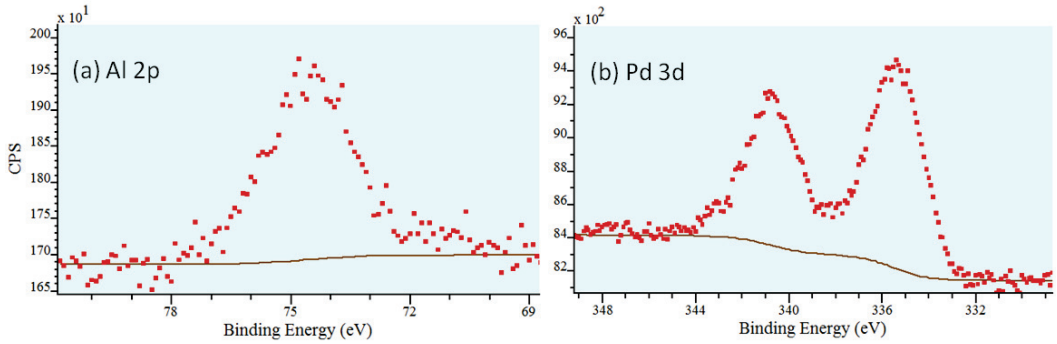

Figure 20: Al 2p (a) and Pd 3d (b) XPS spectra of $Pt_{1.0}Pd_{0.66}$@ZSM-5-PI.

Table 12: Element loadings detected by XPS in $Pt_{1.0}Pd_{0.66}$@ZSM-5-PI sample.

element	C 1s	O 1s	Si 2p	Al 2p	Pd 3d	Na 1s	Pt 4f
wt. %	2.0	48.0	44.7	4.2	0.6	0.5	0

II.2. Bimetallic nanoparticles in hollow ZSM-5 with different structures

PtPd bimetallic particles in hollow ZSM-5 were also prepared by desilication of the zeolite with Na_2CO_3. Pt and Pd were co-impregnated in ZSM-5 crystals and the zeolite was further treated by 1M Na_2CO_3 solution, washed with water and finally reduced at 600°C under H_2 (details in experimental chapter). A TEM image of the final material shows a huge number of very small particles with diameter around 2.5nm encapsulated in a 10 nm thick hollow shell (Fig. 21). The solid looks very

similar to Pt@ZSM-5-DS described in the chapter 5 (Fig. 10 in chapter 5). The sample is denoted $Pt_{0.7}Pd_{0.3}$@ZSM-5-DS with 0.7 wt. % Pt, 0.3 wt. % Pd and a Si/Al at 21 detected by ICP-OES.

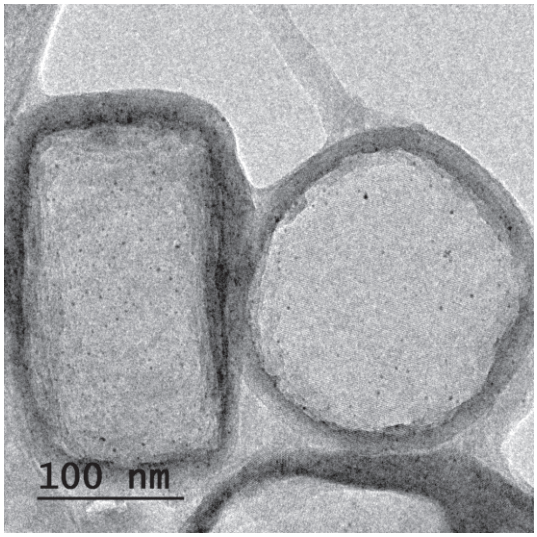

Figure 21: TEM image of $Pt_{0.7}Pd_{0.3}$@ZSM-5-DS obtained by zeolite desilication with a Na_2CO_3 solution with a concentration of 1M.

The solid was further characterized by EDX and the corresponding loadings are reported in Table 13. Due to the relatively low metal loadings and very small particle size, EDX measurements were carried out on 14 areas with a detection diameter around 10 nm, instead of analysing individual particles as in the case of yolk shell materials. Both Pt and Pd are detected in the 14 areas (not shown in the table) with an average Pt/Pd ratio of 2.03, similar to that obtained by ICP-OES analysis (2.33), supporting a homogeneous dispersion of the two metals in the crystals.

Table 13: Element loadings detected by EDX [1] analysis of $Pt_{0.7}Pd_{0.3}$@ZSM-5-DS sample.

O (wt. %)	Al (wt. %)	Si (wt. %)	Pd (wt. %)	Pt (wt. %)	Total	Pt/Pd(wt. %)
48.37	1.31/2[2]	47.65	1.03	1.65	100	2.03/2.33[2]

[1]: Average values from EDX measurements of 14 areas; [2]: ratio detected by ICP-OES.

According to the thickness (~10nm) of the ZSM-5 shell prepared by the desilication method, it would be possible to detect metals encapsulated in the shell by XPS. The relatively intense Pt 4f doublet with binding energies of 70.8 eV and 73.1 eV clearly indicates that Pt is in the form of metallic particles (Fig.22). According to TEM observations, Pt particles are indeed located into the thin ZSM-5 shells, part of which is able to be detected by XPS, in contract to particles in hollow shells prepared by dissolution recrystallization in the presence of TPAOH. However, Pd is not detected by EDX which is quite surprising due to the fact that Pd concentration is approx. half that of Pt. One explanation

could be that Pt particles are distributed throughout the zeolite shell while Pd is preferentially located on the inner surface and thus less detected by XPS.

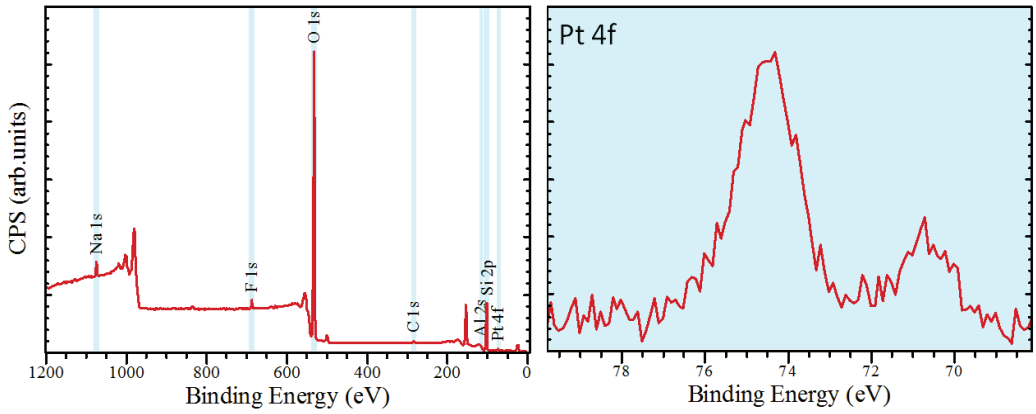

Figure 22: XPS spectra of Pt0.7Pd0.3@ZSM-5-DS (left) and Pt 4f (right).

Another sample of PtPd bimetallic in hollow ZSM-5 was prepared by post impregnating platinum onto 0.45-Pd@ZSM-5-PA (0.45 wt. % Pd loading detected by ICP-OES and PA for Post Aluminum adding) and subsequent reduction in hydrogen. The obtained material is denoted $Pt_{0.8}Pd_{0.45}$@ZSM-5 (0.8 wt. % Pt, 0.45 wt. % Pd and Si/Al=50 detected by ICP-OES) and a representative TEM picture is shown in Fig. 23-b along with a picture of the starting solid $Pd_{0.45}$@ZSM-5-PA (Fig. 23-a). The TEM image shows yolk-shell structures with a big particle inside the cavity and many smaller particles around 3 nm in size in the ZSM-5 shell. EDX confirms that the bigger particle is pure Pd whereas the smaller ones are composed of Pt only. This is further confirmed by XPS measurements (Fig. 24).

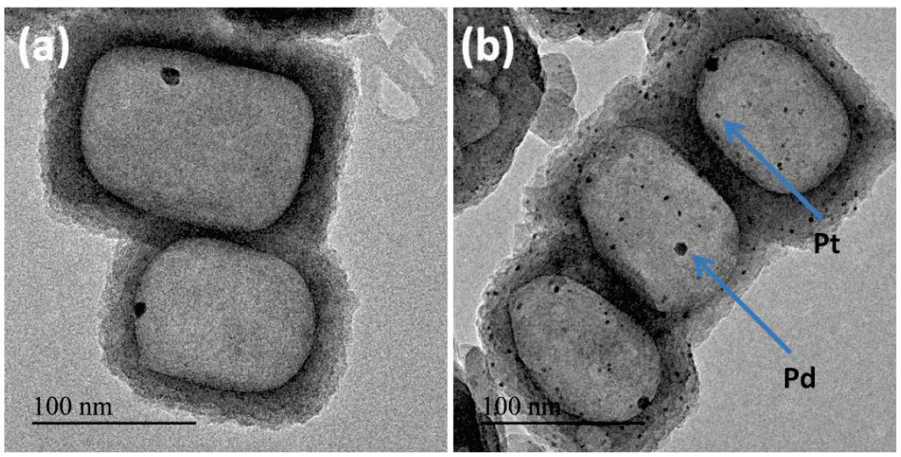

Figure 23: TEM images of $Pd_{0.45}$@ZSM-5-PA (a) and $Pt_{0.8}Pd_{0.45}$@ZSM-5(b).

As Pt 4f peaks with binding energies of 71.3 eV and 74.4 eV are overlapping with those of Al 2p, the de-convoluted spectrum is shown in Fig.24-a. These peaks suggest that Pt is present in the form of metallic particles located in the first 10 nm underneath of the surface, which corresponds to the small particles in the shells in TEM images. In contrast, Pd 3d signal with binding energies between

332 to 344 eV is very noisy, supporting the fact that Pd is mainly contained in the big particle present in each cavity.

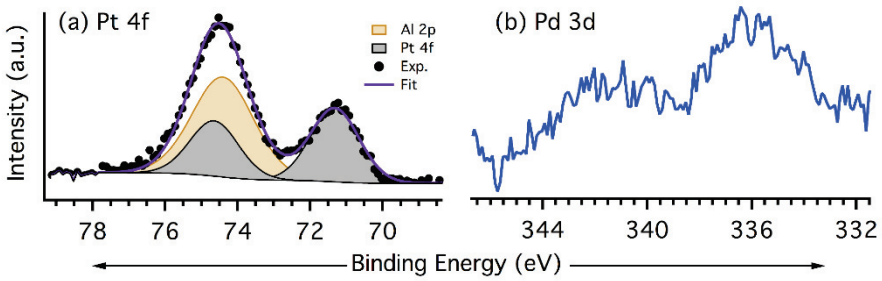

Figure 24: Pt 4f (a) and Pd 3d (b) XPS spectra of $Pt_{0.8}Pd_{0.45}$@ZSM-5 sample.

As it has been discussed in chapter 5, the shell of hollow ZSM-5 prepared by PA method is heterogeneous with an Al-rich surface characterized by a significant roughness under TEM observation (Fig.23). When ZSM-5 hollow crystals are impregnated with a Pt precursor, Pt species exchange with Na^+ in the vicinity of Al atoms instead of entering in the cavities. Then, reduction leads to Pt particles in the shell remaining encapsulated Pd particles intact.

II.3. Sintering tests over AuAg@Sil-1 material

The thermal stability of alloy particles has been tested in an oxidative and humid atmosphere (air+3 vol. % H_2O) at 500°C for 2 hours over $Au_{0.53}Ag_{0.04}$@Sil-1 material. TEM images of the sample before and after sintering are given in Fig.25 and the corresponding particle size distributions are shown in Fig.26. The yolk-shell nanostructure is maintained after the sintering test; moreover, we did not observe the presence of particles outside hollow crystals and the particle size distribution remained identical to that of the original material. Thus, the microporous shell totally prevents metal nanoparticles from sintering at high temperature in an oxidative and humid atmosphere.

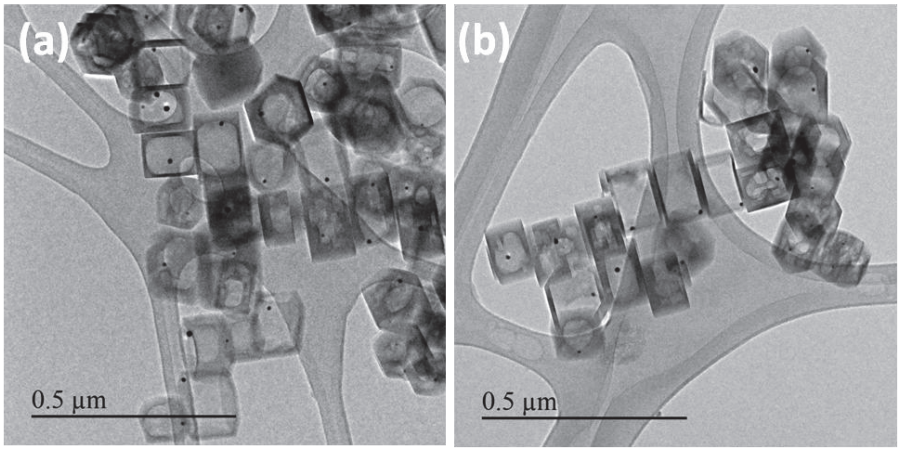

Figure 25: TEM images of $Au_{0.53}Ag_{0.04}$@Sil-1 before (a) and after (b) sintering test.

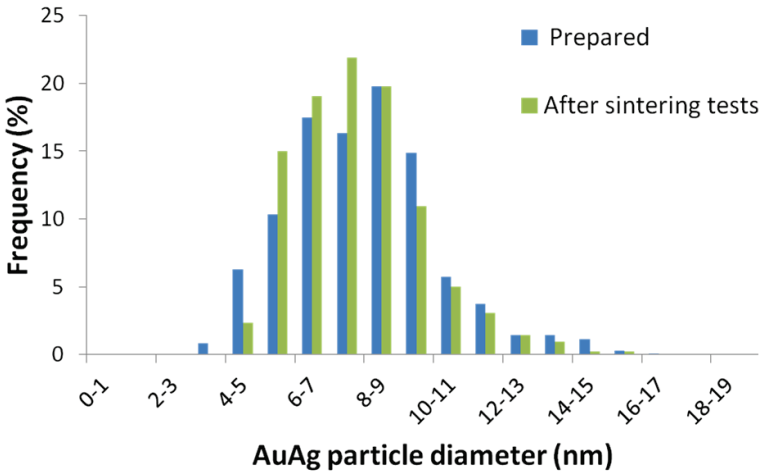

Figure 26: Particle size distribution of $Au_{0.53}Ag_{0.04}$@Sil-1 before (■) and after sintering test(■).

The thermal stability behavior of $Au_{0.53}Ag_{0.04}$@Sil-1 was compared to that of AuAg particles supported on a mesoporous silica MCM-41 material (synthesis details in experimental chapter). TEM images of the sample before and after sintering test clearly show that particles grow from 2 to 20 nm in size when they are submitted to the same sintering conditions used for $Au_{0.53}Ag_{0.04}$@Sil-1 (air+3 vol. % H_2O, at 500°C for 2 hours), see Fig.27. Additionally, the low thermal stability of MCM-41 in moisture atmosphere may also accelerate the particle sintering.

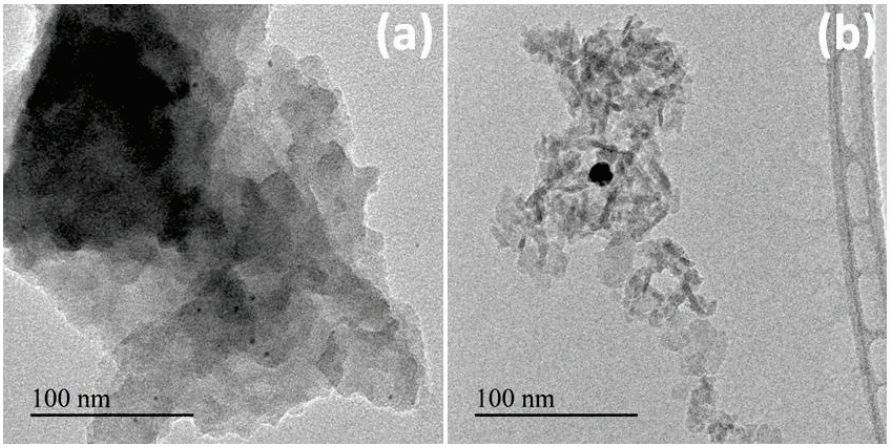

Figure 27: TEM images of AuAg/MCM-41 before (a) and after sintering test (b).

II.4. Synergistic effect of AuAg alloys in CO oxidation reactions

The catalytic properties of AuAg nanoparticle encapsulated in hollow silicalite-1 ($Au_{0.53}Ag_{0.04}$@Sil-1) have been evaluated in the oxidation of CO in the absence (COOx) and in the presence (PROx) of hydrogen. The catalytic results have been compared with those obtained over Au@Sil-1 catalyst, as previously discussed in chapter 3. The evolution of CO_2 yields with temperature for the two catalysts in the absence and in the presence of H_2 are reported in Fig. 28. In the absence of hydrogen, pure gold is almost inactive, even at relatively high temperature. In contrast, AuAg alloys are active at low temperature with an unusual variation of conversions with temperature. In particular, the decrease in activity for T > 45°C is typical from AuAg alloys and could result from O_2 desorption from silver which is presence on the surface of the particle. The high activity of AuAg particles supports the synergetic effect of the two metals, as previously reported by Rousset et al..[6] It is mainly due to the promoted oxygen adsorption and dissociation by Ag species on the surface of the alloy particles. However, $Au_{0.53}Ag_{0.04}$@Sil-1 catalyst seems to be deactivated in the following PROx reactions, in which the catalyst is directly reused after COOx reaction without any regeneration. The catalytic stability of $Au_{0.53}Ag_{0.04}$@Sil-1 catalyst will be studied latter in this chapter.

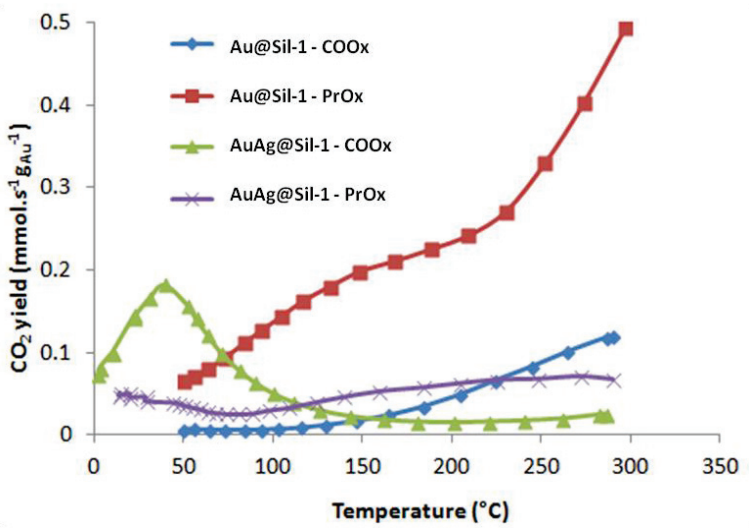

Figure 28 : CO_2 production rates as a function of temperature over 0.28-Au@Sil-1 and $Au_{0.53}Ag_{0.04}$@Sil-1 catalysts in COOx(2%CO+2%O_2 in He) and PrOx reactions (2%CO+2%O_2+48%H_2 in He).

To further evaluate its textural stability under the reaction conditions, the catalyst was studied by TEM and EDX after two cycles of COOx reactions and two cycles of PrOx reactions (Fig. 29 and Table 13). TEM pictures clearly show that the structure of the catalysts was unchanged; in particular, we did not observe particles outside the crystals and the mean particle size was the same. Moreover, the

average composition of particles after catalytic reactions (Au/Ag=12.62) was identical to that of fresh one (Au/Ag=11.47, Table 6), suggesting an impressive stability of our catalyst under the reaction conditions.

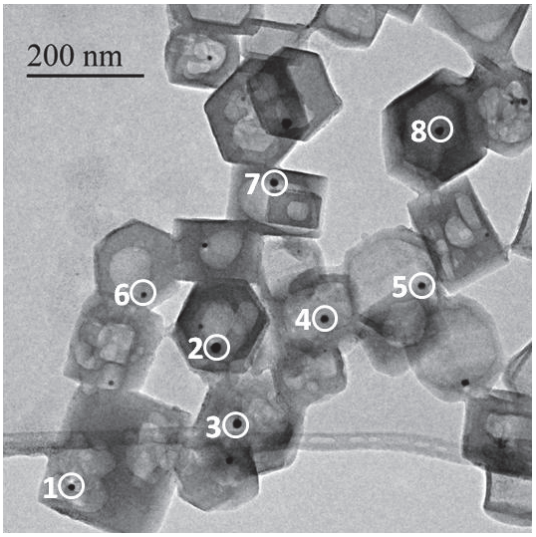

Figure 29: TEM image of $Au_{0.53}Ag_{0.04}$@Sil-1 after CO oxidation. White circles indicating the areas for EDX detecting with the corresponding spot number on the left.

Table 14: The corresponding EDX analysis of the areas indicated by the circles in Fig. 29, the identical number in Fig. 29 and Table 14 represents the same area.

Area	O (wt. %)	Si (wt. %)	Ag (wt. %)	Au (wt. %)	Total	Au/Ag (wt. %)
1	56.90	37.63	0.44	5.04	100	11.45
2	50.03	32.32	0.86	16.79	100	19.52
3	51.82	35.75	0.50	11.93	100	23.86
4	49.49	33.57	1.48	15.47	100	10.45
5	45.58	37.14	1.47	15.80	100	10.75
6	48.99	40.09	1.09	9.83	100	9.02
7	50.58	38.29	0.53	10.60	100	20.00
8	51.09	41.03	0.61	7.27	100	11.92
Average[1]	46.50	38.60	1.14	13.77	100	12.62/13.25[2]

[1]: Average are values are from 17 particles measurements including these 8 results in the table; [2]: 13.25 is the Au/Ag ratio detected by ICP-OES.

The stability of $Au_{0.53}Ag_{0.04}$@Sil-1 catalyst has been confirmed by performing five consecutive reactions of COOx and one reaction of PROx at the end (Fig. 30). For each cycle, the temperature was first set to 300°C and then decreased to 50°C; CO conversions were then measured at each

temperature for approximately 30 minutes (conversions are measured during the second reaction cycle, see details in experimental chapter). For the first and second COOx reactions the catalyst was pretreated at 500°C under H_2 for 2 hours. The CO conversion decreased with time whatever the reaction temperature (300 or 50°C), suggesting deactivation of the catalyst under reaction conditions. However, this deactivation is totally reversible: the catalysts activity is recovered in the second reaction, with the same conversions at 300 and 50°C. We can note that the synergetic effect of Au and Ag is clearly visible by the immediate increase of the conversion when temperature decreases below 150°C (see Fig. 28). The third reaction was similar to the previous ones except that the catalyst was purged in He for 20 minutes before and after the pretreatment. Clearly, the purge in helium has no significant effect on the activity and the stability of the catalyst. Before the 4th reaction, the catalyst was pretreated under slightly oxidative conditions (1% vol. % O_2 in He). Oxygen has a dramatic effect on the activity: the conversion becomes negligible, even at temperatures below 150°C. It is indeed known that only the metallic AuAg particles are active in CO oxidation reactions but not their oxidized compounds, these results are also in agreement with the small conversion in PROx reaction carried over this catalyst after the CO oxidation without regeneration (shown in Fig.28).

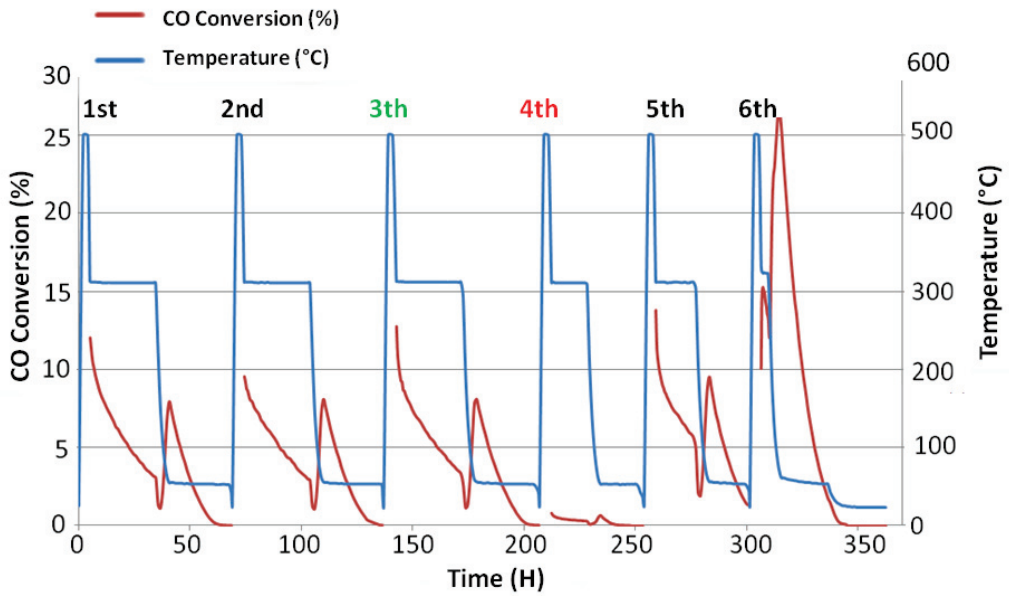

Figure 30: CO conversion and temperature of catalyst bed as function of time over $Au_{0.53}Ag_{0.04}$@Sil-1 catalysts in COOx reactions (2%CO+2%O_2 in He, for the reaction periods of a,b,c,d,e and f) and PrOx reaction (2%CO+2%O_2+48%H_2 in He for the reaction period g). The numbers in order on the figure representing the 6 pretreatments at 500°C for 2 hours with a heating rate of 1°C/min, the atmosphere for these treatment are: 1st and 2nd in pure hydrogen; 3rd, 5th and 6th in pure hydrogen with catalyst purges in He before and after treatment; 4th in 1% O_2 in He with catalyst purges in He before and after treatment.

When the “oxidized” catalyst is pretreated for the 5th time under reductive conditions (pure H_2), the initial activity is recovered (both at 300 and 50°C), clearly indicating that modifications induced by the oxygen treatment are reversible and that the catalysts can be completely regenerated, in agreement with the TEM and EDX analysis on the fresh catalyst and that after reaction (Fig. 29 and Table 13). The 6th reaction has been carried in the presence of hydrogen (PROx reaction). As expected CO conversion drastically increased from 8% to approximately 27% at low temperature, in good agreement with literature results.[7]

These tests clearly demonstrate the reproducibility of the activity of $Au_{0.53}Ag_{0.04}$@Sil-1 in CO oxidation over more than 10 runs. The catalyst is very sensitive to pretreatment conditions (oxidative or reductive) but modifications caused by an oxidative treatment are totally reversible, without modification of the structure, in particular the particle size and composition.

III.Conclusion

In this chapter, alloy particles encapsulated in hollow zeolites have been prepared through co-impregnation and successive impregnations methods. Various bimetallic compositions such as AuAg, PdAg, PtAg and PdPt have been used and they all yielded yolk-shell materials. The particle size distribution (2-15 nm) and metal loadings can be easily adjusted by modifying the concentration of the metal precursor during the impregnation step. The ultra-microporous shells (pore diameter < 0.6 nm) totally prevent sintering processes at high temperature in an oxidative and humid atmosphere. Other types of bimetallic particles in hollow ZSM-5 have also been obtained by applying a desilication method with Na_2CO_3 solutions or by post-impregnation into ZSM-5 hollow shells with an Al-rich surface. These materials provide enormous possibilities in the field of materials science and catalysis. AgAu alloy encapsulated in hollow zeolites shows high activity in CO oxidation at temperatures around 45°C. After reaction, the catalyst is similar to the fresh one as confirmed by TEM and EDX analysis. Moreover, catalytic activities are reproducible even after more than 10 reaction cycles using different pretreatment conditions at 500°C.

We anticipate that through the prevention of Ostwald ripening, our proposed scalable strategy for encapsulating single multi-metallic nanoparticles inside very thin zeolite shells could enable the design of stable, tailor-made catalysts at the nanoscale level for industrial applications.

Bibliography

1. Bell, A.T. The impact of nanoscience on heterogeneous catalysis. *Science* **299**, 1688-1691 (2003).

2. Besenbacher, F., Chorkendorff, I., Clausen, B.S., Hammer, B., Molenbroek, A.M., Nørskov, J.K. & Stensgaard, I. Design of a Surface Alloy Catalyst for Steam Reforming. *Science* **279**, 1913-1915 (1998).

3. Greeley, J. & Mavrikakis, M. Alloy catalysts designed from first principles. *Nat Mater* **3**, 810-815 (2004).

4. Cao, A. & Veser, G. Exceptional high-temperature stability through distillation-like self-stabilization in bimetallic nanoparticles. *Nat Mater* **9**, 75-81 (2010).

5. Wang, G.-H., Hilgert, J., Richter, F.H., Wang, F., Bongard, H.-J., Spliethoff, B., Weidenthaler, C. & Schüth, F. Platinum–cobalt bimetallic nanoparticles in hollow carbon nanospheres for hydrogenolysis of 5-hydroxymethylfurfural. *Nat Mater* **13**, 293-300 (2014).

6. Déronzier, T., Morfin, F., Lomello, M. & Rousset, J.-L. Catalysis on nanoporous gold–silver systems: Synergistic effects toward oxidation reactions and influence of the surface composition. *J. Catal.* **311**, 221-229 (2014).

7. Quinet, E., Piccolo, L., Morfin, F., Avenier, P., Diehl, F., Caps, V. & Rousset, J.-L. On the mechanism of hydrogen-promoted gold-catalyzed CO oxidation. *J. Catal.* **268**, 384-389 (2009).

Conclusions and perspectives:

I. Conclusions

We have developed an original and scalable synthesis pathway that enables the preparation of noble (Au, Pt, Pd and Ag) and transition (Co, Ni and Cu) metal nanoparticles encapsulated in hollow single crystals of MFI-type zeolites (pore size ≈ 0.55 nm) with a wall thickness of approx. 20 nm. It is a one-pot synthesis method in which metal-impregnated crystals are treated by TPAOH solutions to form simultaneously nanoparticles in the cavities by a dissolution recrystallization process. In the particular case of transition metals, phyllosilicates are first formed immediately after TPAOH treatment and nanoparticles are obtained only after reduction at high temperature. A desired particle size (2-15 nm) can be achieved by adjusting the concentration of metal precursor used for impregnation. Moreover, the method has been extended to bimetallic compositions such as PdPt, PtAg, PdAg, and AuAg by impregnating original zeolite crystals with a mixture of metallic precursors and then treating the impregnated zeolite by TPAOH. Each hollow shell thus obtained contains a unique alloy particle, the size and composition of which can be adjusted during the impregnation step. AuAg alloy is a particular case because encapsulated nanoparticles could not be obtained by co-impregnation of zeolite with the mixture if gold and silver precursors. Gold particles were first formed in zeolites, and silver was then added into zeolites crystals before treating with TPAOH. Furthermore, the synergistic effect of Ag and Au in alloyed nanoparticles encapsulated in silicalite-1 was clearly demonstrated by the high activity in CO oxidation at temperature around 45°C. After reaction, the catalyst retained all its structural and chemical characteristics, as confirmed by TEM and EDX analysis. Moreover, catalytic activities were maintained after more than 10 reaction cycles with regeneration process every 2 cycles, showing the long life-time of this yolk-shell material.

In addition, a method to prepare hollow ZSM-5 by desilication with Na_2CO_3 has been developed. This procedure necessitates ZSM-5 crystals in which Al is not homogeneously distributed, with an Al-rich periphery and a Si-rich core. Moreover, dissolved species do not recrystallize and the thickness of ZSM-5 shells can be adjusted down to 10 nm with Si/Al ratios as low as 24. Due to differences in pH values and temperatures, treatments with TPAOH and Na_2CO_3 generally lead to different materials, in particular regarding the number and size of encapsulated particles. For example, many small Pt particles are obtained with Na_2CO_3 whilst TPAOH leads to “yolk-shells” structures, with a unique large particle per cavity.

In the case of transition metals in hollow ZSM-5 prepared by desilication with Na_2CO_3, solids with Co or Ni loadings up to 20 wt. % have been synthesized with a particle size below 10 nm. Actually, particles are very strongly attached to the inner rough surface of the zeolite shell and they are thermally stable even at high reduction temperatures (750°C). In the particular case of Co, we have shown that the particle size could be easily adjusted without modifying the shell thickness by changing the concentration of the Na_2CO_3 solution. These bi-functional catalysts which combine the properties of metal particles with those of zeolite shells (acidity, adsorption capacity, molecular sieving …) are relevant candidates for many applications in catalysis.

One of the challenges in the application of metal nanoparticle-based catalysts is to avoid sintering at high temperature, which leads to particle aggregation and irreversible catalyst deactivation. Different solutions have been proposed, one of them being to isolate particles from one another by a protectable shell. In the case of our novel nanoparticle-encapsulated hollow zeolites, the ultra-microporous shells can totally prevent particle sintering at high temperature both in reductive (750°C in H_2) and oxidative atmospheres, even under more harsh conditions in the presence of H_2O (500°C in $O_2 + H_2O$). Although TOFs of particles in hollow zeolites samples are very high similar or even better than those of supported catalyst, catalytic activities expressed per catalyst volume is relevantly low. Indeed, the solid sites limits particle sintering, of which density is very low leading to low catalytic activities per catalyst volume.

Concerning the application of molecular sieving in catalytic reactions, Pt particles in hollow silicalite-1 and ZSM-5 materials show outstanding properties in terms of size selectivity in the hydrogenation of toluene and mesitylene reactions. The small substrate (toluene, 0.61 nm) can easily reach the embedded particle whereas mesitylene (0.87 nm) cannot. Moreover, in the case of toluene, the catalytic activity is not altered by mass transport through the very thin (20 nm) microporous shell. Pt particles in silicalite-1 are also able to selectively oxidize CO in the presence of propylene, which is known to be a poison when the reaction is performed over Pt-supported amorphous silica. Again, the activity can be attributed to the presence of the zeolite membrane which reduces the access of the alkenes to nanoparticles.

II. Perspectives

The present synthesis route seems to be a very elegant way to isolate nanoparticles with various compositions inside microporous shells. Unfortunately, applications are limited by the pore size of the zeolite and only molecules smaller than the pore diameter can react with nanoparticles. In the case of silicalite-1 and ZSM-5 that the two zeolites studied in this work, the pore diameter is relatively small, typically 0.55 nm. Therefore, an effort has to be made to prepare similar materials but using zeolites with larger pores. For example, particles in hollow FAU or BEA-type zeolites would be particular interesting but their preparation is more difficult. Indeed, the creation of hollow structures requires inhomogeneous crystals, either in terms of composition or in terms of density defects, which cannot always be obtained by direct synthesis. Meanwhile, other compositions and structures of bimetallic particles (for example alloys between transition and noble metals, core-shell or Janus structures …) may also bring novel and improved catalytic properties in many reactions.

From a catalytic point of view, it may be valuable to evaluate with more details on the performances of bifunctional catalysts obtained in this work and compared to those over conventional supported catalysts. Most of the zeolites prepared in this work are in the Na-form and further studies have to be focused on exchange procedures to produce acid catalysts. This could be achieved either by ion-exchange of hollow zeolites with ammonium nitrate or by directly preparing hollow structures from acidic ZSM-5 precursors in the presence of Na-free desilication agents. For example, Pt@ZSM-5 prepared by the desilication route with Na_2CO_3 in which highly dispersed and ultra-thermally stable Pt particles are very closed to the acid shells could be a very promising catalyst for hydroisomerization reactions. The influences of zeolite wall thickness and density of acid sites might be useful to study the reaction mechanism and get optimized catalysts. In addition, Co and Ni particles in hollow acidic ZSM-5 could be applied in the Fisher-Tropsch synthesis with subsequent hydroisomerization and hydrocracking reactions to improved activities and selectivities in short chain hydrocarbons.

For practical applications, the number of nanoparticles per volume unit must be increased by at least an order of magnitude. We showed that TPAOH treatment on metal containing larger MFI crystals (~1 µm) lead to a multi hollow cavities which could be loaded by hundreds metal nanoparticles (Au and Pt) with a less regular in size, however, it is expected that other agents may replace TPAOH and lead to hierarchical hollow zeolites. Improved post-impregnation methods may also be an alertive solution to incorporate nanoparticles in highly porous materials in order to optimize the catalyst volume and increase the metal loading in the zeolite.

Annexe-publication list:

1.

Ultimate size control of encapsulated gold nanoparticles

S. Li, L. Burel, C. Aquino, A. Tuel, F. Morfin, J-L. Rousset and D.Farrusseng

Chemical Communications, **2013**, 49, 8507-8509.

2.

Size-selective hydrogenation at the subnanometer scale over platinum nanoparticles encapsulated in silicalite-1 single crystal hollow shells

S. Li, T. Boucheron, A. Tuel, D. Farrusseng and F. Meunier

Chemical Communications, **2014**, 50, 1824-1826.

3.

Molecular Sieving Driven Selectivity using Encapsulated Pt Nanoparticles in Membrane-like Single Crystal Hollow Zeolites

S. Li, C. Aquino, L. Gueudré, A. Tuel and D. Farrusseng

ACS Catalysis, **2014**, 4, 4299−4303.

4.

Transition-Metal Nanoparticles in Hollow Zeolite Single Crystals as Bifunctional and Size-Selective Hydrogenation Catalysts

S. Li, A. Tuel, D. Laprune, F. Meunier and D. Farrusseng

Chemistry of Materials**, 2015**, 27, 276–282.

5.

New methods for preparing nanoparticles in hollow zeolites (in press)

EU patent, collaborated with IFPEN

6.

Platinum encapsulated hollow zeolite with nanosheet shells as highly active hydrogenation catalysts (to be submitted)

ChemComm

RSC Publishing

COMMUNICATION

View Article Online
View Journal | View Issue

Ultimate size control of encapsulated gold nanoparticles†

Cite this: *Chem. Commun.*, 2013, **49**, 8507

Received 27th June 2013,
Accepted 23rd July 2013

DOI: 10.1039/c3cc44843f

www.rsc.org/chemcomm

Shiwen Li, Laurence Burel, Cindy Aquino, Alain Tuel, Franck Morfin, Jean-Luc Rousset and David Farrusseng*

We report an original and scalable synthesis pathway to produce encapsulated gold nanoparticles. Precise control of the gold particles is achieved in the range of 1–10 nm through the impregnation of silicalite-1 with a controlled concentration of gold solution, followed by dissolution–recrystallization of the zeolite.

Gold nanoparticles attract great attention due to their characteristic localized surface plasmon resonances which find potential applications in biosensing, Raman scattering enhancement and many other fields.[1,2] Investigation into the optical properties of gold nanoparticles with various sizes in different media is a key subject of interest.[3–5] Metal nanoparticles, particularly gold, display unique catalytic properties.[6–10] It has been shown that the particle size is correlated with the Au–Au coordination number which is a key structural feature for catalytic properties.[11,12] Although advanced chemical and physical methods allow for the synthesis of supported gold nanoparticles, they are not thermodynamically stable and ultimately sintering leads to larger particles with a boarder size distribution.[13] On silica, Oswald ripening of gold nanoparticles takes place at 550 °C.[14] The functionalization of the porous silica surface (MCM-41, SBA-15) by amine groups enhances the sintering resistance and allows the synthesis of gold nanoparticles of 4–8 nm. Nevertheless, the dimensions of the gold particle cannot be tailored by using this synthesis pathway.[15] Therefore, there is a need to develop synthetic methods which will allow for the size control and stabilisation of gold nanoparticles in/on a support.[16]

Nanostructured core–shells or yolk–shell materials consist of metal nanoparticle cores encapsulated inside (hollow) shells.[17,18] The metal particles are usually highly monodispersed in size[19–23] and are isolated by the shell which prevents growth by sintering.[14,24] In the case of gold yolk–shell catalysts, the shells are usually made of meso/macroporous oxides or amorphous carbon. In a related process, gold nanoparticles encapsulated in silicalite-1 can be synthesized by preparing silicalite-1 in the presence of gold colloids.[25] However, a significant proportion of gold particles is located on the outer surface of the crystals and the particle size distribution is broad with a significant portion of particles larger than 10 nm in diameter.[25] The size of gold nanoparticles can be decreased by etching using NaCN solution. Nevertheless, this method is ineffective for the synthesis of particles below 5–7 nm as the smallest particles dissolve completely resulting in moderate control of size and distribution.[20] Thus, although chemical synthesis methods for producing gold encapsulated and supported materials have been published, the synthesis of gold nanoparticles with a high degree of size control in the range of 1 to 10 nm has not yet been reported.

We report an original and scalable synthesis pathway which enables the preparation of gold nanoparticles with very high control of size below 7 nm. The desired particle size is readily achieved by adjusting the concentration of gold solution used for the silicalite-1 impregnation and the subsequent dissolution–recrystallization process. The resulting material consists of single gold nanoparticles with controlled size encapsulated in hollow zeolite single crystals.

The preparation of Au@silicalite-1 yolk–shell materials is a multi-step process which is described in Fig. 1. In brief, for a Au@silicalite-1 yolk–shell sample containing 0.52 wt% Au, 0.5 g of silicalite-1 (Fig. 1a) is impregnated with an aqueous solution of $HAuCl_4$ (0.22 M, 0.115 ml) by incipient wetness. The resulting solid is then reduced under H_2 at 350 °C (Fig. 1b). TEM images clearly show that gold nanoparticles are located in the centre of the crystals, where the density of framework defects is maximum (Fig. 1b). Large cavities are then formed by a dissolution–recrystallization process in the presence of TPAOH at 170 °C as previously described elsewhere.[26,27] During this process, the highly defective core of the zeolite crystal is preferentially dissolved and the silica species recrystallizes on the outer surface upon hydrothermal treatment. Since gold nanoparticles are too big to migrate through the microporous zeolite walls,

CNRS, IRCELYON, Université Lyon 1, 2, Av. Albert Einstein, F-69626 Villeurbanne, France. E-mail: david.farrusseng@ircelyon.univ-lyon1.fr; Fax: +33 4 72 44 53 65

† Electronic supplementary information (ESI) available: Powder X-ray diffraction, TEM images, N_2 adsorption isotherms, and synthesis protocol. See DOI: 10.1039/c3cc44843f

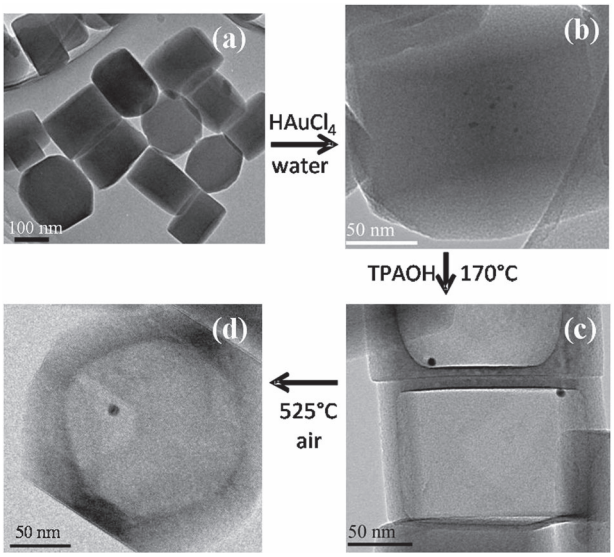

Fig. 1 TEM images of materials at three different steps of the synthesis: (a) starting silicalite-1, (b) Au-impregnated silicalite-1, (c) corresponding hollow Au-silicalite-1 and (d) after calcination.

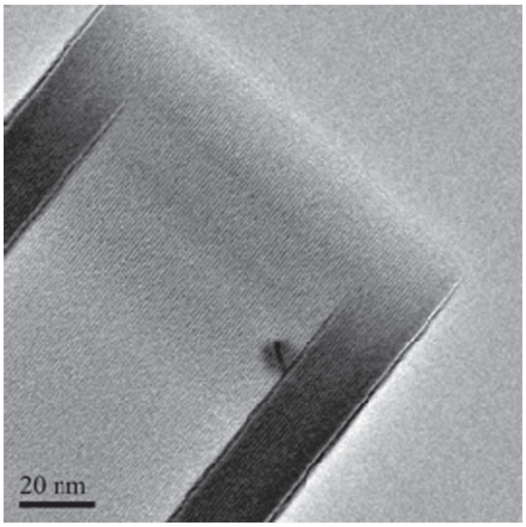

Fig. 2 HRTEM picture of 0.52-Au@silicalite-1 sample showing the single-crystalline nature of the hollow zeolite.

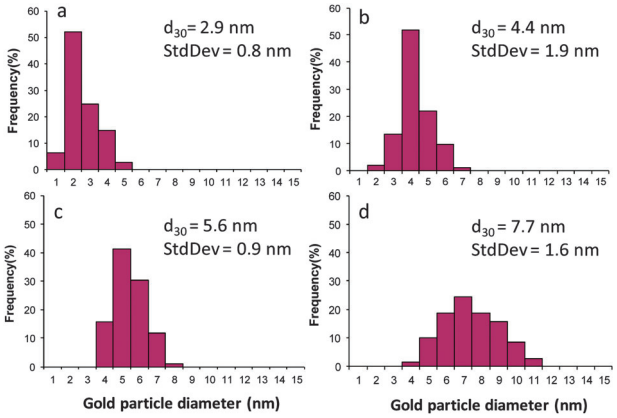

Fig. 3 Gold particle size distribution of (a) 0.08-, (b) 0.28-, (c) 0.52- and (d) 1.2-Au@sillicalite-1.

they remain in the cavity and sinter together into a unique larger particle in an Ostwald ripening process. At this point, each hollow crystal contains one gold nanoparticle which is usually located at an inner-edge of the hollow zeolite (Fig. 1c). Finally, the Au@silicalite-1 composite is calcined at 525 °C in order to remove the template and organic residues, yielding a light pink powder (Fig. 1d). High resolution TEM pictures clearly show the single crystalline nature of the hollow silicalite-1 without apparent crystalline defects such as twinning planes, grain boundary zones or pinholes (Fig. 2). Hence, gold nanoparticles cannot diffuse in and out of internal cavities, preventing ripening mechanisms.

Four different Au@silicalite-1 samples were prepared with different loadings by varying the concentration of $HAuCl_4$ (from 0.05 M to 0.44 M. The samples are designated as *w*-Au@silicalite-1, where *w* is the Au loading (wt%) determined by ICP-OES, see ESI†). The mean size (d_{30}) of gold particles has been calculated from the size distribution population of 300 particles measured by TEM (Fig. 3).[28] The particle size distributions are relatively narrow for all samples as indicated by the standard variation indicators. For example, more than 50% of particles are between 1.5 nm to 2.5 nm in diameter for 0.08-Au@silicatlite-1. The mean particle volume is plotted as a function of the gold loading (*w*) (Fig. 4). Clearly, we can observe that the mean particle volume increases linearly from 12 to 241 nm^3 (corresponding to the diameter (d_{30}) of 2.9 to 7.7 nm, respectively) when gold loading (*w*) increases from 0.08 to 1.2 wt%. The linear correlation is well supported by a theoretical expression (eqn (1)). If one assumes that the metal loading (*w*) is much smaller than the zeolite mass the relationship which links the particle diameter and the metal loading can be expressed as:

$$w = n \cdot \rho \cdot f \cdot (d_{30})^3 \quad (1)$$

where *n* is the concentration of gold particles with diameter d_{30}, ρ the gold density and *f* a shape factor (see ESI†).

As all samples are made with spherical gold particles, ρ and *f* are constant. Assuming that the number of gold particles (*n*) per gram of sample does not vary from sample to sample, a linear relationship is obtained between the volume mean diameter cubed $(d_{30})^3$ and the gold content (*w*) for the *w*-Au@silicalite-1 samples. Clearly, experimental observations follow the theoretical linear relationship in the margin of experimental errors (Fig. 4).

With this linear relationship in hand, it is possible to synthesize a batch of gold nanoparticles with a targeted gold size. For example, to synthesize 1 g of sample with gold particles of 5 nm diameter (d_{30}), corresponding to a volume of 65 nm^3, the gold loading should be equal to 33 mg (0.33 wt%) according to the linear relationship (Fig. 4). This can be readily achieved in practice by adjusting the $HAuCl_4$ concentration. For incipient wetness impregnation the volume of $HAuCl_4$ solution is fixed by the porous volume of the zeolite regardless of the target gold loading (0.23 ml g^{-1} of starting silicalite-1). Hence the gold loading (*w*) is proportional to the $HAuCl_4$ concentration (Fig. 5). Thus, the desired gold particles of 5 nm size can be obtained with an estimated $HAuCl_4$ concentration of 0.13 M.

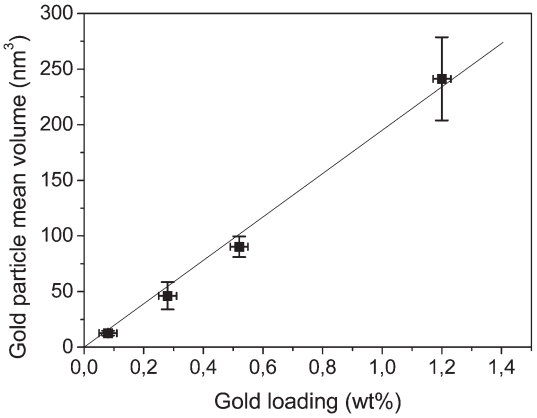

Fig. 4 Mean volume of gold particles measured by TEM as a function of gold loading (*w*). Experimental data (dots) obtained for (a) 0.08-, (b) 0.28-, (c) 0.52- and (d) 1.2-Au@sillicalite-1. The straight line is the fitting result of eqn (1).

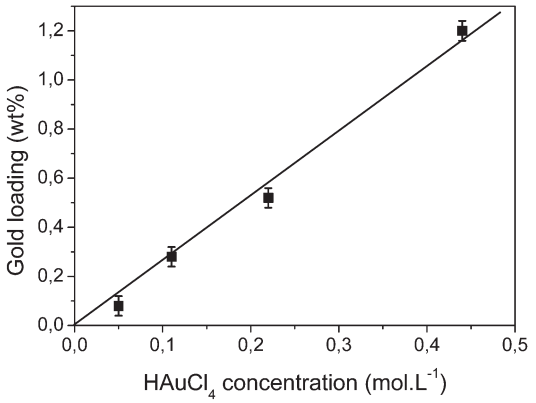

Fig. 5 Gold loading wt% (*w*-Au@silicalite-1) as a function of $HAuCl_4$ concentration.

This high degree of size control of gold nanoparticles cannot be obtained by classical post-impregnation. A post impregnated sample was prepared as a benchmark material. Gold was then introduced by wetness impregnation using a $HAuCl_4$ solution (0.22 M) followed by reduction under H_2 at 350 °C. This post-impregnation synthesis yields a violet powder (denoted as 0.38-Au@silicalite-1 "post-impregnated", see ESI†). The material has a much broader size distribution, typically from a few nanometres to 35–40 nm.

In contrast to the state of the art chemical methods, this original ship-in-a-bottle type synthesis enables the preparation of isolated gold nanoparticles with perfect size control below 10 nm and with a narrow distribution. The desired particle size can be obtained by readily adjusting the concentration of the starting gold solution, This pathway is straightforward since the preparation does not require the synthesis of gold colloids and/or core–shell gold precursors.[18] In addition, our novel method is scalable unlike physical methods such as laser ablation.[29,30] This series of well controlled nanosized gold particles smaller than 10 nm opens a new avenue in catalysis since they can be used under harsh conditions without the issues of growth and leaching. By modifying the synthesis protocol it is possible to encapsulate more than several thousands of nanoparticles in small cavities formed inside much larger zeolite crystals (20–30 μm). All particles are isolated, with a mean size of 5.9 nm, but exhibit a broader size distribution (ESI†). In addition to that, we report here for the first time the synthesis of yolk–shell materials for which a gold nanoparticle is encapsulated in a monocrystalline zeolite shell.

The authors thank scientific services of IRCELYON. This study has been supported by the European Union Seventh Framework Programme FP7-NMP-2010, under grant agreement no 263007 (acronym CARENA).

Notes and references

1 M. C. Daniel and D. Astruc, *Chem. Rev.*, 2004, **104**, 293.
2 S. Eustis and M. A. El-Sayed, *Chem. Soc. Rev.*, 2006, **35**, 209.
3 U. Kreibig and M. Vollmer, *Optical Properties of Metal Clusters*, Springer, Berlin, 1995.
4 S. Link and M. A. El-Sayed, *Int. Rev. Phys. Chem.*, 2000, **19**, 409.
5 K. L. Kelly, E. Coronado, L. L. Zhao and G. C. Schatz, *J. Phys. Chem. B*, 2002, **107**, 668.
6 A. T. Bell, *Science*, 2003, **299**, 1688.
7 G. C. Bond, *Surf. Sci.*, 1985, **156**, 966.
8 M. Boudart, *Catalysis by Supported Metals*, 1969.
9 M. Haruta, *Catal. Today*, 1997, **36**, 153.
10 A. S. K. Hashmi and G. J. Hutchings, *Angew. Chem., Int. Ed.*, 2006, **45**, 7896.
11 J. Radnik, L. Wilde, M. Schneider, M. M. Pohl and D. Herein, *J. Phys. Chem. B*, 2006, **110**, 23688.
12 N. Lopez, T. V. W. Janssens, B. S. Clausen, Y. Xu, M. Mavrikakis, T. Bligaard and J. K. Norskov, *J. Catal.*, 2004, **223**, 232.
13 A. Corma and H. Garcia, *Chem. Soc. Rev.*, 2008, **37**, 2096.
14 C. Wu, Z.-Y. Lim, C. Zhou, W. G. Wang, S. Zhou, H. Yin and Y. Zhu, *Chem. Commun.*, 2013, **49**, 3215.
15 Y. S. Chi, H. P. Lin and C. Y. Mou, *Appl. Catal., A*, 2005, **284**, 199.
16 L. M. Liz-Marzan, *Chem. Commun.*, 2013, **49**, 16.
17 L. M. Liz-Marzan, M. Giersig and P. Mulvaney, *Langmuir*, 1996, **12**, 4329.
18 R. Guettel, M. Paul and F. Schueth, *Chem. Commun.*, 2010, **46**, 895.
19 P. M. Arnal, M. Comotti and F. Schueth, *Angew. Chem., Int. Ed.*, 2006, **45**, 8224.
20 C. Galeano, R. Guettel, M. Paul, P. Arnal, A.-H. Lu and F. Schueth, *Chem.–Eur. J.*, 2011, **17**, 8434.
21 I. Lee, J. B. Joo, Y. Yin and F. Zaera, *Angew. Chem., Int. Ed.*, 2011, **50**, 10208.
22 S. H. Joo, J. Y. Park, C.-K. Tsung, Y. Yamada, P. Yang and G. A. Somorjai, *Nat. Mater.*, 2009, **8**, 126.
23 J. C. Park, H. J. Lee, J. Y. Kim, K. H. Park and H. Song, *J. Phys. Chem. C*, 2010, **114**, 6381.
24 M. Che and C. O. Bennett, *The Influence of Particle-Size on the Catalytic Properties of Supported Metals*, 1989.
25 A. B. Laursen, K. T. Hojholt, L. F. Lundegaard, S. B. Simonsen, S. Helveg, F. Schueth, M. Paul, J.-D. Grunwaldt, S. Kegnoes, C. H. Christensen and K. Egeblad, *Angew. Chem., Int. Ed.*, 2010, **49**, 3504.
26 Y. Wang and A. Tuel, *Microporous Mesoporous Mater.*, 2008, **113**, 286.
27 Y. Wang, M. Lin and A. Tuel, *Microporous Mesoporous Mater.*, 2007, **102**, 80.
28 T. Allen, *Particle Size Measurement, Powder sampling and particle size measurement*, 1968.
29 S. Hashimoto, T. Uwada, H. Masuhara and T. Asahi, *J. Phys. Chem. C*, 2008, **112**, 15089.
30 S. Arrii, F. Morfin, A. J. Renouprez and J. L. Rousset, *J. Am. Chem. Soc.*, 2004, **126**, 1199.

ChemComm

COMMUNICATION

View Article Online
View Journal | View Issue

Cite this: *Chem. Commun.*, 2014, **50**, 1824

Received 13th November 2013,
Accepted 9th December 2013

DOI: 10.1039/c3cc48648f

www.rsc.org/chemcomm

Size-selective hydrogenation at the subnanometer scale over platinum nanoparticles encapsulated in silicalite-1 single crystal hollow shells†

Shiwen Li, Tommy Boucheron, Alain Tuel, David Farrusseng and Frederic Meunier*

Highly controlled "ship-in-a-bottle" platinum nanoparticles in silicalite-1 hollow single crystals have been prepared. This catalyst is highly active for toluene hydrogenation but shows no activity for the hydrogenation of 1,3,5-trimethylbenzene.

The possibility of selectively reacting molecules based on size or shape selectivity reached its pinnacle with the use of zeolites as catalysts.[1,2] Acid or base catalysed reactions have thus been able to target specific compounds in mixtures. The possibility of extending this concept to metal-catalysed reactions has been pursued for several decades with success. Various types of hybrid nanostructures were prepared, typically comprising metallic particles embedded in[1,3–5] or covered by[5–8] porous solids. The latter solids span a wide variety of structures from zeolites[6] to amorphous carbons[7] or oxides.[8]

Mesoporous shells cannot carry out molecular sieve-type separation of molecules smaller than about a nanometer. In contrast, zeolites are crystalline microporous solids, the well-defined pores of which enable a sharp discrimination of the reactants based on size and/or shape. In an ideal zeolite-protected metal catalyst, only reactants with sufficiently small kinetic diameters would be able to cross the zeolite barrier to reach the metallic constituent. The limit of this approach is yet governed by the presence of unprotected metal particles (either located on the external surface of the zeolite constituent or due to the presence of mesoporosity), resulting in imperfect size discrimination. Inadequate encapsulation may not sufficiently limit the diffusion of the metallic atoms and may ultimately result in particle sintering.

Some of us have recently developed an original and scalable synthesis pathway that enables the preparation of gold nanoparticles located in hollow single crystals of silicalite.[9] A desired particle size is achieved by adjusting the concentration of gold solution used for the silicalite-1 impregnation and subsequent dissolution/recrystallization of the core of the crystals. This novel synthesis method is extended here, for the first time, to the case of platinum nanoparticles, which are formed in hollow single crystals of silicalite-1. The outstanding catalytic properties in terms of size selectivity are assessed using the hydrogenation of toluene and mesitylene (*i.e.* 1,3,5-trimethylbenzene), which are similar in size, since the kinetic diameter of toluene and mesitylene is 0.61 and 0.87 nm, respectively.

The preparation of Pt@silicalite-1 materials is a multi-step process involving minor modifications of our previously published method for Au-based samples.[9] In brief, a calcined silicalite-1 is impregnated with an aqueous solution of $Pt(NO_3)_2(NH_3)_4$ and the suspension is continuously stirred until the solvent is totally evaporated. The resulting solid is treated with a tetra-*n*-propylammonium hydroxide (TPAOH) solution in an autoclave at 170 °C for 24 hours. It is during this step that the hollow core of the silicalite-1 is formed, due to dissolution of the defect-rich core. Finally, the Pt@silicalite-1 composite is calcined at 450 °C and reduced under H_2 at 300 °C.

High resolution TEM pictures clearly show the single crystalline nature of the hollow silicalite-1 without apparent crystalline defects such as twinning planes, grain boundary zones or pinholes (Fig. 1, left).

Hence, Pt nanoparticles cannot diffuse out of the internal cavity, preventing the formation of metal particles at the zeolite outer surface. Pt particles are known to migrate and coalesce under H_2 between 600 and 700 °C.[10] As a matter of fact, the Pt@silicalite-1 material is resistant to calcination at 750 °C (Fig. 1, right) and the particle size distribution of the Pt was hardly changed from that obtained at 600 °C, with a slight increase from 10.3 to 10.4 nm (Fig. 2). The increase was probably due to the aggregation of very small Pt molecules present in the cavity, rather than transport and coalescence through the microporous walls of the silicalite-1 crystals.

The catalytic activity of the Pt@silicalite-1 for the hydrogenation of toluene and mesitylene to the corresponding saturated

Institut de Recherches sur la Catalyse et l'Environnement de Lyon (IRCELYON), Université Lyon 1, CNRS 2, Av. Albert Einstein F-69626, Villeurbanne, France. E-mail: frederic.meunier@ircelyon.univ-lyon1.fr; Fax: +33 4 72 44 53 65

† Electronic supplementary information (ESI) available. See DOI: 10.1039/c3cc48648f

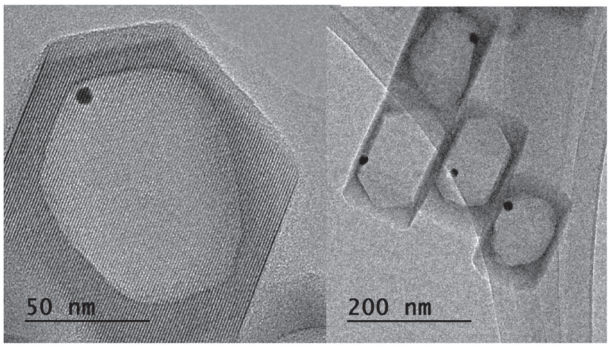

Fig. 1 Left: HRTEM picture of sample Pt@silicalite-1 showing the single-crystal nature of the hollow zeolite calcined at 450 °C and reduced in H_2 at 300 °C. Right: HRTEM picture showing the sample after reduction in H_2 at 750 °C.

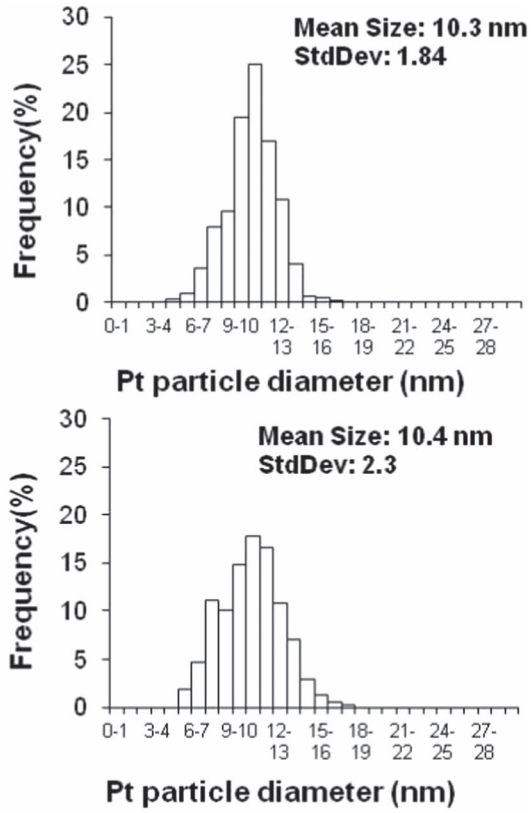

Fig. 2 Pt particle size distribution on Pt@silicalite-1 after reduction in H_2 at 600 (top) and 750 °C (bottom).

compounds was investigated (see Experimental details in the ESI†). The activity of a conventional Pt sample supported on high surface area silica was also measured for these two reactants.

The Pt@silicalite-1 and the Pt/SiO_2 led to a similar conversion *versus* temperature plot for toluene (Fig. 3A). Since the Pt loading was twice higher on the Pt@silicalite-1 and the corresponding dispersion was two-fold lower, as compared to the Pt/SiO_2, essentially identical turnover frequencies were obtained for these two catalysts as far as toluene hydrogenation was concerned (see Fig. S3, ESI†).

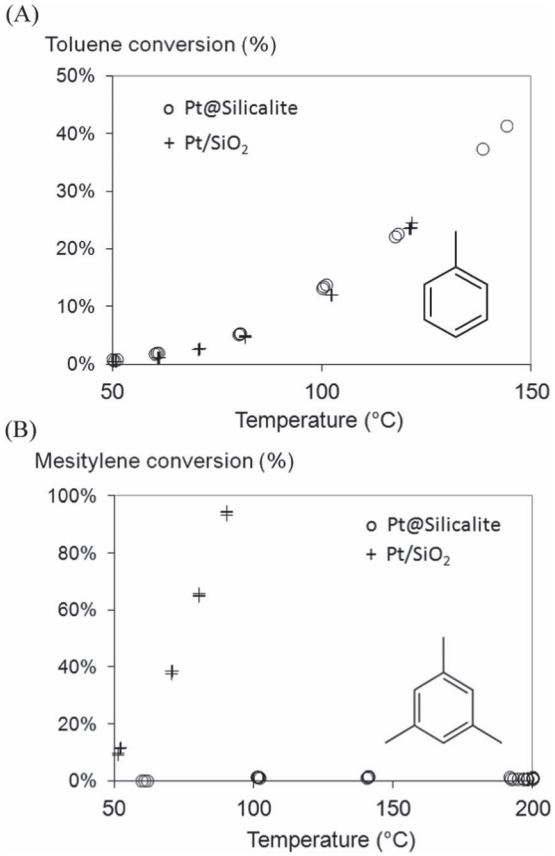

Fig. 3 Conversion during the hydrogenation of (A) toluene and (B) mesitylene over the Pt@silicalite-1 and a Pt/SiO_2. Toluene pressure = 903 Pa, balance H_2. Mesitylene pressure = 61 Pa, balance H_2.

The values of turnover frequencies (*e.g.* 6×10^{-2} s^{-1} at 80 °C) are consistent with those obtained for toluene hydrogenation on other Pt-based catalysts under similar experimental conditions.[11,12] Similarly, the apparent activation energies measured here (*ca.* 55 ± 3 kJ mol^{-1}, Fig. S4 and S5, ESI†) are similar to those reported elsewhere.[11,13]

These data therefore indicate that the silicate-1 hollow box did not significantly hinder either the transport of toluene or that of the reaction product methylcyclohexane.

The case of mesitylene was dramatically different. Mesitylene was readily fully hydrogenated to trimethylcyclohexane over the conventional SiO_2-supported Pt, while a conversion lower than 2% was measured in the case of the Pt@silicalite-1, which was a value within our experimental error (Fig. 3B).

The turnover frequency for mesitylene hydrogenation on the Pt/SiO_2 was only calculated for the data point displaying a conversion lower than 15% and was found to be 7.6×10^{-3} s^{-1} at 41 °C. Note that the TOF for toluene hydrogenation would be expected to be around 4×10^{-3} s^{-1} at 41 °C on the same catalyst. Therefore, the TOFs for hydrogenation of toluene and mesitylene on the Pt/SiO_2 were of the same order of magnitude.

The data reported above indicate that the rate of mesitylene hydrogenation on the Pt@silicalite-1 was at least two orders of

magnitude lower than that on the Pt/SiO_2. We can therefore conclude that the vast majority (at least 99%) of the observed Pt particles were indeed inside the hollow boxes.

The origin of this inhibition was the size exclusion of the mesitylene from the silicalite-1 pores. High resolution TEM images revealed that the zeolite hollow boxes were essentially monocrystalline materials. A unique crystallographic plane orientation was observed on the whole side of a box (data not shown). The N_2 adsorption isotherm revealed that the hollow zeolites were free of mesoporous pinholes.[9] The channel dimensions of silicalite-1 are about 0.56×0.53 nm and toluene can enter the pores while mesitylene is too large and is therefore excluded from the micropores. Adsorption isotherms of toluene and mesitylene on the silicalite-1 hollow boxes (free of Pt) confirm the uptake of toluene and the size exclusion of the larger hydrocarbon from the pores (see Fig. S6, ESI†). The hollow zeolite crystal operates as a zeolite oriented membrane with a cut-off at about 0.7 nm.

Since mesitylene cannot enter the pores of the hollow box, it is reasonable to propose that each hollow box entirely consists of the MFI-type structure, without any significant mesoporosity. Therefore, the cut-off size to access the embedded Pt particles should be above the kinetic diameter of *p*-xylene (= 0.585 nm), which is known to readily diffuse in MFI-type materials and around that of *o*- and *m*-xylene (*ca.* 0.68 nm), which can still enter MFI pores, but whose transport is greatly hindered.[14,15]

In conclusion, we have been able to prepare a new type of catalytic material consisting of single Pt particles embedded in a silicalite-1 monocrystal without measurable Pt particles at the outer surface. This type of well-defined material paves the way for more academic studies and practical applications of shape, size and product selectivity for a wide range of catalytic systems in terms of catalyst composition and reaction mixtures. Of particular interest is the fact that the size of the metal particles contained within the hollow crystal can be much larger than the cavities of the sieving element, contrary to the materials prepared by the methods reported earlier.[1,3,4]

The authors thank the scientific services of IRCELYON. This study has been supported by the European Union Seventh Framework Programme FP7-NMP-2010, under Grant Agreement no. 263007 (acronym CARENA).

Notes and references

1 P. B. Weisz, V. J. Frilette, R. W. Maatman and E. B. Mower, *J. Catal.*, 1962, **1**, 307.
2 S. M. Csicsery, *Zeolites*, 1984, **4**, 202.
3 S. Altwasser, R. Gläser and J. Weitkamp, *Microporous Mesoporous Mater.*, 2007, **104**, 281.
4 S. Goel, Z. Wu, S. I. Zones and E. Iglesia, *J. Am. Chem. Soc.*, 2012, **134**, 17688.
5 A. B. Laursen, K. T. Højholt, L. F. Lundegaard, S. B. Simonsen, S. Helveg, F. Schuth, M. Paul, J.-D. Grunwaldt, S. Kegnæs, C. H. Christensen and K. Egeblad, *Angew. Chem., Int. Ed.*, 2010, **49**, 3504.
6 P. Collier, S. Golunski, C. Malde, J. Breen and R. Burch, *J. Am. Chem. Soc.*, 2003, **125**, 12414.
7 C. Galeano, R. Guttel, M. Paul, P. Arnal, A.-H. Lu and F. Schuth, *Chem.–Eur. J.*, 2011, **17**, 8434.
8 R. N. Devi, F. C. Meunier, T. Le Goaziou, C. Hardacre, P. J. Collier, S. E. Golunski, L. F. Gladden and M. D. Mantle, *J. Phys. Chem. C*, 2008, **112**, 10968.
9 S. W. Li, L. Burel, C. Aquino, A. Tuel, F. Morfin, J. L. Rousset and D. Farrusseng, *Chem. Commun.*, 2013, **49**, 8507.
10 A. K. Datye, Q. Xu, K. C. Kharas and J. M. McCarty, *Catal. Today*, 2006, **111**, 59.
11 J. L. Rousset, L. Stievano, F. J. Cadete Santos Aires, C. Geantet, A. J. Renouprez and M. Pellariny, *J. Catal.*, 2001, **197**, 335.
12 A. A. Taimor, I. Pitault and F. C. Meunier, *J. Catal.*, 2011, **278**, 153.
13 S. D. Lin and M. A. Vannice, *J. Catal.*, 1991, **143**, 554.
14 S. F. Garcia and P. B. Weisz, *J. Catal.*, 1990, **121**, 294.
15 F. C. Meunier, D. Verboekend, J.-P. Gilson, J. C. Groen and J. Pérez-Ramírez, *Microporous Mesoporous Mater.*, 2012, **148**, 115.

ACS Catalysis

Letter

pubs.acs.org/acscatalysis

Diffusion-Driven Selectivity in Oxidation of CO in the Presence of Propylene Using Zeolite Nano Shell as Membrane

Shiwen Li, Cindy Aquino, Laurent Gueudré, Alain Tuel, Yves Schuurman, and David Farrusseng*

IRCELYON, UMR 5256 CNRS- Université Lyon-1, 2 Avenue Albert Einstein, F-69626 Villeurbanne, France

Supporting Information

ABSTRACT: The selective oxidation of CO over C_3H_6 is achieved in yolk-shell Pt@Silicalite-1 catalysts in which Pt nanoparticles are encapsulated in hollow silicalite-1 single crystals. The thin shell operates as a permselective membrane which limits Pt surface poisoning by C_3H_6. From adsorption measurements, we conclude that the catalytic selectivity arises from the fastest diffusion of CO over C_3H_6 through the silicalite-1 membrane.

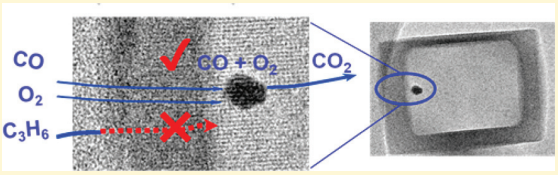

KEYWORDS: *heterogeneous catalysis, Pt nanoparticle, hollow zeolite, selective CO oxidation, poison resistance, diffusion*

The design of acid catalysts by shape selectivity is well established. It deals with the molecular sieving of different substrates/products or preventing the formation of intermediates bulkier than the cavity of zeolite. Such type of selective catalysts are used at industrial scales for major chemical and energy processes such as disproportionation of toluene,[1] alkylation,[2] and MTO.[3] On the other hand, selective oxidation/reduction on metal catalysts is achieved by designing the metal surface with appropriate adsorption features so that the adsorption of the target substrate can be selectively converted.[4−7] Selectivity is addressed by playing on surface sensitivity[8] and alloying effects.[4] Carbon monoxide and alkenes strongly compete for adsorption on noble metal surfaces.[9] The presence of a very small concentration of CO decreases the activity of the hydrogenation of ethylene by several orders of magnitude.[10] Conversely, the process of selective CO oxidation in the presence of alkenes for purification purposes is also a scientific and technical challenge.[9,11,12]

Lately, the concept of controlling the selectivity of metal catalysts by a shell of zeolite membrane was reported. Collier et al. demonstrated the CO selective oxidation in the presence of butane achieved by a zeolite-coated metal/SiO_2 catalyst.[13,14] Kapteijn et al. described a H-ZSM-5-coated Co/SiO_2 catalyst capable of producing a certain range of hydrocarbons in Fischer−Tropsch synthesis.[15−17] Nishiyama et al. showed transport-driven selective hydrogenation on a mixture of linear and branched C_6 alkenes on Pt/TiO_2 beads coated with silicalite-1 polycrystalline layer.[18,19] In all previous studies, a macroscopic layer is coated on metal/SiO_2 grains, and the activity is given by the metal particles underneath the membrane. However, the thickness of the zeolite shell is usually from 200 nm up to several microns,[14,18] which eventually limits the overall reaction rates due to diffusion transport limitations.[18]

The so-called "yolk−shell catalyst" design is an attractive solution which can overcome diffusion limitation. Yolk−shell catalysts are specific materials in which the yolk is a catalyst particle and the shell is a very thin porous layer, generally an inorganic oxide (ZrO_2, TiO_2, and SiO_2) or carbon.[20−24] Recently, PtCo bimetallic nanoparticles encapsulated in carbon hollow spheres were reported for outstanding performances in the hydrogenolysis of HMF to DMF by the group of F. Schüth.[25] This catalyst demonstrated an enhancement in the production of molecular fuel from biomass over the metal catalysis. However, mesoporous shells are not appropriate to separate gas molecules such as light hydrocarbons and permanent gases(CO, CO_2,N_2, etc.) because of the mismatch between the size of membrane cavities (>2 nm) and the sieve of substrates (kinetic diameter <1 nm), thus preventing a sieving separation mechanism.

Recently, we have reported the synthesis of yolk−shell materials which consist of metal nanoparticles (Au, Pt) encapsulated in hollow crack-free silicalite-1 single crystals with a wall thickness of about 20 nm. This enables the preparation of isolated metal nanoparticles with size control from 1 to 10 nm and narrow distribution.[26] The concept of selective hydrogenation driven by molecular sieving property of the reactants using a zeolite shell has been illustrated on a Pt@ hollow silicalite-1.[27] We have shown that toluene (0.61 nm, kinetic diameter) is hydrogenated, whereas mesitylene (0.87 nm, kinetic diameter), which has a larger kinetic diameter than the pore size of siliclaite-1 (0.55 nm), is not.

Unfortunately, for light hydrocarbons and permanent gases, the size exclusion mechanism cannot operate because they can all penetrate into the microporous network. Nevertheless, we can assume that the differences in diffusion rates between two substrates in zeolite membrane shall result in a selective separation, that is, the permselective transport of one reactant through a zeolite layer could enhance catalytic selectivity.[28−30]

Received: September 7, 2014
Revised: October 29, 2014

   dx.doi.org/10.1021/cs501349b | ACS Catal. 2014, 4, 4299−4303

In this study, we have applied Pt nanoparticles encapsulated in thin hollow zeolite shells, hereafter called "Pt@S-1", as effective CO selective oxidation catalysts in the presence of propylene acting as a poison. We demonstrate that the zeolite shell limits transport of propylene to the metal particles while CO is converted by Pt nanoparticles. Two reference catalysts were prepared and tested in order to support our hypothesis.

A detailed recipe of Pt@S-1 "yolk shell" catalyst can be found in previous publications and in the Supporting Information (SI).[27,31] In brief, Pt@S-1 is obtained by treating Pt impregnated silicalite-1 in TPAOH solution at 170 °C. Each hollow shell is approximately 200 nm × 150 nm × 140 nm in size and contains one Pt particle (Figure 1) (less than 5%

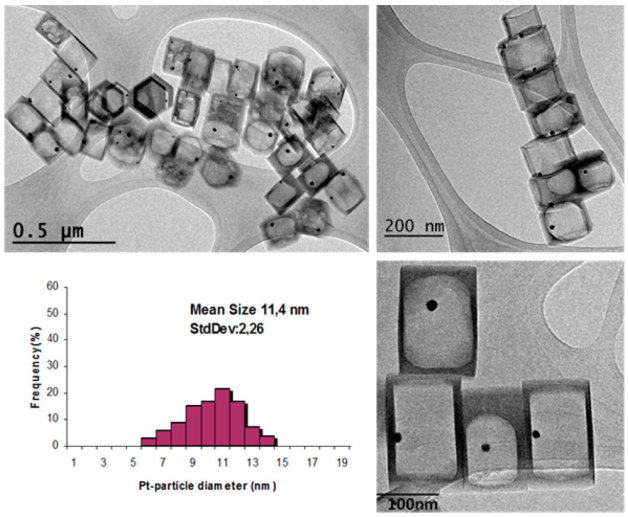

Figure 1. TEM images of Pt@S-1 and size distribution of Pt particles.

hollow zeolites contain more than 1 particle). The HRTEM picture and X-ray diffraction clearly show the single crystal nature of the 20 nm thick walls without apparent defects such as twinning planes, grain boundary zones, or pinholes (see Figure S1). The hollow zeolites are mechanically robust as they cannot be broken upon manual grinding with a mortar and they do not collapse when pressing up to 5 tons. Nitrogen physisorption measurements (at 77 K) are similar to those previously reported for Pt-free hollow silicalite-1 (see Figure S2).[31]

In contrast to materials made of a polycrystalline zeolite shell, the presence of a hysteretic loop with a forced closure at $p/p_0 \approx 0.45$ indicates that the walls of the hollow zeolite do not contain pores larger than 4 nm.[32,33] The mean size of Pt particles of Pt@S-1 has been calculated from size distribution population of 400 particles measured by TEM (Figure 1).[34] The particle size distribution is relatively narrow. More than 50% of particles are between 10 to 12 nm in diameter.

Catalytic data are compared with (0.90 wt %) Pt-supported silicalite-1 (Pt/S-1). It is produced by using the same starting materials as Pt@S-1 but without the TPAOH post-treatment step, which is responsible for desilication (details in SI). Pt/S-1 is characterized by a significant portion of the Pt particles located at the external surfaces (Figure S3), whereas others are embedded in the zeolite crystals. A commercial Pt/SiO_2 supported catalyst obtained from Sigma-Aldrich (0.71 wt % Pt, Figure S4) is used as a second reference sample. The three catalysts are quite similar in terms of Pt loadings and mean Pt particle sizes; 11.4, 8.9, and 7.5 nm for Pt@S-1, Pt/S-1, and Pt/SiO_2, respectively (Table S1). The catalysts differ on the location of the Pt nanoparticles. In Pt@S-1, the Pt particles are encapsulated inside a silicalite-1 box, whereas for the two reference catalysts, the particles are directly accessible to the gas phase. The mechanism of formation of the Pt nanoparticles at the external surface of silicalite-1 crystal in Pt/S-1 goes beyond the scope of this study. Nevertheless, we can assume that during the heat treatment the Pt atoms and/or cluster may diffuse through the zeolite channels to the surface where they can grow.

CO oxidation with or without propylene was carried out in a fixed bed reactor by rising the temperature at a constant rate of 1 °C/min. The compositions (vol %) of the stream were 2% CO, 2% C_3H_6 (when present), 2% O_2 and balance of N_2. As a consequence, O_2 is in excess for the selective oxidation of CO, whereas it is a default for a total combustion of C_3H_6. Molar fractions of reactants and products were measured by a fast-gas chromatograph allowing an analysis every 4 min. The conversions of CO and C_3H_6 (if present) are plotted as a function of the catalyst bed temperature for Pt@S-1 and the reference Pt/S-1 (Pt/SiO_2 in SI, Figure S5) catalysts (Figure 2).

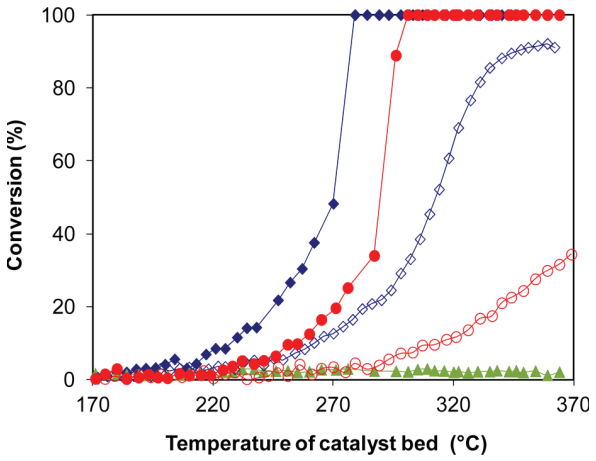

Figure 2. CO conversion in the absence (full symbols) and in the presence (open symbols) of propylene over Pt@S-1(blue ◆, blue ◇), Pt/S1(red ●, red ○), and metal-free hollow silicalite-1(green ▲).

In the absence of propylene, Pt-free hollow silicalite-1 shows a negligible activity, and the CO conversion does not exceed 3%. All Pt-containing catalysts fully convert CO with light-off temperatures between 270 and 310 °C (see Table S2), in good agreement with data from the literature.[35] The origin of the small variation of the light-off temperature for the three samples may be due to the slightly different Pt loading used in the testing (i.e., 0.44, 0.45, and 0.35 mg for Pt@S-1, Pt/S-1, and Pt/SiO_2 (see Table S2), which was also confirmed by CO oxidation catalyzed by different amounts of Pt@S-1 catalyst (see Figure S6 and Table S3).

The introduction of 2% C_3H_6 significantly shifts the light-off temperature of all three catalysts. More importantly, it strongly reduces conversion for the reference catalysts Pt/S-1 and Pt/SiO_2, both exhibiting very similar results (see Figure S5). For these two reference catalysts, the maximum CO conversion reaches only 35−40% at 370 °C with light-off temperatures of ca. 340 °C. As already described by Voltz,[9] propylene partially prevents the adsorption of CO on Pt particles and therefore acts as a surface reversible poison. By contrast to the above

dx.doi.org/10.1021/cs501349b | ACS Catal. 2014, 4, 4299−4303

benchmark catalysts, Pt@S-1 remains highly active in the presence of propylene. Maximum CO conversion reaches 92% at 360 °C, which is more than twice the reference catalysts. At 280 °C, the TOFs (turnover frequencies) over Pt@S-1 are 4 and 8 times larger than over Pt/S-1 in CO oxidation in the absence and presence of propylene, respectively (see Table S2). In addition, the three catalysts' propylene conversions at 350 °C are 2.4%, 4%, and 1.3% over Pt@S-1, Pt/S-1, and Pt/SiO_2 catalysts, respectively (see Figure S5). Pt@S-1 showed the highest CO conversion with limited propylene oxidation. For Pt/SiO_2, all Pt particles are directly accessible to the gas phase and therefore are subject to propylene poisoning. The same applies for Pt/S-1, where most of the Pt particles are located at the external surfaces of the zeolite crystals. It is therefore not surprising that Pt/SiO_2 and Pt/S-1 reference catalysts perform similarly. Moreover, we do not observe any change in the color of the catalyst before and after reaction. The carbon balance for each reaction is generally above 98%, which suggests that the amount of coke formed is negligible.

Obviously, the selective permeability of zeolite shells limits the poisoning effect of propylene while maintaining a high accessibility to carbon monoxide. The transport properties of silicalite-1 and permeation properties of silicalite-1 membranes are well-known and support our hypothesis.

The kinetic diameters of CO (0.376 nm) and C_3H_6 (0.45 nm) are smaller than the pore size of silicalite-1 (0.51 nm × 0.55 nm). Hence, a steric exclusion mechanism cannot be proposed for supporting the catalytic results. For a silicalite-1 membrane, it is acknowledged that the separation mechanism of a mixture of substrates depends first on coverage concentrations of the different species.[36,37] At high coverage, the most strongly adsorbed substrate prevents other substrates from adsorption and thus diffusion. However, at these reaction temperatures (T > 200 °C), we estimate from adsorption isotherm data that the fractional coverage of CO and propylene are lower than 1% (see Figures 3, 4, and S4 and Table1).

Thus, competitive adsorption can be ruled out for the limitation of the transport of propylene. The second mechanism of membrane permselectivity is driven by differences in diffusion rates which are mainly governed by the size of the substrate.[36,38] The effective mass transfer coefficient (Kap) of CO and propylene were measured at low coverage on hollow silicalite-1 in a volumetric measurement system by applying the Linear Driving Force Model (LDF) (Figure 5).[39] We calculate that at room temperature C_3H_6 diffuses more than 200 times slower than CO, which could explain the permselective mechanism of the zeolite shell and thus the poisoning CO resistance of the Pt@S-1 catalyst. Because C_3H_6 can diffuse through the membrane, C_3H_6 can still poison the Pt surface as the concentration of C_3H_6 builds up with time in the hollow zeolite, whereas the CO is depleted by oxidation. The estimation evolution of partial pressure of C_3H_6 and other components at reaction temperature with time would require the modeling of the catalytic and all transport phenomena including the retrodiffusion of CO_2, which is beyond the scope of this study.

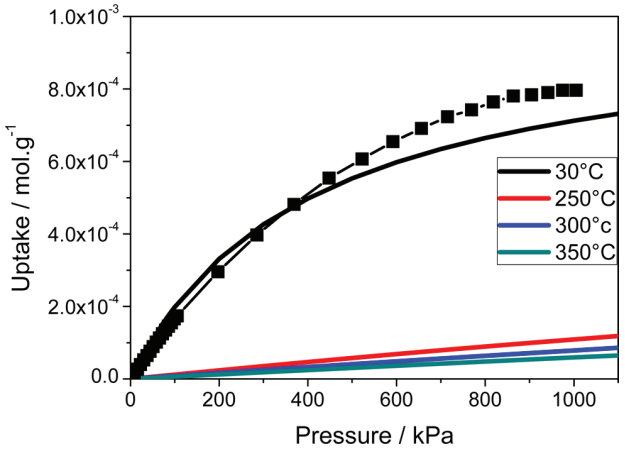

Figure 3. CO adsorption isotherms. Experimental data at 30 °C (full line), fitted data at 30 °C (black square), simulated data at 250, 300, 350 °C.

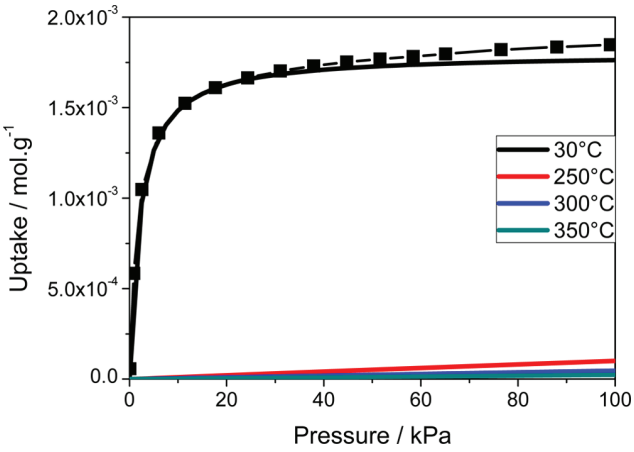

Figure 4. C_3H_6 adsorption isotherms. Experimental data at 30 °C (full line), fitted data at 30 °C(black square), simulated data at 250, 300, 350 °C.

Table 1. Coverage Estimations at Room Temperature and Reaction Conditions for Partial Pressures of 2 kPa

temp	30 °C	250 °C	300 °C	350 °C
coverage	%	%	%	%
CO	<1	<1	<1	<1
C_3H_6	90.4	1.2	<1	<1

We report here an original synthesis pathway for Pt nanoparticles encapsulated in a defect-free, hollow single crystal zeolite with shells around 20 nm thick. In contrast to a classical Pt-impregnated silicalite-1, the hollow zeolite shell prevents Pt particles to grow at the external surface of the crystal. This type of yolk−shell catalyst, which is characterized by large hollow cavities, is minimally appropriate for practical application as the low metal density will result in very large catalyst volume. We showed earlier for gold@silicalite-1 that an increase of 90 times particles concentration can be achieved by starting with larger zeolite crystals.[26] We will report shortly a detailed study of the synthesis process for loading larger number of nanoparticles. We demonstrate for the first time that a single crystal zeolite shell can also act as a permselective membrane which prevents the encapsulated metal particles from poisoning. In the case of CO oxidation in the presence of the reversible poison propylene, the separation mechanism is driven by the difference in the diffusion rates between CO and propylene, the latter being more than 200 times slower at room temperature.

dx.doi.org/10.1021/cs501349b | ACS Catal. 2014, 4, 4299−4303

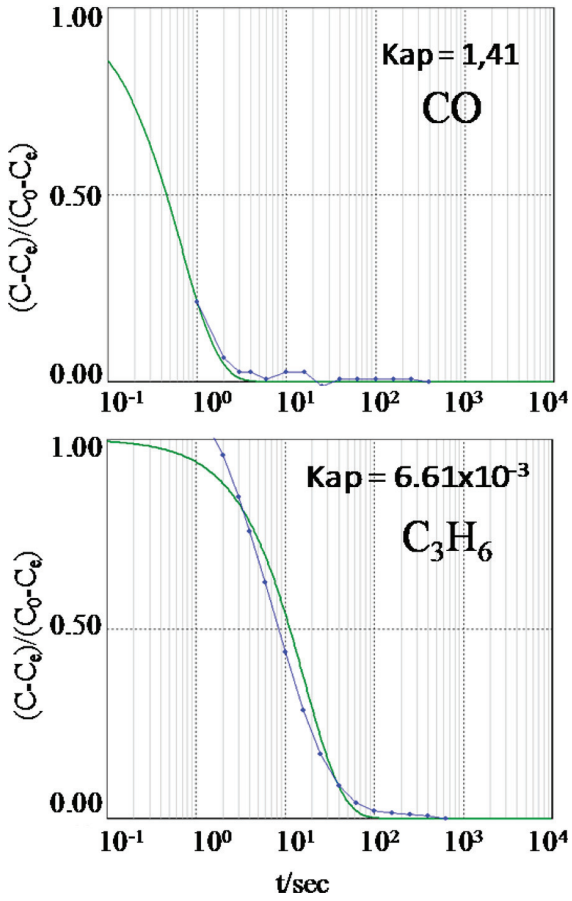

Figure 5. Relaxation pressure in the adsorption of CO (up) and C_3H_6 (down) at 30 °C and corresponding at coverage of 10% (blue squares). LDF model fit (green line).

■ ASSOCIATED CONTENT

Supporting Information

The following file is available free of charge on the ACS Publications website at DOI: 10.1021/cs501349b.

Material preparation, elementary analysis, single adsorption measurements, and breakthrough experiments (PDF).

■ AUTHOR INFORMATION

Corresponding Author

*E-mail: david.farrusseng@ircelyon.univ-lyon1.fr.

Notes

The authors declare no competing financial interest.

■ ACKNOWLEDGMENTS

The authors thank the scientific services of IRCELYON. This study has been supported by the European Union Seventh Framework Programme FP7-NMP-2010, under Grant Agreement No. 263007 (acronym CARENA).

■ REFERENCES

(1) Xiong, Y.; Rodewald, P. G.; Chang, C. D. *J. Am. Chem. Soc.* **1995**, *117*, 9427−9431.
(2) Chen, N. Y.; Garwood, W. E. *Catal. Rev.: Sci. Eng.* **1986**, *28*, 185−264.
(3) Olsbye, U.; Svelle, S.; Bjørgen, M.; Beato, P.; Janssens, T. V. W.; Joensen, F.; Bordiga, S.; Lillerud, K. P. *Angew. Chem., Int. Ed.* **2012**, *51*, 5810−5831.
(4) Studt, F.; Abild-Pedersen, F.; Bligaard, T.; Sørensen, R. Z.; Christensen, C. H.; Nørskov, J. K. *Science* **2008**, *320*, 1320−1322.
(5) Bond , G. *Catalysis by Metals* ; Academic Press : New York , 1962 .
(6) Toulhoat, H.; Raybaud, P. *J. Catal.* **2003**, *216*, 63−72.
(7) Corvaisier, F.; Schuurman, Y.; Fecant, A.; Thomazeau, C.; Raybaud, P.; Toulhoat, H.; Farrusseng, D. *J. Catal.* **2013**, *307*, 352−361.
(8) Sachtler, W. M. H.; Van Santen, R. A. *Adv. Catal.* **1977**, *26*, 69−119 DOI: 10.1016/S0360-0564(08)60070-X.
(9) Voltz, S. E.; Morgan, C. R.; Liederman, D.; Jacob, S. M. *Ind. Eng. Chem. Prod. Res. Dev.* **1973**, *12*, 294−301.
(10) Rioux, R. M.; Komor, R.; Song, H.; Hoefelmeyer, J. D.; Grass, M.; Niesz, K.; Yang, P.; Somorjai, G. A. *J. Catal.* **2008**, *254*, 1−11.
(11) Patience, G. S.; Benamer, A.; Chiron, F. X.; Shekari, A.; Dubois, J. L. *Chem. Eng. Process. Process Intensif.* **2013**, *70*, 162−168.
(12) Koermer , G. S. ; Hratko , L. ; U.S. Patent No. 6,548,446/B1, April 15, 2003 .
(13) Collier, P.; Golunski, S.; Malde, C.; Breen, J.; Burch, R. *J. Am. Chem. Soc.* **2003**, *125*, 12414−12415.
(14) Devi, R. N.; Meunier, F. C.; Le Goaziou, T.; Hardacre, C.; Collier, P. J.; Golunski, S. E.; Gladden, L. F.; Mantle, M. D. *J. Phys. Chem. C* **2008**, *112*, 10968−10975.
(15) He, J.; Yoneyama, Y.; Xu, B.; Nishiyama, N.; Tsubaki, N. *Langmuir* **2005**, *21*, 1699−1702.
(16) Sartipi, S.; van Dijk, J. E.; Gascon, J.; Kapteijn, F. *Appl. Catal., A* **2013**, *456*, 11−22.
(17) Sartipi, S.; Makkee, M.; Kapteijn, F.; Gascon, J. *Catal. Sci. Technol.* **2014**, *4*, 893−907.
(18) Miyamoto, M.; Kamei, T.; Nishiyama, N.; Egashira, Y.; Ueyama, K. *Adv. Mater.* **2005**, *17*, 1985−1988.
(19) Nishiyama, N.; Ichioka, K.; Park, D.-H.; Egashira, Y.; Ueyama, K.; Gora, L.; Zhu, W.; Kapteijn, F.; Moulijn, J. A. *Ind. Eng. Chem. Res.* **2004**, *43*, 1211−1215.
(20) Arnal, P. M.; Comotti, M.; Schüth, F. *Angew. Chem., Int. Ed.* **2006**, *45*, 8224−8227.
(21) Lee, I.; Joo, J. B.; Yin, Y.; Zaera, F. *Angew. Chem., Int. Ed.* **2011**, *50*, 10208−10211.
(22) Joo, S. H.; Park, J. Y.; Tsung, C.-K.; Yamada, Y.; Yang, P.; Somorjai, G. A. *Nat. Mater.* **2009**, *8*, 126−131.
(23) Galeano, C.; Guettel, R.; Paul, M.; Arnal, P.; Lu, A.-H.; Schüth, F. *Chem.—Eur. J.* **2011**, *17*, 8434−8439.
(24) Ikeda, S.; Ishino, S.; Harada, T.; Okamoto, N.; Sakata, T.; Mori, H.; Kuwabata, S.; Torimoto, T.; Matsumura, M. *Angew. Chem., Int. Ed.* **2006**, *45*, 7063−7066.
(25) Wang, G.-H.; Hilgert, J.; Richter, F. H.; Wang, F.; Bongard, H.-J.; Spliethoff, B.; Weidenthaler, C.; Schüth, F. *Nat. Mater.* **2014**, *13*, 293−300.
(26) Li, S.; Burel, L.; Aquino, C.; Tuel, A.; Morfin, F.; Rousset, J.-L.; Farrusseng, D. *Chem. Commun.* **2013**, *49*, 8507−8509.
(27) Li, S.; Boucheron, T.; Tuel, A.; Farrusseng, D.; Meunier, F. *Chem. Commun.* **2014**, *50*, 1824−1826.
(28) van der Puil, N.; Creyghton, E. J.; Rodenburg, E. C.; Sie, T. S.; van Bekkum, H.; Jansen, J. C. *J. Chem. Soc., Faraday Trans.* **1996**, *92*, 4609−4615.
(29) van der Puil , N. ; Janto-Saputro , I. B. ; van Bekkum , H. ; Jansen , J. C. In *Stud. Surf. Sci. Catal.* ; Hakze Chon , S.-K. I. , Young Sun , U. , Eds.; Elsevier : 1997 , *105* , 1341 − 1348 .
(30) van der Puil, N.; Dautzenberg, F. M.; van Bekkum, H.; Jansen, J. C. *Microporous Mesoporous Mater.* **1999**, *27*, 95−106.
(31) Wang, Y.; Tuel, A. *Microporous Mesoporous Mater.* **2008**, *113*, 286−295.
(32) Groen, J. C.; Perez-Ramirez, J. *Appl. Catal., A* **2004**, *268*, 121−125.
(33) Groen, J. C.; Peffer, L. A. A.; Pérez-Ramírez, J. *Microporous Mesoporous Mater.* **2003**, *60*, 1−17.

(34) Quinet, E.; Morfin, F.; Diehl, F.; Avenier, P.; Caps, V.; Rousset, J.-L. *Appl. Catal., B* **2008**, *80*, 195−201.
(35) Alayon, E. M. C.; Singh, J.; Nachtegaal, M.; Harfouche, M.; Van Bokhoven, J. A. *J. Catal.* **2009**, *263*, 228−238.
(36) Savitz, S.; Myers, A. L.; Gorte, R. J. *J. Phys. Chem. B* **1999**, *103*, 3687−3690.
(37) Hampson, J. A.; Rees, L. V. C. *J. Chem. Soc., Faraday Trans.* **1993**, *89*, 3169−3176.
(38) van de Graaf, J. M.; Kapteijn, F.; Moulijn, J. A. *AIChE J.* **1999**, *45*, 497−511.
(39) Sircar, S.; Hufton, J. *Adsorption* **2000**, *6*, 137−147.

CHEMISTRY OF MATERIALS

Article

pubs.acs.org/cm

Transition-Metal Nanoparticles in Hollow Zeolite Single Crystals as Bifunctional and Size-Selective Hydrogenation Catalysts

Shiwen Li, Alain Tuel,* David Laprune, Frédéric Meunier, and David Farrusseng

Institut de Recherches sur la Catalyse et l'Environnement de Lyon, IRCELYON, UMR 5256 CNRS-Université de Lyon 1, 2 Avenue Albert Einstein, 69626 Villeurbanne Cedex, France

Supporting Information

ABSTRACT: Transition-metal nanoparticles (Co, Ni, and Cu) encapsulated in hollow zeolite single crystals were prepared by recrystallization of impregnated bulk MFI crystals in the presence of tetrapropylammonium (TPAOH) solutions. The size and number of particles in hollow MFI depended mainly on the aluminum content. The encapsulation of the nanoparticles prevented them from growing, thus enabling the control of particle size even after high temperature treatments. For low metal loadings (<3 wt %), the mean particle sizes for Co, Ni, and Cu in hollow silicalite-1 were 3.5 ± 0.3, 3.1 ± 0.5, and 1.5 ± 0.2 nm, respectively. In the case of hollow ZSM-5, higher loadings (~8 wt %) could be obtained with mean particle sizes of 17 ± 2 nm, 13 ± 2 nm, and 15 ± 2 nm for Co, Ni, and Cu systems. The mechanism of transition metal nanoparticle formation was markedly different from that of noble metals. At high pH values, transition-metal cations first reacted with dissolved silica species yielding fibrous metal phyllosilicates that were located inside the crystal cavities. The metal phyllosilicates were then converted into nanoparticles upon reduction under H_2 at high temperature (500−750 °C). Silicalite-1 encapsulated Ni particles were used in the catalytic hydrogenation of substituted benzenes and showed an outstanding size-selectivity effect. Ni particles were accessible to toluene but not to mesitylene, confirming that the activity is directly related to the diffusion properties of molecules through the zeolite membrane.

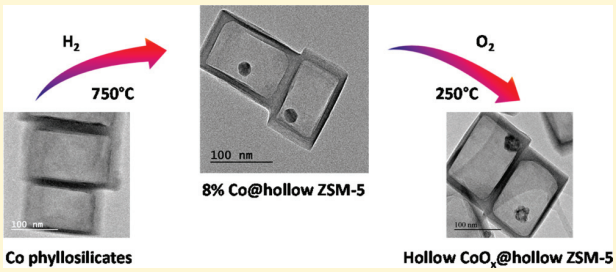

INTRODUCTION

Bifunctional heterogeneous catalysts that combine acid and hydrogenation/dehydrogenation functions form an important class of materials in the chemical industry, especially for fluid catalytic cracking (FCC) and hydro-isomerization processes.[1,2] A simple mechanical mixture of components does not necessarily ensure appropriate proximity between the acid and hydrogenating sites. Catalyst design at the nanoscale level with a hierarchical porosity is essential for obtaining the best operating performances.[3−5] As an example on Fischer−Tropsch synthesis, the introduction of mesoporosity in Co/ZSM-5 increases the activity and selectivity to the gasoline fraction (C5−C11) leading to an enhanced octane number due to the isomerization reactions.[6−8] When the metal particles are embedded into porous matrices, such as core−shell structures, the reactants must diffuse first through the porous layer before reaching the metal center, leading to high selectivity by molecular sieving mechanisms.[9−14] In core−shell systems, the zeolite shell can also determine the product selectivity by favoring the diffusion of less bulky molecules.[15−17] Yet, an excessive thickness of the zeolite shell may lead to undesirable mass transport limitations affecting the productivity of the desired reaction products.[16]

A yolk−shell structure is an alternative catalyst design that consists of metal particles encapsulated inside a hollow shell. The shell is usually made of a very thin layer of porous material that should limit mass transport limitation. Particles are generally monodispersed in size, isolated from each other, and prevented from sintering by Ostwald ripening mechanisms by the porous shell. Examples of such catalyst designs include metal or oxide particles encapsulated in mesoporous spheres made of carbon, SiO_2, and ZrO_2.[18−24]

We have pioneered the synthesis of yolk−shell materials for which the shell is a zeolite single crystal conferring unique catalytic properties. It consists of single noble metal nanoparticles encapsulated in hollow silicalite-1 single crystals (Au@silicalite-1 and Pt@silicalite-1; Figure S1, Supporting Information).[25,26] Some of us have already reported the preparation of hollow silicalite-1 by dissolution/recrystallization of bulk crystals with tetrapropylammonium (TPAOH) solutions.[27−29] The noble metal yolk−shell materials are prepared in a similar manner by treating metal impregnated zeolites in TPAOH solutions.

In this article, we have extended the synthesis of such nanodesigned catalysts to the case of transition metals (Co, Ni, and Cu), which significantly differs from that of noble metal systems. To the best of our knowledge, this is the first report on the encapsulation of transition metal nanoparticles in hollow

Received: October 24, 2014
Revised: December 1, 2014
Published: December 11, 2014

silicalite-1 single crystals. In addition, we report, also for the first time, bifunctional yolk−shell materials displaying outstanding metal nanoparticle dispersion inside ZSM-5 hollow crystals.

EXPERIMENTAL SECTION

Zeolite Synthesis. Silicalite-1 was prepared using tetraethyl orthosilicate (TEOS, Aldrich, 98%) and homemade 1 M TPAOH solutions obtained by reaction of the bromide solution with Ag_2O and water. The gel, with the composition $SiO_2{\cdot}0.4TPAOH{\cdot}35H_2O$ was heated at 170 °C under static conditions for 3 days. The resulting solid was calcined for 12 h at 525 °C in air yielding silicalite-1 crystals of approximately 200 nm × 150 nm × 140 nm in size.

ZSM-5 was synthesized following a published recipe.[30] The gel containing tetraethyl orthosilicate (TEOS, Aldrich, 98%), 1 M TPAOH solutions, and $NaAlO_2$ (Strem Chemicals, 99.9%) with composition $140SiO_2{\cdot}Al_2O_3{\cdot}30TPAOH{\cdot}1240H_2O$ was stirred at room temperature for 7 h, transferred into a Teflon-lined autoclave, and heated under static conditions at 180 °C for 7 days. After crystallization, the autoclaves were cooled, and the solids were recovered by centrifugation, washed with water, and dried overnight at 110 °C. The resulting ZSM-5 was then washed with a 5 M HCl solution at 90 °C for 5 h for the removal of the nonreacted aluminum species, and then centrifuged, washed until pH 7 was achieved, and finally dried at 110 °C in air. The resulting solid was calcined for 12 h at 525 °C in air yielding ZSM-5 microporous crystals that were characterized by an Al gradient (discussed below). Chemical analysis of the calcined zeolite gave a molar ratio Si/Al = 100.

Impregnation Methods. Zeolites were impregnated with aqueous solutions of cobalt, nickel, and copper nitrates ($Co(NO_3)_2{\cdot}6H_2O$, $Ni(NO_3)_2{\cdot}6H_2O$, and $Cu(NO_3)_2{\cdot}3H_2O$), which were all purchased from Sigma-Aldrich. The metal loading was achieved by the impregnation of the starting zeolites (silicalite-1 and ZSM-5) by aqueous solutions of metal precursors (2 mL of aqueous solution/g zeolite). The mixture was then stirred at 50 °C until the complete evaporation of water. A series of samples with different metal loadings was obtained by using metal nitrate solutions of various concentrations, typically from 0.16 to 1.23 mol/L.

Formation of Hollow Structures. Hollow structures were obtained by treating the metal impregnated zeolites in TPAOH solutions at 170 °C.[25,26] Typically, 1 g of zeolite was suspended in 4.15 mL of 1 M TPAOH solution and 3.35 mL of H_2O, and then the mixture was heated at 170 °C under static conditions for 24 h.

Thermal Treatments. All hollow zeolites were calcined in air at 450 °C for 6 h. The materials were then reduced under hydrogen at 750 °C (standard reduction temperature unless otherwise stated) for 3 h. The reduced samples are referred to as Me@Sil-1(x) or Me@ZSM-5(x), depending on the nature of the zeolite (Sil-1: silicalite-1) with Me = Co, Ni, or Cu and x = metal loading obtained by ICP. For selected samples, the reoxidation process was performed under static conditions in an oven at 250 °C for 2 h.

Characterization Techniques. TEM pictures were obtained on a Jeol 2010 LaB6 microscope operating at 200 kV. EDX measurements were performed using an EDX Link ISIS analyzer from Oxford Instruments.

X-ray diffraction (XRD) patterns of the zeolites were recorded on a Bruker (Siemens) D5000 diffractometer using CuKα radiation. Diffractograms were collected between 4 and 70° (2Θ) with steps of 0.02° and 1 s per step.

N_2 adsorption isotherms and BET surface areas were acquired on an ASAP 2010 (Micromeritics) apparatus on calcined samples preliminarily desorbed at 300 °C for 4 h. Chemical analyses were performed at the IRCELYON-CNRS Analytical Core facilities; metal contents were determined by inductively coupled plasma optical emission spectroscopy (HORIBA Jobin Yvon Activa ICP-OES).

Magnetic measurements were carried out at room temperature in an electromagnet (fields up to 21 kOe) using the Weiss extraction method. The degree of reduction of the sample was determined from the amount of metallic cobalt given by the saturation magnetization of the samples, obtained by extrapolating to zero the plot of the magnetization against $1/H$ (H = magnetic field). Temperature-programmed reduction of Co-containing hollow zeolite was performed on a BELCAT-B catalyst analyzer. The zeolite was pretreated at 200 °C/Ar and then treated under 5%H_2/Ar up to to 1000 °C using a rate of 10 °C/min.

NMR spectra were obtained on a Bruker DSX 400 spectrometer equipped with a double-bearing probe-head. Samples are spun at 10 kHz in 4 mm zirconia rotors. ^{27}Al NMR spectra were recorded with a pulse length of 0.6 s ($\pi/12$) and a recycle delay of 250 ms. Thermal analysis data were collected on a SETSYS Evolution-1200 apparatus from SETARAM. Approximately 20 mg of sample was heated from room temperature to 900 °C in 5%H_2/Ar at a heating rate of 10 °C/min.

Catalytic Reactions. The toluene and mesitylene hydrogenations were carried out using a diffuse reflectance FT-IR reaction cell similar to that described in detail elsewhere.[31] The reaction bed of the DRIFTS cell was made of a ceramic crucible. A mass of sample precisely weighing 10 mg was deposited on top of a SiC layer filling up the crucible. The system was always operated at ambient pressure, and the samples were reduced at 450 °C in pure H_2 for 90 min before the catalytic tests. Aromatic reactants were fed individually using a saturator kept at 0 °C, leading to partial pressures of 910 and 59 Pa for toluene and mesitylene, respectively. A flow of 50 mL/min of pure hydrogen was used as reactant carrier gas and fed through one saturator at a time. The reactor effluent was then analyzed using a 10 cm path-length gas cell fitted in a Thermo FT-IR spectrophotometer. The proportion of the reactant and the corresponding saturated product were determined through integration of two spectral regions corresponding to the C−H stretching vibration modes. In the case of toluene, methyl-cyclohexane was the only product observed, while trimethyl-cyclohexane was the only product obtained from mesitylene.

RESULTS AND DISCUSSION

Cobalt Encapsulated in Hollow Silicalite-1. The direct application of the synthesis procedure previously developed for noble metal nanoparticles encapsulated in silicalite-1 to transition metals did not yield the oxide nanoparticles, as was expected.[25,26] In the following, we thoroughly describe the synthesis and characterization of a Co@Sil-1(2.5) sample (Table 1), which is representative of the cases of other transition metals (summarized hereafter). As reported in our previous publications, silicalite-1 crystals are not stable at high temperature under highly alkaline pH conditions.[27−29] Zeolite crystals are partially dissolved, preferentially in the middle, which is the region where the density of framework defects sites

Table 1. Average Metal Particle Size and Aluminum Content in the Various Samples

sample	Si/Al ratio	average particle size (nm)
Co@Sil-1(2.5)	n.a.[c]	3.2
Co@Sil-1(3.1)	n.a.	3.7
Co@Sil-1(8.0)	n.a.	4.3
Co@ZSM-5(2.2)	102	15.1
Co@ZSM-5(7.4)	104	18.8
Ni@Sil-1(1.0)	n.a.	2.7
Ni@Sil-1(2.5)	n.a.	3.5
Ni@ZSM-5(2.6)	101	11.2
Ni@ZSM-5(7.7)	105	14.5
Cu@Sil-1(2.8)	n.a.	9.8(1.5)[a]
Cu@ZSM-5(3.0)	102	15−100(2.5)[b]

[a]Values in parentheses correspond to the average particle size for a second population of particles. [b]The population of large particles was very inhomogeneous. [c]n.a.: not applicable.

dx.doi.org/10.1021/cm503921f | Chem. Mater. 2015, 27, 276−282

is maximum. However, when dissolution is performed with TPAOH under appropriate conditions, dissolved species can recrystallize on the surface, leading to regular hollow crystals with well-defined cavities and walls. After the TPAOH treatment, hollow crystals did not contain particles, contrary to the case of noble metals (Figure S1, Supporting Information). The color of the sample was gray, which indicated the presence of some Co species, and TEM pictures surprisingly revealed the presence of dark long fibers covering the internal surface of the boxes (arrows in Figure 1a,b).

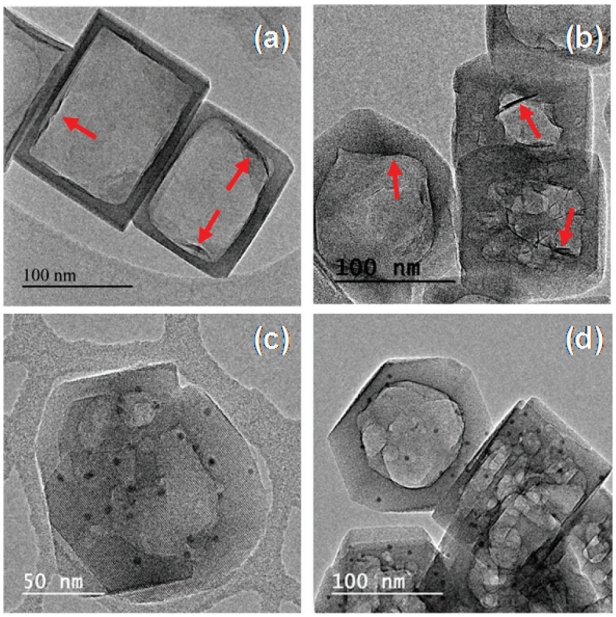

Figure 1. TEM pictures of Co@Sil-1(2.5) before (a,b) and after reduction (c,d) in hydrogen at 750 °C. Arrows in a and b indicate Co-silicate fibers.

This type of fibrous structure is often found in Co/SiO_2 catalysts and corresponds to cobalt phyllosilicates[32−34] In order to characterize the observed fibers, EDX and high resolution TEM measurements were carried out in the higher Co loading sample (Co@Sil-1(8.0), Figure 2d). EDX analysis on the fibers (red circle in Figure 2d) indicated 26 wt % Co, 24.5 wt % Si, and 49.5 wt % O (Figure S3, Supporting Information) corresponding to the formula $CoSi_2O_5{\cdot}2H_2O$, the $Si_2O_5^{2-}$ stoichiometry being characteristic of phyllosilicates according to the Nickel−Strunz classification.[35] The cobalt phyllosilicate structure was confirmed by the interlayer distance to ca. 0.9−0.95 nm, which corresponds to the value generally observed in these structures (Figure S2, Supporting Information).[36] In addition, we did not observe Co in the zeolite wall by EDX analysis (blue circle in Figure 2d and Figure S3, Supporting Information), which suggests that all Co atoms were in the form of Co-silicate fibers.

As fibers were not observed in the absence of Co, we assumed that they were formed during the TPAOH treatment when partial dissolution of the zeolite occurred. The reduction of Co silicate fibers to Co nanoparticles was monitored by temperature program reduction (TPR) and thermal gravimetric analysis (TGA) under hydrogen flow (Figures S4 and S5, Supporting Information). Both techniques indicated that phyllosilicates started to be reduced at 630 °C in agreement

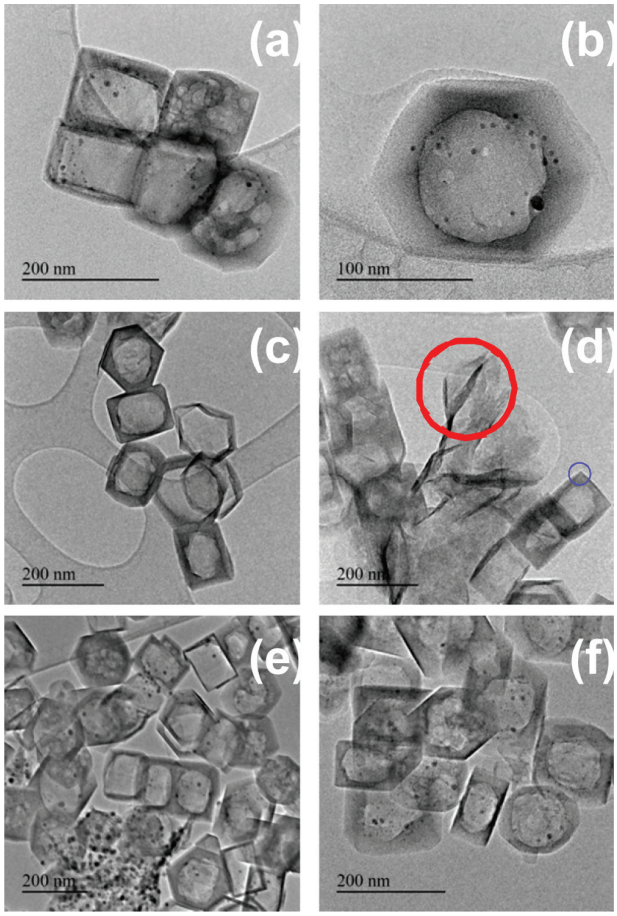

Figure 2. TEM pictures of Co@Sil-1(3.1) after reduction (a,b) and Co@Sil-1(8.0) before (c,d) and after reduction (e,f) in hydrogen at 750 °C. Red and blue circles in panel d indicate, respectively, Co phyllosilicates layers and zeolite walls on which EDX measurements have been performed (the EDX spectra of regions inside the two circles are given in Figure S3, Supporting Information).

with literature data for similar compounds.[37] The mass loss observed after 600 °C in the TGA curve was 0.57%, which could correspond to a reduction of approximately 82% of Co^{2+} to Co° (see Figure S5, Supporting Information). The Co silicate sample was then set to 750 °C for 10 h in 10% H_2 atmosphere to ensure sample reduction before magnetic measurements. The degree of reduction of Co@Sil-1(2.5) was estimated to be 85%, in excellent agreement with TGA results.[37] TEM pictures of a solid reduced at only 500 °C/H_2 were very similar to those of freshly prepared compounds, thus confirming that Co silicates had not been reduced at this lower temperature (not shown). Increasing reduction temperature to 750 °C led to the formation of particles inside hollow crystals, supporting the transformation of phyllosilicates into metallic cobalt (Figure 1c,d). TEM pictures of Co@Sil-1 (2.5) also revealed the presence of minor amounts of fibrous species (not shown), in agreement with the incomplete reduction of Co^{2+} species measured by magnetic measurement. In the case of noble metal encapsulation in hollow silicalite-1 and with comparable metal loading, Au and Pt@Sil-1 materials showed a single particle inside the big unique cavity of the crystal (Figure S1, Supporting Information).[25,26] In contrast, for Co containing hollow zeolite samples, many particles are observed in the

dx.doi.org/10.1021/cm503921f | Chem. Mater. 2015, 27, 276−282

internal cavities (Figure 1c,d). The particle size distribution is quite narrow with a mean size of 3.2 nm (Figure 1c,d and Figure S6a, Supporting Information). Another significant difference with noble metal containing hollow silicalite-1 is that a fraction of the Co particles was occluded in the zeolite walls (Figure 1c). We can propose that these differences with respect to noble metal based systems arose from the formation of the phyllosilicates at the TPAOH treatment step. The Co phyllosilicates formed both at the center of the crystals, where the defect concentration was highest, and near the edges of the crystals. The Co particles subsequently grew from the Co phyllosilicates during the reduction process. Since Co phyllosilicates are hardly mobile as they are attached to the zeolite, the reduction process led to dispersed Co nanoparticles strongly bound to the zeolite walls. In addition, phyllosilicates located at the center of the crystal could somewhat limit the dissolution process resulting in the formation of several cavities instead of one single large cavity as observed in the case of noble metal-based materials (Figure 1d).

With a somewhat higher Co loading of 3.1 wt %, Co@Sil-1(3.1) was similar to the previous solid except that Co particles were less regular in size, with large particles (5−11 nm) coexisting with a population of smaller particles (3.7 nm) (Figure 2a,b, Figure S6b, Supporting Information, and Table 1). For a much larger Co content of 8 wt % (Co@Sil-1(8.0)), a significant proportion of Co phyllosilicates was found outside zeolite crystals (Figure 2c and d), which eventually led to external particles after reduction (Figure 2e and f and Figure S6c, Supporting Information).

The presence of many particles outside hollow crystals for samples with high Co loadings suggested that the maximum incorporation level of Co species inside the silicalite-1 had been exceeded. Increasing Co loading mainly affected the mean particle size but not the average number of particles per cavity. Indeed, we have estimated that there were between 9 to 10 particles per hollow zeolite at three different Co loadings (2.5%, 3.1%, and 8.0%). When loading increased by a factor of 1.2 from 2.5 wt % to 3.1 wt %, the particle volume increased by a factor of 1.5 (the mean particle size changed from 3.2 to 3.7 nm) (Table 1 and Figure S6a,b, Supporting Information). It should be noted that the slight difference between the two factors obviously resulted from the presence of bigger particles at higher loading, with about 13% of particle having a diameter above 5 nm. Even at higher Co loading (8%), the correlation between loading and particle volume was confirmed, despite the presence of particles outside crystals in Co@Sil-1(8.0).

Cobalt Encapsulated in Hollow ZSM-5. The synthesis of Co-containing yolk−shell materials was extended to ZSM-5 as the zeolite shell. The desilication process was different when Al^{3+} was present in the structure. For silicalite-1, the creation of hollow structures in the presence of TPAOH solution was attributed to the preferential dissolution of the core of the crystals, a region with a high density of defects compared to that of the surface layers. If aluminum is homogeneously distributed in ZSM-5 crystals, treatment with TPAOH does not form regular hollow structures, and partial dissolution occurs throughout the crystals.[27,29] In fact, suitable ZSM-5 crystals must show a gradient of composition, exhibiting a Si-rich core and a Al-rich periphery. Hollow structures can thus be formed by the preferential dissolution of Si-rich domains of the crystals.[38] Desilication is generally performed using inorganic bases such as NaOH[39,40] or Na_2CO_3,[41,42] which leads to a significant loss of matter and nonuniform hollow structures in the crystals. We have followed the synthesis from Mei et al., which is known to provide an Al gradient in [Na]ZSM-5 nanocrystals, and we have shown for the first time that very regular ZSM-5 hollow crystals could be obtained upon TPAOH hydrothermal treatment.[30] In contrast to inorganic bases, dissolved species recrystallized in the presence of TPAOH and the overall Si/Al ratio remained equal to the ratio of the starting ZSM-5 (Table 1). X-ray diffraction and nitrogen physisorption measurements showed that the characteristics of synthesized hollow ZSM-5 were similar to those previously reported for hollow silicalite-1 (Figure S7,8, Supporting Information). In particular, the presence of a hysteresis loop in the isotherm confirmed the presence of the inner cavity. TEM images showed that zeolites were completely recrystallized with regular cavities, with a wall thickness similar to that observed on silicalite-1 (Figure 3a). Moreover, the ^{27}Al NMR

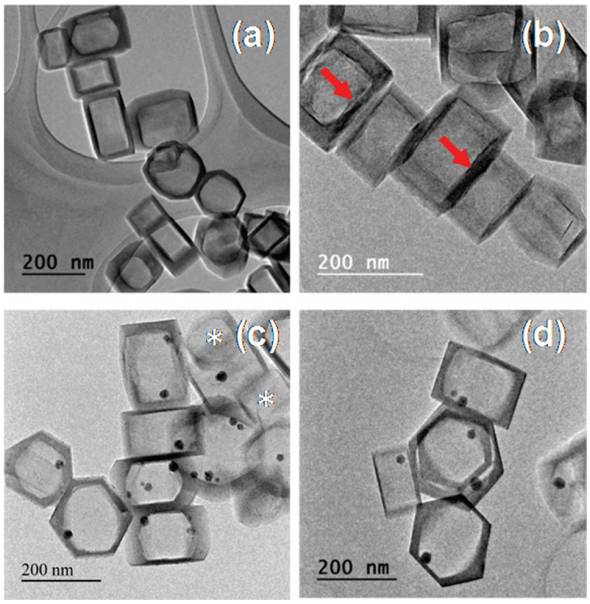

Figure 3. TEM pictures of hollow ZSM-5 (a), Co@ZSM-5(2.2) before (b) and after (c) reduction at 750 °C, and Co@ZSM-5(7.4) (d) after reduction at 750 °C. Arrows in panel b point out phyllosilicate layers on the internal surface of zeolite nanoboxes. Asterisks in panel c indicate empty nanoboxes.

spectrum confirmed that most of the Al species remained at framework positions during the formation of hollow structures, thus providing acidic sites (Figure S9, Supporting Information).

On the basis of these observations, treatments were performed on ZSM-5 impregnated with $Co(NO_3)_2$ solution. The presence of Co species did not alter the dissolution/recrystallization process as the morphology of hollow Co@ZSM-5 samples was similar to that of Co-free materials (Figure 3c,d).

After the TPAOH hydrothermal treatment, fibrous phyllosilicates were also observed. In contrast to the case of silicalite-1, phyllosilicates were scarce and generally formed a thin layer on the internal surface of the cavities (Figure 3b). After reduction under H_2 at 750 °C, Co particles were located only inside the cavity of hollow ZSM-5 crystals (Figure 3c,d), in contrast with Co@Sil-1 materials for which particles were also present in the walls. Another difference with the Co@silicalite-1 system was that the number of particles was generally limited to

dx.doi.org/10.1021/cm503921f | Chem. Mater. 2015, 27, 276−282

2 or 3 per hollow ZSM-5 for a comparable loading of 2.2 wt %. As a result, Co particles in Co@ZSM-5 (2.2) were 15 nm large in diameter, which is approximately 5 times larger than those found in Co@Sil-1(2.5) (Table 1).

The origin of such differences is not clear. We hypothesize that the presence of Al^{3+} limited the formation of Co phyllosilicates in the zeolite matrix. Since Co particles were not entrapped inside the zeolite walls, they were free to move into the cavities during reduction and thus grew by Ostwald ripening. By contrast to Co@silicalite-1 systems, larger Co loading of 7.4 wt % in ZSM-5 (Co@ZSM-5(7.4)) did not yield particles outside the hollow crystals. More than 95% of hollow zeolites contained at least one Co particle as shown in Figure 3d. We can note that increasing the loading by a factor of 3.4 from 2.2 to 7.4 wt % led to an increase of mean particle size from 15 to 19 nm, which corresponded to a 2-fold increase in volume (Figure S10-a,b, Supporting Information). This difference can be explained by the fact that ca. 16% of hollow zeolites in Co@ZSM-5(2.2) did not contain Co particles (see Figure 3c for evidence of empty shells).

The stability and the evolution of the morphology of the particles during oxidation/reduction cycles were followed by TEM (Figure 4). After Co@ZSM-5(7.4) was calcined at 250 °C in air for 2 h, a major modification of the shape of Co particles was noted, characterized by a hollow morphology with an irregular shape (Figure 4a,b). The formation of these structures has already been reported for many nanoparticle systems and has been attributed to a nanoscale Kirkendall effect, arising from a difference in diffusion rates between anions and cations.[43] TEM pictures at high magnification clearly revealed the polycrystalline nature of the cobalt oxide shells, with individual particle size of ca. 3−5 nm (Figure 4c,d). Then, the oxidized Co@ZSM-5(7.4) was reduced under H_2 leading to two populations of Co particles: large particles with a size similar to that observed on freshly reduced solids and very small ones (Figure 4e,f), which were formed by fragmentation and redispersion as already reported in many studies.[44]

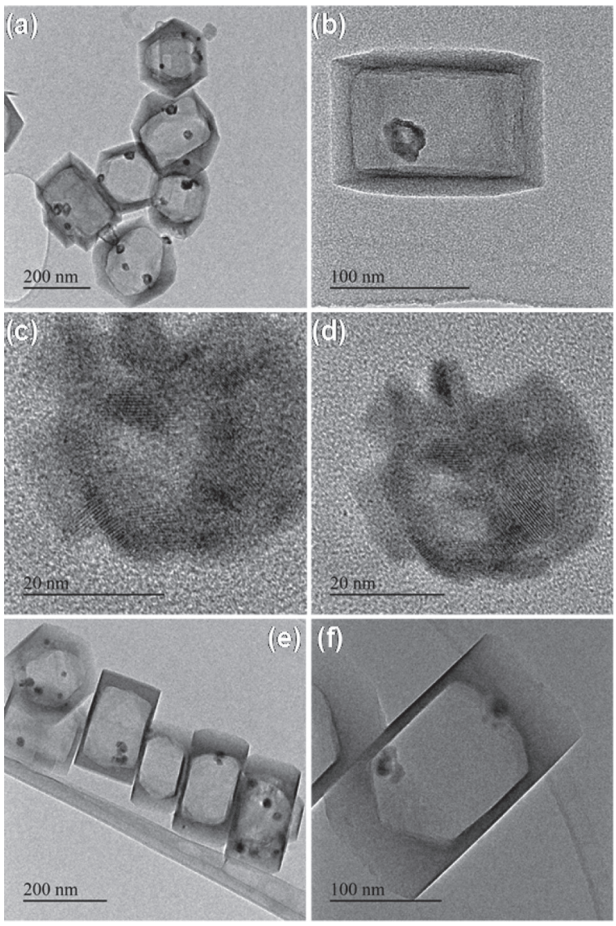

Figure 4. TEM pictures of Co@ZSM-5(7.4) after reoxidation at 250 °C (a,b) and subsequent reduction at 500 °C (e,f). Polycrystalline nature of Co-oxide hollow particles (c,d).

Nickel and Copper Encapsulated in Hollow Zeolites. Nickel- and copper-containing hollow zeolites were prepared following the same procedure (Table 1). For both metals, the mechanisms of formation were similar to that described above for cobalt. Ni and Cu phyllosilicates were formed during the dissolution/recrystallization step in the presence of TPAOH and were then converted to metal nanoparticles upon reduction at high temperature, yielding yolk−shell type materials. The main differences were the size and shape of the particle, as can be expected from the intrinsic properties of metals. In the case of Ni@Sil-1, the mean size of Ni particles varied proportionally to the Ni content as in the case of Co@Sil-1 (Figure S6d,e, Supporting Information, and Table 1). For example, when the loading increased from 1 to 2.5 wt %, the mean particle volume increased by a factor of 2.4.

Nickel particles were much larger in hollow ZSM-5 than in silicalite-1 for a similar Ni content, which is consistent with previously observed trends for Co-based systems (Table 1 and Figure S10c, Supporting Information). The mean particle size for Ni-ZSM-5 (2.6) was 11.2 nm against 3.5 nm for Ni-Sil-1 (2.5). In sample Ni-ZSM-5 (7.7) with a higher Ni loading, much larger particles were formed with well-defined crystallographic shapes, likely due to ripening processes (Figure S11, Supporting Information).

Though similar to Co and Ni-containing zeolites, copper-containing silicalite-1 materials were somewhat different in terms of particle size distribution. Indeed, most of the hollow silicalite-1 crystals contained a bimodal population of Cu particles, as one or two large particles coexisted with very small particles inside the same cavity (Table 1 and Figures S6f and S12, Supporting Information). Increasing the reduction temperature from 500 to 750 °C led to larger particles being formed by aggregation of the small ones (data not shown). However, even at 750 °C, the aggregation mechanism was not complete, and many nanoparticles of 1−2 nm were still present. As for the case of silicalite-1, ZSM-5 crystals containing Cu particles clearly exhibited two distinct populations in the same box: one big aggregate with a size up to 40 nm surrounded by many nanoparticles of ca. 1−2 nm (Figure S13, Supporting Information). In contrast to the case of Cu@Sil-1, only half of the hollow zeolite crystals contained a large particle despite reduction at 750 °C under H_2. However, these crystals were not Cu-free, and TEM pictures revealed that they contained fibrous matter similar to phyllosilicates observed before reduction.

The presence of Cu phyllosilicates in samples reduced at 750 °C suggests that they were much more difficult to reduce than Ni and Co phyllosilicates. The reduction was more effective in silicalite-1, in which Cu-silicates were only detected at trace levels after treatment at 750 °C.

Catalytic Evaluation of Ni@Sil-1(1.0). Ni@Sil-1(1.0) was evaluated in the catalytic hydrogenation of substituted

aromatics, and its catalytic performance was compared to that of a traditional supported Ni-based catalyst. The conversion of toluene and mesitylene (i.e., 1,3,5-trimethylbenzene) were both significant over the supported Ni catalyst (Figure 5).

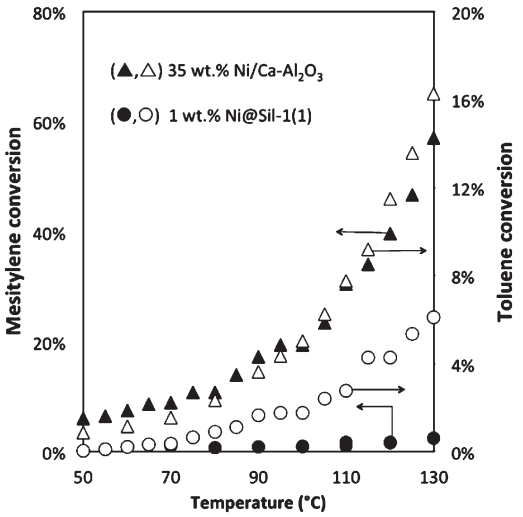

Figure 5. Conversion of toluene (open symbols) and mesitylene (closed symbols) at various temperatures over 9.4 mg of 1 wt % Ni@Sil-1(1.0) (●,○) and 14.2 mg of 35 wt % Ni/Ca−Al_2O_3 commercial catalyst (▲,△).

In contrast, the conversion of mesitylene was essentially negligible over the Ni@Sil-1(1.0), while this sample was still able to convert toluene. Similar to the case of Pt@silicalite-1,[26] these data clearly indicate that the transport of the bulkier mesitylene was suppressed through the zeolite layer. The kinetic diameter of mesitylene is significantly larger than the pore size of silicalite-1, while toluene can readily diffuse into this microporous solid. These data can therefore be rationalized by proposing that the zeolite shell surrounding the Ni particles was essentially free of mesoporous defects and was acting as a near-ideal membrane permeable to toluene but not mesitylene. Moreover, it also supports the absence of particles on the outside part of the nanoboxes, in agreement with the TEM analysis presented above. The molecular sieving properties of these transition metal-based catalysts are mirrored by that obtained over Pt nanoparticles inside hollow silicalite-1 single crystals.[26]

■ CONCLUSIONS

We have reported for the first time the synthesis and characterization of a hollow ZSM-5 single crystal by dissolution−recrystallization of bulk crystals. The starting bulk crystals must exhibit a gradient of composition with a Si-rich core and an Al-rich periphery. In the presence of TPAOH, hollow structures were formed, similar to those obtained with silicalite-1, with regular walls of ca. 20 nm thick. The presence of trivalent acid sites in hollow ZSM-5 was confirmed by ^{27}Al NMR.

Hollow silicalite-1 and ZSM-5 single crystals containing uniform transition metal particles were prepared for the first time. The synthesis involves the dissolution−recrystallization of bulk crystals previously impregnated with the corresponding nitrate solutions. In contrast to Au and Pt @ silicalite-1, all solids were obtained by reduction of fibrous phyllosilicates formed inside the cavities by reaction between silicate and metal species at high pH values and temperature. For hollow silicalite-1 systems at low loading, the mean particle sizes were 3.5 ± 0.3 and 3.1 ± 0.5 nm for Co and Ni, respectively. Larger loading could be obtained in ZSM-5, with mean particle sizes of 17 ± 2 nm for Co and 13 ± 2 nm for Ni. Upon oxidation, Co particles adopted a polycrystalline hollow morphology, resulting from a nanoscale Kirkendall effect.

The molecular sieving of the zeolite shell was demonstrated by the difference in hydrogenation conversions between toluene and mesitylene, the latter being too bulky to pass through the zeolite membrane and reach the nanoparticles. We believe that this new family of bifunctional catalysts showing well-controlled particle size and location opens new exciting perspectives in size-selective and bifunctional catalysis.

■ ASSOCIATED CONTENT

Ⓢ Supporting Information

Particle size distributions of Co-, Ni-, and Cu-containing hollow zeolites (silicalite-1 and ZSM-5) and their characterization by TPR, TEM, N2 adsorption, XRD, TGA, EDX, and NMR. This material is available free of charge via the Internet at http://pubs.acs.org.

■ AUTHOR INFORMATION

Corresponding Author

*E-mail: alain.tuel@ircelyon.univ-lyon1.fr.

Notes

The authors declare no competing financial interest.

■ ACKNOWLEDGMENTS

We thank scientific services of IRCELYON. This study has been supported by the European Union Seventh Framework Programme FP7-NMP-2013, under Grant Agreement number 604277(acronym FASTCARD).

■ REFERENCES

(1) Marcilly, C. *Acido-Basic Catalysis: Application to Refining and Petrochemistry*; TECHNIP Ophrys Editions: Paris, France, 2006; Vol. 2.
(2) Corma, A.; García, H. *Chem. Rev.* **2003**, *103*, 4307.
(3) Verheyen, E.; Jo, C.; Kurttepeli, M.; Vanbutsele, G.; Gobechiya, E.; Korányi, T. I.; Bals, S.; Van Tendeloo, G.; Ryoo, R.; Kirschhock, C. E. A.; Martens, J. A. *J. Catal.* **2013**, *300*, 70.
(4) Koekkoek, A. J. J.; Kim, W.; Degirmenci, V.; Xin, H.; Ryoo, R.; Hensen, E. J. M. *J. Catal.* **2013**, *299*, 81.
(5) Na, K.; Jo, C.; Kim, J.; Cho, K.; Jung, J.; Seo, Y.; Messinger, R. J.; Chmelka, B. F.; Ryoo, R. *Science* **2011**, *333*, 328.
(6) Sartipi, S.; Parashar, K.; Valero-Romero, M. J.; Santos, V. P.; van der Linden, B.; Makkee, M.; Kapteijn, F.; Gascon, J. *J. Catal.* **2013**, *305*, 179.
(7) Sartipi, S.; Parashar, K.; Makkee, M.; Gascon, J.; Kapteijn, F. *Catal. Sci. Technol.* **2013**, *3*, 572.
(8) Sartipi, S.; Alberts, M.; Santos, V. P.; Nasalevich, M.; Gascon, J.; Kapteijn, F. *ChemCatChem* **2014**, *6*, 142.
(9) Cai, J.; Ma, H.; Zhang, J.; Song, Q.; Du, Z.; Huang, Y.; Xu, J. *Chem.—Eur. J.* **2013**, *19*, 14215.
(10) Hojholt, K. T.; Laursen, A. B.; Kegnaes, S.; Christensen, C. H. *Top. Catal.* **2011**, *54*, 1026.
(11) Laursen, A. B.; Hojholt, K. T.; Lundegaard, L. F.; Simonsen, S. B.; Helveg, S.; Schüth, F.; Paul, M.; Grunwaldt, J.-D.; Kegnoes, S.; Christensen, C. H.; Egeblad, K. *Angew. Chem., Int. Ed.* **2010**, *49*, 3504.
(12) Wu, Z.; Goel, S.; Choi, M.; Iglesia, E. *J. Catal.* **2014**, *311*, 458.
(13) Tang, Q.; Zhang, Q.; Wang, P.; Wang, Y.; Wan, H. *Chem. Mater.* **2004**, *16*, 1967.

(14) Goel, S.; Wu, Z.; Zones, S. I.; Iglesia, E. *J. Am. Chem. Soc.* **2012**, *134*, 17688.
(15) Collier, P.; Golunski, S.; Malde, C.; Breen, J.; Burch, R. *J. Am. Chem. Soc.* **2003**, *125*, 12414.
(16) Miyamoto, M.; Kamei, T.; Nishiyama, N.; Egashira, Y.; Ueyama, K. *Adv. Mater.* **2005**, *17*, 1985.
(17) Nishiyama, N.; Ichioka, K.; Park, D.-H.; Egashira, Y.; Ueyama, K.; Gora, L.; Zhu, W.; Kapteijn, F.; Moulijn, J. A. *Ind. Eng. Chem. Res.* **2004**, *43*, 1211.
(18) Galeano, C.; Güttel, R.; Paul, M.; Arnal, P.; Lu, A. H.; Schüth, F. *Chem.—Eur. J.* **2011**, *17*, 8434.
(19) Arnal, P. M.; Comotti, M.; Schüth, F. *Angew. Chem., Int. Ed.* **2006**, *45*, 8224.
(20) Lin, C.-H.; Liu, X.; Wu, S.-H.; Liu, K.-H.; Mou, C.-Y. *J. Phys. Chem. Lett.* **2011**, *2*, 2984.
(21) Joo, S. H.; Park, J. Y.; Tsung, C.-K.; Yamada, Y.; Yang, P.; Somorjai, G. A. *Nat. Mater.* **2009**, *8*, 126.
(22) Park, J. C.; Lee, H. J.; Kim, J. Y.; Park, K. H.; Song, H. *J. Phys. Chem. C* **2010**, *114*, 6381.
(23) Yin, Y.; Chen, M.; Zhou, S.; Wu, L. *J. Mater. Chem.* **2012**, *22*, 11245.
(24) Chen, Z.; Cui, Z.-M.; Niu, F.; Jiang, L.; Song, W.-G. *Chem. Commun.* **2010**, *46*, 6524.
(25) Li, S.; Burel, L.; Aquino, C.; Tuel, A.; Morfin, F.; Rousset, J.-L.; Farrusseng, D. *Chem. Commun.* **2013**, *49*, 8507.
(26) Li, S.; Boucheron, T.; Tuel, A.; Farrusseng, D.; Meunier, F. *Chem. Commun.* **2014**, *50*, 1824.
(27) Wang, Y.; Tuel, A. *Microporous Mesoporous Mater.* **2008**, *113*, 286.
(28) Wang, Y.; Lin, M.; Tuel, A. *Microporous Mesoporous Mater.* **2007**, *102*, 80.
(29) Burel, L.; Tuel, A. *Microporous Mesoporous Mater.* **2013**, *174*, 90.
(30) Mei, C.; Liu, Z.; Wen, P.; Xie, Z.; Hua, W.; Gao, Z. *J. Mater. Chem.* **2008**, *18*, 3496.
(31) Meunier, F. C.; Goguet, A.; Shekhtman, S.; Rooney, D.; Daly, H. *Appl. Catal., A* **2008**, *340*, 196.
(32) Kababji, A. H.; Joseph, B.; Wolan, J. T. *Catal. Lett.* **2009**, *130*, 72.
(33) Puskas, I.; Fleisch, T. H.; Full, P. R.; Kaduk, J. A.; Marshall, C. L.; Meyers, B. L. *Appl. Catal., A* **2006**, *311*, 146.
(34) Grams, J.; Ura, A.; Kwapiński, W. *Fuel* **2014**, *122*, 301.
(35) Strunz, H. N.; Strunz, E. H. *Mineralogical Tables: Chemical-Structural Mineral Classification System*, 9th ed.; Schweizerbart: Stuttgart, Germany, 2001.
(36) Jabłoński, J. M.; Wołcyrz, M.; Krajczyk, L. *J. Catal.* **1998**, *173*, 530.
(37) Lim, S.; Ciuparu, D.; Chen, Y.; Pfefferle, L.; Haller, G. L. *J. Phys. Chem. B* **2004**, *108*, 20095.
(38) Fodor, D.; Pacosova, L.; Krumeich, F.; van Bokhoven, J. A. *Chem. Commun.* **2014**, *50*, 76.
(39) Groen, J. C.; Peffer, L. A. A.; Moulijn, J. A.; Pérez-Ramirez, J. *Microporous Mesoporous Mater.* **2004**, *69*, 29.
(40) Li, J.; Li, X.; Zhou, G.; Wang, W.; Wang, C.; Komarneni, S.; Wang, Y. *Appl. Catal., A* **2014**, *470*, 115.
(41) Kim, Y. H.; Lee, K. H.; Nam, C.-M.; Lee, J. S. *ChemCatChem* **2012**, *4*, 1143.
(42) Fathi, S.; Sohrabi, M.; Falamaki, C. *Fuel* **2014**, *116*, 529.
(43) Yang, Z.; Yang, J.; Bergstrom, J.; Khazen, K.; Pileni, M.-P. *Phys. Chem. Chem. Phys.* **2014**, *16*, 9791.
(44) Sadasivan, S.; Bellabarba, R. M.; Tooze, R. P. *Nanoscale* **2013**, *5*, 11139.

RESUME en français

Les matériaux « cœur-coquille » composés d'une nanoparticule métallique encapsulée à l'intérieur de coquilles inorganiques (oxydes, carbone …) attirent de plus en plus l'attention par leurs propriétés particulières, en particulier dans le domaine de la catalyse. Les particules métalliques sont protégées par la coquille, qui empêche entre autres le frittage et la croissance des particules à haute température. Cependant, les coquilles sont généralement méso à macroporeuses et elles ne peuvent pas jouer le rôle de tamis moléculaire pour les molécules de taille nanométrique. En revanche, les zéolithes sont des solides cristallins microporeux dont les pores bien définis permettent une forte discrimination des réactifs basée sur la taille, la forme ou leur coefficient de diffusion. L'objectif de cette thèse visait à la synthèse de catalyseurs de type cœur-coquille dans lesquels la coquille est une zéolite microporeuse de structure MFI (silicalite-1 et ZSM-5), le cœur étant soit une particule de métal noble (Au, Ag, Pt, Pd), soit des alliages de ces différents métaux, soit enfin un métal de transition (Co, Ni, Cu). Ces catalyseurs ont été appliqués dans des réactions d'hydrogénation sélective (aromatiques substitués) et l'oxydation sélective de CO en présence d'hydrocarbures. Nous avons ainsi montré que la coquille zéolithique, tout en protégeant les particules du frittage, modifie la sélectivité des réactions en interdisant aux réactifs volumineux d'atteindre les sites catalytiques.

TITLE

Metal Nanoparticles Encapsulated in Membrane-like Zeolite Single Crystals - Application to Selective Catalysis

ABSTRACT in english

Nanostructured yolk-shell materials, which consist of metal nanoparticle cores encapsulated inside hollow shells, attract more and more attention in material science and catalyst applications during the last two decades. Metal particles are usually highly mono-dispersed in size and isolated from each other by the shell, which prevents growth by sintering at high temperature. Because they are generally made of meso/macroporous oxides or amorphous carbon, shells cannot carry out molecular sieve-type separation of molecules at the nanometric scale. The aim of the present thesis was to synthesize yolk-shell catalyst with microporous zeolite shells (silicalite-1 and ZSM-5), containing noble (Au, Pt, Pd) transition (Co, Ni, Cu) and alloy metal nanoparticles. Zeolites are crystalline microporous solids with well-defined pores capable of discriminating nanometric reactants on the basis of size, shape and diffusion rate. Zeolite-based yolk-shell catalysts have been applied in selective hydrogenation (toluene and mesitylene) and oxidation (CO) reactions in the presence of hydrocarbons. Zeolite shells not only plaid a key role as membranes, thus changing selectivities as compared to conventional supported catalysts, but they also protected metal nanoparticles from sintering under reaction conditions.

DISCIPLINE

Material science and Catalysis

MOTS CLES/KEY WORDS

Yolk-shell material, heterogeneous catalysis, metal nanoparticles, alloy particles, hollow zeolite, silicalite-1, ZSM-5, selective hydrogenation, selective CO oxidation,

INTITULE ET ADRESSE DE L'U.F.R. OU DU LABORATOIRE

IRCELYON, 2 avenue Albert Einstein, 69626 Villeurbanne, Cedex